Doctoral Dissertation
Doctoral Program in Aerospace Engineering (35^{th}cycle)

Numerical Simulation and Aerodynamic Design of Small-Scale Rotary-Wing for Unmanned Aerial Systems in Terrestrial and Martian Applications

By

Manuel Carreño Ruiz

******

Supervisor(s):
Prof. Domenic D'Ambrosio

Doctoral Examination Committee:
Prof. Jean-Marc Moschetta, Referee, ISAE SUPAERO
Prof. Daniele Ragni, Referee, TU Delft
Prof. Luigi Vigevano, Politecnico di Milano
Prof. Roberto Marsilio, Politecnico di Torino
Prof. Francesco Avallone, Politecnico di Torino

Politecnico di Torino
2023

Declaration

I hereby declare that, the contents and organization of this dissertation constitute my own original work and does not compromise in any way the rights of third parties, including those relating to the security of personal data.

Manuel Carreño Ruiz
2023

* This dissertation is presented in partial fulfillment of the requirements for **Ph.D. degree** in the Graduate School of Politecnico di Torino (ScuDo).

"Luck is what happens when preparation meets opportunity."

Acknowledgements

I want to thank all the professors who positively influenced my aeronautical education at Seville University, Technical School of Madrid (UPM), and Politecnico di Torino. I especially want to thank Professor Domenic D'Ambrosio for his invaluable guidance and always providing the perfect advice during these years. Your example has guided me into becoming a "CFD guy." I would also like to acknowledge Professor Miguel Perez-Saborid for triggering my passion for Fluid Dynamics with his practical lessons in the early stages of my career.

I am grateful to all the students, colleagues, and collaborators with whom I have shared research activities. A special mention goes to the flight mechanics group at Politecnico di Torino. Particularly to Dr. Nicoletta Bloise for her support, thorough work, and making every day better with her optimism.

I would also like to thank family and friends who gave me the extra thrust I needed to successfully cruise through 10+ years of Aeronautical education. I thank my lifetime colleagues, Carmen Velarde and Regina Horas, for their support and friendship during these years. Finally, I would especially like to thank my mother, who has always been there for me, even when I was abroad. Her wise words always create added value and guide me toward the correct path.

Abstract

Small-scale rotary-wing Unmanned Aerial Systems (UAS) have gained increasing attention for various applications such as environmental monitoring, search and rescue, military surveillance, and Martian exploration. However, the design of these UAS requires careful consideration of their aerodynamic performance, particularly of their rotors, which play a crucial role in the overall efficiency and stability of the system. Numerical simulation is a crucial tool for designing small-scale rotors, as experimental testing of these systems can be expensive and time-consuming. However, the accuracy of numerical simulations depends on the fidelity of the models used, and the computational cost of high-fidelity models can be prohibitive.

In this thesis, we explore different numerical approaches to simulate the aerodynamic performance of small-scale rotors, ranging from reduced-order models based on the blade element momentum theory and vortex methods to high-fidelity Computational Fluid Dynamics (CFD) simulations. We can distinguish two low Reynolds number regimes. The very-low Reynolds number regimes, with Reynolds number, comprised between $10^4 - 10^5$, and the ultra-low Reynolds number regime where Reynolds number falls below $10^3 - 10^4$. The former is typically found in small-scale UAS performing terrestrial applications. In this regime, the boundary layers usually present transition to turbulence, and separations bubbles are typical. The former is typically found in high altitudes on Earth and the Martian atmosphere. The exotic combination of high subsonic Mach numbers and ultra-low Reynolds numbers requires thoroughly revising the design guidelines for airfoils and rotors operating in these conditions. Different validation exercises of the flows in these regimes have been performed, showing how computational fluid dynamics, with the appropriate experimental validation, can be used to gain invaluable insight into complex rotor and airfoil aerodynamics. We also discuss different efficient airfoil and rotor geometries designed ad-hoc for the Martian operation regime, stating the substantial differences from traditional lifting surfaces. All the developed reduced

order models used for the design in low Reynolds number conditions have been packed into a Matlab APP, *ROT-8*, including different design and analysis modules for rotors and airfoils.

Building on the previous studies, several UAS terrestrial applications have been assessed, applying the lessons learned on rotor modeling in realistic dynamical systems. These applications are the study of an innovative passive swashplateless rotor, the analysis of multicopter maneuvers, focusing on those close to obstacles, and finally, the assessment and numerical modeling of a multicopter spraying operation in the vineyard scenario. These applications require understanding the dynamic fluid-body interactions coupling aerodynamic and dynamic solvers. We have created a virtual testing environment implementing quadcopters and hexacopters, including a PID controller that allows reproducing real maneuvers like hovering near obstacles or flying and spraying over a vineyard. In particular, for the vineyard application, we couple multicopter maneuvers, aerodynamics, and droplet trajectories to assess the effectiveness of the spray operation. The developed model has been verified with other simplified and well-known reduced-order models, and experimental validation of the multiphase rotor-droplet interactions has been performed.

Contents

List of Figures

List of Tables

Nomenclature

Superscripts

p	considered particle quantity
q	influence particle quantity

Subscripts

σ	regularized quantity
j	panel j quantity

Other Symbols

α	Angle of attack
β	Blade geometrical twist
$\frac{C_l}{C_d}$	Aerodynamic efficiency
$\frac{{C_l}^{1.5}}{C_d}$	Range efficiency
Γ	circulation
γ	Intermittency
μ	dynamic viscosity
ν	kinematic viscosity
Ω	Rotation rate in radians per second
ω	Specific dissipation rate

ω_i	Rotor i angular velocity
ω_S	Vector with the square of the rotor angular velocities: $[\omega_1^2, \ldots, \omega_n^2]^T$
ϕ	Inflow angle
ρ	Density
σ	Smoothing radius
σ_l	Local solidity: $\sigma_l = \frac{Nc(r)}{2\pi r}$
σ_R	Solidity: $\sigma_R = \frac{S_{rotor}}{S_{disk}}$
σ_w	Weighing factor in the objective function
$\vec{\alpha}$	particle strength
$\vec{\omega}$	vorticity
$\vec{a_1}$	panel chord-wise vector
$\vec{a_3}$	panel normal vector
$\vec{u}$	velocity
$\vec{x}$	particle position
d_w	Tip-wall clearence
dA	panel/blade element area
k	Turbulent kinetic energy
K_D	Torque coefficient (PID-Control): $K_D = \frac{Q_i}{\omega_i^2}$
K_T	Thrust coefficient (PID-Control): $K_T = \frac{T_i}{\omega_i^2}$
N	Number of blades
R_h	Rotor hub radius
Re_θ	Momentum thickness Reynolds number

RF lifting line Relaxation Factor

T/P Rotor power loading

U_∞,V Freestream velocity

vol particle volume

BL Blade loading: $BL = \dfrac{C_T}{\sigma}$

c Airfoil chord

C_f Chord-wise skin-friction coefficient

C_P rotor power coefficient: $C_P = \frac{P}{\rho \pi \Omega^3 R^5}$

C_p Pressure coefficient

C_Q rotor torque coefficient: $C_Q = \frac{Q}{\rho \pi \Omega^2 R^5}$

C_T rotor thrust coefficient: $C_T = \frac{T}{\rho \pi \Omega^2 R^4}$

C_d Airfoil drag coefficient: $C_d = \dfrac{d}{\frac{1}{2}\rho V^2 c}$

C_l Airfoil lift coefficient: $C_l = \dfrac{l}{\frac{1}{2}\rho U_\infty^2 c}$

D Rotor diameter

d Airfoil drag

f Pedrizzetti's relaxation factor

FM Figure of merit: $FM = \dfrac{C_T^{1.5}}{\sqrt{2}C_P}$

h spacing between particles

l Airfoil lift

M Freestream Mach number (airfoils) and tip Mach (rotors)

P Rotor power consumption

Q Rotor torque

R Rotor radius

r radial coordinate

Re Reynolds number: $\frac{U_\infty\, c}{\nu}$ (Airfoils) and $\frac{\Omega\, 0.75R\, c_{0.75R}}{\nu}$ (Rotors)

RPM Rotation rate in revolutions per minute

T Rotor thrust

Tu Turbulence Intensity

TVR Turbulent Viscosity Ratio

W_{Mars} Weight under Martian gravitational acceleration

x_{re} Boundary layer reattachment location

x_{sep} Boundary layer separation location

x_{tr} Boundary layer transition location

Acronyms / Abbreviations

ADRC Active Disturbance Rejection Control

AMI Arbitrary Mesh Interface

AMR Adaptive Mesh Refinement

AOA Angle Of Attack

BCD Bounded Central Differences

BEM Blade Element Method

BVI Blade Vortex Interaction

CD Central Difference

CFD Computational Fluid Dynamics

CFL Courant Friedrich Levy

CSF Continuum Surface Force

DEP Double Edged Plate

DES Detached Eddy Simulation

DNS Direct Numerical Simulation

DOF Degree Of Freedom

DPM Dispersed Phase Model

FVW Free Vortex Wake

GPR Gaussian Process Regression

ILES Implicit Large Eddy Simulation

K-H Kelvin-Helmholtz

LBM Lattice Boltzmann Method

LCTM Local Correlation-Based Transition Model

LE Leading Edge

LES Large Eddy Simulation

LSB Laminar Separation Bubble

MAV Micro Aerial Vehicle

ML Machine Learning

MRF Moving Reference Frame

MRF Multiple Reference Frame

MSH Mars Science Helicopter

MUSCL Monotonic Upwind Scheme for Conservation Laws

NZPG Non-Zero Pressure Gradient

PID Proportional-Integral-Derivative

PIV Particle Image Velocimetry

PPP Plant Protection Product

RANS Reynolds-Averaged Navier Stokes

ROAMX Rotor Optimization for the Advancement of Mars eXploration

ROM Reduced Order Model

SOU Second Order Upwind

SST Shear Stress Transport

T-S Tolmien-Schlitching

TE Trailing Edge

TEF Trailing Edge Flap

UAM Urban Air Mobility

UAS Unmanned Aerial System

UASS Unmanned Aerial Spraying System

UIUC University of Illinois Urbana-Champaign

URANS Unsteady Reynolds Averaged Navier Stokes

VOF Volume Of Fluid

VPM Vortex Particle Method

WALE Wall-Adaptive Local Eddy-viscosity

WENO Weighted Essentially Non-Oscillatory

ZPG Zero Pressure Gradient

Chapter 1

Introduction

1.1 Motivation

The motivation for this research is to develop a better understanding of the aerodynamics of small-scale rotors and to provide guidance for designing more efficient and reliable unmanned aerial systems (UASs) for terrestrial and Martian applications. In particular, the performance of micro aerial vehicles (MAVs) in low-density conditions, such as the Martian atmosphere or high altitudes in the Earth's atmosphere, is especially challenging due to the extremely low Reynolds number that they encounter [24]. Generating lift/thrust in these conditions requires high speeds, which are also limited due to transonic effects. The different geometries necessary for these operation regimes require evaluating the performance prediction capabilities of different reduced-order models (ROMs) typically used for rotor performance estimations, such as the blade element momentum (BEM) method, the free vortex wake (FVW) method, or the vortex particle method (VPM). Despite the increasingly growing computational power available for research and industry, ROMs are still mandatory for preliminary design phases due to the significantly demanding computational cost of higher fidelity CFD simulations. A thorough comparative analysis, trading off these approaches' accuracy and computational cost, is mandatory at these reduced Reynolds number conditions, as the conclusions may possibly differ from those obtained at higher Reynolds numbers. The transition to turbulence is another complication in the numerical analysis performed in this regime. Transition modeling is not widely embraced in the community, mainly due to its high empirical content and the

need to fine-tune the models for different applications. The flow is not expected to undergo natural transition to turbulence for low Reynolds numbers applications. This means that the critical Reynolds number for the amplification of Tolmien-Schlitching (T-S) waves is not reached. For a flat plate with no pressure gradient, this value is around 500,000 and reduces as the pressure gradient increases [182]. For Reynolds numbers of 100,000 and below, boundary layers rarely undergo natural transition as the pressure gradient required to drop the critical Reynolds number to that level is too high for the boundary layer to withstand, resulting in separation. However, the laminar-turbulent transition may occur due to the exponential growth of the Kelvin-Helmholtz (K-H) instability in the separated shear layer [205]. This transition mechanism usually results in the formation of laminar separation bubbles (LSB), which alter the effective camber and thickness of the airfoil and, therefore, its performance [95]. Separation bubbles tend to be short and thin for higher Reynolds numbers, limiting their influence on airfoil performance. Separation bubbles are longer and thicker in the ultra-low Reynolds number regime, profoundly impacting performance. The study of LSB in this regime is critical as the relative importance of turbulence is reduced, and therefore, transition models tend to fail in predicting the transition location and, thus, the LSB morphology. Scale-resolving simulations such as Large Eddy Simulations (LES) and Direct Numerical Simulations (DNS) have been proven to predict this transition mechanism accurately [205, 83, 52]. However, they are computationally intensive, and only a few simplified test cases have been tested. Therefore, improving the transition models for this flow type is crucial.

This research aims to improve the performance of small-scale UAS applications in agriculture, infrastructure inspection, and disaster response. Apart from improving performance predictions using numerical models, it is also interesting to focus on understanding the complete UAS depending on its application. In this work, we aim to investigate several problems linked to rotor aerodynamics in different applications. One of these applications is the use of multirotors in agricultural spraying operations. The interaction between the rotor wake and the droplets is vital to reduce the drifting of plant protection products (PPPs) that can be potentially harmful to our health and reduce the efficiency of the operation [59]. Another critical operation of UAS is the flight close to obstacles. The ground and ceiling effects have been extensively studied in the literature, but the knowledge of the wall effect is still quite limited. When a multicopter approaches a wall, the rotor nearest to it experiences reduced thrust, leading to a global tilting moment that dangerously brings the vehicle close

to the wall [63]. It is, therefore, interesting to analyze the forces and moments induced by the vertical surfaces to ensure controllers can handle them. Finally, this work aims to improve the understanding of novel UAS approaches. One of these alternatives currently under investigation is using passive swashplateless rotors in coaxial helicopters. These rotors are partially articulated with a coupled lag-pitch hinge, and the blades' passive response to a synchronized sinusoidal input torque generates the desired control moments [153]. The numerical modeling of this type of rotor is extremely challenging due to the passive nature of the response and the complex aerodynamics of this pitching-lagging motion in an already rotating reference frame.

1.2 Literature Review

1.2.1 Very-Low Reynolds number Airfoil Aerodynamics

The regime of very low Reynolds numbers corresponds to the interval of Reynolds numbers based on the airfoil chord, ranging from 10,000 to 100,000. Within this particular range, the transition to turbulence typically occurs after the boundary layer's separation, which may reattach in the configuration of a laminar separation bubble. The significance of laminar separation bubbles in the low Reynolds number regime lies in their substantial contribution to the non-linearity observed in the $C_l(\alpha)$ curves of airfoils. This non-linearity leads to a marked deviation, even at small angles of attack (AOA), from the conventional expression $C_l = 2\pi(\alpha - \alpha_{L=0})$ as posited by Prandtl's thin airfoil theory. The transition process within separation bubbles occurs at significantly lower Reynolds numbers than the conventional natural transition threshold. The amplification of Tollmien-Schlichting (T-S) waves is similar to that observed in natural transition. However, adverse pressure gradients result in the premature separation of the flow, which in turn induces Kelvin-Helmholtz (KH) instability in the separated shear layer. This instability causes the shear layer to roll up into vortices, ultimately leading to the onset of turbulence, as noted by Schlichting [182]. According to Hain [94], turbulent flow can effectively transport momentum toward the wall, which in turn aids in the reattachment of the separation bubble. The aerodynamic coefficients are influenced by the presence of a separated flow region, which alters the effective camber and thickness of the airfoil, as noted by Hansen et

al. [95]. The position and dimension of the LSB can vary depending on the Reynolds number and AOA. In very-low Reynolds number conditions, it is common for airfoils to exhibit trailing edge separation without reattachment at low angles of attack. As the AOA increases, the adverse pressure gradient intensifies, causing the separation point to shift upstream. This phenomenon facilitates an earlier transition. In cases where the separation point is located far enough upstream to enable the complete transition to turbulent flow, the flow reattaches in the vicinity of the trailing edge. An escalation in the angle of attack shifts the separation point toward the leading edge. At a certain threshold of AOA, the adverse pressure gradient becomes exceedingly intense, leading to the complete detachment of the turbulent boundary layer. This phenomenon causes a significant separation on the airfoil's suction side, resulting in a stall. Stall may be defined as a drop in lift coefficient followed by a dramatic increase in the drag coefficient. We will see how this classical definition of stall does not apply to ultra-low Reynolds number airfoils as they show a high lift regime even after leading-edge separation. Their drag increases significantly, but the lift does not drop.

Various authors have analyzed the behavior of airfoils at low Reynolds numbers through experimental and numerical means. The UIUC Applied Aerodynamics Group conducted extensive experimental testing [204] on multiple airfoils, leading to the establishment of design guidelines for low Reynolds number airfoils. As a result of this research, the SD7003 has become one of the most widely used low Reynolds airfoils. McGhee, Walker, and Millard conducted a comprehensive experimental study [133] at NASA Langley on the Eppler 387 airfoil, which is also widely used for low Reynolds numbers, to investigate the airfoil's characteristics. In [148], the Particle Image Velocimetry (PIV) experimental technique was employed to conduct a comparative analysis of the separation bubble of the SD7003 airfoil in three distinct facilities. Recently, there has been a growing interest in Mars flight, prompting a research team in Japan to study various airfoils, including the Ishii airfoil, at remarkably low Reynolds numbers as of 23,000. [10, 12].

Two of the earliest computational approaches are by Eppler et al. [79, 73], and Drela et al. [74, 75], the latter creating Xfoil, an efficient but yet successful design tool that couples inviscid analysis based on the panel method and integral boundary layer approaches to account for viscous effects. The e^N method is incorporated in Xfoil for transition prediction, yielding remarkable outcomes despite its relatively minimal computational expense. Radespiel et al. [163] presented more advanced

techniques that combine Reynolds-Averaged Navier-Stokes (RANS) with the e^N method. Subsequently, local correlation-based transition models (LCTM) were developed, including the empirical methodology introduced with the γ-Re_θ model by Menter and Langtry [137, 115], and the phenomenological methodology established with the Laminar-Kinetic Energy Model by Walters and Cokljat [214]. With a few exceptions, the literature lacks sufficient documentation on implementing the γ-Re_θ transition model for airfoils operating in the very-low Reynolds number regime. Babajee [14] employed the RANS equations along with the γ-Re_θ transition model to forecast transition occurring in the suction side of the airfoils of low-pressure turbines blades. In the study conducted by Choudhry [61], an examination of long separation bubbles on thick airfoils was performed utilizing two distinct models, namely the γ-Re_θ transition model and the laminar-kinetic energy model. Salimipour [173] presents a modified version of the laminar-kinetic energy model, which is then compared to the γ-Re_θ transition model in the very-low Reynolds number regime for a NACA 0012 airfoil. Götten's study [91] provides a comprehensive validation of the γ-Re_θ transition model across multiple airfoils, specifically at Reynolds numbers greater than 200,000. Several authors have also performed high-fidelity Large Eddy Simulation (LES) or Direct Numerical Simulation (DNS) on conventional airfoils operating at low Reynolds numbers. These approaches do not need a transition model since they can resolve smaller turbulence length scales and numerically capture transition. Therefore, LES and DNS results are valuable references for tuning transition models.

The airfoil SD7003 has been subjected to rigorous testing and has become a popular benchmark. Galbraith and Visbal [84] proposed applying a Discontinuous Galerkin technique to conduct Implicit Large Eddy Simulations (ILES) . Uranga et al. [206] provided evidence supporting the efficacy of Implicit Large Eddy Simulation (ILES) in the computation of separation-induced transition, simulating Reynolds numbers as low as 22,000. De Wiart [52] analyzed the aforementioned airfoil using an ILES, and then, a DNS was conducted to support the findings. Catalano and Tognaccini [55] introduced Large Eddy Simulations that employ a second-order scheme for the chordwise and wall-normal directions and Fourier colocations in the span-wise direction. The authors challenge the findings presented in Galbraith and Visbal's study [84], which assert that a high-order scheme is indispensable for accurately representing laminar separation bubbles. There is no reason why second-order schemes cannot capture adequate separation-induced transition apart from the

stringent temporal and spatial discretization requirements. The airfoil in question has also been analyzed using RANS methodologies. Windte, Scholz, and Radespiel [227] utilized a $k-\omega$ model in conjunction with a e^n transition model to make predictions regarding transition to turbulence. Catalano and Tognaccini [54, 56] have suggested alterations to the $k-\omega$ SST turbulence model to accurately simulate lower Reynolds number flows. De Santis, Catalano, and Tognaccini [67] proposed a modification to the γ transition model formulated by Menter et al. [139] aimed at improving the production of turbulent kinetic energy within separation bubbles. During the framework of this Thesis, an attempt to enhance the production of turbulent kinetic energy in separation bubbles by adjusting the s_1 parameter in the γ-Re_θ transition model introduced by Langtry [114] was performed. This work is detailed in Carreño and D'Ambrosio [39] and Chapter 3 of this document. We show how the explored transition model may be tuned with more or less success for a given airfoil, depending on the characteristics of this and the operating conditions. However, it is worth mentioning that in the case of a rotor, the complexity grows as every radial station presents different geometries and is subject to different Reynolds numbers and angles of attack.

1.2.2 Ultra-Low Reynolds number Airfoil Aerodynamics

Numerical and experimental studies have been conducted on the design of airfoils for atmospheric conditions on Mars. The Ultra-low Reynolds number regime is defined as the range of Reynolds numbers between 1,000 and 10,000. Kunz [111] conducted a comprehensive numerical investigation on the aerodynamics of efficient airfoils and rotors operating in this regime. Valuable experimental data obtained in the Martian Wind Tunnel at Tohoku University has been published by researchers from Japan, who have also pursued Martian flight [143, 10, 199, 9, 11]. One of the most useful research items for validation purposes is the work performed by Munday [143] on triangular airfoils. His experimental results serve to validate various numerical methodologies, including unstructured finite volume Navier-Stokes solvers [24, 44] and high-order DNS solvers [37] under ultra-low Reynolds number conditions. The primary area of focus for the Japanese researchers is the performance of airfoils under low Reynolds conditions and the development of a fixed-wing aircraft, as evidenced by their work in [8, 10, 12]. Koning et al. [105, 108] conducted thorough aerodynamic and optimization analyses of airfoils for Martian rotors. The authors

propose a multi-objective optimization strategy to maximize lift and minimize drag concurrently. Their findings suggest that sharp leading-edge geometries exhibit superior aerodynamic efficiency compared to conventional geometries. The high computational cost of this approach stems from the utilization of URANS within the optimization loop as a solver. The Mars Science Helicopter (MSH) developed under the Rotor Optimization for the Advancement of Mars eXploration (ROAMX) project [65] employs a sharp double-edged plate as its airfoil [102]. Bézard and Désert have conducted extensive numerical and experimental research on airfoils [24, 23, 70, 69] in the context of designing a coaxial helicopter at ONERA. The authors employ Xfoil [75] in their study to develop an airfoil design that is globally optimal across various Reynolds numbers and angles of attack. The ultra-low Reynolds number regime has also been studied within this thesis's framework. We conducted numerical simulations in these works and developed efficient Martian airfoil designs using coupled Adjoint-based CFD analysis [46, 45, 47]. Chapter 3 includes a detailed explanation of this methodology. Another approach is presented to generate sharp leading-edge geometries starting from baseline airfoils obtained with XFOIL. This methodology is fast and allows the generation of state-of-the-art performances in a few hours using a standard laptop.

1.2.3 Numerical Methods for Rotor Aerodynamics

This section summarizes the different approaches described in literature to compute rotor performance. The methods described in the following lines present variable fidelities, and they have associated different computational costs. We can divide these methodologies into three macro groups. Reduced order models, classical CFD methods based on Navier-Stokes equations, and Lattice Boltzmann solvers.

1.2.3.1 Reduced Order Models

Generally, these methodologies are computationally cheaper and are typically used for design and optimization applications. They exploit discretized forms of simplified formulation of the governing equations of fluid dynamics. To compute rotor performance, these methods require an accurate airfoil aerodynamic database for low Reynolds numbers applications. Even though computing a polar for a rotor with varying airfoils might be computationally intensive, it is an operation that needs to be

done just once for a given rotor. A fast and relatively accurate alternative to CFD to compute airfoil databases is a panel method coupled with an integral boundary layer formulation such as XFOIL [75]. For helicopter applications with high Reynolds numbers, lifting surface models have been used to compute rotor aerodynamics without using airfoil databases. However, for smaller-scale applications with small associated Reynolds numbers, the potential theory is insufficient to compute airfoil performance, and lifting line implementations combined with airfoil polars are a common choice. Examples of lifting surface codes exist, such as the Non-Linear Vortex Lattice combined with 2D airfoil data presented in [100]. In the following lines, we describe possibly the three most popular reduced-fidelity models to calculate rotor performance; the blade element momentum method, the free vortex wake method, and the vortex particle method.

Blade Element Momentum Methods

Blade element methods are widely used to predict the aerodynamic loads on rotors, propellers, and wind turbine blades. The BEM theory is a steady-state method that combines the general momentum theory and the blade element theory. The method predicts the sectional lift and drag of each blade element using an aerodynamic database. These forces are used to compute the local thrust and torque which in turn affect the inflow velocity predicted by the momentum theory. This poses a non-linear problem that can be tackled iteratively or using a non-linear solver such as the Newton-Raphson technique. Once the solution converges, the loads on the blades are integrated over the span to obtain the overall rotor performance.

This method is fast and reasonably accurate for high aspect ratio blades, assuming negligible crossflow effects and a primarily two-dimensional flow hypothesis. However, the lack of explicit wake modeling compromises the accuracy of this approach, particularly in hovering conditions where BVI may occur. Some popular BEM approaches, among many others presented in the literature, include PropCode [21], QBlade [128], JBlade [190], JavaProp [98] and QProp [76].

Free Vortex Wake Methods

The free vortex wake method is an unsteady approach that models the wake behind the rotor as a series of vortex filaments shed from the blade's trailing edges. These

vortices are convected downstream with the local velocity field and interact with the incoming wind, producing a complex flow field. By integrating the velocity fields, the updated position of the vortices can be computed. The velocity of the vortices is obtained by computing the induced velocities from all the other vortices using the Biot-Savart formula. These codes include empirical models to account for the evolution of the vortex core's, making them sensitive to model parameters. While the free vortex wake method considers the wake's modeling and provides improved estimates of inflow angles [24], it requires significantly more computational resources. The cost of the Free Vortex Wake approach is generally three orders of magnitude higher than the BEM method and even four orders of magnitude in some cases with slow convergence. However, it remains significantly cheaper than CFD calculations by approximately four to five orders of magnitude. Some popular free vortex wake codes include CAMRADII [144], PUMA from ONERA [117], and Qblade [127]. This methodology is well-suited for flows where the relative wind helps to stabilize the vortex systems, such as wind turbines or propellers with a significant advance ratio. In hovering cases, where the vortex system generally becomes unstable, this approach becomes limited and may be challenging to converge. These convergence issues typically arise for hovering rotors with a relatively low thrust coefficient that present a compact vortex system and the BVI becomes very intense. The presence of an axial velocity, on the other hand, tends to stabilize the solution [97]. Nonlinearities in the airfoil aerodynamic database, especially when stall and post-stall models are used, can cause further convergence issues.

Vortex Particle Methods

The Vortex Particle Method (VPM) is an alternative approach to simulate the unsteady flow around a rotor. In this method, the fluid flow is represented by numerous particles that follow the fluid equations of motion. This method can be considered a free vortex wake method because the vorticity field is discretized into particles, and these are convected with the flow following the vorticity form of the Navier-Stokes momentum equations. However, unlike the classical FVW that models the evolution of the core of the vortex filaments, the VPM also solves an equation to update the vortex particle strength, and therefore they deserve a special mention. VPM is an interesting method for simulating the unsteady flow around the rotor, but it is computationally expensive and requires a large number of particles to produce

accurate results. Acceleration methods such as the Fast Multiple Method enable simulations with many particles with contained computational costs. One advantage of the VPM is its ability to account for wake mixing, as it does not require direct connectivity of vortex structures. It is well-suited for hovering flows and multi-rotor interactions. Although more computationally expensive than the FVW, VPM offers greater freedom in the wake topology and a more accurate evolution of the vortex strength. These approaches were developed in the last decades of the past century, with significant contributions from Winckelmans [225], but they have recently gained popularity in the simulation of Unmanned Aerial Systems (UAS) with distributed propulsion in the context of Urban Air Mobility (UAM) and other applications. Two codes implementing different variations of this technique are DUST [140] and FLOWVPM [5]. Another advantage of these approaches is the ability to perform variable fidelity simulations by adjusting the number of particles used to discretize the wake vorticity is discretized.

1.2.3.2 Navier-Stokes based Computational Fluid Dynamics

Moving into classical CFD methods, RANS simulations predict the steady-state flow around a rotor. RANS simulations solve the averaged Navier-Stokes equations for the mean flow field in a moving reference frame rotating with the rotor, and they incorporate turbulence models to predict the effects of turbulence in the mean flow. RANS simulations are computationally efficient compared to their transient counterparts and are widely employed for predicting the performance of rotary wings [160, 112, 22, 49]. Unsteady Reynolds-averaged Navier-Stokes (URANS) simulations, on the other hand, solve the Navier-Stokes equations in an inertial reference frame while imposing the rotor boundary condition by rotating the grid. URANS simulations are more computationally demanding than RANS simulations but can provide more accurate results when large-scale unsteady phenomena are relevant. For isolated rotors with far-field boundary conditions, the whole domain can be rotated. On the other hand, if the computational domain is not axisymmetric or multiple rotors need to be modeled, two regions must be created: a static region to accurately impose the boundary conditions and dynamic regions to account for rotor rotation. Various approaches can be used to interface these regions, two popular alternatives being the sliding grid approach and the chimera method for overset grids. Detached Eddy Simulations (DES) combine URANS and large eddy simulation

(LES) methods. In DES, URANS simulations are performed where the grid resolution is insufficient to resolve turbulent scales, such as in boundary layers. On the other hand, the LES mode is employed in separated regions where grid requirements are not so stringent, primarily modeling the small-scale turbulence while resolving the larger eddies. With an adequate grid resolution, DES can capture secondary instabilities of vortex systems, which often occur on hovering rotors when the pitch of the helical vortex system is small [96]. Scale-resolving simulations have strict grid requirements with second-order reconstruction schemes. Higher-order solvers (n > 2) are typically preferred due to their ability to capture the helical vortex system of a rotor on coarser grids. Several authors [229, 212, 1, 213] have investigated the use of higher-order schemes in combination with hybrid RANS-LES approaches for rotor simulations. These authors demonstrate how wake instabilities generate secondary braids surrounding the original vortex systems. Depending on the grid, solver selection, and rotor being studied, these instabilities might dominate, creating a 'vortex soup' in the wake. While this effect is recognized as non-physical, its underlying causes are currently under investigation. In recent decades, the aerospace community has relied on second-order finite volumes or finite difference schemes for CFD simulations. Two well-known commercial solvers validated for industrial rotor applications are Simcenter STAR-CCM+ and Ansys Fluent. These codes implement second-order finite volume schemes, including both upwind and central difference versions. Recently, STAR-CCM+ also included third-order central differences and Monotonic Upwind Schemes for Conservation Laws (MUSCL) . MUSCL and Weighted Essentially Non-Oscillatory (WENO) schemes are two popular families schemes implemented in codes such as OVERFLOW [62], OVERTURNS [15] or UCNS3D [7]. Higher-order solvers come with a computational overhead compared to low-order schemes. However, this overhead usually pays off by increasing the computational efficiency of computations for a given accuracy level, but this is not certain. In these lines, [196] presents an analysis with different order WENO and MUSCL schemes for the Caradonna-Tung rotor test case [36] and the PSP rotor test case [219] using the RANS solver in UCNS3D modeling rotation with a Moving Reference Frame (MRF) . They show how their fourth-order schemes present a large overhead with a small increase in integrated load predictions. Therefore, the third-order scheme could achieve the same accuracy level in a finer grid with improved efficiency. For scale-resolving simulations, this requirement becomes more

stringent as CFL has to remain close to unity even for implicit integration schemes, and therefore this would favor the use of higher-order solvers.

The application of methodologies traditionally developed for helicopter flows to small-scale rotors used in small-scale UAS must be carefully analyzed due to the low Reynolds numbers present in these blades at usual rotation rates. For a constant tip speed velocity, decreasing the radius of a rotor while maintaining the aspect ratio results in a drop in the Reynolds number computed at the 75% radial station proportional to the radius reduction. Furthermore, the inner sections operate at low velocities and always face lower Reynolds numbers. A commercial 20 cm radius UAS rotor operating in standard conditions at typical rotation rates will present Reynolds numbers around 100,000. Without extremely high freestream turbulence levels that trigger bypass transition, the flow will present a non-negligible laminar region in this regime. Towards the root, a rotor operating in design conditions, presenting an attached flow or near trailing edge separation, will likely remain laminar. As the radial coordinate increases, the Reynolds number will increase, and the flow will be more prone to separation and thus transition to turbulence due to the amplification of the Kelvin-Helmholtz instability developing in the separated shear layer. This transition mechanism usually generates Laminar Separation Bubbles on the suction side of small-scale blades. These bubbles increase the airfoil's effective camber, generating subtle differences in rotor performance. Incorporating a transition model is necessary to predict this flow's boundary layer state with RANS and URANS approaches. As mentioned in the case of airfoils, transition models are not widely extended in the rotorcraft community either. On the other hand, LES allows the prediction of separation-induced transition, but the spatial and temporal resolution required would be too large to compute transition on the rotor's suction side accurately. Using a commercial second-order finite volume solver, the cell count would be in the order of 10^9 cells with a time step of roughly 0.01 degrees per time-step for between 10 and 20 revolutions. This rough estimate of the potential computational cost of such an approach emphasizes the need for transition modeling for very low Reynolds numbers.

1.2.3.3 Lattice Boltzmann Method

The lattice Boltzmann method (LBM) has recently become popular in modeling rotating flows. LBM represents the fluid by a distribution function that evolves

over time according to kinetic equations. The distribution function represents the probability of finding a fluid particle at a particular location and velocity. The method uses a lattice grid to discretize the physical domain, and the fluid particles collide and interact on the lattice nodes. LBM has several advantages over traditional CFD methods based on solving the Navier-Stokes equations. Firstly, it is computationally efficient and can be easily parallelized on a distributed computing platform. Secondly, it is a mesoscopic method that can simulate the flow at a resolution between the macroscopic and microscopic scales. Thirdly, LBM is easy to implement and can handle complex boundary conditions, such as porous media or moving boundaries. PowerFLOW is a lattice Boltzmann code that can perform Very Large Eddy simulations on small-scale rotors as shown in [53, 167]. With this approach, they can tackle separation-induced transition and predict separation bubbles in the suction side of rotors operating in low Reynolds number conditions. They corroborated the presence of these separation bubbles using an oil visualization technique. A popular open-source LBM implementation is OpenLB [110]. A thorough review of this methodology can be found in [185].

1.2.4 Rotor Design for Martian Conditions

Developing UAS capable of operating within the Martian atmosphere is an interesting and contemporary subject matter. The recent successful flight of the Ingenuity helicopter has demonstrated its feasibility. The operational conditions for a rotary wing on Mars are determined by the atmospheric gas density and viscosity, as well as the necessary rotation speed and rotor diameter. As a result, the rotary wing operates primarily within the ultra-low Reynolds number regime (10^3<Re<10^4), where the flow is expected to be laminar. The region at the tip is situated within the lower limits of the very-low Reynolds number regime, characterized by a range of 10^4<Re<10^5. This region is susceptible to experiencing a transition from laminar to turbulent flow due to separation-induced effects. These conditions are typical of rotor blades utilized by UAS that operate within the Martian atmosphere or at significantly elevated altitudes, such as 30 kilometers, within the Earth's atmosphere. The recent successful flights of the Ingenuity helicopter on Mars have generated interest in exploring the Martian terrain by utilizing UAS. The task of flying on Mars presents several challenges for various reasons. Although the gravitational force on Mars is approximately 38% of that on Earth, the planet's density is two

orders of magnitude lower than that of Earth. As a result, the capacity of traditional rotors to generate adequate thrust is restricted. The speed of sound on Mars is approximately 75% of the velocity of sound on Earth when measured at sea level. The aforementioned limitation constrains the increased rotational velocity needed to generate sufficient thrust owing to the transonic phenomena. High angular velocities can induce a torque rise, implying larger loads on the motors that could cause overheating. This represents a major issue due to the difficulty of cooling these in such a thin atmosphere. The conditions of low-density flight are also observed at high altitudes on Earth, which pose the additional challenge of increased gravitational force.

Balaram and Koning have conducted extensive analyses on the aerodynamics and optimization of rotors and airfoils for the Martian environment, as evidenced by their publications [17, 16, 105, 108]. These studies have informed the design of the JPL Martian helicopter and continue to inform ongoing efforts to enhance its design. These efforts concluded with the proposal of a new set of Martian UAS with larger payloads known as the Mars Science Helicopters [101]. Bèzard and Desert have conducted extensive numerical and experimental research on rotors aimed to operate on Martian conditions [24, 23, 70, 69]. Their research includes the presentation of a design of a coaxial helicopter. The works cited earlier employ Reduced Order Models (ROMs) and Computational Fluid Dynamics (CFD) of higher fidelity to assess blades. However, both rely on ROMs for the optimization process. American researchers use CAMRADII [144], while their French counterparts employed the PUMA (Potential Unsteady Methods for Aerodynamics) software developed at ONERA [117]. Both Free Vortex Wake (FVW) methods can accurately track the wake's evolution and simulate Blade Vortex Interaction (BVI) , which can significantly impact hovering conditions. The codes above utilize a Lifting-Line methodology to simulate the rotors, employing a database of 2D airfoils. It is also worth mentioning that the Japanese Space Agency (JAXA) [203, 10, 197, 207] and the University of Maryland [66, 187, 80] have also contributed to the development of Martian rotor development.

Within the framework of this thesis, several efforts have been made to investigate this phenomenon. The main results of this investigation are shown in Chapter 5 and in References [44, 46, 38, 45, 47]. These works show a novel approach to designing efficient Martian blades that combine a preliminary design using the Blade Element Method and an ulterior refinement using coupled Adjoint-based CFD analysis. This

approach presents a computationally feasible methodology for integrating CFD simulations into the optimization process.

1.2.5 Passive Swashplateless Rotors

Unmanned Aerial Systems (UAS) have experienced exponential growth for various civil and military applications. The most popular types of UAS are possibly multi-copters, fixed-wing drones, and coaxial helicopters. As mentioned in [151], a popular category of drones is the planar quadrotor; in light of their stringent form factor, the aforementioned 6-DOF device is equipped with only four actuators, which makes it an under-actuated UAS. Consequently, they cannot regulate both position and orientation independently. This limitation has led to efforts to realize fully actuated drones able to fly in all orientations at the cost of added complexity. Researchers and manufacturers aim to enhance simplicity, robustness and reduced costs and weight for applications without full independent attitude control. One of the solutions in this direction is coaxial helicopters, which applicability has been proven with the Mars Helicopter *Ingenuity*, recently launched by NASA [17], which is also an example of the role played by UAS in complex scenarios. Most coaxial helicopters obtain attitude control using a swashplate that allows the orientation of the rotor disk to generate corresponding forces and moments in the desired direction [161]. However, the mechanical complexity of the swashplate is a potential problem for the popular guideline of UAS design, which prioritizes vehicle weight and cost. Several attempts to eliminate the swashplate performed by researchers can be classified into active and passive solutions. Among the active approaches, a possible solution is the Trailing Edge Flap (TEF) concept, which generates a differential thrust between blades and creates the desired moment. This concept has been used since the early 20th century and was introduced by Corradino d'Ascanio, an Italian inventor and engineer, following early work from Juan de la Cierva [119]. This approach is still used in some relatively modern designs, such as those proposed by Kaman Aerospace. However, it is not as popular nowadays due to the large drag penalty that the deflection of an external TEF generates [103]. Recently, Paulos et al. [152] presented a novel passive rotor approach, including an anti-symmetric coupled lag-pitch hinge that allowed the production of differential thrust in both blades generating adequate control moments by simply modulating the amplitude and phase of the motor input voltage. This concept allows the construction of a coaxial helicopter in which one rotor profits

from this concept, and the second one is used to compensate for the generated torque. This innovative approach has been extensively tested experimentally by Paulos et al. [152–154] and other active swashplateless designs have been studied numerically in [103]. However, we are unaware of numerical studies regarding the aerodynamics of this passive swashplateless concept apart from the preliminary investigation performed by Carlotta Manca [126] during her MSc thesis carried out in our department.

1.2.6 Numerical Simulation of UAS maneuvers

Unmanned Aerial Systems (UASs) have experienced significant growth across different fields in recent years, as discussed in a comprehensive review by Idrissi [99]. These sectors include urban air mobility, particularly in the context of smart cities, and agriculture, specifically in precision operations, as Radoglou [164] highlighted. The advancements in robotics, communication, and Big Data have enabled UAS missions to achieve a high degree of automation and safety, as elaborated in the survey conducted by Bloise [30]. It is crucial for interdisciplinary researchers to effectively address the challenges and opportunities posed by the diffusion of UAS in different sectors. The performance of multicopters with low inertia is notably impacted by disturbances that could compromise the mission's outcome. Previous work has concentrated on examining the disruptions caused by aerodynamic impact and has employed an Active Disturbance Rejection Control (ADRC) technique to sustain stability in the presence of external disturbances, as demonstrated in Zhang [232]. The authors of the papers [131, 132] introduce a disturbance rejection mechanism for Micro Air Vehicles (MAV) utilizing two control algorithms that are activated based on the process. Similarly, Kazim [104] explores the control of position and attitude in scenarios characterized by severe external disturbances, such as windy environments. The authors introduce a robust adaptive control mechanism incorporating aerodynamics, wind gust, and control models within a six-degree-of-freedom Unmanned Aerial System (UAS) dynamics solver. In the previous work, a Proportional-Integral-Derivative (PID) controller is tuned by incorporating an adaptive control term. Additionally, in work by Bolandi [31], an optimized PID is integrated to enhance the system's ability to reject disturbances.

Assessing flight near surfaces such as walls or the ground is important for various applications in areas characterized by obstacles or buildings. These applications

include but are not limited to inspection, delivery, and spraying operations. Furthermore, in such instances, the vehicle is subjected to external forces and torques resulting from aerodynamic phenomena, which have the potential to lead to severe accidents. Consequently, the system requires an efficient sensing and control algorithm to facilitate autonomous navigation in near-surface conditions. Incorporating aerodynamic proximity effects into the control law significantly benefits accident prevention and safety. The article by Matus Vargas [132] provides an overview of the impact of ground effect on multirotor. Meanwhile, Shi [186] analyzes the effect of obstacles on airflow. Paz [156] evaluates the impact of the proximity of the ground on the performance of a UAS at various velocities during flight. The phenomenon of the wall effect has been the subject of investigation in the research conducted by Conyers [63] and Du Mutel de Pierrepont Franzetti [77]. These studies provide empirical evidence regarding the forces and moments experienced by the unmanned aerial system (UAS) at various distances from the wall. The previous experimental results are essential to develop a model including this effect. The article [166] presents a numerical investigation that centers on the disturbance phenomena resulting from aerodynamic interactions between rotors and adjacent walls. Garofano Soldado [85] presents a numerical-experimental analysis of propellers in ground effect at different tilt angles. Interestingly, as the tilt angle increases, the problem transitions from ground effect to wall effect.

Chapter 7 presents a significant innovation in the field by integrating a Computational Fluid Dynamics (CFD) solver to assess the Unmanned Aerial System (UAS) condition through a closed-loop feedback control mechanism that can progressively minimize the error magnitude. Our simulations incorporate a conventional Proportional-Integral-Derivative (PID) approach for quadcopter and hexacopter control. Nevertheless, the framework can be expanded to encompass other control algorithms with greater intricacy. According to Salih [172], and Wang [218], the implementation of PID control is prevalent in the industrial process for UAS autopilot design due to its ability to balance robustness and performance. For more information on various methods related to PID UAS control, refer to [200]. Chapter 7 presents an implementation of a cascade proportional-integral-derivative (PID) controller to regulate position, altitude, and attitude. This controller is applied to quadcopters and hexacopter in different missions simulated with computational fluid dynamics. To the author's knowledge, this particular methodology concerning unmanned aerial systems (UAS) flights is not well-documented in literature. Ventura Díaz [213]

proposed a comparable methodology for urban air mobility, which involves utilizing loosely-coupled high-fidelity computational fluid dynamics (CFD) simulations in conjunction with the reduced-order model CAMRAD-II to attain a trimmed cruise condition. Conversely, several authors have conducted simulations of quadcopters with different motions, though lacking a control strategy or the comprehensiveness of a 6-degree-of-freedom simulation. An example is the work by Paz [156], which simulates a moving quadcopter close to an obstacle, but the motion is imposed.

1.2.7 Rotary wing UAS in Agriculture: The Drift Problem

In several Asian countries, like Japan, South Korea, and China, unmanned aerial spray systems (UASSs) have grown considerably over the past 30 years. This trend started in Japan and spread to South Korea, China, and now worldwide. The first studies focussed on flat rice and corn canopies in agricultural research. The main goal of these studies was to get an even spread and the best penetration. Even though agricultural spraying techniques have improved, spray drift is still a big problem. Drift occurs when fine Plant Protection Products (PPPs) droplets are spread beyond their intended target driven by airflow. This problem has become very important in the context of pesticide risk assessment. Many researchers have looked into the factors that affect this phenomenon, such as the altitude and speed of the flight, the type of nozzle, the pressure of the injection, and the speed of the wind [147, 60, 3, 216]. Reference [82] presents an Unmanned Aerial Spray System (UASS) adaptive control law that depends on the weather conditions. The goal of this control law is to make sure that pesticides are accurately deposited in the target. Scagnellato [176] looks at how wind affects spray distribution and shows how to use an adaptable guidance algorithm in windy conditions.

The case of 3-dimensional crops, typically arranged in rows, such as orchard trees, creates additional challenges. In the case of this particular canopy, there is an elevated likelihood of off-target losses into the inter-row region. Therefore, it is imperative to thoroughly examine the impact of various flight and spray parameters on achieving the required pesticide distribution and canopy penetration for diverse crops, as evidenced by several studies [134, 129, 215, 120]. Optimizing how sprays are used in vineyards is an interesting topic because the land is sloped and uneven, and the vines are planted in long, narrow rows. Sarri [175] analyzes this scenario. The circumstances above present numerous obstacles, leading to complex precision

spraying procedures and emphasizing the significance of the flight mode in optimizing product deposition on the crop while simultaneously reducing drift towards the inter-row area. The article by Biglia [26] looks at how different operational parameters affect spray coverage and deposition in vineyards.

The interaction between spray and rotors has been experimentally tested both in the open field [230] and in wind tunnel facilities [123, 92], where the authors investigate drift with varying wind speed, spray volume, and nozzle characteristics. Drift is also addressed in [59], where the authors survey solutions to reduce the inevitable drift by optimizing the rotor, nozzle setup, spray system, and flight parameters. Concurrent with experimental investigations, numerical simulations have examined the downwash flow characteristics of multi-rotor systems. The study presented in [231] employs a lattice Boltzmann methodology to investigate the wake characteristics of a hexacopter used for plant protection. Additional computational methodologies encompass the examination of droplet trajectories by utilizing a dispersed phase model (DPM), as evidenced in the works of [228, 224, 217]. The Lagrangian particle model relies on injection inputs, including droplet diameter, momentum, and spray angle, which are challenging to predict with precision and are a priori unknown. The inputs may be predicted using experimental approaches [147], empirical approximations [118], and numerical simulations [72, 116]. The previous computational works were performed using a volume-of-fluid (VOF) approach.

This research presents some contributions to understanding the drift problem, with a focus on how rotors and droplets interact with each other. Chapter 8 and the publications in collaboration with Nicoletta Bloise and the flight mechanics research team at Politecnico di Torino [27–29, 43] provide an overview of the critical aspects of this research activity, focussing on the vineyard scenario.

1.3 Chapters Summary

The work done during this Ph.D. has been packed thematically into different sections.

- Chapter 1: Motivation, literature review, summary, and contributions.
- Chapter 2: Detailed methodology of the numerical approaches used and developed during the thesis.

- Chapter 3: Very Low and Ultra Low Reynolds Numbers Airfoil Aerodynamics. This chapter presents an airfoil analysis distinguishing between the Ultra-low and Very-low Reynolds number regimes. We assess different fidelity tools ranging from a panel method coupled with an integral boundary layer formulation to Large Eddy Simulations, paying special attention to the transition to turbulence. We propose several efficient geometries for Martian conditions and discuss passive flow control approaches to ensure the presence of an optimal separation bubble on the airfoil's suction side.

- Chapter 4: Experimental Validation of Hovering Rotor Performance Prediction. In this chapter, we show different numerical tools, commercial and in-house, that allow rotor performance predictions. We assess the influence of 2D aerodynamic databases on the performance of ROMs. Experimental validation of the different approaches is performed at different Reynolds numbers with tests performed in a climatic chamber.

- Chapter 5: Ultra-Low Reynolds Number Rotor Aerodynamics: Design and Optimization. We present a hybrid fidelity optimization approach combining the BEM method and an Adjoint-CFD coupled analysis to enhance rotor performance. These geometries are then analyzed using Navier-Stokes simulations and Large Eddy Simulations.

- Chapter 6: Numerical Modeling of Swashplateless Rotors. This chapter assesses this innovative UAS concept using Computational Fluid Dynamics (CFD) coupled with a 6 Degrees Of Freedom (DOF) solver to compute the passive response of the blades. A reduced-order model has been developed to assess the performance of these rotors at a contained computational cost.

- Chapter 7: Numerical Modeling of UAS Maneuvers. This chapter assesses and verifies a virtual environment for general UAS testing. In particular, we developed a digital twin for a quadcopter. The UAS includes a PID algorithm that allows the virtual testing of different missions. We performed simulations of the quadcopter in-wall effect assessing the ability of the controller to achieve a near-wall hovering condition. A virtual disk approach has also been validated to allow longer physical times in the simulations without an excessive computational cost.

- Chapter 8: Numerical Modeling of an Unmanned Aerial Spraying System. In this chapter, we have created a virtual testing environment to test UAS spraying operations in vineyards. In particular, we developed digital twins for a quadcopter and a hexacopter equipped with a spraying system. The influence of spray parameters has been assessed by evaluating the amount of droplet deposition on the target. Experimental validation of the numerical model was performed in a wind-tunnel facility.
- Chapter 9: Conclusions, summary and future directions

1.4 Publications

This Thesis includes the partial content of the following peer-reviewed journal publications led by the author:

- M. Carreño Ruiz and D. D'Ambrosio. Validation of the $\gamma - Re_\theta$ Transition Model for Airfoils Operating in the Very Low Reynolds Number Regime. *Flow, Turbulence and Combustion*, pages 1–30, 2022
- M. Carreño Ruiz, M. Scanavino, D. D'Ambrosio, G. Guglieri, and A. Vilardi. Experimental and numerical analysis of hovering multicopter performance in low-Reynolds number conditions. *Aerospace Science and Technology*, 128:107777, 2022
- M Carreño Ruiz, N. Bloise, G. Guglieri, and D. D'Ambrosio. Numerical Analysis and Wind Tunnel Validation of Droplet Distribution in the Wake of an Unmanned Aerial Spraying System in Forward Flight. *Drones*, 6(11), 2022
- M. Carreño Ruiz and D. D'Ambrosio. Aerodynamic optimization and analysis of quadrotor blades operating in the Martian atmosphere. *Aerospace Science and Technology*, 132:108047, 2023
- M. Carreño Ruiz, L. Renzulli and D. D'Ambrosio. Airfoil Optimization for Rotors Operating in the Ultra-Low Reynolds Number Regime. *Physics of Fluids*, 2023. (Accepted for publication)

And the following conference proceedings:

- N. Bloise, M. Carreño Ruiz, D. D'Ambrosio, and G. Guglieri. Preliminary design of a remotely piloted aircraft system for crop-spraying on vineyards. In *2020 IEEE International Workshop on Metrology for Agriculture and Forestry (MetroAgriFor)*, pages 1–6. IEEE, 2020

- M. Carreño Ruiz, M. Scanavino, D. D'Ambrosio, G. Guglieri, and A. Vilardi. Experimental and numerical analysis of multicopter rotor aerodynamics. In *AIAA Aviation 2021 Forum*, Virtual Event, August 2021. AIAA 2021-2539

- M. Carreño Ruiz and D. D'Ambrosio. Validation and application of aerodynamic simulations in the Martian atmosphere. In *26th Conference of the Italian Association of Aeronautics and Astronautics-AIDAA 2021*, 2021

- N. Bloise, M. Carreño Ruiz, D. D'Ambrosio, and G. Guglieri. Wind tunnel testing of remotely piloted aircraft systems for precision crop-spraying applications. In *2021 IEEE International Workshop on Metrology for Agriculture and Forestry (MetroAgriFor)*, pages 378–383. IEEE, 2021

- M. Carreño Ruiz, A. Manavella, and D. D'Ambrosio. Numerical and experimental validation and comparison of reduced order models for small scale rotor hovering performance prediction. In *AIAA SciTech 2022 Forum*, January 2022. AIAA 2022-0154

- M. Carreño Ruiz and D. D'Ambrosio. Aerodynamic Optimization of Quadrotor Blades Operating in the Martian Atmosphere. In *AIAA SciTech 2022 Forum*, San Diego, CA, January 2022. AIAA-2022-0743

- M. Carreño Ruiz, F. Bellelli, and D. D'Ambrosio. Numerical Investigation on the Aerodynamic Design of Quadrotor Blades Operating in the Martian Atmosphere. In *EUCASS 2022*, 2022

- N. Bloise, M. Carreño Ruiz, E. Mai, D. D'Ambrosio, and G. Guglieri. Analysis and Design of Unmanned Aerial Systems for Precision Agriculture applications on Vineyards. In *EUCASS 2022*, 2022

- L. Scagnellato, M. Lecce, N. Bloise, M. Carreño Ruiz, E. Capello, and G. Guglieri. Adaptive path planning for spraying UAS in vineyard under variable wind condition. In *ICAS 2022*, 2022

- M. Carreño Ruiz, N. Bloise, E. Capello, D. D'Ambrosio, and G. Guglieri. Assessment of Quadrotor PID Control Algorithms using six-Degrees of Freedom CFD simulations. In *2022 61st IEEE Conference on Decision and Control (CDC)*, 2022

- M. Carreño Ruiz and D. D'Ambrosio. Hybrid Fidelity Optimization of Efficient Airfoils and Rotors in Ultra-Low Reynolds Numbers Conditions. In *AIAA SciTech 2023 Forum*, National Harbor, MD, January 2023. AIAA-2023-0652

- M. Carreño Ruiz, N. Bloise, E. Capello, D. D'Ambrosio, and G. Guglieri. Assessment of Quadrotor Near-Wall behaviour using six-Degrees of Freedom CFD simulations. In *AIAA SciTech 2023 Forum*, National Harbor, MD, January 2023. AIAA-2023-2272

- Manuel Carreño Ruiz and Domenic D'Ambrosio. ROT8: A Matlab App for Low Reynolds number Airfoil and Rotor Aerodynamic Design. In *AIAA AVIATION 2023 Forum*, San Diego, CA, June 2023. AIAA-2023-3379

Chapter 2

Numerical Methods

This chapter briefly overviews the different methodologies used to calculate airfoil and rotor performance. These methodologies include in-house developed tools, open-source software, and commercial codes. This chapter also includes a detailed explanation of the implementation of the γ-Re_θ transition model in STAR-CCM+. The increased level of detail is necessary to fully understand the fine-tuning of the aforementioned model presented in Chapter 3.

2.1 Panel method: Xfoil

XFOIL is a software tool that integrates a panel method based on potential flow theory and an integral boundary layer formulation described by Drela [75]. The purpose of its creation was to assess the effectiveness of airfoils under conditions of low Reynolds numbers. XFOIL can determine the pressure distribution and incorporate the effects of laminar separation bubbles and mild trailing edge separation. This work is based on the XFOIL 6.99 version, executed through Matlab using the library presented in reference [78]. The code is modified to render it robust to non-convergent simulations or software failure. These changes are key to avoiding interrupting the optimization procedure detailed in Chapter 3. XFOIL employs the e^N envelope method to predict transition to turbulence. This method looks at the highest amplified frequency at a specific location on the airfoil downstream from the instability point to estimate the magnitude of the disturbance. Transition is assumed to occur when the integrated amplitude tops a value defined empirically.

The equation below relates the value of N_{crit} with the freestream turbulence intensity Tu.

$$N_{crit} = 8.43 - 2.4ln(Tu) \tag{2.1}$$

Uranga [205] demonstrates that Xfoil can predict transition caused by separation, provided that turbulence intensity is appropriately adjusted. It is possible to replicate the pressure plateau and posterior recovery phenomena. However, the skin friction results do not capture the significant negative skin friction observed inside separation bubbles before reattachment of the boundary layer. This aspect will become important when treating ultra-low Reynolds number flows due to the non-negligible contribution of skin friction to the total drag.

The convergence of Xfoil frequently fails at elevated subsonic Mach numbers. To prevent the rejection of good geometries only due to convergence issues, Xfoil is executed at the incompressible limit. The pressure distributions are corrected using Kàrman-Tsien's compressibility correction, which is subsequently integrated to derive the lift and drag coefficients.

2.2 *ROT8*

ROT8[1] [51] is a code developed during this thesis with the invaluable collaboration of MSc students Andrea Manavella [125], Mario Alì [6] and Francesco Bellelli [20] who developed their Thesis under my co-supervision. This Matlab App compiles several rotor ROMs to give the user a choice in modeling fidelity. The graphic interface can easily set up the simulations and optimization algorithms. Using user-defined Matlab functions, we have tried to achieve a high level of interaction with the code. For instance, rotor parameterizations, objective functions, and the polar input can be defined this way. Although the code was created to handle the extremely low Reynolds number regime found on Mars, the employed corrections do not affect simulations for higher Reynolds numbers. The App and Xfoil [75] are connected to allow for coupled inviscid-viscous analysis of airfoils and semi-automatic polar calculation for the rotor's airfoils. We offer a simulation module that can calculate loads and wake characteristics and a design module that allows

[1]The code will be uploaded in the following repository: https://github.com/MCarrenoRuiz/ROT8

users to optimize rotors and airfoils, setting specific goals and constraints. Doing so can avoid complicated and time-consuming communications between various software during an optimization procedure. Additionally, the identical handling of the geometry inputs makes it possible to compare the effects of the wake modeling on performance directly and realistically.

2.2.1 Blade Element Method

The current implementation applies the conventional double-link methodology, which involves an iterative process that continues until the convergence of the induction factors of momentum and blade element theory is achieved. The equations representing the axial and tangential induction factors at a specific radial location are:

$$a = \frac{(V_x^2 + V_t^2)c(C_l cos(\phi) - C_d sin(\phi))N}{8\pi r V_\infty^2 (1 + a')} \tag{2.2}$$

$$b = \frac{(V_x^2 + V_t^2)c(C_d cos(\phi) + C_l sin(\phi))N}{8\pi r^2 V_\infty (1 + a')\Omega} \tag{2.3}$$

where V_∞ is the flight speed, $V_x = V_\infty(1 + a')$ is the axial velocity, $V_t = \Omega r(1 - b' - b_{visc})$ is the tangential velocity and $\phi = tan^{-1}(\frac{V_x}{V_t})$ is the inflow angle. a' and b' represent the induction factors in the previous iteration. These are under-relaxed to ensure convergence.

The present study includes generating an aerodynamic database essential for interpolating lift and drag coefficients. This has been accomplished through CFD simulations and Xfoil, as demonstrated in Chapter 4. The implementation of Prandtl's tip and hub loss corrections, which are commonly utilized, was carried out using Glauert's formulation as documented in [90]. The computation of the tip and loss factors is performed as follows:

$$F_{tip} = \frac{2}{\pi} \arccos \left(e^{-\frac{N}{2}\frac{R-r}{r \sin \phi}} \right) \tag{2.4}$$

$$F_{hub} = \frac{2}{\pi} \arccos \left(e^{-\frac{N}{2} \frac{r - R_h}{r \sin \phi}} \right) \tag{2.5}$$

The computation of a global correction factor can be expressed as the product of the tip correction factor, denoted as F_{tip}, and the hub correction factor, denoted as F_{hub}, resulting in $F = F_{tip} \cdot F_{hub}$. Various approaches can be employed to incorporate this factor into the BEM formulation. In this code, the correction is applied directly to the circulation, as demonstrated in [5] for the vortex particle method, to ensure a consistent implementation across all three Reduced Order Models presented in this document.

The code incorporates the classical angular momentum correction, as described in Kunz [111], which accounts for the viscous swirl. This correction is denoted as b_{visc} and is calculated using the formula $\frac{2V_\infty a' C_d}{\Omega r C_l}$. The viscous swirl model will have minimal impact on the outcomes at typical Reynolds numbers for micro air vehicles operating in standard conditions. This is because the model approaches zero asymptotically as the inverse of aerodynamic efficiency increases. Including this correction in the code is deemed necessary for completeness, as the authors have employed it to calculate the aerodynamic efficiency of Martian blades operating at a Reynolds number lower than 10,000, as shown in Chapter 5 and Ref. [41]. In these cases, its influence will not be negligible.

The Blade Element Momentum (BEM) methodology demands geometric data that specifies the blade, including the radial distributions of chord and twist. The rotor performance prediction tool offers the highest speed among its peers, with a computational expense of approximately 10^{-4} CPU hours. Due to its rapidity and straightforward nature, it is among the most frequently used for design applications. In the context of aerodynamics at very-low Reynolds numbers, it has been observed that blades with high figure of merit tend to possess smaller aspect ratios than conventional blades, as reported in prior studies [24, 46, 45]. This may lead to potential errors regarding the prediction of local angles of attack, which are a crucial aspect of the design process. A potential cause for these errors is the loss of the two-dimensionality of the flow due to centrifugal effects.

The thrust on each panel is calculated as the sum of the vertical component of both lift and drag; the drag and lift on each panel are computed as:

$$dD = c_d(\alpha)\frac{1}{2}\rho\left[\left(\vec{V}\cdot\vec{a}_1\right)^2 + \left(\vec{V}\cdot\vec{a}_3\right)^2\right]dA \tag{2.6}$$

$$dL = c_l(\alpha)\frac{1}{2}\rho\left[\left(\vec{V}\cdot\vec{a}_1\right)^2 + \left(\vec{V}\cdot\vec{a}_3\right)^2\right]dA \tag{2.7}$$

Then, considering that the angle between the lift (perpendicular to the velocity in the plane defined by the vectors $\vec{a}_1$ and $\vec{a}_3$) and the vertical axis is

$$\phi = \beta - \alpha \tag{2.8}$$

where β is the angle between $\vec{a}_1$ and the horizontal axis, we can calculate that

$$dT = dL\cos(\phi) - dD\sin(\phi) \tag{2.9}$$

because drag is perpendicular to lift, as shown in Figure 2.1.

The torque is calculated as the product of the horizontal component of both lift and drag and the radial position of the blade element control point.

$$dQ = r[dL\sin(\phi) + dD\cos(\phi)] \tag{2.10}$$

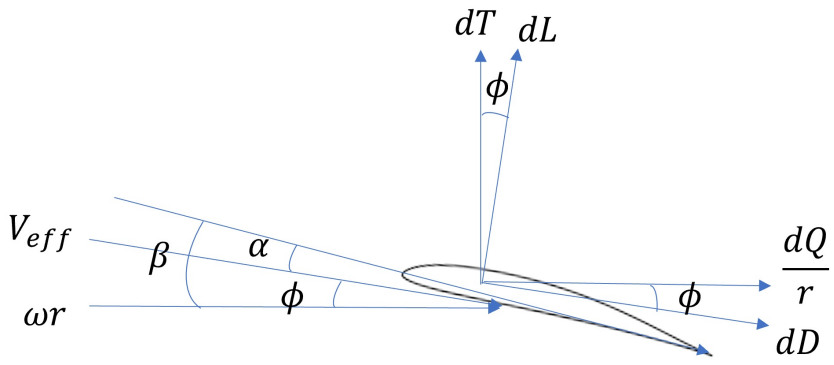

Fig. 2.1 Thrust and torque calculation

The thrust and torque calculations in the ROMs presented in the following sections are analogous to those shown above for the BEM model. Vectors $\vec{a}_1$ and $\vec{a}_3$ have been defined according to Van Garrel's [210] panel definition.

2.2.2 Free Vortex Wake

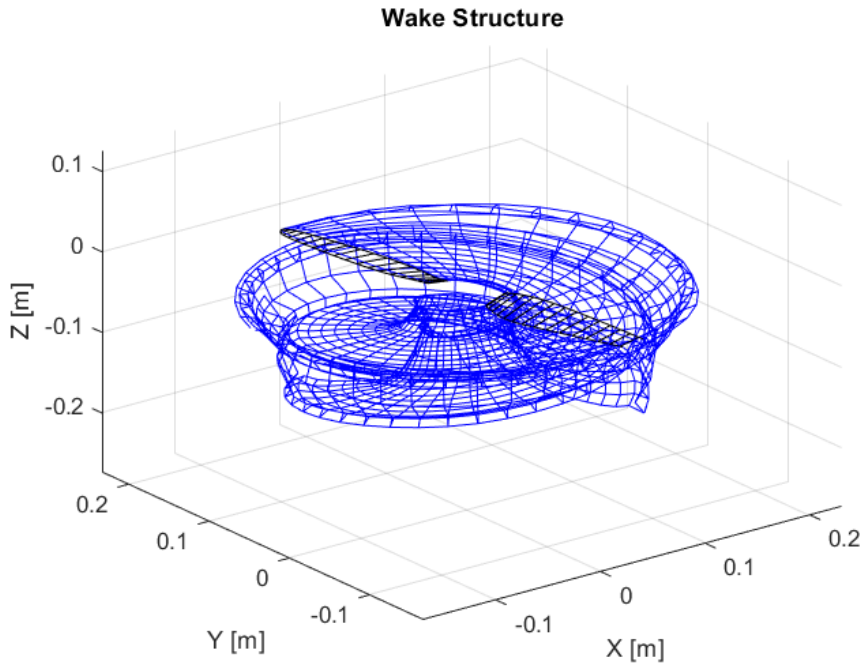

Fig. 2.2 Vortex filaments forming the wake behind a hovering Tmotor 15x5 after 1 revolution.

The FVW code was created as part of the Master's Thesis project documented in [6]. The MATLAB environment was utilized to develop the code, which is inspired by van Garrel's work [210]. Subsequent modifications to the code are detailed in the following lines. The employed approach utilizes the lifting line theory for rotor modeling, wherein including the airfoil's polar renders the problem non-linear. This feature is particularly crucial at low Reynolds numbers, where the lift curves deviate from linear behavior. The rotor model is integrated with the Free Vortex Wake (FVW) approach to simulate the wake, which can undergo deformation due to the velocities induced by the global vortex system created by the rotor.

The blade elements are represented as horseshoe vortices that rotate along with the blade. The circulation at every blade panel j is determined as

$$\Gamma_j = \frac{[c_l(\alpha)]_j \frac{1}{2} \left[\left(\vec{V}_j \cdot \vec{a}_{1,j} \right)^2 + \left(\vec{V}_j \cdot \vec{a}_{3,j} \right)^2 \right] dA_j}{\sqrt{\left[\left(\vec{V}_j \times d\vec{l}_j \right) \cdot \vec{a}_{1,j} \right]^2 + \left[\left(\vec{V}_j \times d\vec{l}_j \right) \cdot \vec{a}_{3,j} \right]^2}} \tag{2.11}$$

The velocity $\vec{V}_j$ is computed on the control points on the blade panel. The chordwise and normal versors on the panel are denoted by $\vec{a}_{1,j}$ and $\vec{a}_{3,j}$ respectively, following van Garrel's notation [210]. The panel area is represented by dA_j, while $d\vec{l}_j$ denotes the filament length or spanwise panel width.

The velocity computed at the control point of the panel j is calculated as

$$\vec{V}_j = \vec{V}_{wind} + \vec{V}_{ind,pan} + \vec{V}_{ind,fil} - \vec{\Omega} \times \vec{r} \tag{2.12}$$

In the previous expression $\vec{\Omega}$ denotes the angular velocity of the blade, while $\vec{r}$ represents the vector radius of the panel control point from the axis origin. $\vec{V}_{wind}$ denotes the wind velocity relative to the rotor, while $\vec{V}_{ind,pan}$ indicates the induced velocities by the vortex system that models the blade. Additionally, $\vec{V}_{ind,fil}$ represents the induced velocity resulting from the vortex filaments in the wake. The lift coefficient is interpolated from an aerodynamic database of the blade's airfoils. The induced velocities are computed by applying a desingularized version of the Biot-Savart law. This study's approach employed for desingularization is based on Van-Garrel's method [210]. However, it differs from the original approach in that it incorporates a regularization technique independent of the vortex filament length, similar to the method implemented in Qblade [127]. This code adapts the approach employed by Qblade by raising the exponent of the core radius r_c to 4, ensuring the dimensional consistency of the expression below.

$$\vec{u}_\Gamma = \frac{\Gamma}{4\pi} \frac{(r_1 + r_2)(\vec{r}_1 \times \vec{r}_2)}{r_1 r_2 (r_1 r_2 + \vec{r}_1 \cdot \vec{r}_2) + r_c^4} \tag{2.13}$$

This correction aims to mitigate the rotor scale's impact on the model's parameters. The study by Ali [6] shows how this formulation enhances the blade loading prediction. Nevertheless, solver stability is often compromised, particularly in hovering calculations, due to the self-induced vortex system lacking an inflow.

As the lift coefficient is a non-linear function of the angle of attack, a function of circulation, Eq. (2.11) is iteratively solved as shown in Eq. (2.14).

$$\Gamma_j^{k+1} = \Gamma_j^k + RF(\Gamma_j - \Gamma_j^k) \tag{2.14}$$

where RF is a relaxation factor, which is necessary to avoid the divergence of Γ_j^k. The convergence criterion is

$$\frac{|\max_j(\Gamma_j^{k+1} - \Gamma_j^k)|}{|\max_j \Gamma_j^k| + 1} \leq toll \tag{2.15}$$

The initial presumption for the Γ_j distribution is a value of 1 at the initial time step. Afterward, the code allocates the converged circulation distribution obtained at the preceding time interval as an initial guess.

The previous section demonstrated the implementation of Prandtl's tip and hub loss corrections, commonly utilized to account for the effects of hub and tip. Neglecting these effects would result in an incomplete analysis. Consequently, the circulation derived from Equation 2.14 is multiplied by the product of two factors, namely $F = F_{tip} \cdot F_{hub}$.

After achieving convergence in panel circulation, the blade undergoes rotation following the predetermined time step and rotation rate. The wake emits two distinct types of vortex filaments. The spanwise circulation variation results in the emission of trailing vortices, while the temporal variation of circulation generates shed vortices, satisfying the Bjerkness-Kelvin theorem. Determining the convection of individual vortex filaments involves numerical integration of the aggregate velocities induced on each filament by the other vortex filaments. The code implements a second-order predictor-corrector scheme for temporal integration. Incorporating a Lamb-Oseen viscous core model, as demonstrated in Bhagwat [25], allows the temporal growth of the vortex due to dissipation effects. Furthermore, a correction is implemented to the viscous core radius to model the vortex stretching effect, as Sants [174] outlined. Following the previous revisions, the core radius denoted by r_c can be expressed as follows:

$$r_c = \sqrt{\frac{5.026 \cdot \delta_\nu \cdot \nu(t + S_c)}{1 + \varepsilon}} \tag{2.16}$$

The present model is characterized by two different parameters, namely δ_v and S_c. The tuning of these parameters allows balance between reliable induction and solution stability. The impact of these parameters has been comprehensively examined in the analysis presented in references [174, 6]. The symbols t and ε denote the age and strain rate of the vortex, respectively.

The velocity induced by individual vortex filaments at each vortex node must be evaluated at every time step. The relationship between the number of vortices and time is linear, while the computational cost exhibits a quadratic increase with respect to the number of revolutions. Hence, the computational expense is susceptible to the solver setup and the inflow parameters. The default settings use 15 evenly distributed panels along the radial direction with a simulation duration corresponding to twelve complete rotor revolutions. The computational expense ranges from 10^{-1} to 1 CPU hour, notably less than that of CFD simulations but considerably higher than the blade element momentum method described above. Achieving complete parallelization of induction calculations results in a noteworthy decrease in simulation duration when implemented on parallel computing systems.

Figure 2.2 illustrates a complete revolution of the vortex wake structure acquired for the Tmotor 15"x5" blade analyzed in Chapter 4. The hovering state results in the wake rolling around the tip vortex and passing near the blade.

2.2.3 Vortex Particle Method

The Viscous VPM software, developed using the MATLAB programming language, was created during the Master's thesis [20] carried out in our department. The evaluation of the circulation distribution on the blade is conducted through the use of the lifting line theory, as referenced in the free vortex wake formulation. The process involves creating a collection of vortex particles every time step, which are employed to discretize the vorticity field. Prandtl's Tip, and Hub corrections were reintroduced to address the impact of hub and tip effects, as performed in the free vortex wake formulation.

The particles are generated from the trailing edge of the blade according to the spanwise variation (trailing vortex particles, shed chordwise) and the time variation (shed vortex particles, shed spanwise) of the circulation on the blade, as shown in

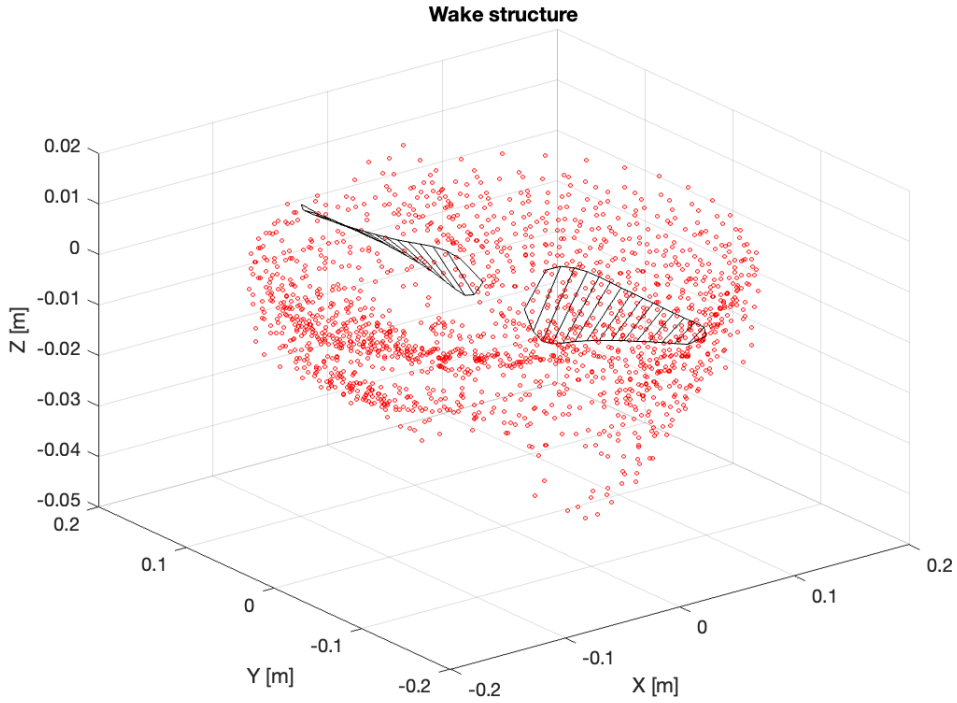

Fig. 2.3 Vortex particles forming the wake behind a hovering Tmotor 15x5 after 1 revolution.

Ref. [162]. Then, they are evolved according to the VPM evolution equations [226],

$$\frac{d\vec{x}^p}{dt} = -\frac{1}{4\pi}\sum_{q=1}^{N_p}\frac{|\vec{x}^p(t)-\vec{x}^q(t)|^2+\frac{5}{2}\sigma^2}{(|\vec{x}^p(t)-\vec{x}^q(t)|^2+\sigma^2)^{\frac{5}{2}}}(\vec{x}^p(t)-\vec{x}^q(t))\times\vec{\alpha}^q(t) \tag{2.17}$$

$$\begin{aligned}\frac{d\vec{\alpha}^p}{dt} = \frac{1}{4\pi}\sum_{q=1}^{N_p}\Bigg[&\frac{|\vec{x}^p(t)-\vec{x}^q(t)|^2+\frac{5}{2}\sigma^2}{(|\vec{x}^p(t)-\vec{x}^q(t)|^2+\sigma^2)^{\frac{5}{2}}}\vec{\alpha}^p(t)\times\vec{\alpha}^q(t)+\\ +3&\frac{|\vec{x}^p(t)-\vec{x}^q(t)|^2+\frac{7}{2}\sigma^2}{(|\vec{x}^p(t)-\vec{x}^q(t)|^2+\sigma^2)^{\frac{7}{2}}}(\vec{\alpha}^p(t)\cdot(\vec{x}^p(t)-\vec{x}^q(t))\times\vec{\alpha}^q(t))(\vec{x}^p(t)-\vec{x}^q(t))+\\ &+105\nu\frac{\sigma^4}{(|\vec{x}^p(t)-\vec{x}^q(t)|^2+\sigma^2)^{\frac{9}{2}}}(vol^p\vec{\alpha}^q(t)-vol^q\vec{\alpha}^p(t))\Bigg]\end{aligned} \tag{2.18}$$

The assessment of the induced velocity of particles on one another involves utilizing a high-order algebraic function to regularize the Biot-Savart kernel. The transpose scheme (vortex stretching term) and particle strength exchange (viscous diffusion

term) model the circulation strength. The computational expense of the evolution equations is of $\mathcal{O}(N_p^2)$ due to its formulation as an "N-body problem", where N_p denotes the number of particles present in the simulation. The Fast Multipole Method [93] algorithm exaFMM [201] is used, enabling a calculation with a computational cost of $\mathcal{O}(N_p)$. The implementation of Pedrizzetti's relaxation scheme [157] is applied to maintain the divergence-free condition of the velocity field. The circulation strength of the particles is updated at every time step Δt as:

$$\vec{\alpha}^p(t)new = (1 - f\Delta t)\vec{\alpha}^p(t)_{old} + f\Delta t, \vec{\omega}_\sigma^p(\vec{x}^p, t) \left| \frac{\vec{\alpha}^p(t)_{old}}{\vec{\omega}_\sigma^p(\vec{x}^p, t)} \right| \tag{2.19}$$

The relaxation factor denoted by f is frequently fixed at 0.02. A scheme for particle splitting and merging, as outlined in Ref. [225], was implemented to prevent numerical instabilities and Lagrangian distortion. The temporal evolution of the equations is computed using a third-order low-storage four-step Runge-Kutta scheme. The dimension of the core radius is a tuning parameter that increases the fidelity of the approach; the smaller the core size, the better the vorticity field is represented at the expense of a higher computational cost. Using the default settings the rotor is discretized using a uniform paneling with 15 elements. The simulation duration is equivalent to twelve complete revolutions of the rotor, deemed adequate for achieving convergence of both thrust and torque on a global and local scale, given the specific rotor and operational parameters used in this work. The computational time ranges from 25 to 30 CPU hours. This duration exceeds that of the FVW code yet falls significantly below the cost of CFD simulations. An example of the vortex particle wake structure obtained for the test case presented in Chapter 4 is illustrated in Figure 2.3.

2.3 Simcenter STAR-CCM+

Simcenter STAR-CCM+ is a commercial Computational Fluid Dynamics (CFD) software offering different solvers for various flow problem types. STAR-CCM+ implements a Finite Volume Method (FVM), which discretizes the governing equations of fluid flow into a set of algebraic equations on a grid of cells. This linear system is solved with an algebraic multigrid (AMG) solver. The solvers and models used in this research will be briefly described in the lines below. A special treatment is given

to the γ-Re_θ transition model due to the analysis of different formulations presented in Chapter 3. Please refer to the user guide [189] for additional details.

2.3.1 Finite Volume Solver

During this research, we used the coupled flow solver, which accurately computes compressible and incompressible regimes by preconditioning the system. This is necessary for rotor flows as they are characterized by a range of Mach numbers close to 0 at the hub and generally over Mach 0.3 for high rotation rates on small-scale rotors. Mach number can be even higher for blades operating in the Martian atmosphere as the rotation rates are generally higher to compensate for the low density and also due to the reduced speed of sound in an atmosphere mainly formed of carbon dioxide.

The only exception where the segregated solver was used is the multiphase Volume of Fluid simulations described in Chapter 8 due to the incompatibility of the VOF solver with the coupled solver. The main advantage of using a segregated solver is the reduced memory requirements. Computational cost is comparable, and the coupled solver is advantageous as it presents a linear scaling with the cell count, whereas, for the segregated solver, this is not a given. The coupled flow solver is also more robust when strong source terms are present in the equations. This is the case of rotating flows. In the following lines, the numerical scheme for the coupled solver will be described. Please refer to reference [189] for the segregated solver details.

The coupled flow model simultaneously solves continuity, momentum, and energy equations. The Navier-Stokes equations in integral form for an arbitrary control volume V with a differential surface area dS are expressed are:

$$\frac{\partial}{\partial t}\int_V \mathbf{U}dV + \int_S \mathbf{F}\cdot d\mathbf{A} = \int_S \mathbf{G}\cdot d\mathbf{A} + \int_V \mathbf{S}dV \tag{2.20}$$

where:

$$\mathbf{U} = \begin{bmatrix} \rho \\ \rho\mathbf{v} \\ \rho E \end{bmatrix} \tag{2.21}$$

$$\mathbf{F} = \begin{bmatrix} \rho\mathbf{v} \\ \rho\mathbf{v}\mathbf{v} + p\mathbf{I} \\ (\rho E + p)\mathbf{v} \end{bmatrix} \tag{2.22}$$

$$\mathbf{G} = \begin{bmatrix} 0 \\ \tau \\ \tau \cdot \mathbf{v} + k \triangledown T \end{bmatrix} \tag{2.23}$$

and **S** represents any additional source term in the equations. Regarding our application, this term is important to add centripetal and Coriolis accelerations when solving rotating flows in non-inertial reference frames.

As previously mentioned, preconditioning is required to avoid numerical errors and provide efficient flow solutions at all speeds [223]. This code multiplies the transient term of the system by a preconditioning matrix:

$$\Gamma \frac{\partial}{\partial t} \int_V \mathbf{Q} dV + \int_S [\mathbf{F} - \mathbf{G}] \cdot d\mathbf{A} = \int_V \mathbf{S} dV \tag{2.24}$$

with

$$\mathbf{Q} = \begin{bmatrix} \rho \\ \mathbf{v} \\ T \end{bmatrix}$$

and Γ is:

$$\Gamma = \begin{bmatrix} \theta & 0 & \rho_T \\ \theta\mathbf{v} & \rho\mathbf{I} & \rho_T\mathbf{v} \\ \theta H - \delta & \rho\mathbf{v} & \rho_T H + \rho c_p \end{bmatrix} \tag{2.25}$$

and:

$$\rho_T = \frac{\partial \rho}{\partial T}|_p \tag{2.26}$$

For ideal gases

$$\delta = 1; \quad \rho_T = -\frac{p}{RT} \tag{2.27}$$

θ is defined as:

$$\theta = \frac{1}{U_R^2} - \frac{\rho_T}{\rho c_p} \tag{2.28}$$

The Reference velocity U_R is selected to improve the system's conditioning. This objective is achieved by imposing a constraint on the reference velocity, which must be either equivalent to or superior to the local convection or diffusion velocity.

Another constraint involves accounting for the impact of local pressure variations to enhance numerical stability in stagnation zones by preventing the amplification of pressure disturbances. The reference velocity is defined as:

$$U_R = min\left[max\left(|\mathbf{v}|, \frac{\nu}{\Delta x}, \varepsilon\sqrt{\frac{\delta p}{\rho}}, U_{Rmin}, \right), U_{Rmax}\right] \tag{2.29}$$

where Δx is the cell length scale over which the diffusion occurs, and δP is the pressure difference between adjacent cells. For compressible flows, the maximum reference velocity U_{Rmax} is limited to the local speed of sound, a. The scaling parameter ε is set to 2.

Surface and Volume integrals

STAR-CCM+ evaluates surface integrals using the second-order midpoint rule, multiplying the face center value by the face area. Face center values are unknown and therefore have to be interpolated from cell center values by applying the discretization schemes detailed in the following sections. On the other hand, volume integrals are approximated by the product of the mean source term value at the cell center and the volume of the cell.

Reconstruction Schemes

The discretized form of equation 2.20 requires the values of the conservative variables and their gradients at the faces of the cells. How the solution is reconstructed from cell center values has significant implications for the accuracy and stability of the scheme.

STAR-CCM+ offers different discretization schemes. The schemes used in our RANS simulations are the Second-Order Upwind (SOU) and the 3rd-order Monotonic Upwind Scheme for Conservation Laws (MUSCL). However, different solvers were used for scale-resolving simulations, as upwind schemes are known to produce an unnatural decay of turbulent kinetic energy. An analysis of the use of different schemes for large eddy simulations of separation-induced transition is shown in Chapter 3. In particular, we assessed the Bounded Central Difference (BCD) scheme and the Hybrid MUSCL 3rd-order/Central difference schemes with

different blending factors showing how a certain degree of upwind blending must be included trading-off accuracy, and stability. Regarding Detached Eddy Simulations (DES), STAR-CCM+ offers the possibility of blending BCD and the SOU schemes depending on the flow characteristics. In other words, the scheme will aim to use the SOU in RANS regions and BCD in LES regions. For specific details on the schemes, refer to [189].

Inviscid fluxes

STAR-CCM+ offers two options to evaluate inviscid fluxes, Weiss-Smith preconditioned Roe's scheme [222] and Liou's AUSM+ scheme [122].

In this work, Roe's scheme has been used. This upwind scheme considers that the fluxes at the interface contain relevant information propagating throughout the domain with speed and direction according to the eigenvalues and eigenvectors of the system. Using this flux-splitting approach, the flux at a given face may be expressed as:

$$\mathbf{f}_f = \frac{1}{2}(\mathbf{f}_0 + \mathbf{f}_1) - \frac{1}{2}\Gamma|\mathbf{A}|\Delta\mathbf{Q} \tag{2.30}$$

In the previous expression, "0" and "1" stand for the cells on either side of the face, Γ is the previously shown preconditioning matrix, $\Delta\mathbf{Q} = (\mathbf{Q}_1^r - \mathbf{Q}_0^r)$ and $|A|$ is defined as:

$$|A| = M|\Lambda|M^{-1} \tag{2.31}$$

where Λ is the diagonal matrix of eigenvalues and M is the modal matrix that diagonalizes $\Gamma^{-1}\dfrac{\partial f}{\partial Q}$

Diffusive fluxes

The diffusive flux g on the face $j+\frac{1}{2}$ is defined as the product of a diffusion coefficient, the gradients of the variable ϕ, and the surface area vector:

$$g_{j+\frac{1}{2}} = (\Gamma\nabla\Phi\mathbf{a})_{j+\frac{1}{2}} \tag{2.32}$$

STAR-CMM+ uses the second-order accurate approximation shown in the equation below to maintain the global accuracy of the scheme.

$$\nabla\Phi_{j+\frac{1}{2}} = (\Phi_{j+1} - \Phi_j)\alpha + \overline{\nabla\Phi_{j+\frac{1}{2}}} - (\overline{\nabla\Phi_{j+\frac{1}{2}}} \cdot \mathbf{ds})\alpha \tag{2.33}$$

where:

$$\alpha = \frac{\mathbf{a_{j+\frac{1}{2}}}}{\mathbf{a_{j+\frac{1}{2}}} \cdot \mathbf{ds}}; \quad \mathbf{ds} = \mathbf{x_{j+1}} - \mathbf{x_j}; \quad \overline{\nabla\Phi_{j+\frac{1}{2}}} = \frac{\nabla\Phi_{j+1} + \nabla\Phi_j}{2} \tag{2.34}$$

$\mathbf{x_j}$ and $\mathbf{x_{j+1}}$ are the centroids position of cell-j and that of its neighbor cell $j+1$, which both share face $j+\frac{1}{2}$, while $\mathbf{a_{j+\frac{1}{2}}}$ is the face area-vector.

Substituting the above in equation 2.33:

$$\begin{aligned} D_{j+\frac{1}{2}} = \Gamma_{j+\frac{1}{2}} \nabla\Phi_{j+\frac{1}{2}} \cdot \mathbf{a_{j+\frac{1}{2}}} = \\ \Gamma_{j+\frac{1}{2}} \left[(\Phi_{j+1} - \Phi_j)\alpha \cdot \mathbf{a_{j+\frac{1}{2}}} + \overline{\nabla\Phi_{j+\frac{1}{2}}} \cdot \mathbf{a_{j+\frac{1}{2}}} - (\overline{\nabla\Phi_{j+\frac{1}{2}}} \cdot \mathbf{ds}) \cdot \alpha \cdot \mathbf{a_{j+\frac{1}{2}}} \right] \end{aligned} \tag{2.35}$$

where $\Gamma_{j+\frac{1}{2}}$ is an harmonic average of cell values. The second and third terms in equation (2.35) model cross-diffusion effects, and they are key in ensuring high accuracy for non-orthogonal meshes.

Gradients

STARCCM+ follows these steps in order to compute the gradients:

1. computing the unlimited reconstruction gradients. In this context, unlimited means that the gradients may be reconstructed without protecting them from exceeding the minimum and maximum values of the neighboring cells. The Hybrid Gauss-Least Squares method[142] has been used during this work;
2. limiting the reconstruction gradients.

Hybrid Gauss-Least Squares Method enables the calculation of the unlimited reconstruction gradients for the cell-j $(\nabla\Phi)^u_{r,j}$ according to the following formula:

$$(\nabla\Phi)^u_{r,j} = \sum_f (\Phi_{j+1} - \Phi_j) w_f \tag{2.36}$$

with:

$$w_f = \beta w_f^{LSQ} + (1-\beta) w_f^G \tag{2.37}$$

$$w_f^{LSQ} = \left[\sum_f \frac{\mathbf{ds} \otimes \mathbf{ds}}{\mathbf{ds} \cdot \mathbf{ds}} \right]^{-1} \frac{\mathbf{ds}}{\mathbf{ds} \cdot \mathbf{ds}} \tag{2.38}$$

$$\mathbf{ds} = \mathbf{x_{j+1}} - \mathbf{x_j} \tag{2.39}$$

$$w_f^G = \frac{\mathbf{a_f}}{V_j + V_n} \tag{2.40}$$

Φ_j and Φ_{j+1} are data values in cell-j and its neighbor $J+1$, $\mathbf{a_f}$ is the face area-vector, V_j and V_{j+1} are the respective cell volumes, and β represents a blending factor for Gauss-LSQ gradient. The blending factor above determines which proportions of the two computing options are used to compute the gradient. Up to this point, the reconstruction gradients are unlimited, and this means that the reconstructed face values can fall outside the range of cell values found in cells with common faces.

STAR-CCM+ limits the reconstruction gradients by searching the minimum and maximum bounds of the neighboring cell values. A scale factor $\alpha_{j+\frac{1}{2}}$ is defined that expresses the ratio of the limited and unlimited values (limiter), that is:

$$(\nabla\Phi)_{r,j} = \alpha_{j+\frac{1}{2}} (\nabla\Phi)^u_{r,j} \tag{2.41}$$

And for each cell-j, the quantities:

$$\Phi_j^{max} = max(\Phi_j, \Phi_{neighbours}) \tag{2.42}$$

$$\Phi_j^{min} = min(\Phi_j, \Phi_{neighbours}) \tag{2.43}$$

$\Phi_{neighbors}$ represents the cell value in each neighbor with a common face with cell-j. Defining the following variables:

$$\Delta_{max} = \Phi_j^{max} - \Phi_j \tag{2.44}$$

$$\Delta_{min} = \Phi_j^{min} - \Phi_j \tag{2.45}$$

$$\Delta_{j+\frac{1}{2}} = \Phi_{j+\frac{1}{2},} - \Phi_j = \mathbf{S_j} \cdot (\nabla\Phi)^u_{r,j} \tag{2.46}$$

Where:

$$\mathbf{ds_{j+\frac{1}{2}}} = x_{j+\frac{1}{2}} - x_j \tag{2.47}$$

Then

$$r_{j+\frac{1}{2}} = \begin{cases} \frac{\Delta_{j+\frac{1}{2}}}{\Delta_{max}} & for \quad \Delta_{j+\frac{1}{2}} > 0 \\ \frac{\Delta_{j+\frac{1}{2}}}{\Delta_{min}} & for \quad \Delta_{j+\frac{1}{2}} \leq 0 \end{cases} \tag{2.48}$$

Venkatakrishnan's limiter is defined as follows [211]:

$$\alpha_{j+\frac{1}{2}} = \frac{2r_{j+\frac{1}{2}} + 1}{r_{j+\frac{1}{2}}(2r_{j+\frac{1}{2}} + 1) + 1} \tag{2.49}$$

Limiters prevent spurious or unphysical oscillations in the solution, which would otherwise appear close to regions where gradients are very pronounced. This is the employed limiter during this work.

2.3.2 The γ-Re$_\theta$ transition model

The γ-Re$_\theta$ transition model, originally proposed by Menter [137], is a two-equations local correlation-based transition model (LCTM) that solves one transport equation for the intermittency, γ, and another one for the transition onset momentum thickness Reynolds number, $\overline{Re}_{\theta_t}$. It is coupled with the SST k-ω turbulence model, also developed by Menter [135]. The two transport equations are integrated in time to obtain an effective value for the intermittency, γ_{eff}, which affects the turbulent kinetic energy equation of the $k-\omega$ SST model as follows [115]:

$$\rho \frac{Dk}{Dt} = \nabla \cdot [(\mu + \sigma_k \mu_t) \nabla k)] + \gamma_{eff} P_k - \min[\max[\gamma_{eff}, 0.1], 1] D_k \tag{2.50}$$

In Eq. (2.50), P_k and D_k are the original production and destruction terms of the SST k-ω model, respectively. The production term is defined as:

$$P_k = G_k + G_{nl} + G_b \tag{2.51}$$

Which represent the turbulent production, the non-linear production, and the buoyancy production terms, respectively. The destruction term is defined as:

$$D_k = \rho \beta^* f_{\beta^*} (\omega k - \omega_0 k_0) \tag{2.52}$$

where ρ is the density β^* is a model coefficient, f_{β^*} is the free-shear modification factor, and ω_0 and k_0 are the ambient turbulence values that counteract decay as shown in [194].

The "effective" value of the intermittency, γ_{eff}, is calculated as the maximum between the value of the intermittency coming from the transport equation, γ, and that given by the separation-induced transition correction, γ_{sep}:

$$\gamma_{eff} = \max(\gamma, \gamma_{sep}) \tag{2.53}$$

where

$$\gamma_{sep} = \min\left(s_1 \max\left[0, \frac{Re_v}{3.235 Re_{\theta_c}} - 1\right] e^{-\left(\frac{R_T}{20}\right)^4}, 2\right) F_{\theta_t} \tag{2.54}$$

In Eq. (2.54), s_1 is a parameter that controls kinetic energy injection in the separated region. The latter is the region where the strain-rate (or vorticity-rate) Reynolds number, Re_v, is significantly larger than the critical Reynolds number, Re_{θ_c}, which arises from an empirical correlation as a function of $\overline{Re}_{\theta_t}$. The critical Reynolds number indicates where intermittency first starts to increase in the boundary layer. The scalar value 3.235 represents the ratio between Re_v and Re_{θ_c} when the shape factor, H, is equal to 3.5, which represents the separation point according to Polhausen's method, in a boundary layer subject to an adverse pressure gradient, as shown in Menter [137].

The STAR-CCM+ implementation, until version 2021.1, uses a value of 2.193 instead of 3.235, as shown in equation Eq. (2.55).

$$\gamma_{sep} = \min\left(s_1 \max\left[0, \frac{Re_v}{2.193 Re_{\theta_c}} - 1\right] e^{-\left(\frac{R_T}{15}\right)^4}, 5\right) F_{\theta_t} \tag{2.55}$$

The value of 2.193 is associated with the maximum ratio between Re_v and Re_{θ_c} in a Blasius profile, and it appears in the first version of the γ-Re$_\theta$ transition model [113]. A small change is also present in the damping term, decreasing the denominator from 20 to 15, and the limiting value of the maximum intermittency increases from 2 to 5. These changes would, in theory, move the transition point slightly upstream and make the transition process faster due to the higher limit of the effective intermittency.

Since version 2021.2, STAR-CCM+ code was updated, and the separation-induced transition correction is now the formulation shown in Eq.(2.54).

The intermittency equation is written as:

$$\rho\frac{D\gamma}{Dt} = \nabla\cdot[(\mu+\frac{\mu_t}{\sigma_\gamma})\nabla\gamma] + P_\gamma - E_\gamma \tag{2.56}$$

The production term, P_γ, and the destruction term, E_γ, are defined as [115]

$$P_\gamma = F_{Length}c_{a1}\rho S[\gamma F_{onset}]^{0.5}(1-c_{e1}\gamma) \tag{2.57}$$

$$E_\gamma = c_{a2}\rho W\gamma F_{turb}(c_{e2}\gamma - 1) \tag{2.58}$$

In Eqs. (2.57)–(2.58),F_{onset} and F_{turb} are trigger functions that activate intermittency production and deactivate relaminarization, respectively. Coefficients c_{a1}, c_{a2}, c_{e1} and c_{e2} are model constants that we set equal to the values originally suggested by Menter [137]. F_{Length} and Re_{θ_c}, the latter embedded in F_{onset}, are empirical correlations expressed as functions of $\overline{Re}_{\theta_t}$. Originally, these correlations were considered proprietary and were not disclosed, thus pushing numerous authors to develop calibrations to fit existing experimental data. For example, Malan [124] proposed a calibration of the model that was implemented in STAR-CCM+ until, finally, Langtry [114] disclosed the original calibration that is also implemented in the CFD code. Both calibrations are compared in the following section.

The transport equation for the transition onset momentum thickness Reynolds number is defined as:

$$\rho\frac{D\overline{Re}_{\theta_t}}{Dt} = \nabla\cdot[\sigma_{\theta_t}(\mu+\mu_t)\nabla\overline{Re}_{\theta_t}] + P_{\theta_t} \tag{2.59}$$

Such an equation connects the empirical correlation to the onset criteria in the γ-equation. It accounts for non-local effects due to changes in the freestream turbulence, Tu, and the pressure gradient at the edge of the boundary layer. In Eq. (2.59), the production term,P_{θ_t}, is defined as:

$$P_{\theta_t} = c_{\theta_t}\frac{\rho}{t}(Re_{\theta_t} - \overline{Re}_{\theta_t})(1-F_{\theta_t}) \tag{2.60}$$

where c_{θ_t} is model constant, t is a time scale, and F_{θ_t} is a blending function that ensures that inside the boundary layer, the production term is turned off and also

that the transported scalar $\overline{Re}_{\theta_t}$ matches the value of the empirical correlation $Re_{\theta_t} = f(\lambda_\theta, Tu)$ in the freestream. The original version of the model contained such a correlation that had been previously assessed by other authors such as Abu-Ghannam and Shaw [2]. Langtry [115] modified the $Re_{\theta_t} = f(\lambda_\theta, Tu)$ correlation to improve results for low turbulence intensity simulations. He noted that when the boundary layer undergoes laminar separation, the model predicted a reattachment location downstream of the actual position in the experiments. The discrepancy was attributed to insufficient production of turbulent kinetic energy in the separated shear layer when the freestream turbulence intensity is small. Therefore, the correction embedded in Eqs. (2.53) and (2.54) was included in the transition model. The former increases the production of turbulent kinetic energy in separated regions, allowing intermittency to exceed unity.

Empirical correlations

As mentioned in the previous section, the empirical correlations integrating transition physics into the model were initially declared proprietary. Suluksna et al. [198, 124] performed a calibration of these models for unstructured parallelized codes, which is the default calibration used in STAR-CCM+. In what follows, we will refer to these correlations as to the Saluksna-Juntasaro Calibration. Finally, Langtry [114] disclosed the original calibration of the model. There are three empirical correlations needed to close the model. The first one is the critical momentum thickness Reynolds number, $Re_{\theta c}$, which can be considered the point at which the turbulence intensity begins to grow before transition. The second correlation, F_{length}, is designed to control the transition length. And the other correlation needed is the functional relationship between the transition momentum thickness Reynolds number, which represents the transition point observed experimentally, and the freestream turbulence intensity and Thwaites' parameter, $Re_{\theta_t} = f(\lambda_\theta, Tu)$.

In Chapter 3, we will test both calibrations and comment on the effect of including the pressure gradient in the case of Menter's correlation. The Suluksna-Juntasaro calibration defines the following correlations for $Re_{\theta c}$ and F_{length}:

$$Re_{\theta c} = min\left(\overline{Re}_{\theta_t}, 0.615\overline{Re}_{\theta_t} + 61.5\right) \tag{2.61}$$

$$F_{length} = min\left(300, exp(7.168 - 0.01173\overline{Re}_{\theta_t}) + 0.5\right) \tag{2.62}$$

Regarding Menter's calibration, we used the empirical correlations provided in Langtry [114], which are expressed as:

$$Re_{\theta c} = \begin{cases} A_1 + A_2\overline{Re}_{\theta_t} + A_3\overline{Re}_{\theta_t}^2 + A_4\overline{Re}_{\theta_t}^3 + A_5\overline{Re}_{\theta_t}^4, & \overline{Re}_{\theta_t} \leq 1870; \\ B_1 + B_2\overline{Re}_{\theta_t} + B_3\overline{Re}_{\theta_t}^2 + B_4\overline{Re}_{\theta_t}^3, & \overline{Re}_{\theta_t} > 1870 \end{cases} \tag{2.63}$$

$$F_{length} = F_{length_1}(1 - F_{sublayer}) + 40F_{sublayer} \tag{2.64}$$

where F_{length_1} is defined as:

$$F_{length_1} = \begin{cases} C_1 + C_2\overline{Re}_{\theta_t} + C_3\overline{Re}_{\theta_t}^2, & \overline{Re}_{\theta_t} < 400; \\ D_1 + D_2\overline{Re}_{\theta_t} + D_3\overline{Re}_{\theta_t}^2 + D_4\overline{Re}_{\theta_t}^3, & 400 \leq \overline{Re}_{\theta_t} < 596; \\ D_1 + D_2\left(\overline{Re}_{\theta_t} - D_3\right), & 596 \leq \overline{Re}_{\theta_t} < 1200; \\ E, & \overline{Re}_{\theta_t} \geq 1200 \end{cases} \tag{2.65}$$

and $F_{sublayer}$ is defined as:

$$F_{sublayer} = exp\left[-\left(\frac{\omega d^2}{200\nu}\right)^2\right] \tag{2.66}$$

The values of the numerical coefficients A_i, B_i, C_i, D_i, and E can be found in Langtry [114]. These correlations are significantly more complex than those Suluksna-Juntasaro used, including higher-order polynomials and differentiation for different turbulence intensities conditions implicitly through $\overline{Re}_{\theta_t}$. The correlations used in both cases for Re_{θ_t} are those proposed in [114]:

$$Re_{\theta_t} = \begin{cases} \left(1173 - 589.428Tu + \dfrac{0.2196}{Tu^2}\right) F(\lambda_\theta), & Tu < 1.3\%; \\ 331.5\left(Tu - 0.5658\right)^{-0.671} F(\lambda_\theta), & Tu > 1.3\% \end{cases} \tag{2.67}$$

The only difference is that the Suluksna-Juntasaro calibration sets $F(\lambda_\theta)$ to 1, so that the correlation is independent from the pressure gradient, while Langtry [114]

defines $F(\lambda_\theta)$ as:

$$F(\lambda_\theta) = \begin{cases} 1 - \left(-12.986\lambda_\theta - 123.66\lambda_\theta^2 - 405.689\lambda_\theta^3\right) e^{-\left(\frac{Tu}{1.5}\right)^{1.5}}, & \lambda_\theta < 0; \\ 1 + 0.275\left(1 - e^{-35\lambda_\theta}\right) e^{\left(\frac{-Tu}{0.5}\right)}, & \lambda_\theta > 0 \end{cases} \tag{2.68}$$

Thwaites' parameter, λ_θ, is defined as:

$$\lambda_\theta = \frac{\theta^2}{\nu}\frac{dU}{ds} \tag{2.69}$$

but the boundary layer transition momentum thickness is not calculated as an integral quantity due to the great cost this would generate for unstructured parallelized codes. This quantity is estimated locally from the value Re_{θ_t}. Therefore equation (2.67) must be solved iteratively.

2.3.3 Adjoint Solver

The adjoint method effectively predicts the impact of numerous input parameters on specific engineering quantities of interest in a numerical simulation. It measures the sensitivity of objective functions with respect to input parameters, including design variables or boundary condition values. The adjoint analysis comprises two main stages. Initially, it is necessary to compute the steady-state solution for the physical phenomenon being studied. The second step involves the evaluation of the adjoint of the simulated physics based on the primal solution obtained in the previous step.

In the adjoint workflow, primal solutions are computed in 3 main steps. Initially, design parameters (D) are defined, which drive the grid morphing in a topological optimization. The relation between the design parameters and the grid (X) depends on the morphing strategy. Then the governing equations are solved, expressing its solution as Q. Finally, the solution is post-processed to compute the engineering quantities we aim to optimize. In this work, these quantities are aerodynamic efficiency for airfoils and power loading for rotors, as described in chapters 3 and 5. These operations are computed sequentially and can be mathematically expressed as: X(D), Q(X), L(Q,X). The inputs of this sequence are the design parameters, and the

output is the objective function. The adjoint of the primal solution is computed in reversed order to the sequence as mentioned above.

The adjoint algorithm provides the gradients of the objective function L with respect to the design parameters. This gradient may be used in an optimization algorithm to optimize the objective function. These gradients are also known as the sensitivity of the objective function with respect to the design parameters and can be expressed as the following chain of Jacobians:

$$\frac{dL}{dD} = \left[\frac{\partial L}{\partial X} + \frac{\partial L}{\partial Q}\frac{\partial Q}{\partial X}\right]\frac{dX}{dD} \tag{2.70}$$

The rightmost term, $\frac{dX}{dD}$ is the jacobian of the operation X(D). The rows of the matrix represent gradients, and the columns represent tangents. When the number of variables becomes large, computing equation 2.70 with full Jacobians increases memory requirements. An alternative is to work with tangents of the Jacobian of the X(D) operation. In other words, working with the columns of the system:

$$\frac{dL}{dD_i} = \left[\frac{\partial L}{\partial X} + \frac{\partial L}{\partial Q}\frac{\partial Q}{\partial X}\right]\frac{dX}{dD_i} \tag{2.71}$$

This reduces the memory requirements, but the computational time scales linearly with the number of design parameters due to the increased number of tangents. As normally, the number of objectives is much smaller compared to the number of design variables, an efficient way to address the aforementioned issue is to compute the transpose of the derivative system for a given gradient of the jacobian:

$$\frac{dL_j}{dD}^T = \frac{dX}{dD}^T\left[\frac{\partial L_j}{\partial X}^T + \frac{\partial Q}{\partial X}^T\frac{\partial L}{\partial Q}^T\right] \tag{2.72}$$

To compute the gradient for a given objective, $\frac{dL_j}{dD}^T$, the terms shown in equation 2.72 have to be computed. The term $\frac{dX}{dD}^T$ can be interpreted as the sensitivity of the mesh with respect to the design parameters. The term $\frac{\partial L}{\partial Q}^T$ represents the sensitivity of the reports with respect to the solution. The term $\frac{\partial L_j}{\partial X}^T$ stands for the sensitivity

of the objective with respect to the mesh. The two previously defined terms are used to compute the sensitivity of the objectives with respect to the grid, which is defined as the term enclosed by squared brackets. For detailed information of the algorithms used by STAR-CCM+ to compute these terms refer to reference [189].

2.3.4 Multiphase Flow

Chapter 8 addresses the problem of rotor-droplet interactions in UAS spraying applications. This problem involves two different immiscible fluids, air and water. To address the interactions between these phases, one may select different approaches that fall into Lagrangian and Eulerian subgroups. The former models the interactions between both phases, whereas in the latter, these are resolved. This work will use a Volume Of Fluid (VOF) approach to characterize a hollow cone nozzle. This simulation will provide velocity distributions of the droplets forming the spray. This information will then be used to inject Lagrangian particles into a larger-scale simulation. Simcenter STAR-CCM+ implementation of these two models is briefly described below.

2.3.4.1 Lagrangian Particles

The spray droplets injected in our simulations are modeled as material spherical particles. Sprays tend to generate droplet diameter distributions that may vary by an order of magnitude. This means that the inertia of these droplets will vary three orders of magnitude. This greatly impacts the drift problem, and it is important to consider this variation to estimate droplet deposition patterns.

The motion of a particle may be described by solving the linear momentum conservation law, shown in Equation 2.73.

$$m_p \frac{\mathbf{v}_p}{dt} = \mathbf{F}_g + \mathbf{F}_{vm} + \mathbf{F}_d + \mathbf{F}_p + \mathbf{F}_{sl} \tag{2.73}$$

where the forces acting on the particle are, from left to right, the gravity force, the virtual mass force, the drag force, the pressure gradient force, and the shear lift force. The drag coefficient proposed in [181] has been used to compute the drag

force. For the calculation of the shear lift, the expression provided in [191] has been employed.

2.3.4.2 Volume of Fluid Approach

The Volume of Fluid Multiphase Model pertains to the family of interface-capturing techniques for predicting the distribution and movement of the interface of immiscible phases. The mesh resolution must be sufficient for this modeling approach to resolve the location and shape of the interface between phases.

The distribution of the phases in the domain is determined by the volume fraction of phase *i*, which may be defined as:

$$\alpha_i = \frac{V_i}{V} \tag{2.74}$$

where V is the volume of a given cell, and V_i is the volume of phase i in that cell. Therefore, the volume fraction defines the proportion of a phase. The sum of the volume fractions for all phases must add up to 1.

To calculate the evolution of the phases in the simulation, this approach solves an extra scalar transport equation for the volume fraction as shown in Equation 2.75.

$$\frac{\partial \alpha_i}{\partial t} + \nabla \cdot (\alpha_i \mathbf{u}) = S_{\alpha_i} - \frac{\alpha_i}{\rho_i}\frac{D\rho_i}{Dt} - \frac{1}{\rho_i}\nabla \cdot (\alpha_i \rho_i \mathbf{u}_{d,i}) \tag{2.75}$$

The Courant Friedrich Levy (CFL) number should be kept below 0.5, even for implicit time integration schemes to avoid interphase blurring. To avoid this restrictive condition on the global time step, a multi-stepping approach for the volume fraction transport equation has been used, allowing the global CFL condition to be relaxed and, thus, reducing the computational cost of the simulations. STAR-CCM+ provides two multi-stepping approaches, an explicit approach and an implicit one. The explicit approach automatically calculates the number of steps to satisfy a target CFL. On the other hand, in the implicit formulation, the number of iterations is user-specified. It is, therefore, interesting to use an adaptive time-stepping scheme to ensure sufficiently low local CFL values to maintain a sharp interphase.

The problem presented in Chapter 8 is the spraying process in a hollow cone nozzle. To model the generation of droplets, we will address the problem of resolving

the Air-Water interface. In a biphase simulation, the liquid volume fraction is an indicator function defining the phase. A value of 1 corresponds with "phase 1" (water), and a value of 0 corresponds with "phase 2" (air). Therefore, only one equation has to be solved as the other phase will be obtained to ensure that their sum equals 1. The interphase can be defined with a value of the volume fraction 0.5. The cells in the interphase region must be refined to capture a sharp interphase. Due to the different scales involved in the problem, an Adaptive Mesh Refinement (AMR) strategy is mandatory to capture the water-air interphase without refining the whole computational domain. This AMR must be performed automatically every time step due to the dynamic nature of the problem. The Continuum Surface Force (CSF) approach, first described by Brackbill [32], is included to model the surface tension, which is known to be necessary to reproduce the atomization process [118] adequately.

2.3.5 6-DOF solver

Simcenter STAR-CCM+ allows you to model the motion of rigid bodies in response to applied forces and moments. In a rigid body, the relative distance between internal points does not change; therefore, it is sufficient to solve the equations of motion for the body's center of mass. A continuum body is a rigid body coupled with a fluid boundary, representing the surface of the rigid body. Simcenter STAR-CCM+ calculates the body's motion in response to the fluid forces and moments at the coupled boundary. The effect of the motion of the rigid body on the fluid is accounted for by moving the entire fluid mesh rigidly. Simcenter STAR-CCM+ calculates the resultant force and moment acting on the body due to user-defined forces and moments and the pressure and shear forces.

The resultant force and moment acting on the body can be written as:

$$\vec{F} = \vec{F}_p + \vec{F}_\tau + \vec{F}_g + \sum \vec{F_{ext}} \tag{2.76}$$

$$\vec{M} = \vec{M}_p + \vec{M}_\tau + \sum \vec{M_{ext}} \tag{2.77}$$

where $\vec{F_{ext}}$ represents user-defined forces and $\vec{M_{ext}}$ represents user-defined moments, which you can define directly or as the result of user-defined forces. For

example, in Chapter 6, we define a user-defined moment to model the friction of the hinge as shown in Eq.6.7. $\vec{F}_g$ is the gravity force. $\vec{F}_p$ and $\vec{M}_p$ are the fluid pressure force and moment acting on the body. $\vec{F}_\tau$ and $\vec{M}_\tau$ are the fluid shear force and moment, respectively.

For a single body with no kinematic restrictions present, we retrieve the classical 6-DOF free-body solver. This solver has been used in Chapters 7 and 8 to analyze multicopter maneuvers. The linear and angular momentum conservation laws shown below are integrated in this case.

$$\begin{aligned} \left.\frac{d\vec{C}}{dt}\right|_1 &= \vec{F} \\ \left.\frac{d\vec{\Gamma}}{dt}\right|_1 &= \vec{M} \end{aligned} \tag{2.78}$$

Two or more bodies are connected by one or more joints that stipulate certain kinematic constraints. Therefore, the kinematic constraint condition restricts the position of the bodies relative to each other. We will employ hinge joints to couple the blades and the hub in Chapter 6.

The general equation that describes the dynamic behavior of a multi-body system is:

$$\overleftrightarrow{m}\,\ddot{\vec{q}} = \vec{f} \tag{2.79}$$

where q is the vector of generalized coordinates, f is a generalized force, and m is the block-diagonal matrix of the inertia matrices of the rigid bodies. The equation of motion is combined with a constraint condition that restricts the kinematic degrees of freedom of the bodies:

$$\phi(\vec{q},t) = 0 \tag{2.80}$$

A constraint is expressed as a linear condition on the accelerations of the bodies. In our case, the constraint is a hinge-type constraint that maintains the rotation axis of the blades in the desired position at every time. Computing the second derivative yields:

$$J\ddot{\vec{q}} = \vec{Q} \tag{2.81}$$

where J is the Jacobian matrix of ϕ, $\ddot{\vec{q}}$ is the acceleration of the bodies, and Q is a vector that absorbs terms that are quadratic in the velocities [184].

A constraint force is added to the system to enforce the acceleration conditions of the constraints. By introducing the Lagrangian multiplier λ of all constraints, the workless constraint force is given by:

$$\vec{f}_c = J^T \lambda \tag{2.82}$$

A vector $\vec{\lambda}$ is sought such that the constraint force $\vec{f}_c$ in combination with any external force $\vec{f}$ such as gravity produces a motion that satisfies the constraints.

$$\overleftrightarrow{m}\,\ddot{\vec{q}} = J^T\vec{\lambda} + \vec{f} \tag{2.83}$$

Solving for $\ddot{\vec{q}}$:

$$\ddot{\vec{q}} = \overleftrightarrow{m}^{-1} J^T\vec{\lambda} + \overleftrightarrow{m}^{-1}\vec{f} \tag{2.84}$$

yields the following linear system of equations:

$$A\lambda = b \tag{2.85}$$

$$A = J\,\overleftrightarrow{m}^{-1} J^T \tag{2.86}$$

$$B = -J\,\overleftrightarrow{m}^{-1}\vec{f} + Q \tag{2.87}$$

λ can be computed by solving the linear system shown in Eq.2.85 and then, $\vec{q}$ con be obtained by integrating twice Eq.2.84.

The integration to obtain the coordinates vector q is performed numerically. Therefore, some constraint drift occurs due to numerical integration errors. The aim of constraint stabilization is to bound this drift preventing its accumulation over time. Following Baumgarte [18], constraint stabilization is applied by modifying Eq.2.88:

$$J\ddot{\vec{q}} = \vec{Q} - 2\alpha J\dot{q} + \frac{\partial \phi}{\partial t}\beta^2\phi \tag{2.88}$$

where α and β are parameters of the stabilization method.

Chapter 3

Very-Low and Ultra-Low Reynolds Number Airfoil Aerodynamics

This chapter includes the partial content of the papers:

- M. Carreño Ruiz and D. D'Ambrosio. Validation of the $\gamma - Re_\theta$ Transition Model for Airfoils Operating in the Very Low Reynolds Number Regime. *Flow, Turbulence and Combustion*, pages 1–30, 2022
- M. Carreño Ruiz, M. Scanavino, D. D'Ambrosio, G. Guglieri, and A. Vilardi. Experimental and numerical analysis of hovering multicopter performance in low-Reynolds number conditions. *Aerospace Science and Technology*, 128:107777, 2022

The accurate aerodynamic modeling of airfoils for rotary wing applications is relevant to the overall blade performance predictions. Reduced Order Models (ROMs) typically used to analyze rotor flows require an airfoil aerodynamic database to compute different blade elements' lift and drag components. For higher Reynolds numbers, where boundary layers are likely to be attached and turbulent, panel methods can provide very good estimations of airfoil performance. In the Reynolds numbers under study, the flow is likely to be laminar if the boundary layer remains attached, and the laminar-turbulent transition will occur only after the separation of the boundary layer. We can distinguish two Reynolds number regimes. The ultra-low Reynolds number regime comprises Reynolds numbers in the range $10^3 - 10^4$

and the very-low Reynolds number regime between $10^4 - 10^5$. A laminar regime for low and moderate angles of attack usually characterizes the former. Laminar separation bubbles on the suction side of the airfoils with turbulent reattachment typically dominate the latter. The presence of transition poses significant modeling challenges. Numerical simulations must couple a transition model to a turbulence model to adequately reproduce the evolution of separation bubbles. This is actually important to adequately capture the airfoil performance as the separation bubble modifies the effective camber and thickness and, thus, the lift and drag coefficients.

3.1 Very-Low Reynolds number

3.1.1 RANS Turbulence and Transition Modelling

The present study uses the CFD code STAR-CCM+, which offers three transition models coupled with RANS equations, namely a) turbulence suppression, b) γ transition, and c) γ-Re$_\theta$ transition. The turbulence suppression approach requires the knowledge of the transition point and, therefore, could be used to check the ability of RANS solvers to reproduce separation bubbles [56], but not to determine the transition point. The γ transition model is a one-equation intermittency-based model, which Menter et al. improved [139] to correct deficiencies in the γ-Re$_\theta$ model with the further advantage of integrating a single equation and of being Galilean invariant. However, the implementation of this model in STAR-CCM+ lacks a separation-induced transition correction constant C_{SEP}, which is necessary to tune the production of turbulent kinetic energy in separated regions, controlling the separation bubble's length. Therefore, this work focuses on the γ-Re$_\theta$ transition model.

3.1.1.1 Numerical simulation and validation

Physical/mathematical model and numerical method

The physical/mathematical model used to simulate the flowfield is based on the compressible unsteady Reynolds-Averaged Navier Stokes (URANS) equations. As mentioned, the turbulence model is the two-equations SST k-ω model, coupled with

the two-equations γ-Re_θ transition model. The commercial CFD software STAR CCM+, in particular, version 14.06.12, offers the implementation used in this Chapter. The calculation of inviscid fluxes adopts a second-order upwind reconstruction combined with Roe's scheme, whereas the evaluation of viscous fluxes uses a second-order approximation, as detailed in Chapter 2. Even though the generation of separation bubbles is an unsteady process characterized by vortex shedding [84], time-resolved simulations are not always required. The mean separation bubble is usually steady, so we could use a RANS solver. However, the periodic vortex shedding is intense in situations close to the bubble bursting. The mean values of lift and drag obtained with unsteady simulations significantly differ from those of the steady solver. In this regard, Pauley [150] suggests that the bursting of the bubble, described for the first time by Gaster [86], is associated with an averaged vortex shedding. The URANS simulations shown in section 3.1.1.4 employ an implicit second-order time integration scheme with a time step of 0.01 turnovers. The time step length ensures that the vortex shedding regime is resolved and allows for the convergence of the inner solver, which runs for ten iterations every time step.

Computational domain and boundary conditions

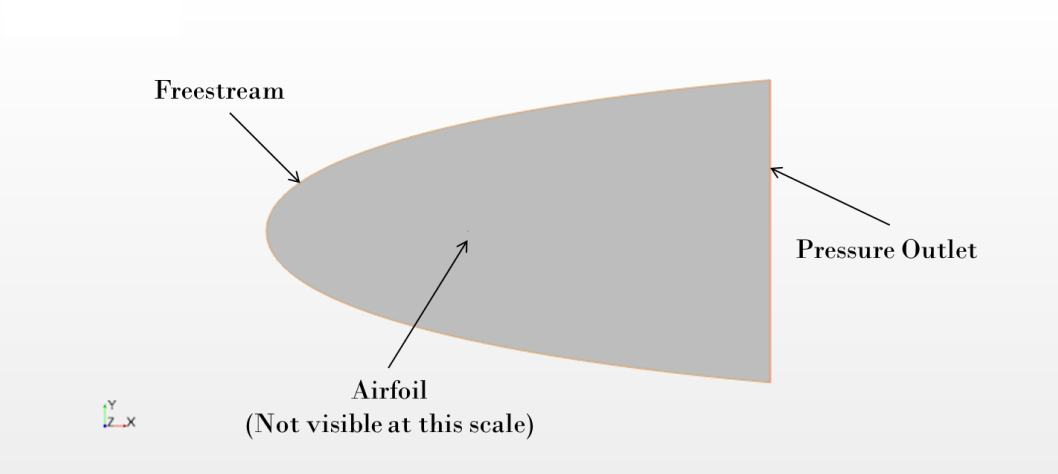

Fig. 3.1 Fluid domain and boundary conditions.

The adopted computational domain is visible in Figure 3.1. Its extension is about 1000 chords in the streamwise direction (400 upstream and 600 downstream) and

600 (at the outlet section) in the transversal direction. We chose such a large domain to minimize the influence of the far-field boundary conditions, as recommended for the NACA 0012 test case in the NASA Turbulence Modeling Resource [168]. We enforce the freestream, inflow boundary conditions (Mach number, and static pressure and temperature) on a parabolic-shaped "inflow" surface, and we impose the freestream pressure on the "outflow" flat surface normal to the freestream direction. No-slip, adiabatic wall conditions are set on the airfoil surface. As we will show in the next section, the freestream is always aligned with the x-axis, and the airfoil is rotated (and the grid is re-meshed) to account for changes in the angle of attack. The boundary conditions for the turbulent kinetic energy and the specific dissipation rate are null wall flux and a fixed freestream value. The boundary conditions for intermittency are a value of 1 at the freestream and zero wall flux. The boundary conditions for the transition momentum thickness Reynolds number derive from (2.67) in the freestream (without using the pressure gradient correction) and consist in a null flux at the walls.

Grid generation and refinement analysis

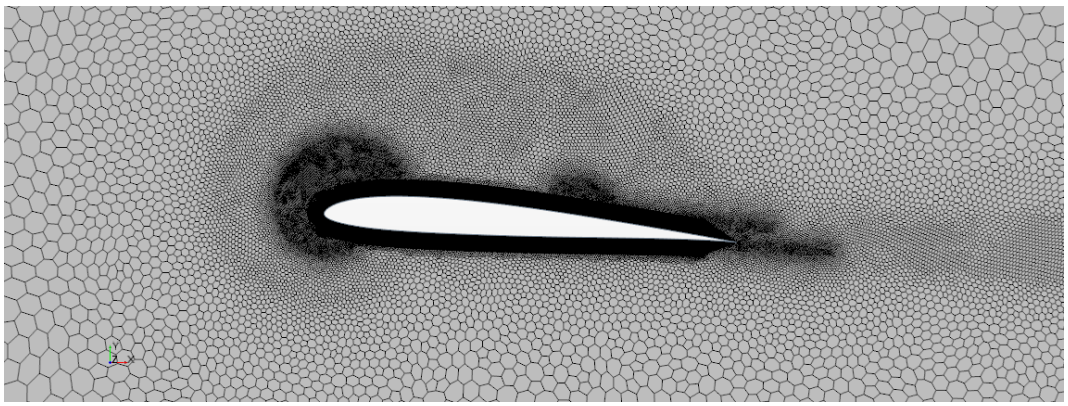

Fig. 3.2 Medium/Medium grid for airfoil SD7003 at $\alpha = 4^o$ and Re=60,000.

We built the computational meshes using the automated, unstructured polyhedral mesh generation software embedded in STAR-CCM+ in combination with a prism layer mesh in the near-wall region. As suggested in [159], polyhedral cells can potentially speed up simulation convergence as information spreading might be enhanced by having more neighboring cells than quadrilateral or triangular grids. That is a positive feature for low-Reynolds numbers simulations incorporating a

transition model since the former usually suffer from slow convergence rates. Since the computational domain is huge, an adaptive mesh refinement (AMR) strategy has been implemented based on pressure and velocity gradients to reduce the number of cells where they are not needed, for example, in the far-field region, where gradients are almost zero. In addition, the AMR approach is quite useful in the low-Reynolds number regime, where the flowfield can change drastically with the angle of attack, moving from fully attached boundary layer situations to the formation of separation bubbles or even massive separations. Figure 3.2 shows an example of the effect of the AMR strategy. One can see that the grid is quite fine near the leading edge due to the large local pressure and velocity gradients, but also in the separated shear layer and wake regions due to the large velocity gradients. The refined area in the central-rear region of the suction side is associated with the reattachment of a separation bubble. A prism layer with $y^+ < 1$ helps to properly resolve the wall region, as required by this transition model [115]. The grid independence study shown in Table 3.3 has been carried out for airfoil SD7003 at Reynolds 60,000 and $\alpha = 4^o$. Three different grid generation strategies, namely coarse, medium, and fine, have been defined for the prism layer and polyhedral mesh as shown in Tables 3.1 and 3.2. From now on, we will adopt the medium/medium grid combination, as it is a good compromise between computational cost and the correct determination of aerodynamic coefficients and flowfield features. It is important to point out that the number of cells associated with AMR strategies is not constant and can vary up to a factor of 2 when massive separation is present, especially at high angles of attack and noticeably low Reynolds numbers.

Table 3.1 Adaptive Mesh Refinement mesh size specifications.

Grid	**Minimum cell size(%c)**	**Maximum cell size(%c)**
Coarse	0.4	4000
Medium	0.3	3000
Fine	0.2	2000

3.1.1.2 Freestream turbulence conditions

Transition is very sensitive to freestream turbulence conditions. In the γ-Re_θ model, sensitivity to freestream turbulence intensity is obtained through the empirical correlations defined in Eqs. (2.67) and (2.68). Turbulence intensity can be measured

Table 3.2 Prism layer mesher specifications.

Grid	**Chordwise spacing(%c)**	**Nº of Layers**	**Wall Cell Thickness(%c)**
Coarse	0.6	25	0.004
Medium	0.3	50	0.004
Fine	0.15	75	0.004

Table 3.3 Grid Independence study for the airfoil SD7003 at Re=60,000, $\alpha = 4^o$.

Grid/Prism Layer	**Nº of cells**	$\frac{x_{sep}}{c}$	$\frac{x_{re}}{c}$	C_l	C_d
Medium/Coarse	43,774	0.176	0.781	0.6025	0.02730
Coarse/Medium	58,510	0.181	0.742	0.6007	0.02591
Medium/Medium	69,834	0.181	0.741	0.6020	0.02585
Fine/Medium	103,480	0.181	0.741	0.6021	0.02581
Medium/Fine	135,581	0.181	0.742	0.6047	0.02580
Fine/Fine	167,084	0.182	0.741	0.6016	0.02574

experimentally, but another variable associated with the length scale of turbulence is needed, for example, the specific dissipation rate, ω, whose determination is challenging and whose value is not always available in existing data. In addition, computational domains used in CFD simulations are usually large to reduce the influence of the boundary conditions, but since turbulence intensity decays as the flow approaches the body, the effective value of turbulence intensity in front of the airfoil can be significantly smaller than the value given at the numerical inlet boundary. A solution to this problem is increasing the turbulence intensity at the computational inflow to match the experimental value at the leading edge [61]. Provided that turbulence intensity and turbulent viscosity ratio near the airfoil are known from experiments, the following equations provide an initial guess for their freestream "inlet" values [189]:

$$Tu = (Tu)_{inlet}\left(1+\frac{0.1242x\rho U_\infty (Tu)^2_{inlet}}{\mu (TVR)_{inlet}}\right)^{\text{-0.5435}} \tag{3.1}$$

$$TVR = (TVR)_{inlet}\left(1+\frac{0.1242x\rho U_\infty (Tu)^2_{inlet}}{\mu (TVR)_{inlet}}\right)^{\text{-0.087}} \tag{3.2}$$

The turbulent viscosity ratio and turbulence intensity can be defined using turbulent kinetic energy and the specific dissipation rate as shown in the following equations:

$$Tu = \frac{\sqrt{\frac{2}{3}k}}{U} \tag{3.3}$$

$$TVR = \frac{k}{\omega\mu} \tag{3.4}$$

An issue related to freestream turbulence conditions is that meshes are usually coarse near freestream boundaries, which prevents an accurate resolution of the freestream turbulence decay. In connection to this point, Menter [139] stated that inlet values for the eddy viscosity ratio affect the turbulence intensity decay and that this affects the transition location. Spalart [194] suggested introducing a source term in the turbulent kinetic energy equation that maintains constant the value of the turbulence intensity, thus overriding the previously mentioned issues. This option is available in STAR-CCM+, and it was adopted in this study, allowing to set the turbulence intensity at the inlet to the actual value measured in the experiments. In this way, the effect of the eddy viscosity ratio should not be very significant because turbulence intensity stays artificially constant. We tested the hypothesis by performing a sensitivity analysis by varying the turbulence conditions at the inlet. We found out that the effect of the TVR is almost negligible as long as the latter is large enough to avoid the turbulence model staying dormant. The magnitude of the minimum TVR value tends to increase with freestream turbulence intensity. Figure 3.3 shows that the boundary layer remains laminar for small values of inlet TVR, and the flow around the airfoil is inconsistent. A TVR equal to 1 seems to work adequately, despite being higher than the value suggested by Rumsey [169] for the SST model. The explanation is that probably the values recommended in [169] were intended for the use of the SST turbulence model to predict transition without transition model, setting the freestream turbulence conditions in such a way that the model remains dormant near the leading edge and then it switches on mimicking the transition.

Concerning the freestream value of turbulence intensity, Schlichting [182] states that, based on experimental data, the effect of Tu values smaller than 0.1% is irrelevant. On the other hand, Langtry [115] sets $Tu = 0.027\%$ as the lower limit for

numerical stability. Therefore, selecting Tu between 0.027% and 0.1% at freestream is a reasonable choice for comparisons with LES simulations that use an ideal freestream to reduce computational costs. Unfortunately, the correlation $Re_{\theta_t} = f(Tu, \lambda_\theta)$ suggested by Langtry [115] and shown in Eq. (2.67) is in fact sensitive to Tu values in this range, as shown in Table 3.4. In summary, despite some authors using the freestream Tu as a tuning parameter to fit existing experimental data or LES simulations, we believe the limiting value of Tu should not be larger than 0.1%. In fact, since the correlation for Re_{θ_t} in Eq. (2.67) is based on many experimental data obtained at different turbulence intensities, using Tu as a tuning parameter for the transition model would not be consequential. The simulations presented in this section employ a freestream turbulence intensity of 0.03% to allow a reasonable comparison with LES simulations, which assume an ideal freestream. The turbulent viscosity ratio is equal to 1.

Table 3.4 Effects of turbulence inflow conditions on performance. Airfoil SD7003, Re=60,000, $\alpha = 8^o$.

Tu(%)	**TVR**	C_l	C_d
0.03	0.001	0.9188	0.04105
0.08	0.001	0.7418	0.04285
0.43	0.001	-0.0318	0.02895
0.03	0.01	0.9223	0.04095
0.08	0.01	0.9291	0.03911
0.43	0.01	-0.0060	0.02986
0.03	0.1	0.9225	0.04090
0.08	0.1	0.9304	0.03909
0.43	0.1	0.9299	0.03709
0.03	1	0.9225	0.04089
0.08	1	0.9304	0.03908
0.43	1	0.9294	0.03707
0.03	10	0.9225	0.04090
0.08	10	0.9304	0.03908
0.43	10	0.9396	0.03706

Test case: Low Reynolds number airfoil SD7003

Figure 3.4 shows the velocity field around the SD7003 airfoil at Reynolds 60,000 using Menter correlations. We can clearly see how, at 4 degrees, a long separation

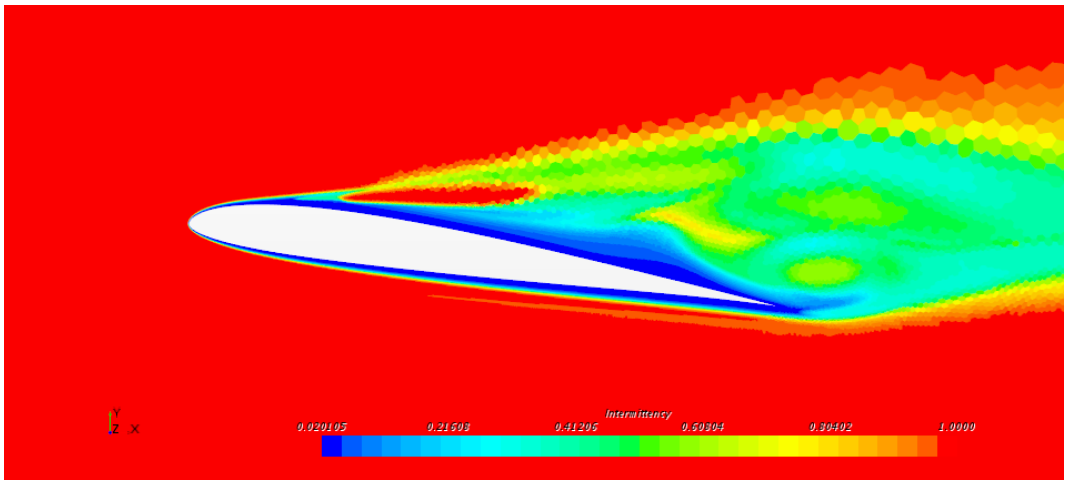

(a) TVR=0.01

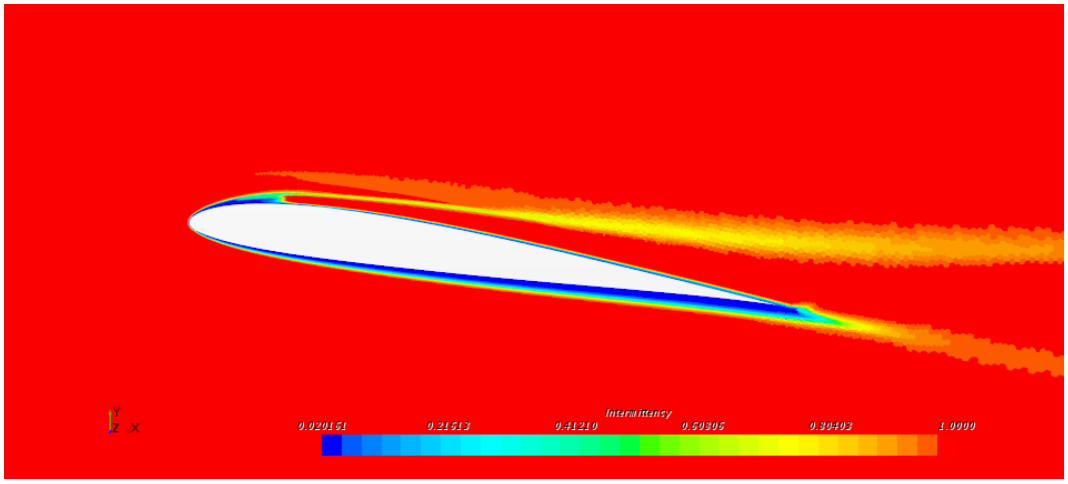

(b) TVR=1.00

Fig. 3.3 Intermittency contours for airfoil SD7003 at $\alpha = 8^o$, Re=60,000, $Tu = 0.43\%$.

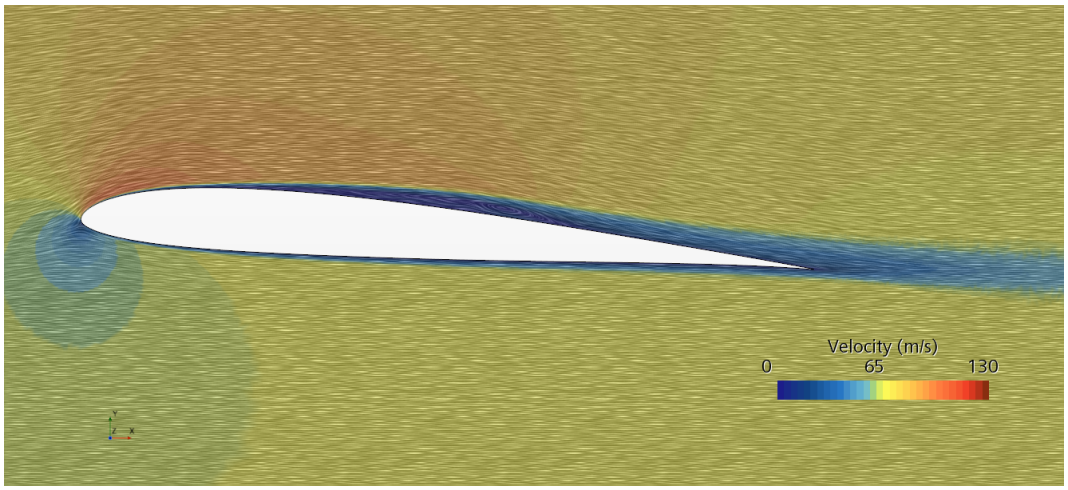

(a) AOA=4º

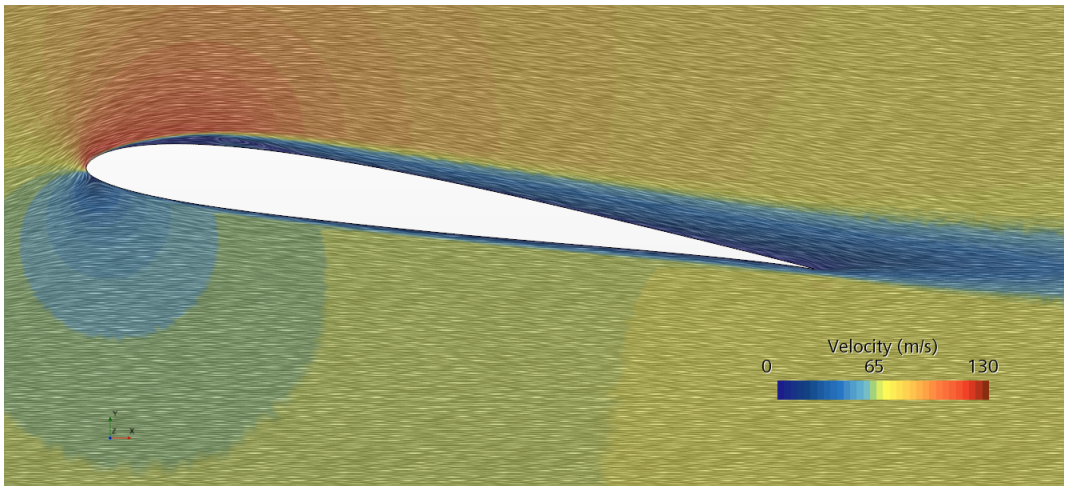

(b) AOA=8º

Fig. 3.4 Velocity fields with line convolution integrals using Menter correlations. $Re = 60,000$.

bubble is captured over the central region of the suction side. As we increase the angle of attack to 8 degrees, the bubble moves upstream toward the leading edge, following the expected behavior. Tables 3.5 and 3.6 present the performance coefficients and separation and reattachment locations for two different angles of attack of the low Reynolds number airfoil SD7003, utilizing both Suluksna-Juntasaro's (S-J) and Menter's calibrations. These calibrations were compared with available experimental data and LES simulations conducted by Ol [148] and Galbraith [84], respectively. It is noteworthy that Menter's calibration performs markedly better than S-J. However, it is unsafe to generalize this trend to other airfoils, as larger thicknesses and curvatures may introduce variations linked to the pressure gradient correction included in Menter's correlation. The skin friction and pressure distributions on the suction side have a unique behavior when a laminar separation bubble forms, as described in [183]. This distinct behavior is visible in Figures 3.5 and 3.6. The pressure distribution displays a plateau with a nearly constant value equal to the pressure at the separation point. In contrast, the skin friction distribution initially decreases due to the adverse pressure gradient that triggers the boundary layer separation. The separated shear layer becomes unstable and sheds vortices that impinge the airfoil surface, creating high skin friction regions on the airfoil surface, and the boundary layer locally reattaches. By time-averaging this process, we retrieve the usual representation of the separation bubble first described by Gaster [86], which generates a rapid descent of the skin friction and posterior reattachment of the boundary layer. Transition to turbulence in the separated shear layer is triggered by K-H instability [35]. PIV measurements by Park [149] demonstrate that transition in a laminar separation bubble occurs in a finite length and that the interval between the transition onset and the transition completion contains the end of the pressure plateau.

Table 3.5 Aerodynamic coefficients and laminar separation bubble characteristics for different models. Re=60,000, $\alpha = 4^o$.

	$\frac{x_{sep}}{c}$	$\frac{x_{tr}}{c}$	$\frac{x_{re}}{c}$	C_l	C_d
Menter	0.202	0.518	0.660	0.600	0.0221
Suluksna-Juntasaro	0.184	0.53	0.743	0.600	0.0257
LES (Galbraith [84])	0.23	0.55	0.65	0.59	0.021
PIV (Ol [148])	0.18	0.47	0.58	-	-
DNS (Carton de Wiart [52])	0.209	-	0.654	0.602	0.0196

Table 3.6 Aerodynamic coefficients and laminar separation bubble characteristics for different models. Re=60,000, $\alpha = 8^o$.

	$\frac{x_{sep}}{c}$	$\frac{x_{tr}}{c}$	$\frac{x_{re}}{c}$	C_l	C_d
Menter	0.035	0.158	0.280	0.922	0.0409
Suluksna-Juntasaro	0.037	0.178	-	0.868	0.0557
LES (Galbraith [84])	0.04	0.18	0.28	0.92	0.043

For comparison purposes, we define the transition location shown in Tables 3.5 and 3.6 as the point where the skin friction starts to drop, as these locations agree better with Galbraith [84]. They probably represent the onset of transition described in Park [149]. Figures 3.5 and 3.6 illustrate the comparison of the friction and pressure coefficients between RANS simulations and LES simulations performed by Galbraith [84] at a Reynolds number of 60,000 and an angle of attack of 4^o and 8^o respectively. Menter's correlation performs remarkably well, almost perfectly reproducing the pressure coefficient in both cases. However, there are some noticeable differences between the friction coefficients. Specifically, Menter's correlation generates an early transition, more pronounced at 8^o, characterized by a sudden drop in the friction coefficient. Furthermore, the value of the friction coefficient obtained by LES after reattachment is significantly larger than that obtained by RANS. S-J calibration produces negative friction coefficient values toward the trailing edge, indicating a lack of flow reattachment. The transition model cannot produce a sufficiently large value of the friction coefficient after reattachment for these Reynolds numbers and freestream turbulence conditions, which could lead to enhanced turbulent separation and an early stall. Figure 3.7 reveals that, for a considerably lower Reynolds number, this effect is even more evident, and the skin friction coefficient plot does not indicate the presence of a reattachment point. Table 3.7 shows that lift and drag coefficients calculated with Menter's correlation are not significantly different from those predicted by Galbraith [84]. This could be due to the accurate prediction of the separation bubble, as evidenced by the plateau in the pressure distribution, even though it is not perfectly closed due to the greater importance of pressure drag than the shear drag. It is also evident that the prediction capabilities of the model deteriorate as the Reynolds number decreases and the angle of attack increases.

In Chapter 2, we described the two different formulations (Eqs. (2.55) and (2.54)) designed to increase the intermittency value above 1. That is necessary to compensate

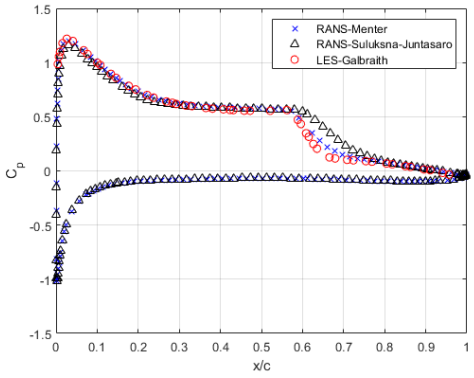

(a) Pressure coefficient.

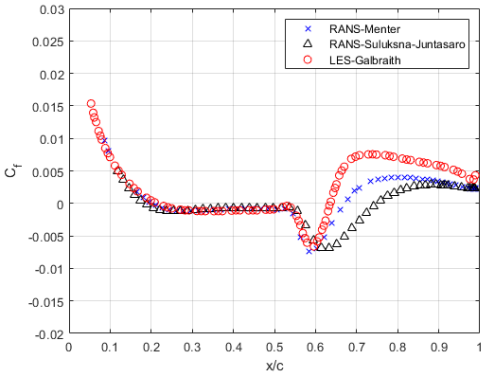

(b) Skin friction coefficient.

Fig. 3.5 Pressure and skin friction coefficients at the suction side of airfoil SD7003 at Re=60,000, $\alpha = 4^o$.

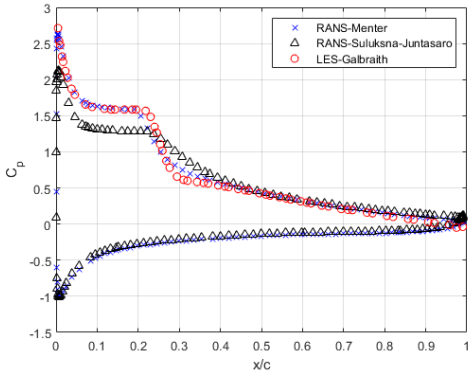

(a) Pressure coefficient.

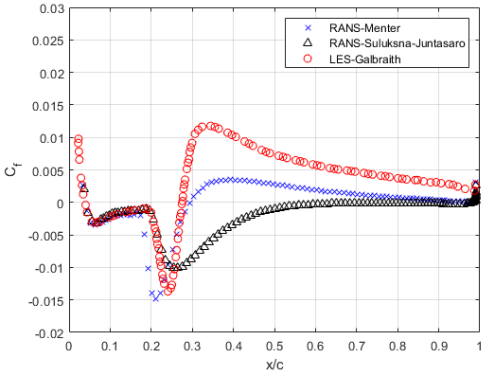

(b) Skin friction coefficient.

Fig. 3.6 Pressure and skin friction coefficients at the suction side of airfoil SD7003 at Re=60,000, $\alpha = 8^o$.

for the transition model's intrinsic lack of turbulent kinetic energy production in case of separation-induced transition, as explained in Langtry [115]. The first formulation (Eq. (2.55)), was introduced by Menter [138] and was later updated by Langtry [114] (Eq. (2.54)) to adjust the slightly premature transition observed in the tested cases. STAR-CCM+ implemented Eq. (2.55) until version 2021.1 and updated it to Eq. (2.54) since version 2021.2. We tested both separation-induced transitions, as shown in Table 3.8. The original correction performs much better if one compares the airfoil aerodynamic coefficients with those reported by Galbraith et al. [84]. Regarding the separation bubble characteristics captured by the new formulation (Eq. (2.54)), the bubble length is too large, whereas the transition point

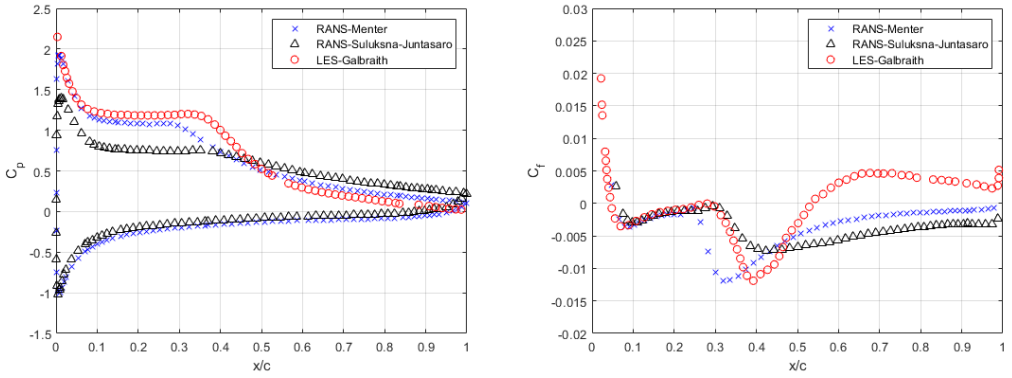

(a) Pressure coefficient.

(b) Skin friction coefficient.

Fig. 3.7 Pressure and skin friction coefficients at the suction side of airfoil SD7003 at Re=30,000, $\alpha = 8^o$.

is slightly delayed and not too far from the high-fidelity simulations. The slightly delayed transition was expected due to modifying the 2.193 constant in Eq. (2.55) to 3.235 in Eq. (2.54). To explain why the reattachment location is downstream compared to the original correction, we present the effective intermittency in the flow field in Figure 3.8. The decrease in the limiting value of this quantity from 5 to 2 reduces the turbulence kinetic energy production and, therefore, considerably delays reattachment. These results suggest that a hybrid correction, which postpones transition using the value of 3.235 and employs a faster turbulence kinetic energy production mechanism, could outperform the previous two corrections. In the rest of the section, we will use the original correction (Eq. (2.55)) as it works better than the updated correction (Eq. (2.54)) in the considered regime. Another interesting conclusion we can draw from Figure 3.8 concerns the relatively high values of the effective intermittency in separated regions. In the case of the original separation-induced correction (Eq. (2.55)), the effective intermittency reaches values well above 3. Thus, when the flow separates, the production term can be over 300% larger than in the natural or bypass transition, making the solution less sensitive to F_{length} and $Re_{\theta c}$. That is probably the reason for the apparent independence of the results from the choice of Suluksna-Juntasaro's or Menter's calibration when the pressure gradient correction is unused, as discussed in the next section.

Table 3.7 Aerodynamic coefficients and laminar separation bubble characteristics for different models and empirical correlations. Re=30,000, $\alpha = 8^o$.

	$\frac{x_{sep}}{c}$	$\frac{x_{tr}}{c}$	$\frac{x_{re}}{c}$	C_l	C_d
Menter	0.054	0.250	-	0.828	0.070
Suluksna-Juntasaro	0.066	0.303	-	0.71	0.086
LES (Galbraith [84])	0.05	0.25	0.53	0.89	0.070

Table 3.8 Aerodynamic coefficients and laminar separation bubble characteristics for different separation-induced transition corrections using Menter correlations. SD7003 airfoil, Re=60,000, $\alpha = 4^o$.

	$\frac{x_{sep}}{c}$	$\frac{x_{tr}}{c}$	$\frac{x_{re}}{c}$	C_l	C_d
Menter-Original (Eq.(2.55))	0.202	0.518	0.660	0.600	0.0221
Menter-Updated (Eq.(2.54))	0.185	0.535	0.769	0.603	0.0259
LES (Galbraith [84])	0.23	0.55	0.65	0.59	0.021

Table 3.9 Aerodynamic coefficients and laminar separation bubble characteristics for different models and empirical correlations. Re=60,000, $\alpha = 6^o$.

	$\frac{x_{sep}}{c}$	$\frac{x_{tr}}{c}$	$\frac{x_{re}}{c}$	C_l	C_d
Menter	0.098	0.317	0.44	0.767	0.0287
LES (Galbraith [84])	0.11	0.34	0.45	0.748	0.0319

3.1.1.3 Transition model fine-tuning for low Reynolds numbers

The previous section shows two main flaws of the γ-Re$_\theta$ transition model. One is the low wall shear stress predicted after transition, which will eventually arise in a premature stall. The second one is the early transition and reattachment at intermediate angles of attack (6° to 8°), as suggested by the lower values of the drag coefficient in comparison to the LES results, which descend from a smaller size of the separation bubble. This can be seen in Table 3.6 and Figure 3.6 for $\alpha = 8^o$, but it is more evident at 6 degrees as shown in Table 3.9. Even though the reattachment locations look close or even downstream in the case of 8 degrees, the slower rise of the skin friction coefficient due to this transition model slightly delays reattachment, and at that chord position, the pressure has almost completed its recovery towards

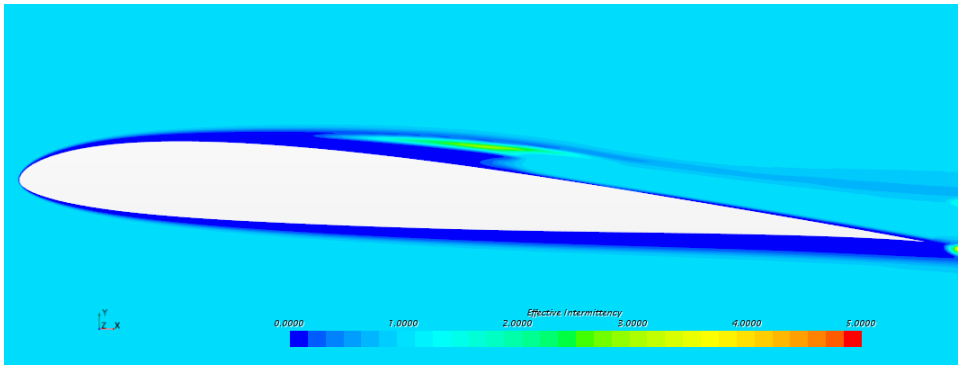

(a) Original separation-induced transition (Eq.(2.55)).

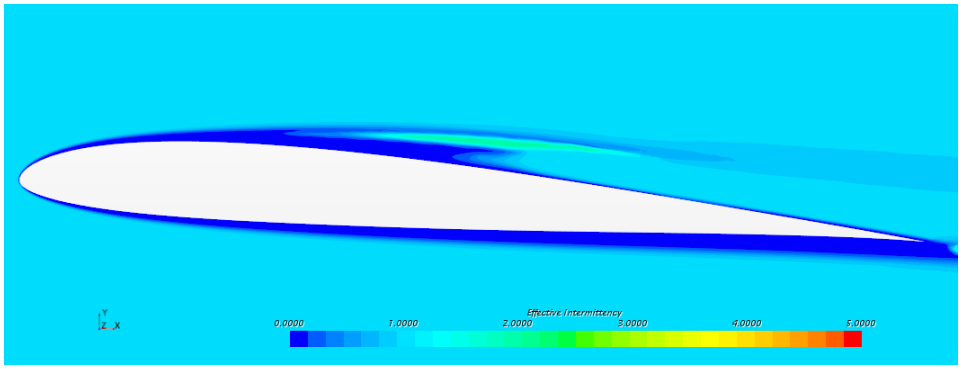

(b) Updated separation-induced transition (Eq.(2.54)).

Fig. 3.8 Effective intermittency around airfoil SD7003 at Re=60,000, $\alpha = 4^o$.

the inviscid distribution. These two issues require turbulence intensity production to be tuned specifically depending not only on the position on the suction side of the airfoil but also on the angle of attack. This fact makes a simple tuning of the model using constant values of the parameters a difficult task. Figure 3.9 shows an attempt to adjust the parameter s_1 to fit aerodynamic coefficients provided by Galbraith [84] using Menter's calibration. Menter [137] included such a parameter to increase the turbulence intensity produced after transition, controlling in this way the size of the bubble and the drag coefficient simply and effectively. However, Figure 3.9 clearly shows that it is impossible to accurately fit results for different angles of attack using a constant value of s_1, especially for the highest angle of attack. In light of what we saw in the previous section, such an effect could even be larger at lower Reynolds numbers. Corral [64] presented observations in this direction, who realized that a constant value of s_1 was not enough and established a relationship between s_1 and $\overline{Re}_{\theta_t}$. The noticeably low value of s_1 required for $\alpha = 6^o$ puts in evidence the previously mentioned early reattachment for intermediate angles

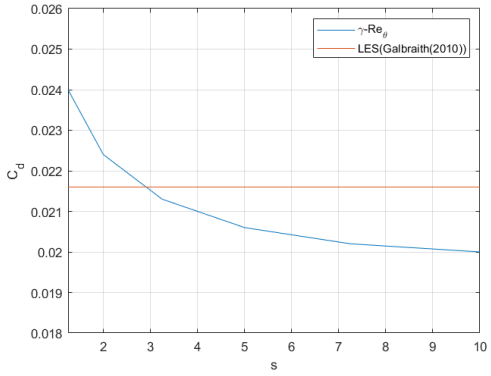

(a) $\alpha = 4^o$.

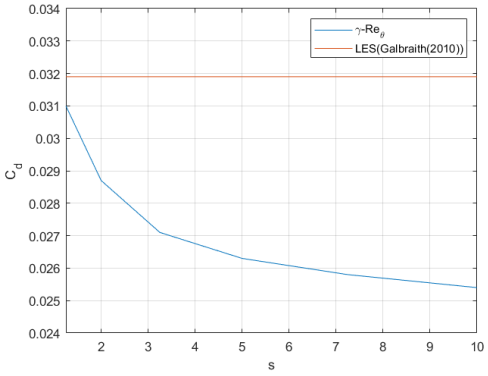

(b) $\alpha = 6^o$.

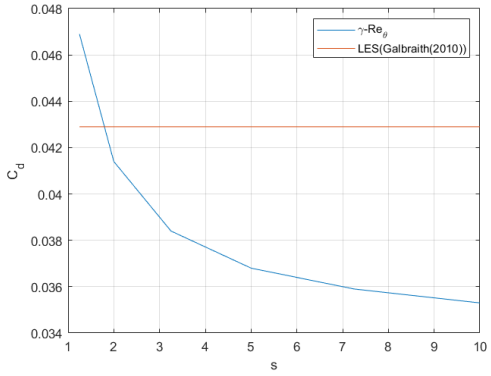

(c) $\alpha = 8^o$.

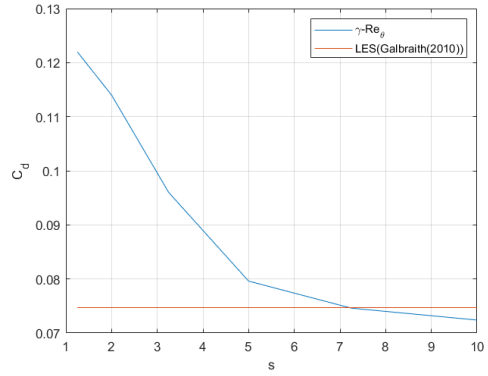

(d) $\alpha = 11^o$.

Fig. 3.9 Drag coefficient of airfoil SD7003 as a function of s_1 at Re=60,000.

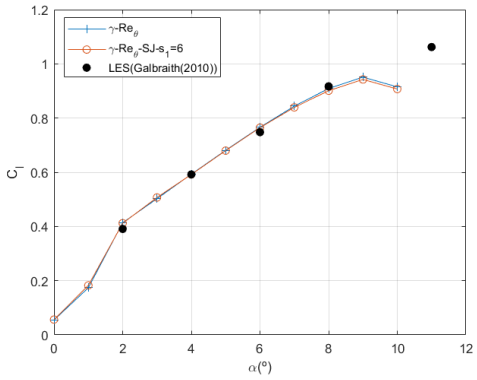

(a) Lift coefficient.

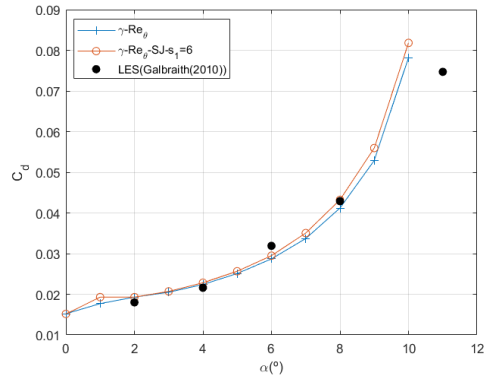

(b) Drag coefficient.

Fig. 3.10 Lift and drag coefficients of airfoil SD7003 at Re=60,000

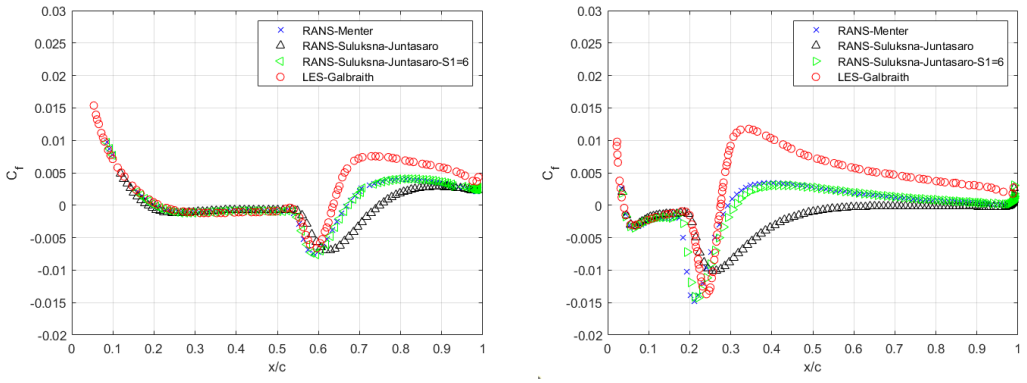

(a) $\alpha = 4^o$. (b) $\alpha = 8^o$.

Fig. 3.11 Skin friction coefficients at the suction side of airfoil SD7003 at Re=60,000.

of attack. That indicates that also transition happens too early, probably for two reasons. The first cause is that the pressure gradient correction noticeably reduces the momentum thickness transition Reynolds number. The second reason is that the original separation-induced transition correction starts producing turbulent kinetic energy too early, as shown in the previous section. Malan et al. [124] suggest that the pressure gradient correction introduced by Menter in Eq. (2.68) produces a double accounting of pressure gradient effects on transition momentum thickness because the turbulence intensity will grow naturally in the presence of an adverse pressure gradient. Therefore the pressure gradient effects are being considered implicitly by the previously explained mechanism and explicitly through Eq. (2.68). Such a double accounting could cause the premature transition predicted by Menter's correlations. At the same time, the relatively high value of s_1 required for $\alpha = 11^o$ shows that, at high angles of attack, the small skin friction coefficient calculated by the model after the transition is not sufficient for keeping the turbulent boundary layer attached as predicted by the LES simulations. That causes a wide separation on the suction side with a consequent rise in the drag coefficient and a decrease in the lift coefficient, as is typical in stalled airfoils. Leaving aside the highest angle of attack, the original value of $s_1 = 2$ seems to be an acceptable compromise to fit the drag coefficient values for angles of attack of 4, 6, and 8 degrees.

In the previous section, we showed that Suluksna-Juntasaro's calibration, which does not include the pressure gradient correction, moves the transition point slightly downstream and that the computed values agree better with Galbraith's results [84]. However, the reattachment point position is excessively downstream, increasing

the bubble's length and, thus, the drag coefficient. To find a compromise between Suluksna-Juntasaro's and Menter's calibration, we tested the first for different values of s_1. Table 3.10 shows that, by increasing the s_1 value to 6, Suluksna-Juntasaro's calibration still predicts well the transition location, and, at the same time, the reattachment position and drag coefficient values get close to those predicted by the Menter's calibration. Table 3.10 also highlights that the Menter's correlation without the pressure gradient correction (ZPG) behaves like Suluksna-Juntasaro's calibration. Figures 3.10 and 3.11 evidence that this is true not only for $\alpha = 4^o$ and also that $s_1 = 6$ in Suluksna-Juntasaro's calibration provides similar results to those obtained with Menter's calibration, which uses the pressure gradient correction, for all tested angles of attack. That indicates that the pressure gradient and the separation-induced corrections play a similar role. Either directly or indirectly, they both enhance the production of turbulence intensity in separated regions. The main drawback of the pressure gradient correction is that Menter's calibration predicts transition upstream than the S-J correlation. As mentioned earlier, this is possibly related to a double accounting of the pressure gradient effects. The tuned version of Suluksna-Juntasaro's calibration, on the other hand, produces more turbulence kinetic energy because of the increased value of the s_1 parameter and, despite starting slightly later, predicts transition and reattachment closer to the LES-predicted positions compared to the Menter's correlation. This analysis allows for several conclusions. First, the pressure gradient correction presented in Menter's correlations causes a slightly premature transition. A second conclusion is linked to the observation that Menter's correlation without the pressure gradient correction and Suluksna-Juntasaro's correlation produce similar results. This fact may indicate that for this type of transition, simple $Re_{\theta c}$ and F_{length} correlations (such as S-J's) perform as well

Table 3.10 Aerodynamic coefficients and laminar separation bubble characteristics for different models and s_1 values. SD7003 airfoil, Re=60,000, $\alpha = 4^o$.

	$\frac{x_{sep}}{c}$	$\frac{x_{tr}}{c}$	$\frac{x_{re}}{c}$	C_l	C_d
Menter	0.202	0.518	0.660	0.600	0.0221
Menter-ZPG	0.184	0.544	0.767	0.597	0.0264
Suluksna-Juntasaro-s_1=2	0.184	0.530	0.743	0.600	0.0257
Suluksna-Juntasaro-s_1=6	0.202	0.536	0.680	0.593	0.0228
LES (Galbraith[84])	0.23	0.55	0.65	0.59	0.021

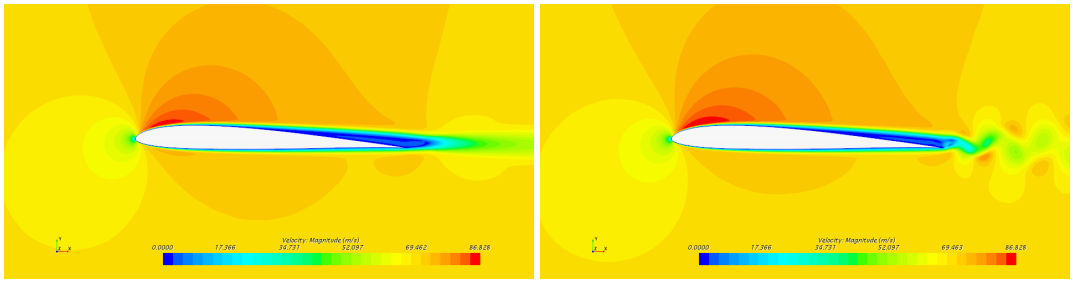

(a) Steady Solver. (b) Unsteady Solver.

Fig. 3.12 Instantaneous velocity magnitude around airfoil SD7003 at $\alpha = 2^o$ and Re=23,000

as complex and general correlations (such as Menter's) and therefore that the priority should be fine-tuning the separation-induced transition correction. Thus, even though the s_1 constant is a very effective way of fixing the length of the separation bubble for specific cases, it seems clear that setting it as a constant makes it very difficult to fit a broad range of angles of attack with different kinds of separation bubbles. Furthermore, introducing a second parameter, independent of s_1, would be functional in controlling the position and length of the separation bubble simultaneously.

3.1.1.4 Enhanced performance predictions using the unsteady solver

The γ-Re$_\theta$ transition model switches from laminar solutions when the intermittency is close to zero to turbulent solutions when the intermittency approaches the unit value. In the previous chapters, we focused on transition and the capturing of separation bubbles. At Reynolds numbers around 60,000, only angles of attack below 1^o show a fully laminar suction side, but these angular values are below the range of interest for rotor and wing applications, which usually work around the optimum angle of attack. However, the range of angles of attack for which the flow remains laminar becomes broader for decreasing Reynolds numbers, and at Re=20,000, can arrive up to 3^o and 4^o. We pointed out in [46] that, in some cases, steady laminar solutions display differences compared with time-accurate solutions of the Navier-Stokes(N-S) equations. This fact has also been corroborated by other authors in the context of ultra-low Reynolds numbers [70]. At small angles of attack, steady-state N-S solutions predict a stable, separated region behind the airfoil trailing edge, but time-accurate simulations indicate a vortex-shedding regime. The periodic vortex shedding generates an average lift enhancement due to the low pressure generated by these high-velocity regions on the suction side. Figure 3.12 shows a

comparison between the velocity magnitude around the airfoil SD7003 at Re=23,000 and $\alpha = 2^o$. The vortex shedding generated near the trailing edge affects the velocity magnitude distribution around the airfoil and thus its performance, as shown in Table 3.11. For higher angles of attack, as the intermittency begins to increase, the averaging introduced by the turbulence model dampens the instability, and the steady and unsteady solutions converge. Figure 3.13 summarizes the influence of using an unsteady solver. Between 0^o to 3^o, one can see that all unsteady simulations provide almost identical results, including laminar simulations. At 4^o, we notice that using Menter's calibration, the unsteady solver with transition model shows a noticeable drop in the lift coefficient compared to the other numerical and experimental data. That is because the production of turbulent kinetic energy is large enough to dampen the unsteadiness, and the URANS solution converges with the RANS solution. The early prediction of transition is probably due to the inclusion of the pressure correction term, as we can see that the S-J correlations, which do not include this correction, can accurately predict the lift coefficient at 4^o. From 5^o upwards, we can appreciate convergence between experimental, URANS, and RANS results. On the other hand, the laminar solution starts diverging from the experimental results.

An additional case where unsteady simulations are necessary is for angles of attack close to the bursting of the separation bubble, where RANS solutions tend to oscillate. We can distinguish two situations. In some cases, the unsteady solver generates a steady-state solution; in others, the unsteadiness persists in the form of vortex shedding on the suction side of the airfoil, as noted in [125]. Interestingly, if such a vortex shedding is time-averaged, as shown in [150, 125], one obtains a closed separation bubble. That is because, in some cases, the position of the separation bubbles destabilizes the separated laminar boundary layer before the turbulence model is activated, and the vortex shedding regime generates local instantaneous reattachment of the boundary layer that switches off the production term in the turbulent kinetic energy (see Eq. (2.50)). For these particular angles of attack, the simulation is close to a fully laminar situation. For low Reynolds number, this is not a problem and, as we can appreciate in Figure 3.13, the laminar solutions approximate well the airfoil performance at low angles of attack. However, such behavior is not limited to low Reynolds numbers and small angles of attack, as shown in [125]. Therefore, one should be cautious in simulating within this range of angles of attack to avoid invalid results. In this work, we encountered the above-described situation only at small angles of attack, where the transition should have been close to the

trailing edge. Therefore, it seems reasonable to time-average the vortex shedding solution to compute separation bubble characteristics and aerodynamic performance. Such a scenario occurs more frequently using Suluksna-Juntasaro's calibration than Menter's, as the latter is prone to activate the transition before the laminar boundary layer becomes unstable.

The analysis shows that the unsteady solver is very advantageous. It significantly improves the performance predictions for airfoils operating at low angles of attack when the flow remains laminar and in situations close to the bursting of the separation bubble. Once the transient behavior terminates, steady and unsteady solvers solutions converge, and the expensive unsteady simulations are no more convenient.

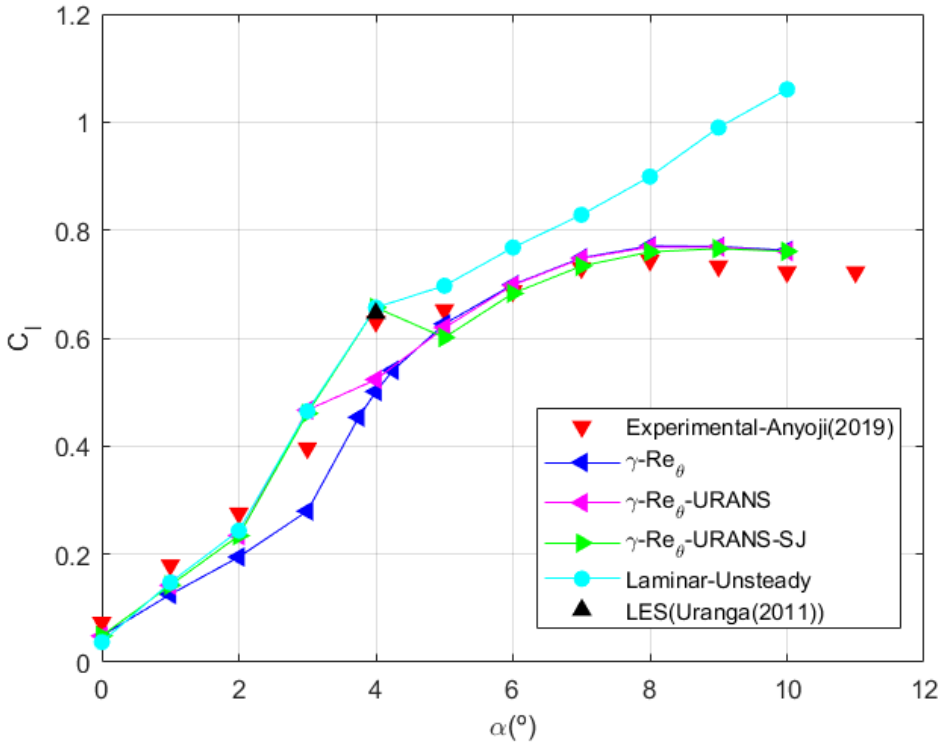

Fig. 3.13 Lift coefficient of airfoil SD7003 at Re=23,000 for different solvers compared with experimental (Anyoji [8]) and high fidelity numerical data (Uranga [205]).

Table 3.11 Aerodynamic coefficients applying the steady and the unsteady solver. Re=23,000, $\alpha = 2^o$.

Solver	C_l	C_d
Steady	0.193	0.0273
Unsteady	0.237	0.0283
Difference(%)	+22.80	+3.66

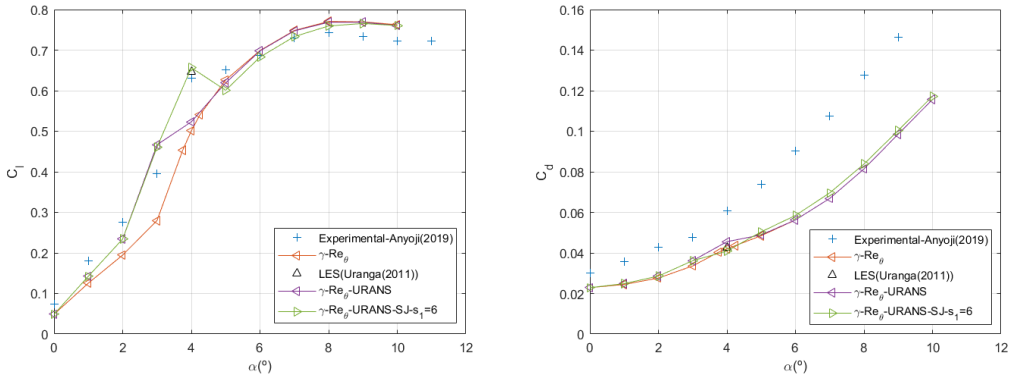

(a) Lift coefficient.

(b) Drag coefficient.

Fig. 3.14 Lift and drag coefficients of airfoil SD7003 at Re=23,000

3.1.1.5 Application: Low Reynolds number airfoils: Eppler 387, Ishii and Selig/Donovan 7003.

We tested the previously developed model with different airfoils and Reynolds numbers over a wide range of angles of attack to check its applicability. We chose three popular low Reynolds number airfoils, which have been extensively tested and are known to have separation bubbles on their suction side. We carried out unsteady simulations at low angles of attack and switched to steady simulations once the unsteady solver provided steady-state solutions. In Figures 3.14 and 3.18, the computed values of the aerodynamic coefficients are the time-averaged values for the unsteady simulations and the values provided by the steady solver for higher angles of attack, except when specified otherwise.

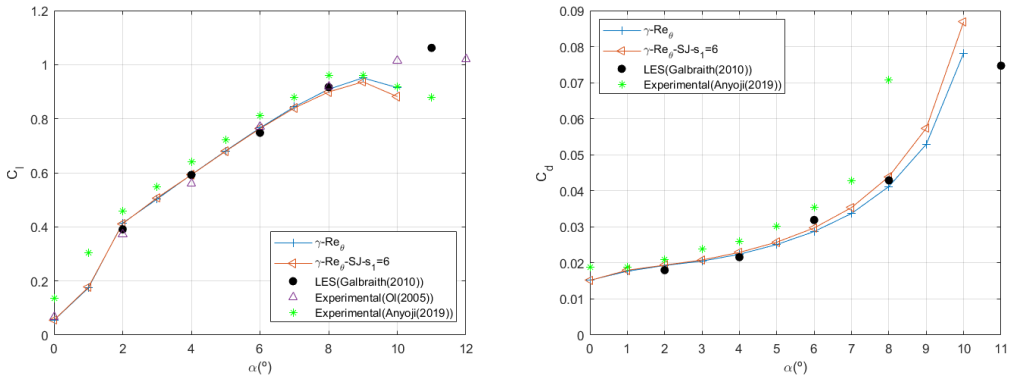

(a) Lift coefficient. (b) Drag coefficient.

Fig. 3.15 Lift and drag coefficients of airfoil SD7003 at Re=60,000.

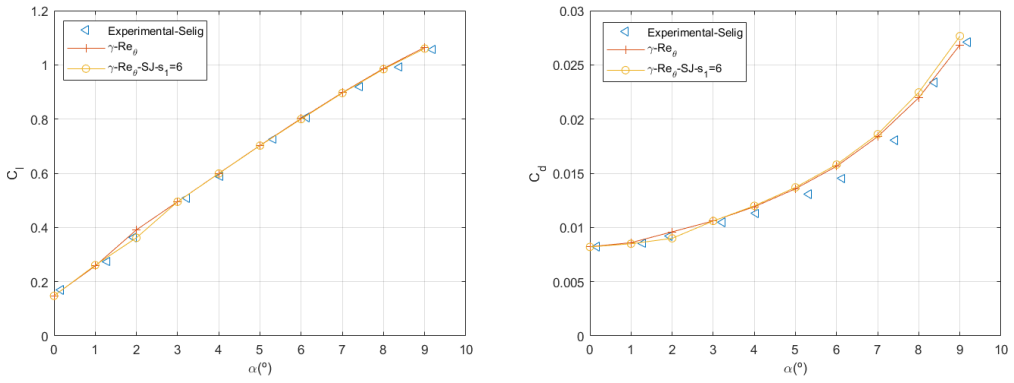

(a) Lift coefficient. (b) Drag coefficient.

Fig. 3.16 Lift and drag coefficients of airfoil SD7003 at Re=200,000 compared with experimental data from Selig [204].

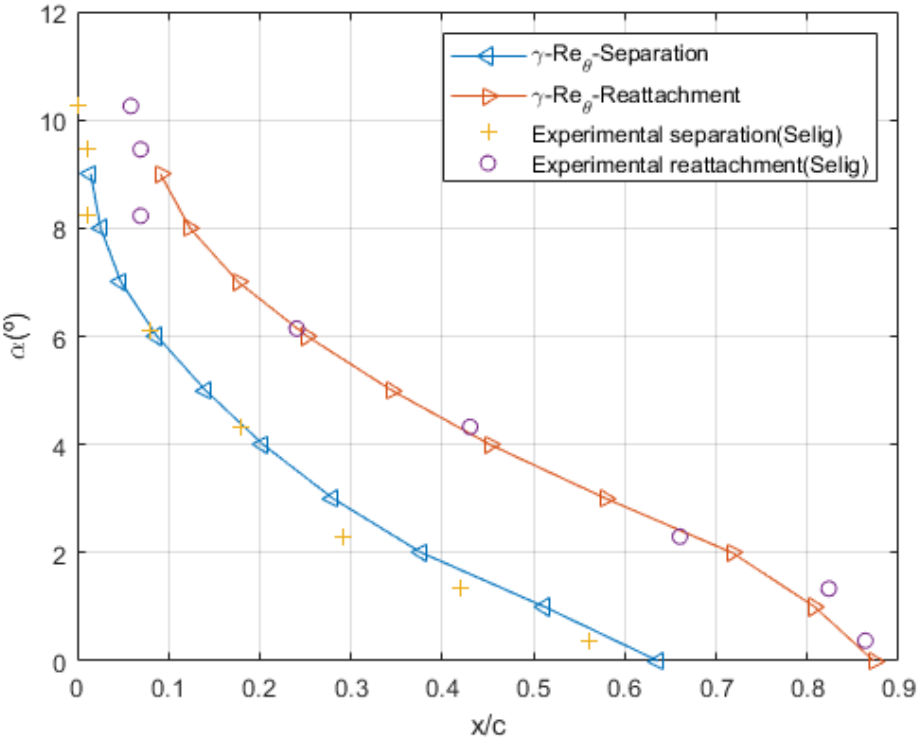

Fig. 3.17 Comparisons between computational and experimental location of upper surface flow features for the SD7003 airfoil at Re=200,000

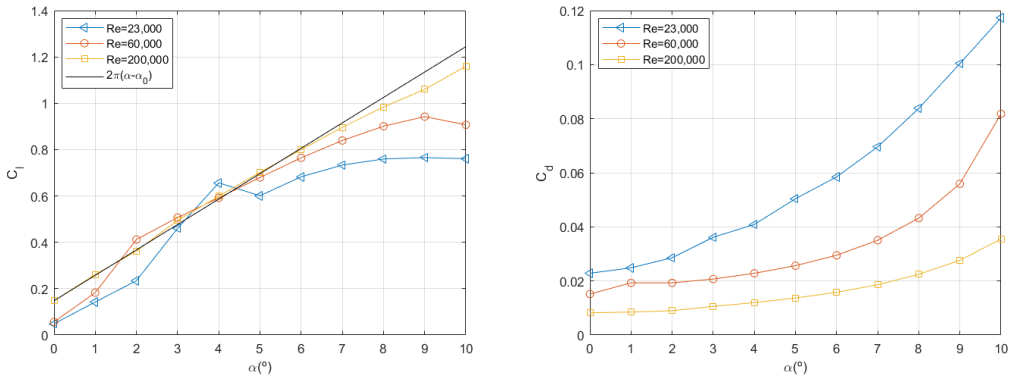

(a) Lift coefficient. (b) Drag coefficient.

Fig. 3.18 Lift and drag coefficients of airfoil SD7003 for several Reynolds numbers computed with the Saluksna-Juntasaro calibration with the s_1 parameter set to 6.

Selig/Donovan 7003 (SD7003) airfoil

For this airfoil, in addition to the Re=60,000 results that we used for tuning, we tested two more Reynolds number conditions, Re=23,000 and Re=200,000. They represent two extreme conditions for the so-called very-low Reynolds number regime, and, in both cases, they present a separation bubble as shown by several authors [204, 8].

Considering a Reynolds number of 23,000, Figure 3.14 shows a steady solver solution and two unsteady solutions, one obtained using Menter's calibration and the other using Suluksna-Juntasaro's calibration with s_1 set to 6. As noted in the previous section, the absence of the pressure gradient correction slightly delays the transition and results in larger separation bubbles. Both unsteady polars show a significant increase in the lift for angles of attack ranging between 0°and 4°. At this Reynolds number and for small angles of attack, the flow is laminar along most of the airfoil, and the solution captures the vortex shedding regime typically seen for slightly lower Reynolds numbers when the transition is incomplete. The vortex shedding affecting part of the suction side of the airfoil generates relatively low-pressure regions, which produce a lift enhancement, as noted in [46] in the ultra-low Reynolds number regime. Once the transition begins, the turbulence model is activated, the unsteadiness fades, and a steady flow pattern is predicted even with the unsteady solver. Suluksna-Juntasaro's calibration offers an excellent agreement with LES data for an angle of attack of 4^o for both lift and drag coefficients. Considering the non-linearity of the lift curve at such low Reynolds numbers, the agreement of the lift coefficient with results presented in [8] is satisfactory. However, the drag coefficient is too high compared to our predictions and the results presented by [205].

Figure 3.15 shows the lift coefficient and the drag coefficient for Re = 60,000, including additional experimental results not presented in the previous section. The experimental results in [8] display lift and drag coefficients that seem too high. Such a trend might be related to a misalignment of the airfoil relative to the flow. In any case, we can observe that both the results in [8] and ours predict a premature stall compared to the results presented by [148, 84]. Before stall, the agreement between the drag and lift coefficients reported by [148, 84] and ourselves is satisfactory.

Figure 3.16 illustrates the results for a considerably larger Reynolds number, 200,000. In this case, the agreement is excellent with experimental results from Selig [204] both in lift and drag, and both calibrations produce almost identical predictions.

Figure 3.17 shows the flow characteristics on the suction side compared to those obtained experimentally by Selig [204] using an oil visualization technique. The size of the separation bubble is, for the considered angles of attack, consistent with the experiments by Selig [204] where we can observe a trailing edge bubble that moves upstream as the angle of attack increases.

Finally, we compare the airfoil aerodynamic coefficients for the three tested Reynolds numbers. Figure 3.18 shows that the developed numerical model can capture the non-linear very-low Reynolds number effects. At Re=200,000, the lift coefficient is almost linear and matches very well with the potential airfoil theory because the separation bubble has a reduced height and is stationary for the considered range of angles of attack. On the other hand, at Re=23,000, the $c_L(\alpha)$ curve has a characteristic s-shape due to the increase in the lift when the boundary layer reattaches and closes the separation bubble. It is interesting to note that near the angle of attack that corresponds to the first reattachment, the curves at low Re have a lift coefficient higher than those at high Reynolds numbers, as confirmed in [205] also. An intuitive explanation for such a behavior is that, at a low Reynolds number, the mean separation bubble is thicker, and therefore, for a short range of angles of attack, the effective camber of the airfoil is increased. The effect of increased effective camber due to the thickness of the separation bubble has been studied by [95] for slightly higher Reynolds numbers. The drag coefficient also presents some non-linearities, but the effect of the Reynolds number is much more evident as the curves shift upwards and the curvature of their typical parabolic shape increases as the Reynolds number decreases.

Ishii airfoil

The lift coefficients obtained by our simulations are systematically higher than the experimental data and the LES data by Anyoji [10]. We suspect that there might be a mismatch between the definition of the zero angle of attack in [10] and the present study, as the Ishii airfoil, has a thick trailing edge, which could generate uncertainty on the definition of the chord line. The overprediction with respect to the LES data at small angles of attack, when the flow is still laminar, as shown by our CFD simulations and also visible in the smoke visualization by Anyoji [8], reinforces the idea that a geometrical mismatch is responsible for the discrepancies. To offer a reasonable comparison, Figure 3.19 shows our simulation results shifted by an angle

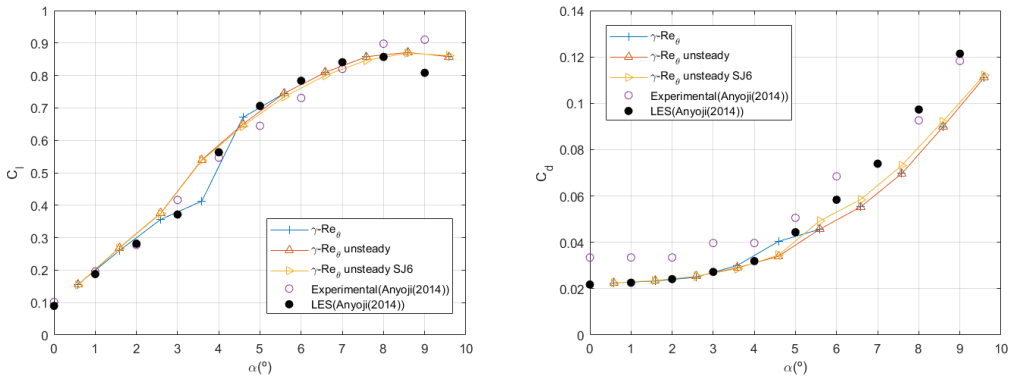

(a) Lift coefficient. (b) Drag coefficient.

Fig. 3.19 Lift and drag coefficients of the Ishii airfoil at Re=23,000. Our results have been shifted by $+0.587^o$.

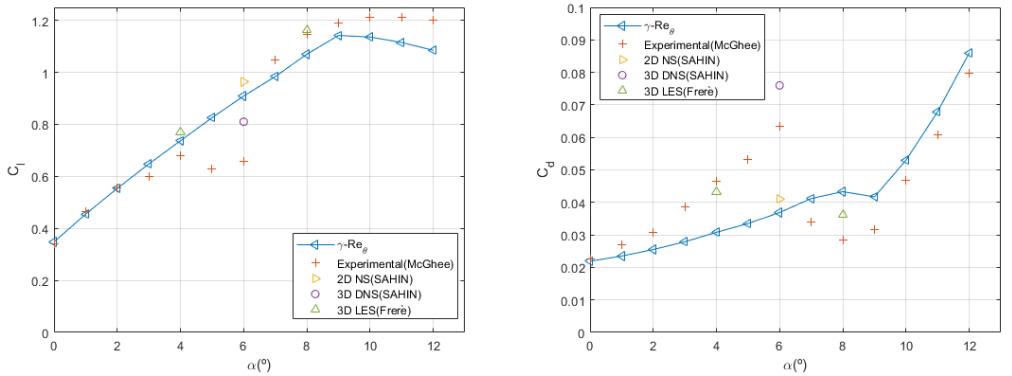

(a) Lift coefficient. (b) Drag coefficient.

Fig. 3.20 Lift and drag coefficients of the Eppler 387 airfoil at Re=60,000

of $+0.587^o$ so that our numerical results fall on the line joining the LES data between 0^o and 1^o. For the smallest angles of attack, where the flow should remain laminar, both lift and drag coefficients agree with LES data. The experimental drag coefficient presented in Anyoji [10] shows a noticeable difference between LES results and our shifted numerical results. In [10], the authors recognized the discrepancy and reported that its cause was yet to be determined.

Eppler 387 (e-387) airfoil

The aerodynamic characteristics of the e-387 airfoil we show in Figure 3.20 reveal a broad variability in the data obtained by different methods. For clarity, we present

only one set of experimental data, but we remind that distinct facilities, and even runs in the same facility, produced inconsistent results, as reported in McGhee [133]. In general, some 3D instabilities may be responsible for the boundary layer separation without reattachment at angles of attack between 3^o and 8^o, thus affecting the mean value of the flow. It is worth mentioning that this separated regime is not found in all facilities and seems to be very sensitive to freestream turbulence levels [133]. The simulations presented in this section are 2D and therefore cannot capture such instabilities, but there is a good agreement between our results and the 2D Navier-Stokes simulations performed by Sahin [171]. This latter reports remarkable discrepancies between the 2D Navier-Stokes and the 3D DNS results obtained on the e-387 airfoil at Re=60,000. The reason for such a drastically different behavior between the two previously considered airfoils and the e-387 is probably related to the higher camber of the latter.

3.1.2 Large Eddy Simulations

We present a study using LES to predict the flow transition on the SD7003 airfoil operating in the very-low Reynolds number regime, as analyzed in the previous section. We analyze different numerical settings for LES. In particular, we focus on the effects of choosing higher-order and less dissipative schemes. We compare the turbulent kinetic energy production in the separation bubble using the RANS model described in the previous section and LES. A comparison between WALE and dynamic Smagorinsky subgrid-scale models is also presented.

We have extruded the SD7003 geometry spanwise for a distance of 0.1 chords. Several authors [83, 55] have found this distance sufficient to compute flow statistics at low and moderate angles of attack. The lateral boundaries have been meshed conformally and assigned periodic boundary conditions. Several grids were tested to assess the influence of the resolution on capturing small-scale structures. The finest grid has around 15 million cells. The midplane of this grid is shown in Figure 3.21. It is clear how the suction side is resolved much more than the pressure side, as it is where transition is expected to occur. Simulations have been performed using 128 cores of 4 Intel Xeon Scalable Processors Gold 6130 2.10 GHz. The time step used in our simulation is 0.002 convective turnovers. The inner solver runs for 10 iterations, sufficient for residuals to drop between 2 and 3 orders of magnitude.

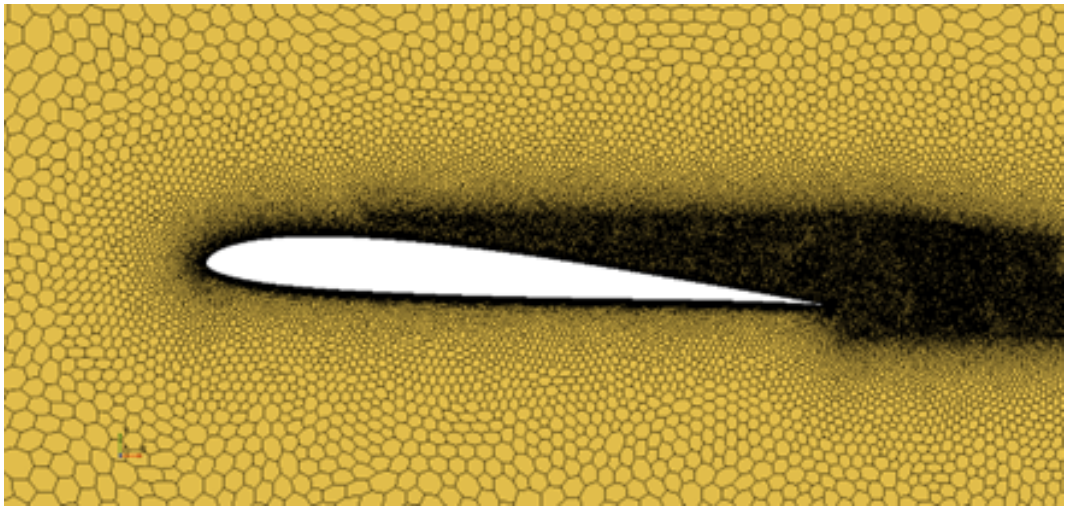

Fig. 3.21 Computational mesh. Plane at z=0.05c.

Simulations run for 20 turnovers, and statistics are computed within the last 10. Our Reynolds number is 60,000, and the Mach number is fixed at 0.2.

Wall Adaptive Local Eddy-viscosity (WALE) sub-grid turbulence modeling [145] approach and Lilly's implementation [121] of the Dynamic Smagorinsky model by Germano [88] have been compared. We have assessed different spatial reconstruction schemes provided in STAR-CCM+. The suggested scheme is a second-order Bounded Central Difference (BCD) scheme. We have compared this scheme with a third-order Central Difference (CD3) scheme, a third-order Monotonic Upwind Scheme for Conservation Laws (MUSCL3), and a hybrid scheme blending third-order central difference and upwind schemes (CD/MUSCL3). Third-order schemes show no relevant overhead compared with the bounded central difference scheme implemented in STAR-CCM+. If we compare it with the standard second-order upwind scheme, the overhead is approximately 10%. With these small overheads, the improvement in the accuracy provided by third-order and bounded central difference schemes will pay off and compensate for the additional computational costs, as shown by Ricci et. al [165].

Figure 3.22 shows the Q-criterion isosurface obtained with the CD3 scheme, showing a spurious structure outside the boundary layer evidencing the solver's instability. On the other hand, the MUSCL3 scheme and the hybrid CD/MUSCL3 scheme with a blending factor of 0.15 were stable and robust, as shown in Figures

3.23 and 3.24. In both cases, separation, transition, and reattachment are captured. However, the fully upwind scheme predicted a delayed transition and reattachment compared to the CD/MUSCL3 scheme. This is probably associated with upwind schemes being more dissipative and not conserving kinetic energy. Figure 3.25 shows the friction coefficient for our simulations, and the one presented by Galbraith & Visbal [84]. It is worth mentioning that the Mach number in their simulations is 0.1. However, we believe this difference is probably insufficient to account for the discrepancies in Figure 3.25. Our simulations present a delayed separation transition and reattachment, showing separation bubbles with the same length but shifting toward the trailing edge. The difference between our simulations shows that dissipation is still important, and therefore, we should perform ulterior grid refinements to ensure that this phenomenon is not grid-related. In any case, we can extract some interesting considerations. The first consideration is that reducing the blending factor clearly reduces the dissipation. We can also appreciate how the Dynamic Smagorinsky approach presents a higher level of turbulent kinetic energy production, anticipating the reattachment of the boundary layer. This can also be appreciated in Figure 3.27. We can also conclude that the Bounded Central Difference Scheme implemented in STAR-CCM+ appears less dissipative than the Hybrid third-order scheme for a blending factor of 0.15. The value of 0.15 is possibly too conservative and could be further reduced, rendering the scheme more accurate. However, care should be taken as the scheme will eventually present instabilities as shown in Figure 3.22.

Figure 3.27 compares the turbulent kinetic energy in our RANS simulation with the LES performed using different schemes. We can again appreciate the shifting of our separation bubble towards the trailing edge. It is worth mentioning that the RANS model follows the re-calibration performed in the previous section, which used Galbraith ILES results [84] as a reference. In any case, we can appreciate how the global agreement is good. Figure 3.26 shows the averaged velocity fields, which present a separation bubble in both cases. Again, it is appreciable how the bubble is slightly shifted towards the trailing edge in the LES simulation. An interesting comment is that the LES simulation predicts a much sharper closure of the separation bubble associated with a higher friction coefficient after reattachment. This under-prediction of skin friction becomes more severe for decreasing Reynolds numbers, as shown in the previous section (Also in [39]) and is related to excessive damping of turbulent kinetic energy production close to the airfoil wall in the RANS model as

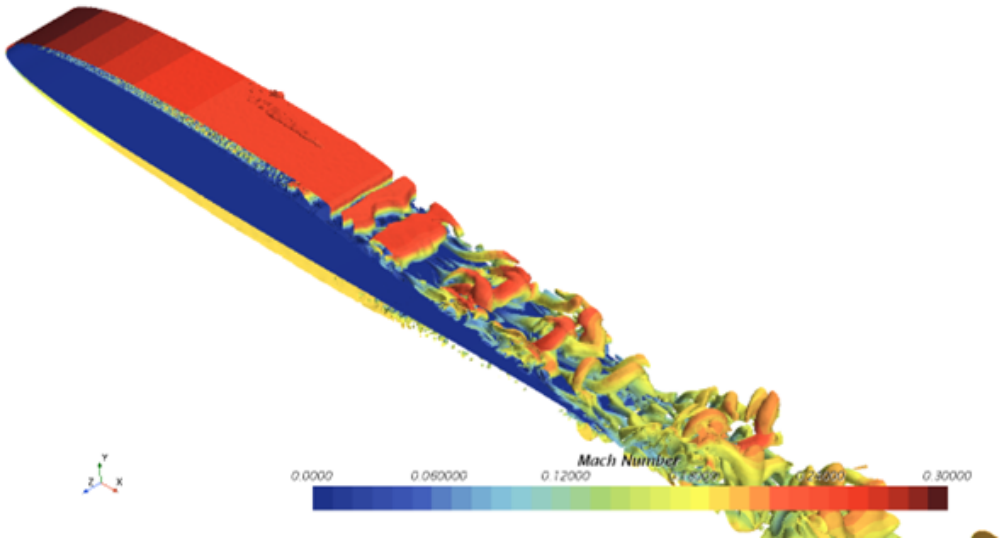

Fig. 3.22 Q-criterion=500 Isosurface colored with Mach number. CD3 Scheme.

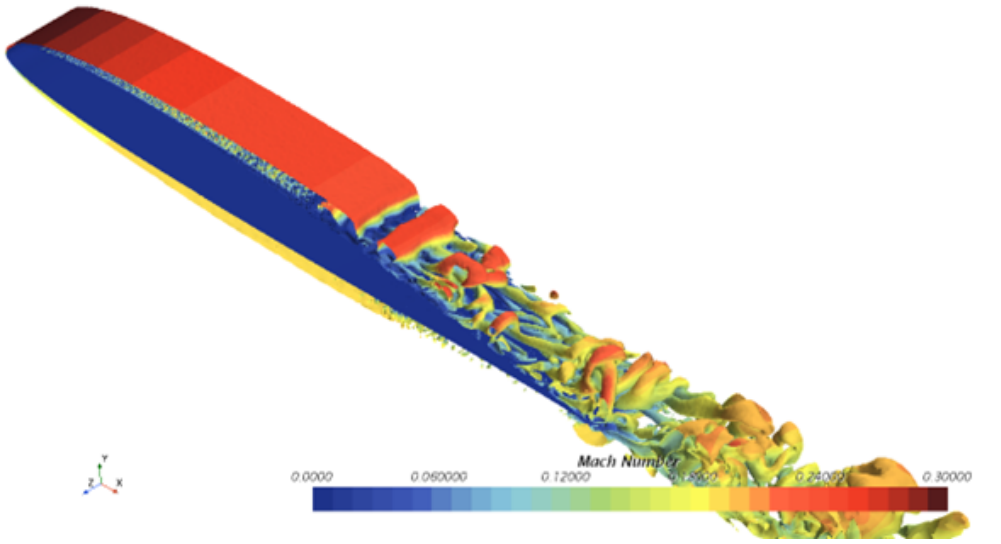

Fig. 3.23 Q-criterion=500 Isosurface colored with Mach number. MUSCL3 Scheme.

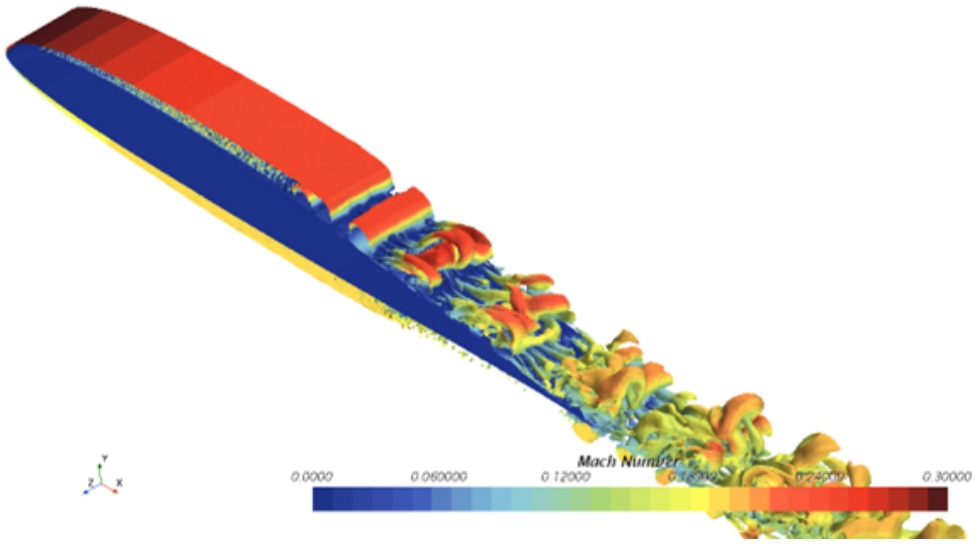

Fig. 3.24 Q-criterion=500 Isosurface colored with Mach number. MUSCL3/CD3 Scheme with 15% upwind blending.

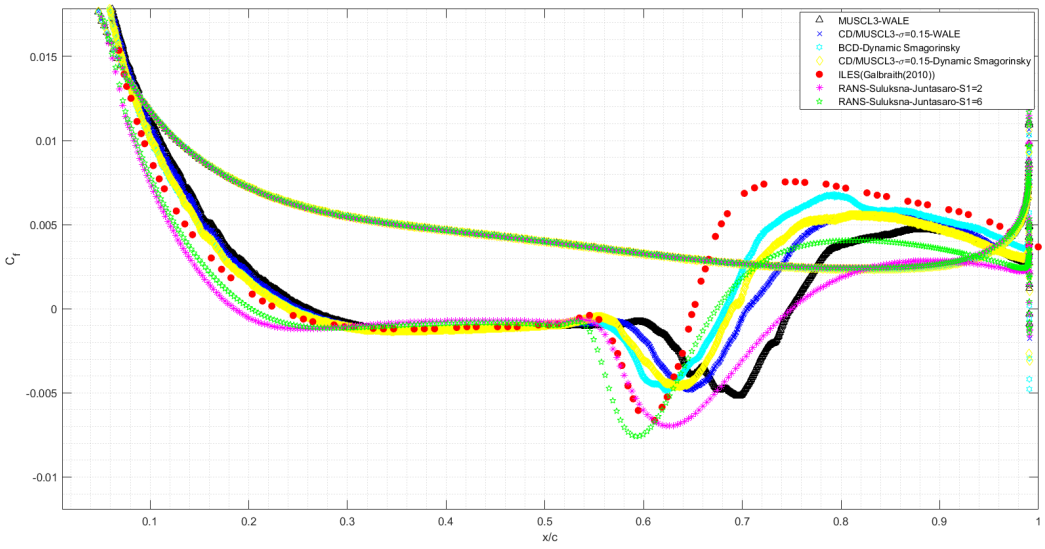

Fig. 3.25 Time-averaged friction coefficient at the plane z=0.05.

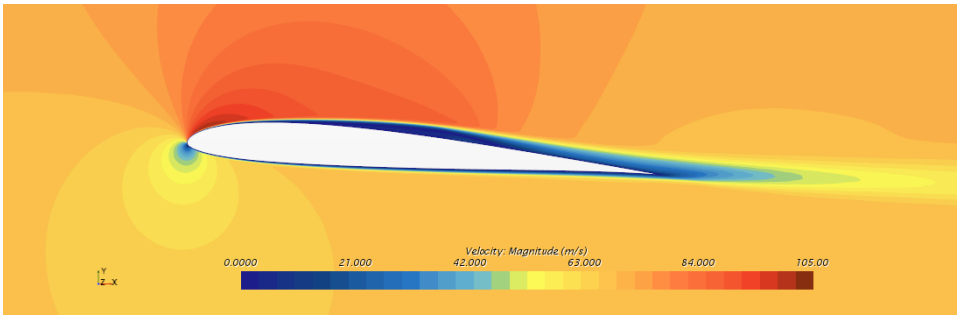

(a) RANS Suluksna-Juntasaro $S_1 = 6$.

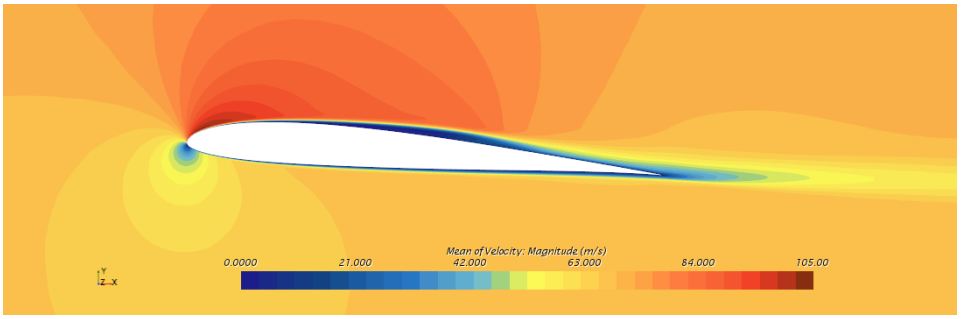

(b) LES-Dynamic Smagorinsky SGS model-Bounded Central Differences Scheme.

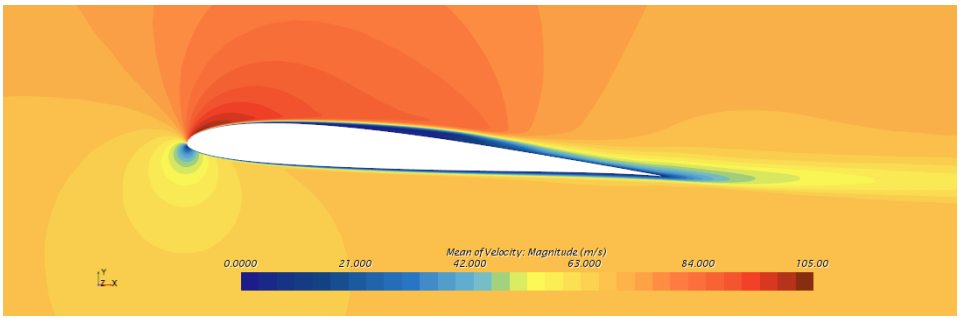

(c) LES-Dynamic Smagorinsky SGS model-third order MUSCL/CD ($\sigma = 0.15$) hybrid Scheme.

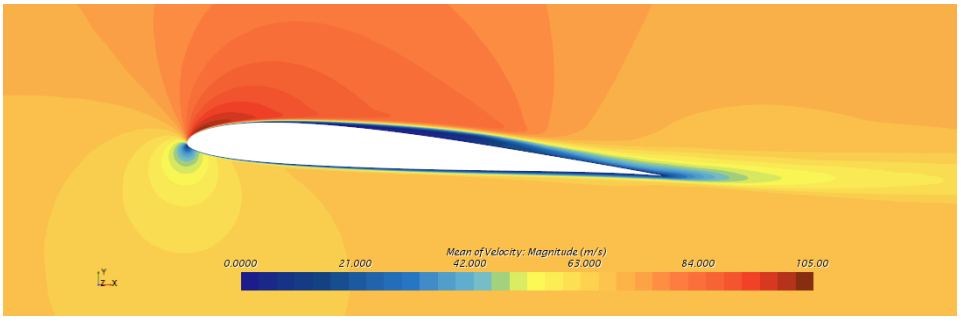

(d) LES-WALE SGS model-third order MUSCL/CD ($\sigma = 0.15$) hybrid Scheme.

Fig. 3.26 Mean Velocity Magnitude around airfoil SD7003 at Re=60,000, $\alpha = 4^o$.

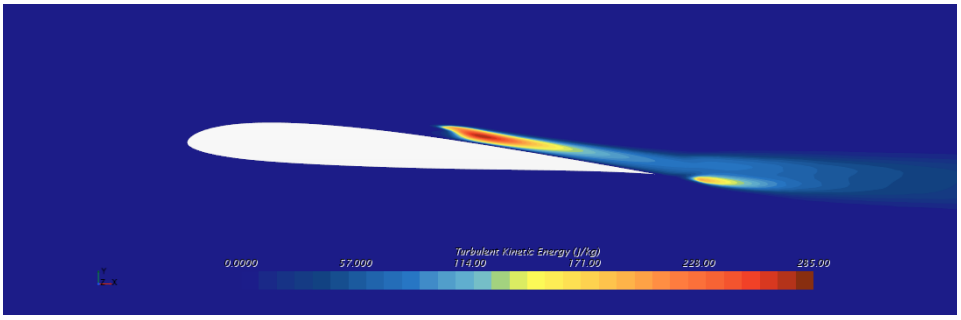

(a) RANS Suluksna-Juntasaro $S_1 = 6$.

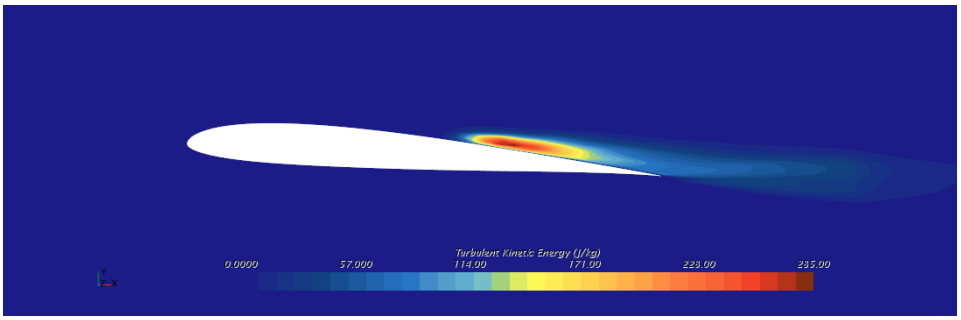

(b) LES-Dynamic Smagorinsky SGS model-Bounded Central Differences Scheme.

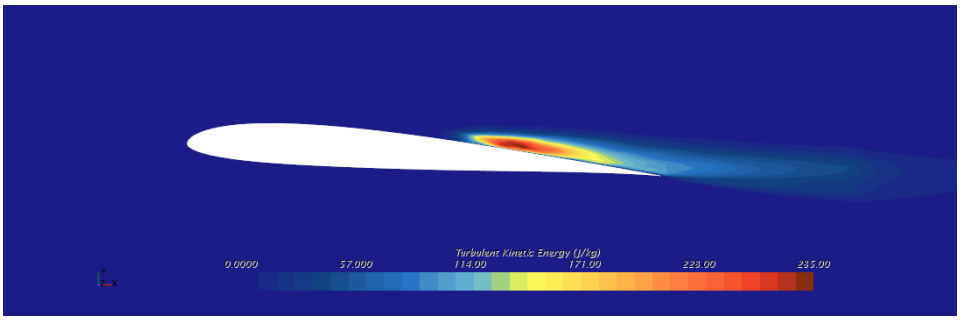

(c) LES-Dynamic Smagorinsky SGS model-third order MUSCL/CD ($\sigma = 0.15$) hybrid Scheme.

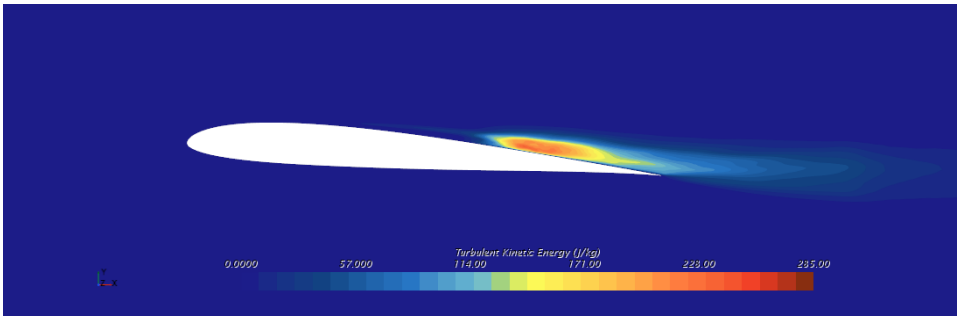

(d) LES-WALE SGS model-third order MUSCL/CD ($\sigma = 0.15$) hybrid Scheme.

Fig. 3.27 Turbulent kinetic energy around airfoil SD7003 at Re=60,000, $\alpha = 4^o$.

shown in Figure 3.27. Despite these discrepancies, Figure 3.26 illustrates how useful a well-tuned transition model can be, allowing accurate performance predictions with two-dimensional simulations with a computational cost of around 1 CPU hour compared with around 40,000 CPU hours for these LES. Furthermore, it allows the possibility of increasing the accuracy in RANS complex three-dimensional simulations, for which an LES is currently unaffordable, such as the flow over a rotor.

3.1.3 Discussion

In this section, we present numerical results demonstrating the effectiveness of the γ-Re_θ transition model in reproducing the transition behavior of airfoils using 2D simulations. The accuracy of the model improves with increasing Reynolds number. Our tests show that Menter's calibration provides better predictions than the original Suluksna-Juntasaro's calibration, despite a questionable double accounting of the effect of pressure gradients. Both calibrations fail to reattach the boundary layer at the lowest Reynolds numbers after transition, but this problem improves as the Reynolds number increases. We tested two different formulations of the separation-induced transition (Eqs. (2.54) and (2.55)) and concluded that the original formulation (Eq. (2.55)) performs better due to a higher limit in the effective intermittency. We found that a constant value of the parameter s_1 was insufficient for reliable tuning of the model to data over a wide range of angles of attack. In order to minimize error with respect to available LES data, we adjusted the separation-induced transition parameter s_1 to a value of 6 in Suluksna-Juntasaro's calibration. The model replicates well the performance predictions made using Menter's calibration. However, the transition occurs at a slightly more upstream position in Menter's calibration due to a pressure correction that lowers the trigger value of the momentum thickness required to begin producing turbulent kinetic energy. Suluksna-Juntasaro's calibration with the adjusted constant s_1 predicts the transition location closer to the LES results if compared to Menter's correlations, maintaining the accuracy in the airfoil performance coefficients obtained with the latter. Therefore, introducing another parameter in the separation-induced transition correction would be functional to simultaneously control the bubble length and position without re-tuning all the model correlations.

The results are surprisingly similar when comparing the calibrations of Suluksna-Juntasaro and Menter (without pressure gradient correction). This may be due to the fact that the model's separation-induced transition terms produce high levels of turbulent kinetic energy in separated regions, which overrides the usual production mechanisms used to simulate natural or bypass transition. Using a URANS model for low and intermediate angles of attack resulted in significant vortex shedding, which increased the lift coefficient of the airfoil and matched high-fidelity numerical data and experimental results. As the turbulence model becomes active in a more significant part of the airfoil, the vortex-shedding regime weakens and eventually forms a steady bubble. When studying different calibrations' influence on the vortex shedding regime, we noticed that Menter's calibration early transition dampens vortex shedding at a lower angle of attack than the finely tuned SJ calibration. This may underestimate the lift coefficient at low and intermediate angles of attack. For popular low-Reynolds number airfoils like SD7003 and Ishii, there is a satisfactory agreement between the computed numerical solutions and available high-fidelity numerical simulations and experimental data for Reynolds numbers ranging from 23,000 to 200,000. The transition model can accurately predict the expected nonlinearity of the $c_L(\alpha)$ curve at very-low Reynolds numbers caused by flow separation and reattachment for low and intermediate angles of attack. However, simulations predict premature stall for high angles of attack. The main limitation of the 2D simulations is evident when computing the polar of the e-387 airfoil, which has a larger camber than the previous two airfoils. High-fidelity simulations show that the flow around this airfoil has a three-dimensional structure that significantly affects the pressure distribution on the body surface, a feature that RANS simulations cannot reproduce.

Large Eddy Simulations were performed with different reconstruction schemes and subgrid stress models. Simulations using bounded central differences and a dynamic Smaginsky subgrid stress model captured separation-induced transition and presented the closest agreement with other LES data found in literature. They show a slightly delayed transition, but the overall trend is captured. These discrepancies could be associated with the grid resolution, the slightly higher Mach number we are simulating, and differences in the outer domain that modify the effective angle of attack. In any case, we show how the mean velocity distribution around the airfoil and the turbulent kinetic energy production are coherent in location and magnitude.

When comparing the LES and RANS solutions, the problem of lack of turbulent kinetic energy production close to the wall after reattachment is apparent. LES

presents a much sharper reattachment, reducing the thickness of the separation bubble. It is also clear how attempting to solve one problem by tuning the s_1 parameter has created another. Indeed, the wall shear stress is slightly increased, but in doing this, the transition location is predicted slightly upstream. We previously commented on how two parameters in the separation-induced correction would be interesting in controlling the location and intensity of the injected turbulent kinetic energy. Apart from this modification, working on the damping functions is interesting, allowing a greater turbulent kinetic energy close to the wall, which might help achieve accurate wall shear stress values. It seems clear that for low Reynolds numbers, due to the increased dimension of the separated region, more attention needs to be given to the location of the injection of turbulent kinetic energy in separation-induced transition to reproduce local flow features using RANS accurately.

3.2 Ultra-Low Reyolds number

This section discusses airfoil performance prediction and optimality in the Ultra-low Reynolds number regime. It presents two optimization alternatives, one using XFOIL and another using a coupled CFD-Adjoint analysis. These two approaches use continuous geometrical parameterizations, i.e., no sharp edges. Then, the sharp leading-edge geometries and the influence of these in creating optimal separation bubbles are analyzed. Finally, well-resolved Navier-Stokes evaluations and Large Eddy Simulations (LES) are presented on a sharp leading-edge geometry to provide more confidence in the numerical approach and reinforce the assumption of laminar flow, at low and moderate angles of attack.

3.2.1 Laminar Flow Assumption

The present study centers on investigating airfoils that operate at Reynolds numbers of 10,000 and Mach number of 0.5. This flow condition is typically found on the outboard sections of rotors employed in Martian operations. Under this regime, the Reynolds number is always lower than the critical one for viscous instabilities or Tolmien-Schlitching waves to grow enough to trigger transition to turbulence by the natural transition mechanism. The onset of turbulence, however, may be initiated by an inviscid or Kelvin-Helmholtz instability that causes the shear layer to roll

up. Eventually, the vortical structures will experience instabilities, fragmenting into smaller structures. The phenomenon referred to as separation-induced transition is identified by a significant generation of turbulent kinetic energy within the separated shear layer, which facilitates the turbulent reattachment process [114]. The transition mechanism for an SD7003 airfoil operating at Reynolds 60,000 and an angle of attack of 4 degrees has been successfully replicated through high-fidelity numerical simulations [84, 205, 52] and also shown in the previous section. These simulations demonstrate the formation of a separation bubble followed by turbulent reattachment. Nevertheless, the identical airfoil exhibited laminar separation without transition at Reynolds number 10,000 [83, 205]. The study by Van Dyke [209] demonstrates the phenomenon of leading-edge separation and posterior laminar reattachment without transition to turbulence on a flat plate at Reynolds 10,000 and an angle of attack of 2.5 degrees. According to Pauley's research [150], the primary factor governing laminar separation bubbles at low Reynolds numbers is the Kelvin-Helmholtz instability, while the transition to turbulence plays a secondary role. The study conducted during this thesis on transition models (Chapter 3 and Ref.[39]) demonstrates that the γ-Re_θ transition model can effectively predict transition at Reynolds 60,000; however, its reliability diminishes when applied to the lower transitional regime. This finding highlights the limitations of the γ-Re_θ model in accurately predicting transitional flows at lower Reynolds numbers. The activation of the turbulent term suppresses the phenomenon of the vortex emission regime. Following Pauley's findings, the lack of reliability of transition models within this range and the impracticality of executing three-dimensional scale-resolving simulations in an optimization endeavor due to its computational expense leads to the assumption of laminar flow for Reynolds numbers around 10,000 even though it is not a given. The study by Koning [108] demonstrates a favorable concurrence between laminar and transitional simulations when utilizing a e^N model for a sharp leading edge airfoil at moderate angles of attack. This finding provides additional corroboration for the assumption of laminar flow in the case of Reynolds 10,000, which Bézard [24, 23] and our investigation follows. This is motivated by smaller radii of the rotor analyzed compared to those studied by Koning et al. [106] resulting in slightly lower chord-based Reynolds numbers.

3.2.2 Fitness function to optimize airfoils for rotor performance

The most common and logical selection of the fitness function for airfoil optimizations is the lift-to-drag ratio, or aerodynamic efficiency [108, 45]. Other authors[70] claim that using a combination of maximum aerodynamic efficiency, $\frac{C_l}{C_d}$, and the maximum range efficiency, $\frac{C_l^{1.5}}{C_d}$, provides less aggressive geometries. In the following lines, we will perform a theoretical analysis to demonstrate what value should be optimized depending on the problem constraints for rotor performance optimization. The quantity of interest in rotor optimization is the power loading, defined as the ratio between the rotor thrust and consumed power. According to the classical blade element theory definitions of thrust and power [119], we can express this ratio as:

$$T/P = \frac{0.5N_b\rho\int_{r_h}^{R}((\Omega r)^2+V_{ind}^2)c(r)(C_l(\alpha,M,Re,r)cos(\phi)-C_d(\alpha,M,Re,r)sin(\phi))\,dr}{0.5N_b\rho\int_{r_h}^{R}\Omega r((\Omega r)^2+V_{ind}^2)c(r)(C_d(\alpha,M,Re,r)cos(\phi)+C_l(\alpha,M,Re,r)sin(\phi))\,dr} \tag{3.5}$$

The dependency with r in the lift and drag coefficients shows that we are considering a varying airfoil throughout the span. For a given blade element located in position r and omitting the dependencies on the drag and lift coefficients for clarity, we can simplify the expression to:

$$\Delta(T/P) = \frac{C_l cos(\phi)-C_d sin(\phi)}{(\Omega r)(C_d cos(\phi)+C_l sin(\phi))} \tag{3.6}$$

the radial station now determines the Mach number and the airfoil, which is assumed constant within the blade element. Now, assuming a uniform induction across an annular portion of the disk corresponding to the blade element, we can estimate the induction angle according to the BEM theory:

$$\phi = \arctan(\frac{V_{ind}}{\Omega r}) = \arctan(\frac{\sqrt{\frac{\Delta T_{req}}{2\rho\Delta A}}}{\Omega r}) = \frac{\sqrt{\frac{0.5N_b\rho((\Omega r)^2+V_{ind}^2)c(r)(C_l cos(\phi)-C_d sin(\phi))\Delta r}{4\rho\pi r\Delta r}}}{\Omega r} + o(\phi^3) \quad (3.7)$$

To simplify this derivation and due to its limited influence, we neglect the tangential induction factor in the previous equation. Introducing the local solidity as:

$$\sigma_l = \frac{N_b c(r)}{2\pi r} \quad (3.8)$$

we can simplify Eq.3.7 into:

$$\phi = \sqrt{\frac{\sigma_l(1+\phi^2)(C_l cos(\phi)-C_d sin(\phi))}{4}} \quad (3.9)$$

This equation is non-linear in ϕ and needs to be solved numerically. However, if we compare the first and second terms of the numerator:

$$\frac{C_d sin(\phi)}{C_l cos(\phi)} = \frac{tan(\phi)C_d}{C_l} << 1 \quad (3.10)$$

this term will only be relevant near the hub where the aerodynamic efficiency is very low and significant induction angles are obtained. An optimized airfoil at Reynolds 10,000 presents an efficiency of around 18, and induced angles are 10-15 degrees. Therefore, the errors will be contained within 1%.

Expanding in Taylor series, we can obtain the following:

$$4\phi^2 = \sigma_l C_l(1+\phi^2)(1-\frac{\phi^2}{2}) = \sigma_l C_l(1+\frac{\phi^2}{2}+O(\phi^4)) \quad (3.11)$$

therefore:

$$\phi = \sqrt{\frac{2\sigma_l C_l}{8 - \sigma_l C_l}} \tag{3.12}$$

Equation 3.6 can be simplified according to eq. 3.10 to obtain:

$$\Delta(T/P) = \frac{1}{\Omega r(\frac{C_d}{C_l} + tan(\phi))} \tag{3.13}$$

Then, we can expand the tangent in Taylor series and substituting ϕ we obtain:

$$\Delta(T/P) = \frac{1}{\Omega r(\frac{C_d}{C_l} + \sqrt{\frac{2\sigma_l C_l}{8 - \sigma_l C_l}})} \tag{3.14}$$

This expression shows how, for a given rotation rate and radial station, the increasing aerodynamic effect positively impacts power consumption, but minimizing the lift coefficient also has a positive effect due to reduced induced drag. However, one should only compare T/P ratios for equal thrusts. Therefore one could fix a certain thrust level for a specific blade element, $\Delta T_r eq$ as:

$$\Delta T_{req} = \frac{1}{2}\rho\Omega^2 r^2 \sigma_l 2\pi\Delta r(C_l(1+\phi^2)(1-\frac{\phi^2}{2})) = \frac{1}{2}\rho\Omega^2 r^2 \sigma_l 2\pi\Delta r C_l(1+\frac{\phi^2}{2}+O(\phi^4)) \tag{3.15}$$

given that we are in a given radial station provided a local thrust requirement, we can establish the following relationship between solidity, lift coefficient, and rotation rate:

$$\Omega^2 \sigma_l C_l(1+\frac{\sigma_l C_l}{8-\sigma_l C_l}) = K = K_2^2 = \frac{\Delta T_{req}}{\rho\pi r^3 \Delta r} \tag{3.16}$$

$$\Omega = \sqrt{\frac{K(r, \Delta T_{req}/\Delta r, \rho)}{\sigma_l C_l(1+\frac{\sigma_l C_l}{8-\sigma_l C_l})}} = \frac{K_2(r, \Delta T_{req}/\Delta r, \rho)}{\sqrt{\sigma_l C_l(1+\frac{\sigma_l C_l}{8-\sigma_l C_l})}} \tag{3.17}$$

$$\Delta(T/P) = \frac{1}{K_2(r, \Delta T_{req}/\Delta r, \rho)(\frac{1}{\sqrt{C_l \sigma_l (1 + \frac{\sigma_l C_l}{8 - \sigma_l C_l})}} \frac{C_d}{C_l} + \frac{1}{2})} \tag{3.18}$$

$$f = \sqrt{\sigma_l C_l (1 + \frac{\sigma_l C_l}{8 - \sigma_l C_l})} \frac{C_l}{C_d} = \sqrt{\sigma_l (1 + \frac{\sigma_l C_l}{8 - \sigma_l C_l})} \frac{C_l^{\frac{3}{2}}}{C_d} \tag{3.19}$$

this last equation shows the objective function that should be maximized at each radial station. We can appreciate how using the rotation rate as a design variable makes the lift coefficient and solidity more critical, as they tend to increase the thrust coefficient. This result shows how an optimal airfoil must attempt to have maximum aerodynamic efficiency. However, it must do it at a high lift coefficient to achieve the thrust restriction at a lower rotation rate, reducing power consumption in this way.

Another non-negligible factor omitted until this point is the tip loss factor due to three-dimensional effects. We can approximate this effect by correcting the local circulation. According to Kutta's formula, this is equivalent to modifying the lift coefficient with the Prandtl Tip-loss correction formulated by Glauert [89]. Due to the weak dependency that the term summed to unity in the square root has on the global expression and to simplify the analysis, the tip-loss correction will not be applied to the lift coefficient present in that term.

$$f = \frac{C_l}{C_d} \sqrt{(1 + \frac{\sigma_l C_l}{8 - \sigma_l C_l}) \sigma_l C_l} \left(1 - \frac{2}{\pi} \arcsin \left(e^{-\frac{B}{2} \frac{R - r}{r \sqrt{\frac{2 \sigma_l C_l}{8 - \sigma_l C_l}}}} \right) \right)^{\frac{3}{2}} \tag{3.20}$$

It is difficult to perform further analytical comparisons, but the tip loss function will decrease as we increase the lift coefficient. The decrease of this function compared to the growth with the square root will determine the actual function that

should be optimized. To further analyze this expression, let us split the function in two:

$$f = \sqrt{\sigma_l} f_1 f_2 \tag{3.21}$$

with

$$f_1 = \sqrt{C_l(1+\frac{\sigma_l C_l}{8-\sigma_l C_l})}\left(1-\frac{2}{\pi}\arcsin\left(e^{-\frac{B}{2}\frac{R-r}{r\sqrt{\frac{2\sigma_l C_l}{8-\sigma_l C_l}}}}\right)\right)^{\frac{3}{2}} \tag{3.22}$$

and

$$f_2 = \frac{C_l}{C_d} \tag{3.23}$$

Figure 3.28 shows how the effect of the tip correction is negligible at the mid-span of the blade, with f_1 showing a square-root behavior. However, as we increase the radial station, the curve slope is decreased and becomes noticeably affected by the solidity. We can also appreciate a limited influence of the non-linear lift coefficient term inside the square root. This analysis is simplified due to the lack of inclusion of the Reynolds numbers and Mach effects. However, despite these simplifications, it shows that depending on the radial station and solidity, the objective function varies from being the aerodynamic efficiency to the maximum range efficiency. Therefore, we can conclude that aerodynamic efficiency is a necessary but not sufficient condition for airfoil optimality in rotor applications. An optimal airfoil should be the most efficient at a certain lift coefficient that depends on the problem parameters. This suggests that a multiobjective optimization considering both drag and lift coefficients as objectives will provide us with a family of optimal airfoils (Pareto's front) for different rotor design conditions and radial stations. Once this Pareto front is obtained in the $C_l - C_d$ plane, it is possible to show that $\frac{C_l}{C_d}$ and $\frac{C_l^{1.5}}{C_d}$ conditions are contained in this front. We can compute these values by finding the point of the Pareto front in which the slope is determined according to Eqs. 3.24 and 3.25.

$$Max(\frac{C_l}{C_d}) - - > \frac{d(\frac{C_l}{C_d})}{dC_l} = \frac{C_d - C_l\frac{dC_d}{dC_l}}{C_d^2} = 0 - - > \frac{dC_d}{dC_l} = \frac{C_d}{C_l} \tag{3.24}$$

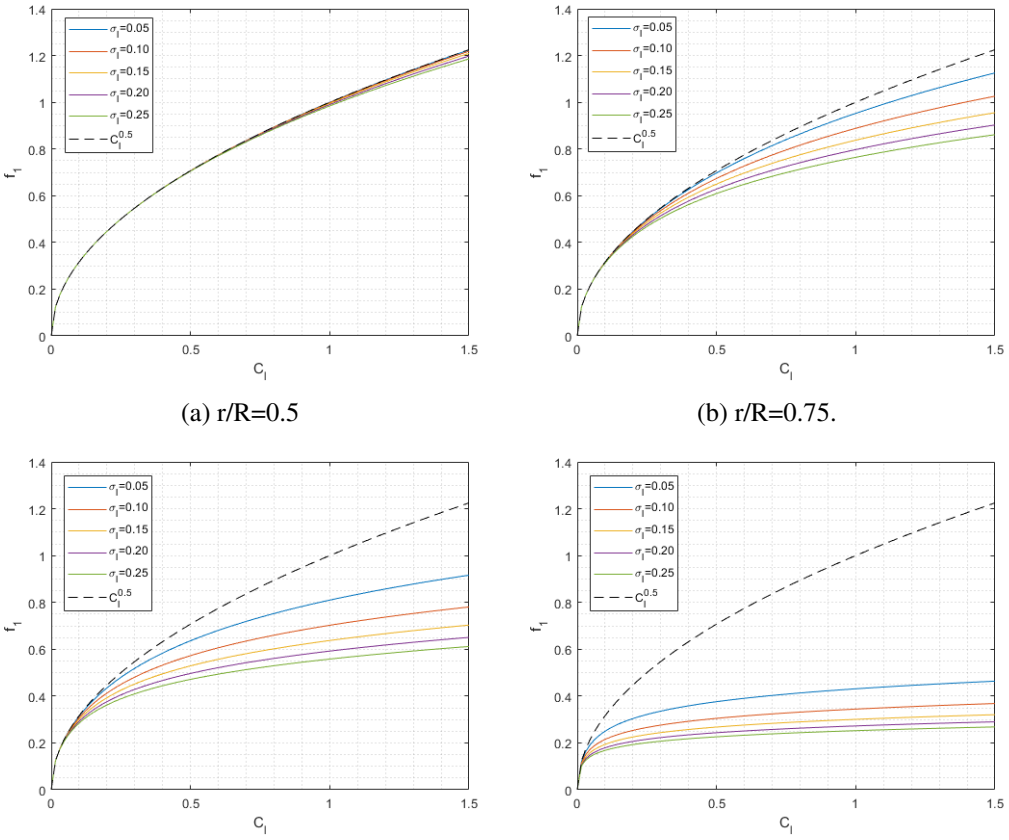

(a) r/R=0.5

(b) r/R=0.75.

(c) r/R=0.85.

(d) r/R=0.95.

Fig. 3.28 f_1 function for different radial stations and solidities.

$$Max(\frac{C_l^{1.5}}{C_d}) - - > \frac{d(\frac{C_l^{1.5}}{C_d})}{dC_l} = \frac{1.5C_l^{0.5}C_d - C_dC_l^{1.5}\frac{dC_d}{dC_l}}{C_d^2} = 0 - - > \frac{dC_d}{dC_l} = \frac{1.5C_d}{C_l} \quad (3.25)$$

3.2.3 Experimental Validation of Navier-Stokes simulations

Low Reynolds number flows on airfoils are characterized by strong flow separation accompanied by periodic vortex shedding at relatively low angles of attack. Separation in this Reynolds number regime does not necessarily induce stall in its classical terms, but a dedicated design is necessary to optimize the airfoil efficiency. Experimental data that could be used to validate numerical methods on which airfoil and blade optimization tools are based are not very common, mostly because very few facilities worldwide can operate at Martian-like density. A noticeable exception is the Mars Wind Tunnel (MWT) at Tohoku University, Japan [9], which can test airfoils at low pressure to simulate the Martian atmosphere in a test section of 100 by 150 mm. Reynolds numbers of the order of magnitude 10^3 can be reached in incompressible and compressible regimes. We validated the CFD tool that we will use throughout this project, STAR-CCM+, with experimental lift and drag measurements on a triangular airfoil tested at the MWT at Mach=0.5 and Re=3000 [143]. The simulations are fully 3D, as the wing spans the entire test section width, and wall effects may affect separation. Upper walls, with a 1.3° divergence, are also included for possible blockage effects. The mid-plane section is shown in Figure 3.29, showing the growing boundary layers on the outer wall, justifying the need for divergent walls.

A slight unsteadiness is noticed starting at AOA=6°, which becomes stronger as the angle of attack increases. At 6 degrees, a quasi-2D vortex shedding is obtained. Then these vortices become unstable and break down into three-dimensional structures, as shown in Figure 3.31. The difference in the flow characteristics is related to the flow separation position. When the flow separates at the apex, the flow remains quasi-2D over the surface of the airfoil. Conversely, when separation occurs at the leading edge, the flow is more likely to become three-dimensional. Later in this Chapter, we will present an example of leading-edge separation with two-dimensional flow. We show how actually the flow may undergo leading edge

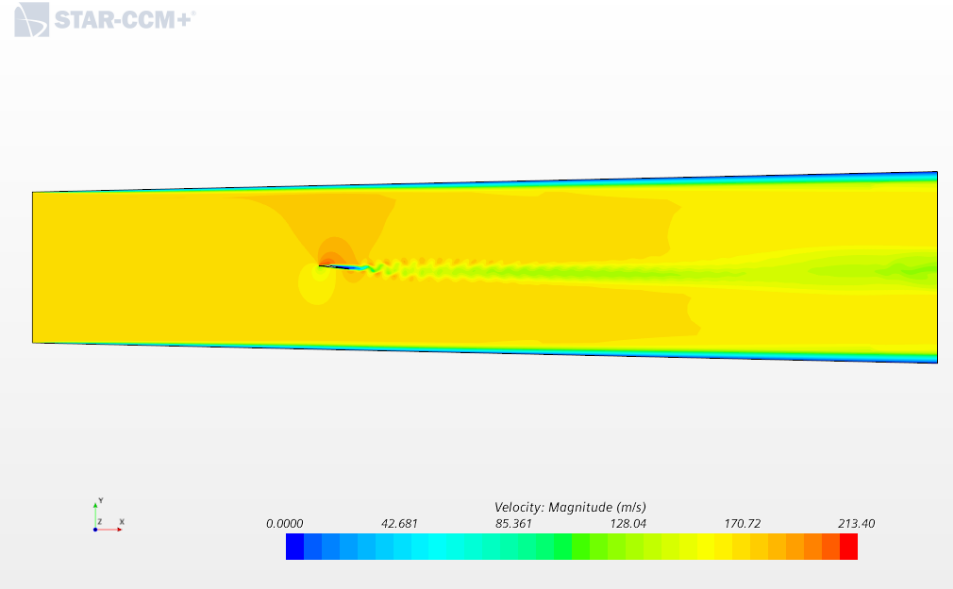

Fig. 3.29 Numerical simulation of the triangular airfoil wing at AOA=6º. Velocity magnitude.

separation, but the average flow reattaches before the apex forming an oscillating laminar separation bubble that periodically emits vortices downstream of the apex.

Averaged values for drag and lift coefficients are reported in Figure 3.32. We can appreciate an overall satisfactory agreement between numerical and experimental results from Munday [143] with slightly higher discrepancies for the highest angles of attack where the flow is highly unsteady and possibly the temporal and spatial discretizations may need refining.

This agreement shows how well-resolved Navier-Stokes evaluations using a low-order (Second) finite volume solver can capture ultra-low Reynolds number aerodynamics even for 3-Dimensional unsteady flows. These results align with Bézard's [24], which also used STAR-CCM+ to solve the same problem, and Caros' [37], who performed DNS on this airfoil using PyFR. This study also shows a good agreement between 2D simulations and periodic 3D simulations for low and moderate angles of attack. This fact provides confidence in using 2D simulations to estimate airfoil performance in this regime for low and moderate angles of attack.

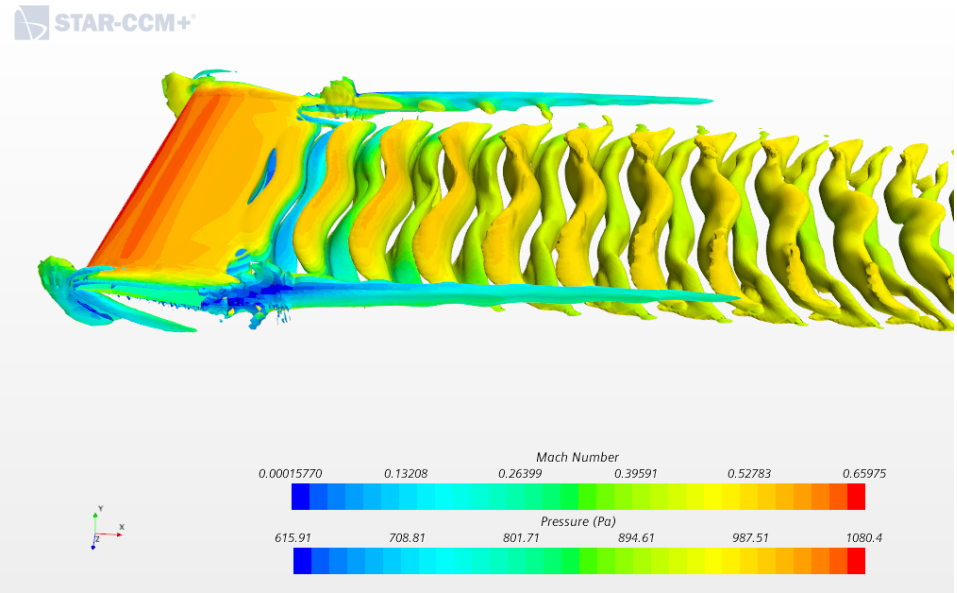

Fig. 3.30 Numerical simulation of the triangular airfoil wing at AOA=6º. Wall pressure and Q-criterion iso-surfaces colored with Mach number contours.

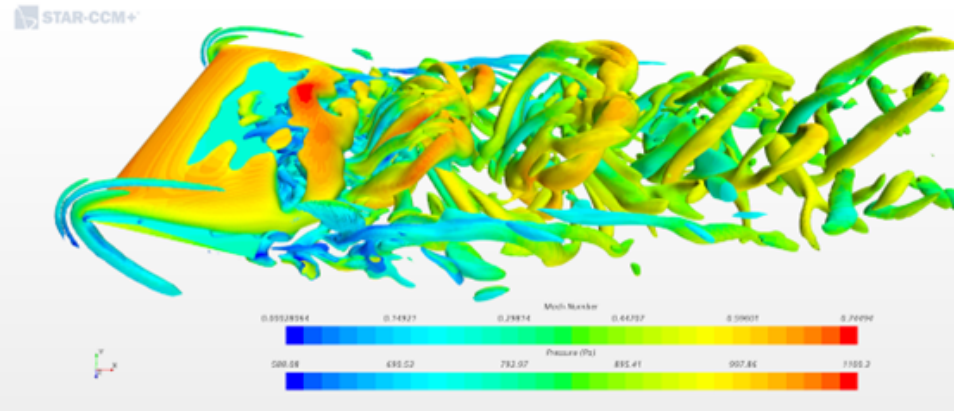

Fig. 3.31 Numerical simulation of the triangular airfoil wing at AOA=14º. Wall pressure and Q-criterion iso-surfaces colored with Mach number contours.

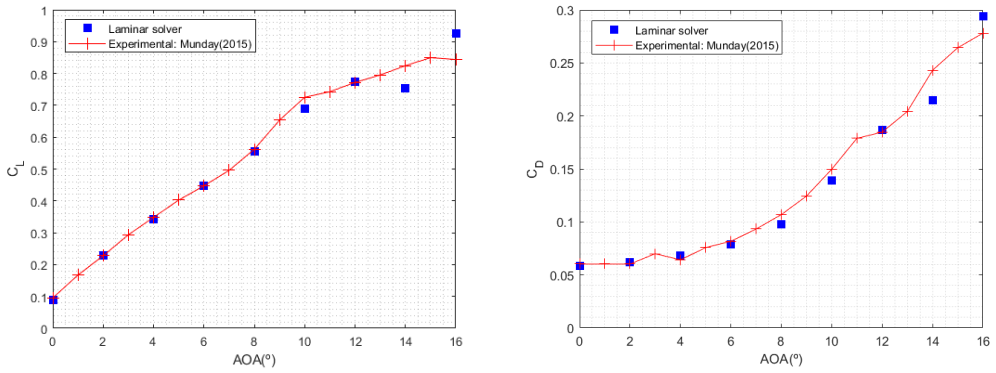

(a) Lift coefficient. (b) Drag coefficient.

Fig. 3.32 Lift and drag coefficients of the Triangular Airfoil wing. Re=3,000

3.2.4 Airfoil Parametrizations

We present two airfoils parametrizations in this work. A classical NACA 4-digits formulation to perform an initial sweep of the design space, and then we will show how a more general CST parametrization can improve the performance of the NACA series airfoils.

3.2.4.1 NACA 4-digits

The NACA airfoils are a specific type of aerodynamic airfoils studied and parameterized by the National Advisory Committee for Aeronautics. Their shape is uniquely described by the digits that follow the "NACA" acronym. The NACA 4-digits define the airfoil in this way:
-the first digit (**m**) expresses the maximum camber as a chord percentage
-the second digit (**p**) expresses the distance between the maximum camber position and the LE as 10% multiples of the chord.
-the last two digits (**t**) express the thickness as a chord percentage
The mathematical formulation of the airfoil is the following:

$$\begin{aligned} y_C &= \frac{m}{p^2}(2px - x^2) \quad for\ 0 \le x \le p \\ y_C &= \frac{m}{(1-p)^2}[(1-2p) + 2px - x^2)] \quad for\ p \le x \le 1 \end{aligned} \tag{3.26}$$

$$y_t = \pm\frac{t}{0.2}(0.2969\sqrt{x} - 0.1260x - 0.3516x^2 + 0.2843x^3 - 0.1015x^4) \tag{3.27}$$

$$\begin{aligned} x_U &= x - y_t \sin\theta \\ y_U &= y_C - y_t \cos\theta \\ x_L &= x + y_t \sin\theta \\ y_L &= x_C - y_t \cos\theta \\ with \quad \theta &= \arctan\frac{dy_C}{dx} \end{aligned} \tag{3.28}$$

3.2.4.2 Class Shape Transformation (CST)

The CST parametrization can ideally describe every type of geometric curve using as many degrees of freedom as necessary. The CST formulation proposed by Kulfan and Bussoletti [109, 57] is expressed below. The approach consists of recreating the desired shape with two principal functions. The first is called *class function C(x)* and the second is the *shape function S(x)*

$$\frac{y}{c} = C(\frac{x}{c})\, S(\frac{x}{c}) + \frac{x}{c}\frac{\Delta zte}{c} \tag{3.29}$$

where Δz_{te} represents the trailing edge thickness. The *class function* expresses the class of the represented curve, and its mathematical formulation is underlined below.

$$C(\frac{x}{c}) = (\frac{x}{c})^{N_1}\,(1-\frac{x}{c})^{N_2} \quad for\, 0 \le \frac{x}{c} \le 1 \tag{3.30}$$

In our analysis, we have fixed $N_1 = 0.5$ e $N_2 = 1$, to have a round leading edge and sharp trailing edge as shown in Figure 3.33.

The shape function is a form factor for the *class function*. Its formulation uses the summation of the $n+1$ Bernstein polynomials characterized to have unitary results on [0,1] interval as shown in equation 3.31.

Using a series of appropriate weighting coefficients ($n+1$ b_i coefficients) on the precedent definition, we arrive at the final formulation of the *shape function*.

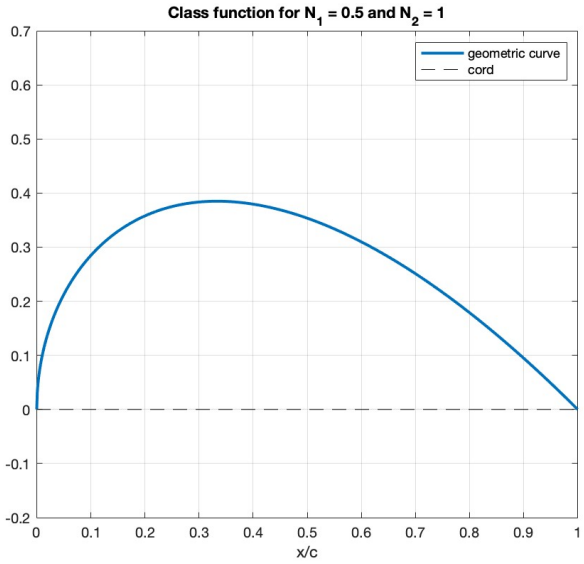

Fig. 3.33 *class function* parameters.

Figure 3.34 presents an example of an airfoil generated using our 8-parameter CST parametrization, which employs Bernstein polynomials of order 3 for both the upper and lower airfoil surfaces. The four parameters corresponding to the upper side are [1,1,1,1], and the lower side of the airfoil is characterized by [0.3,0.5,0.8,0]. In the optimization activity regarding airfoils for the Martian atmosphere, we impose a minimum relative thickness of 1% except for the regions near the trailing and leading edges. The maximum relative camber is limited to 10%, and only positively camber airfoils are considered.

$$S(\frac{x}{c}) = \sum_{i=0}^{n} [b_i \, K_{i,n} \, (\frac{x}{c})^i \, (1-\frac{x}{c})^{n-i}] \tag{3.31}$$

3.2.5 Methodology

3.2.5.1 Xfoil

As discussed in Chapter 2, the pressure plateau and posterior recovery can be reproduced but cannot predict the characteristic negative skin friction before reattachment. Due to the ultra-low Reynolds numbers, transition will only happen after boundary layer separation due to the amplification of Kelvin-Helmholtz instabilities. As men-

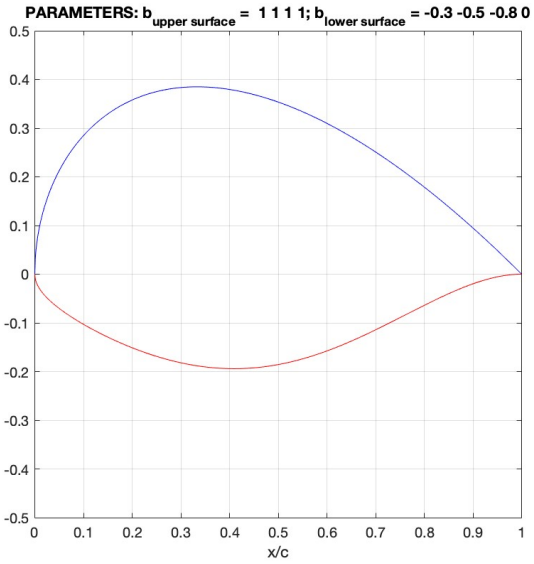

Fig. 3.34 Example of an airfoil generated with the CST parametrization.

tioned in the previous section, according to Pauley et al. [150], at very low Reynolds numbers, the main responsible for the formation of laminar separation bubbles is the inviscid instability, with turbulence in the separated shear layer taking a secondary role. Therefore, we cannot expect XFOIL to capture this phenomenon adequately due to the steady nature of the solver. Consequently, in this work, the use of XFOIL will be limited to attached flow conditions. To this purpose, we have set a very large value of exponent N to avoid unphysical reattachment caused by the flow transition that provides unrealistic airfoil efficiency values. Figure 3.35 shows how for low angles of attack, where the flow is attached, XFOIL solutions with different critical exponent (N_{crit}) values collapse due to the laminar nature of the flow. On the other hand, we can see how, for large values of the critical exponent, the flow separates, increasing the drag coefficient, and the lift coefficient remains almost constant. As N_{crit} is decreased, we can see how a reattachment of the boundary layer is achieved, characterized by a sudden increase in lift and high-efficiency values. However, these values depend highly on the N_{crit} value. It is, therefore, presumable that using XFOIL in an optimization algorithm will provide geometries that trigger transition in the place of efficient airfoils. To avoid this, in this section, we run XFOIL with Ncrit equal to 14 and assume that the values obtained after flow separation are not to be considered. Following considerations in Chapter 2, XFOIL runs at low

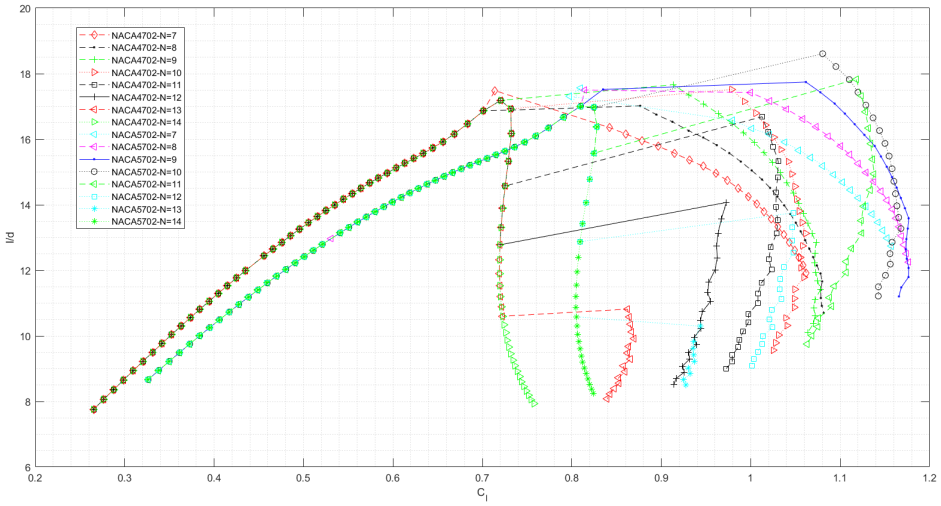

Fig. 3.35 Efficiency vs. lift coefficient for NACA 4702 and 5702 at Reynolds number of 10,000 using XFOIL with different N_{crit}.

Mach numbers, and then pressure distributions are corrected with Kàrman-Tsien's compressibility correction.

3.2.5.2 Adjoint Solver

The steady adjoint solver in STAR-CCM+, described in Chapter 2, is used to calculate the sensitivity of an objective function with respect to the design parameters d_i. The cost function selected for the airfoil design study is the aerodynamic efficiency, E:

$$E = \frac{c_L}{c_D} \tag{3.32}$$

We defined the control points with an offset of 3 mm from the actual airfoil surface (Figure 3.36). Their displacement along the direction of the gradient vector following a so-called steepest descent approach increases the objective function. We preferred to avoid using the airfoil as a response surface because such a choice may create dimples while moving the offset points generates smoother wall surfaces. Of course, we apply a floating condition at the airfoil boundary to allow its morphing. The grid can deform freely until reaching a maximum efficiency or, conversely, a minimum airfoil thickness. Then the chord is normalized to 1 meter to allow an

(a) Control point definition around the airfoil.

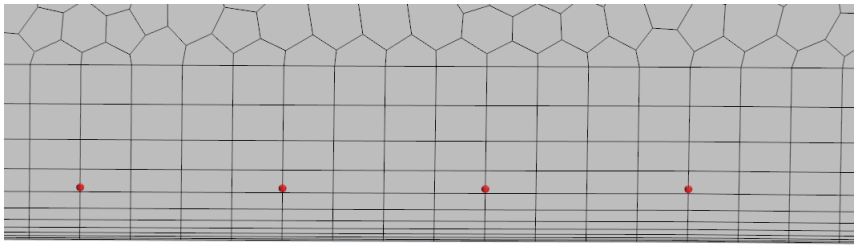

(b) Near-body detail.

Fig. 3.36 Definition of control points used for grid morphing.

adequate comparison of aerodynamic coefficients. Equation (3.33) shows the rule governing the displacement of the control points in each adjoint iteration:

$$d_i = d_{i-1} + \frac{h_{step}\nabla E}{max(|\nabla E|)} \tag{3.33}$$

Here, h_{step} represents the adjoint step, which defines the displacement of the most sensitive control point for each adjoint iteration. That value is set to 0.5 mm to avoid excessive grid deformation. It also ensures that the first-order approximation of the gradient is still valid and enables faster convergence of the aerodynamic (primal) solution. The primal solution is computed using a steady solution of the compressible Navier-Stokes equations. Désert [70] shows that while the flow is not entirely separated from the leading edge, a steady approach could reasonably capture the flow characteristics. The steady approach makes the optimization process very fast. After optimization, loads of the resultant airfoils will be computed using the compressible unsteady Navier-Stokes equations following the procedure shown in the following sections to ensure accurate performance predictions.

3.2.5.3 CFD

The compressible unsteady Navier Stokes (NS) equations are the foundation of the numerical model that calculates airfoil performance. We apply a third-order central difference spatial discretization with a 15% upwind blending to stabilize the solution. We use a time step of 0.01 turnovers, with a turnover definition of c/U_∞. The simulations described in this study use an implicit second-order temporal integration approach. The inner solver executes for 10 iterations each time step and allows residuals to drop 2-3 orders of magnitude while ensuring that the vortex shedding regime is resolved. To allow for statistical convergence, the simulation runs for 100 turnovers. The performance data for airfoils provided in this research was acquired by averaging unstable loads throughout a 20-turnover sampling window.

The adopted computational domain and boundary conditions are set identically to those described in section 3.1.1.1 for the transition model simulations.

The computational grid adopts polygonal cells and a near-wall prism layer to capture the high gradients in the boundary layer and ensure mesh orthogonality close to the body surface. Since the boundary layer separation occurs at the leading edge for some angles of attack, in these cases, the prism layer is limited to a thin zone near the wall, despite the small Reynolds number. Indeed, it would be useless to emphasize the wall-normal grid resolution when, in fact, capturing strong gradients arising in all directions requires an adequately refined mesh. On these occasions, we prefer to limit the thickness of the prism layer by increasing the number of polygonal cells in the overlying area, where the unsteady vortex-shedding structure requires good resolution. For this purpose, we also include a wake refinement as shown in Figure 3.37. The number of prism layers is 16, and the near-wall distance ensures a y+ value below 1. Table 3.12 shows the grid settings used to construct three different meshes to demonstrate grid independence in the next section. Figure 3.37 refers to the grid with a base size of 1 meter, the selected grid for the 2D simulations presented in this section. The base size is a reference length used to scale grid control settings to refine the mesh uniformly.

Due to the challenging flow characteristics, we conducted a convergence study on the spatial and temporal resolution for one of the sharp leading-edge geometries proposed in the next sections. The results are shown in Tables 3.13 and 3.14. The grid and time-step settings described in the previous section correspond to a base

Table 3.12 Grid specifications.

Base size (m)	**Chordwise size (%c)**	**Wake Size (%c)**	**Prism Layer Thickness (%c)**
2	0.2	0.8	1
1	0.1	0.4	0.5
0.5	0.05	0.2	0.5

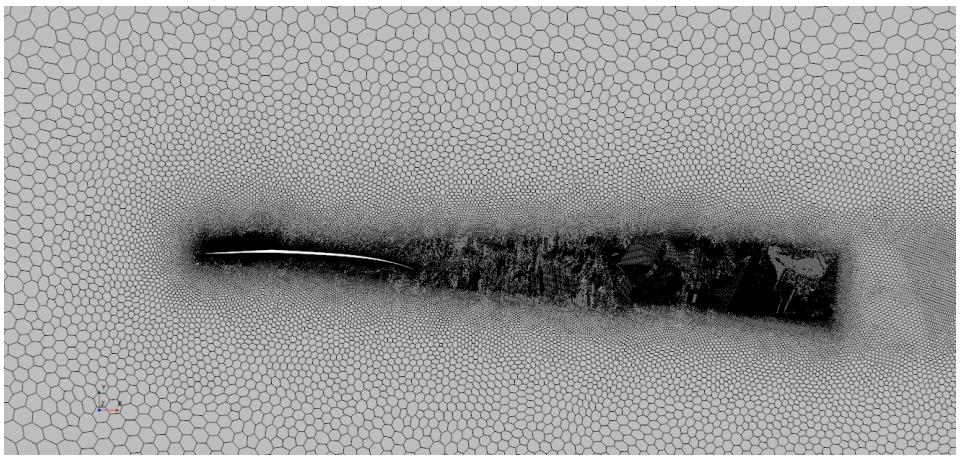

(a) Wake Refinement.

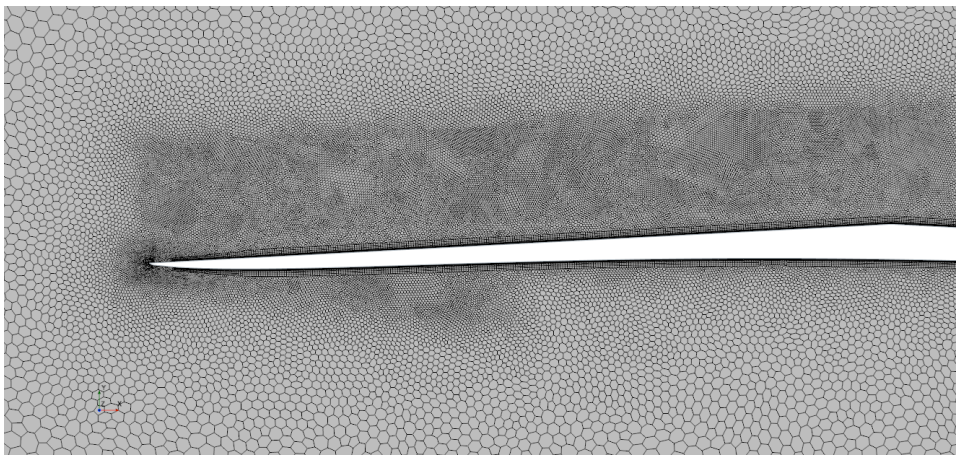

(b) Near-body detail.

Fig. 3.37 Mesh around Pareto Optimal airfoil at Cl=0.866 with a sharp leading edge obtained slicing with a 7.5 degrees plane, AOA=4.5°.

Table 3.13 Grid Convergence Study.

Base Size (m)	**Cells**	C_l	C_d
2	80,000	0.915	0.0471
1	200,000	0.945	0.0475
0.5	550,000	0.948	0.0477

Table 3.14 Time-Step convergence Study.

Time-Step (Turnovers)	C_l	C_d
1/50	0.925	0.0470
1/100	0.945	0.0475
1/200	0.941	0.0474

size of 1 meter and a time-step of 0.01 turnovers. In both cases, halving the resolutions produces variations below 0.5% on the results, demonstrating independence concerning the temporal and spatial resolutions. We performed the study for the airfoil discussed in section 3.2.8 with a sharp leading edge at an angle of attack of 4.5 degrees, a Reynolds number equal to 10,000, and Mach equal to 0.5. An equivalent grid independence analysis can be found in Ref. [45] for the PoliTO-2 airfoil.

3.2.5.4 Comparing XFOIL and CFD

In this section, a comparison between XFOIL and CFD is presented. This analysis aims to show that when the flow is attached, XFOIL can capture airfoil performance. Table 3.15 compares at 4 degrees for NACA 4702 and NACA 5702, showing differences below 5% between XFOIL and CFD. Figures 3.38 and 3.39 show how the Kàrman-Tsien correction improves the incompressible prediction for the pressure side and most of the suction side except the suction peak, which is overpredicted. This is possibly caused by an underestimation of the boundary layer thickness caused by not accounting for compressibility effects in the Von Kàrman equation solved by XFOIL. In any case, we can see how the integral loads are globally improved.

Figures 3.40, 3.41 and 3.42 show how the lift and drag coefficients and thus the aerodynamic efficiency are in good agreement for low angles of attack. After the angle of attack for which the maximum efficiency is achieved, XFOIL predicts an almost constant lift with increased drag. On the other hand, CFD predicts a high-lift

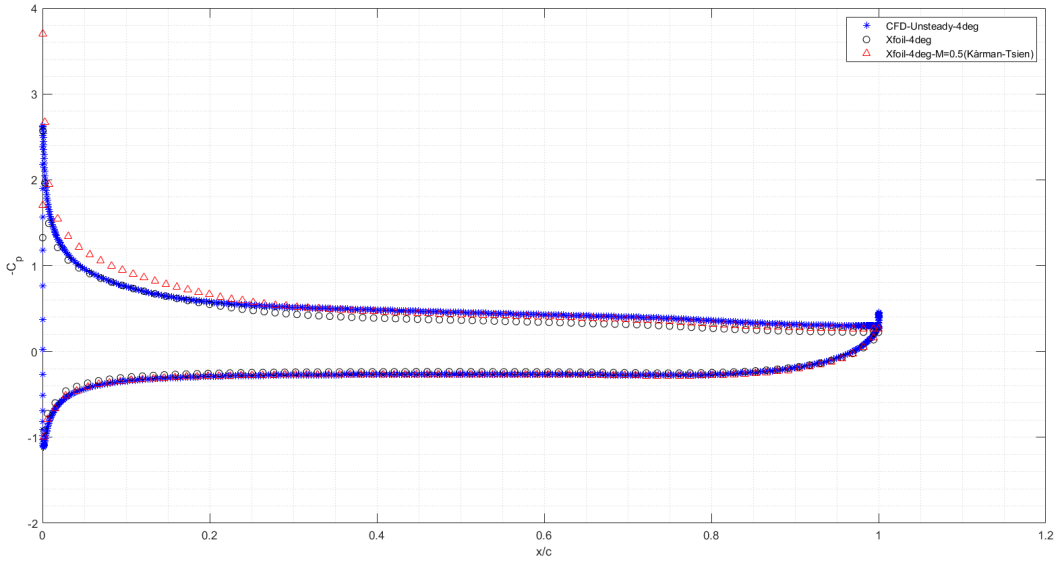

Fig. 3.38 Pressure coefficient for NACA4702 at Reynolds number 10,000.

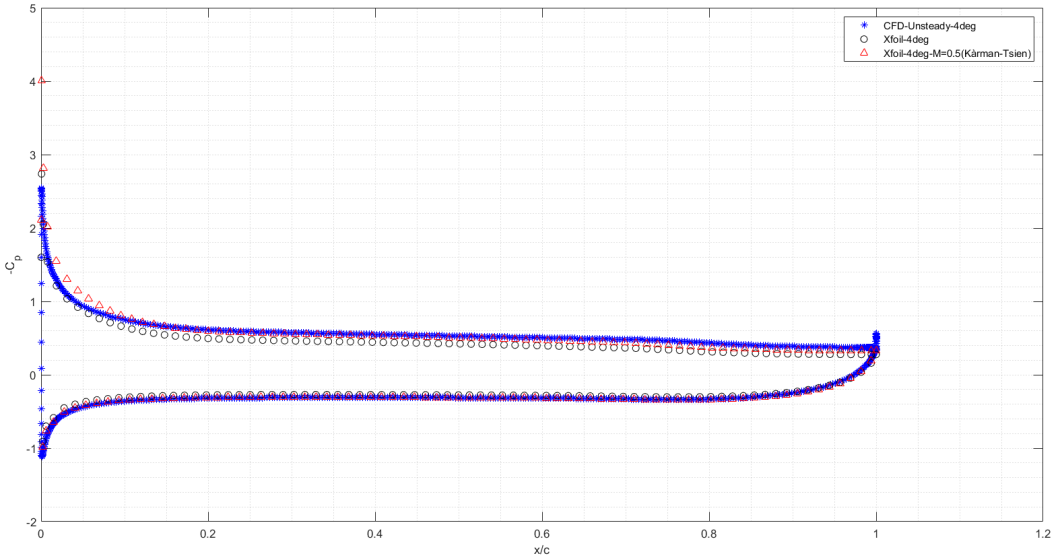

Fig. 3.39 Pressure coefficient for NACA5702 at Reynolds number 10,000.

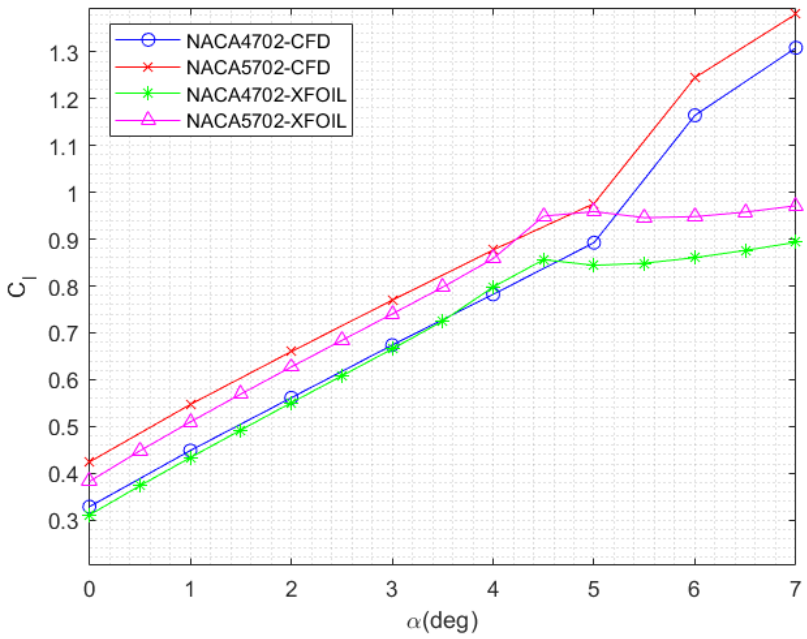

Fig. 3.40 Lift coefficient vs. angle of attack for NACA 4-digit series airfoils at Reynolds number of 10,000 using XFOIL with N=14 and Navier-Stokes evaluations.

regime caused by the low-pressure vortex cores emitted from the leading edge. The drag also increases, but the overall efficiency remains relatively high for a short range of angles of attack. It seems clear that XFOIL can capture the attached regime reasonably well.

Table 3.15 Airfoil performance predictions with XFOIL and CFD for two NACA airfoils at an angle of attack of 4 degrees.

	NACA 4702		**NACA 5702**	
	C_l	C_d	C_l	C_d
XFOIL+Kàrman-Tsien	0.802	0.0480	0.862	0.0514
CFD	0.782	0.0466	0.877	0.0522
Difference(%)	2.6	3.0	-1.7	-1.5

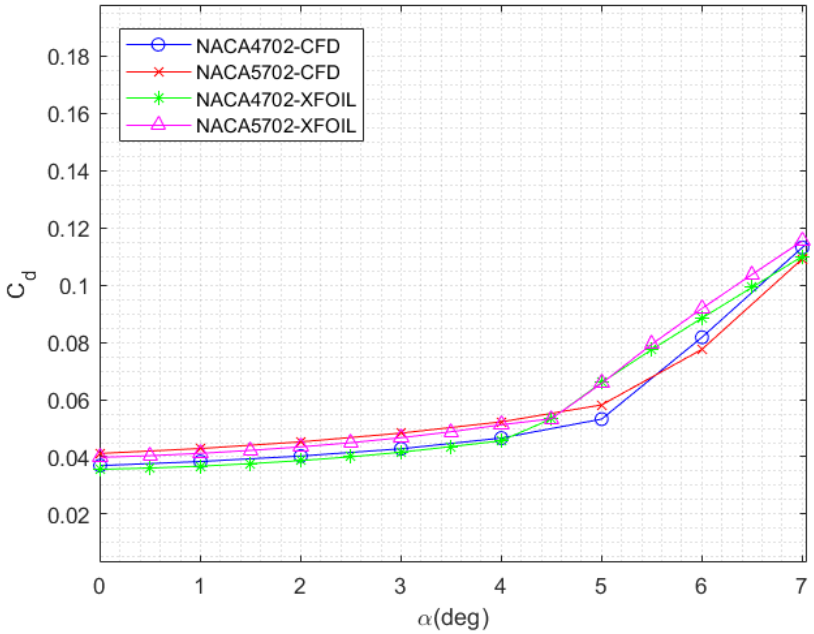

Fig. 3.41 Drag coefficient vs. angle of attack for NACA 4-digit series airfoils at Reynolds number of 10,000 using XFOIL with N=14 and Navier-Stokes evaluations.

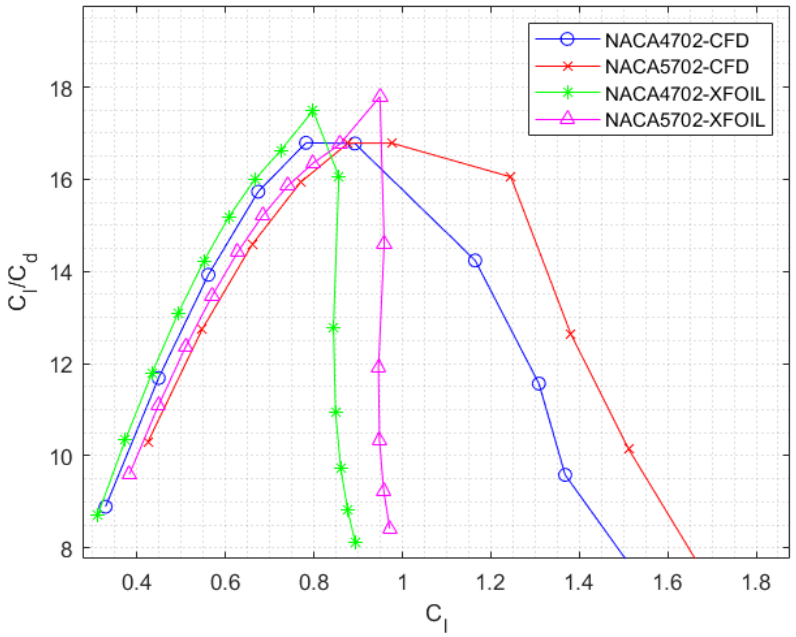

Fig. 3.42 Efficiency vs. lift coefficient for NACA 4-digit series airfoils at Reynolds number of 10,000 using XFOIL with N=14 and Navier-Stokes evaluations.

3.2.6 Airfoil Design at Reynolds number of 10,000

This section presents different design approaches for airfoils in this regime. Initially, we show an evaluation of all the 2% thickness airfoils in the NACA 4-digits family to get a preliminary view of the range in which optimal parameters should fall. Then a multiobjective optimization using XFOIL with the CST parametrization is performed. And finally, we present an adjoint-based CFD optimization.

3.2.6.1 Evaluation of the NACA 4-digits family

In this section, we evaluate the whole NACA XX02 family using XFOIL to obtain an overall idea of the optimal camber and maximum camber positions. Following the development shown in Section 3.2.2, we have plotted both the aerodynamic efficiency and the maximum range efficiency, evidencing that depending on the objective, the optimal camber varies. Figure 3.43 shows how a camber between 3% and 5% are adequate values to maximize aerodynamic efficiency. On the other hand, if we want to maximize the range efficiency, we need to go towards cambers between 5% and 7%. Regarding the maximum camber position, for most cambers, the optimal is between 70% and 80%, which present almost identical performances. The upper envelope formed by all the curves would represent the same airfoils as those found in the Pareto front in a multi-objective optimization with fitness functions Cl and Cd using the NACA XX02 family.

3.2.6.2 Multiobjective Genetic Optimization using XFOIL

Using lift and drag coefficients as objective functions, we suggest a Multi-Objective Optimization (MOO) employing a Genetic Algorithm (GA) using, in this case, the CST airfoil parametrization. The applied algorithm is `gamultiobj`, incorporated in MATLAB. This method implements a variation of NSGA-II [68], an elitist genetic algorithm. From a population of 300 individuals, it chooses 35% Pareto points that evolved over 100 generations. The parameters and settings that define the genetic algorithm are enumerated in Table 5.1. For efficiency and convergence issues, we sweep angles of attack and select the angle of attack of maximum efficiency. This seems to restrict the generality of our analysis. Still, due to the choice of the N-factor parameter, the maximum efficiency angle of attack is very close to the maximum lift

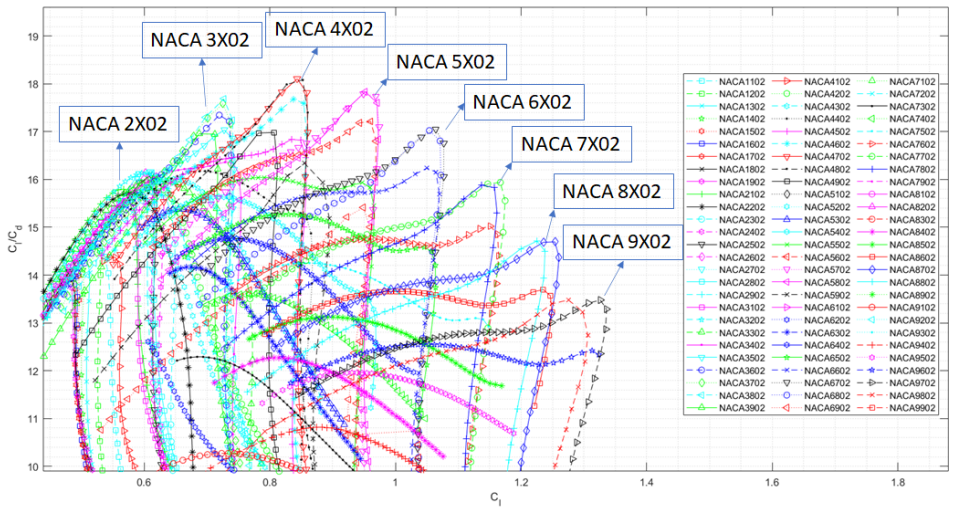

Fig. 3.43 Aerodynamic efficiency vs. lift coefficient for NACA 4-digit series airfoils at Reynolds number of 10,000 using XFOIL with N=14.

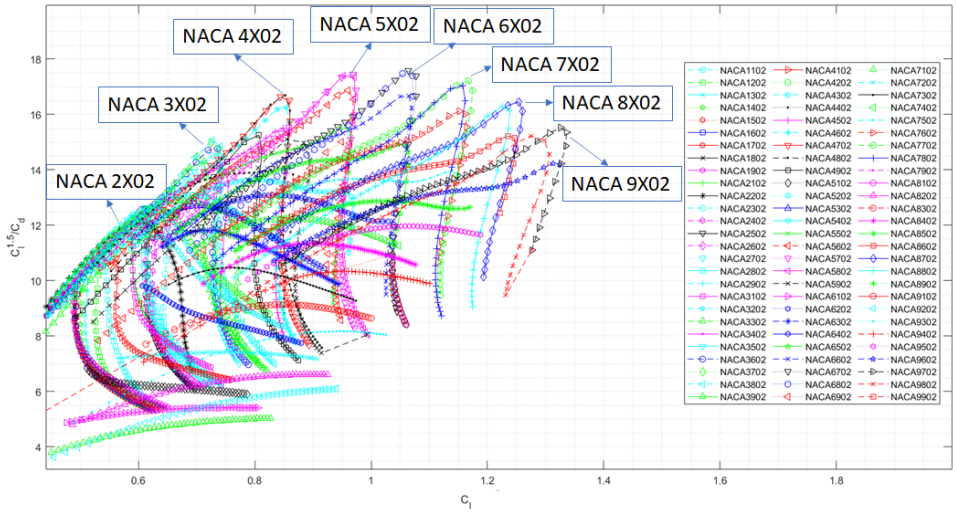

Fig. 3.44 Maximum range efficiency vs. lift coefficient for NACA 4-digit series airfoils at Reynolds number of 10,000 using XFOIL with N=14.

Table 3.16 Genetic algorithm settings.

Setting	Value
Number of Variables	8
Population	300
Mutation	Adaptive Feasible
Cross-Over Rate	0.8
Pareto set Fraction	0.35
Generations	100

coefficient angle of attack due to the inability of XFOIL to predict separated unsteady flows. Therefore, increasing the angle of attack beyond the maximum efficiency will drop the efficiency at a constant lift, so these angles of attack would not be part of the Pareto front.

Figure 3.45 shows the resultant Pareto front obtained in our Multi-objective optimization. Over 100 non-dominant airfoils form the front. Figure 3.46 shows some of these airfoils. As we saw for the NACA series, the optimal camber increases as we increase the target lift coefficient. An unexpected result can be appreciated for the lower lift coefficients. We can see how airfoils present a relatively thick and rounded geometry near the leading edge. This goes against the traditional design guidelines of ultra-low Reynolds numbers airfoils, typically thin with small radii of curvature at the leading edge. We believe that the genetic algorithm promotes these geometries to avoid leading-edge separation and, hence, the non-convergence of XFOIL. We can calculate the aerodynamic and maximum range efficiencies from this Pareto front, shown in Figure 3.47. We selected the most performing airfoil from each efficiency metric. These geometries are shown in Figure 3.48. It is clear that they share genes regarding the leading edge shape and thickness but with different maximum cambers. Figure 3.49 shows how for lower lift coefficient values, the lower cambered geometry is more efficient using both metrics; however, the higher camber extends the efficiency window to higher lift coefficients. These trends are comparable to those observed for the NACA family.

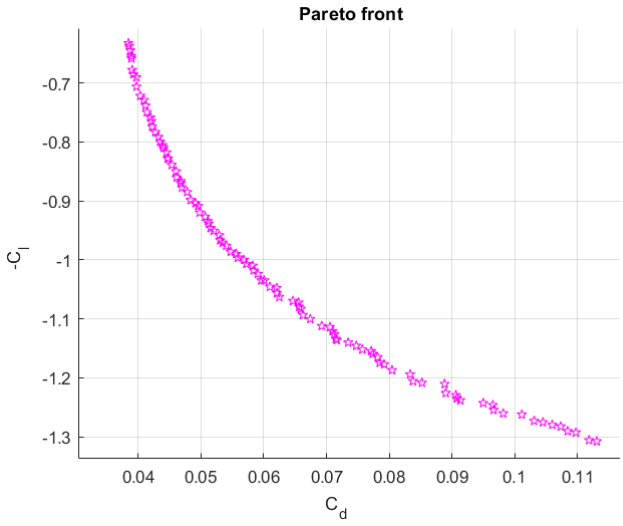

Fig. 3.45 Pareto front using the CST parametrization with XFOIL as a solver at Reynolds number 10,000 and Mach number 0.5.

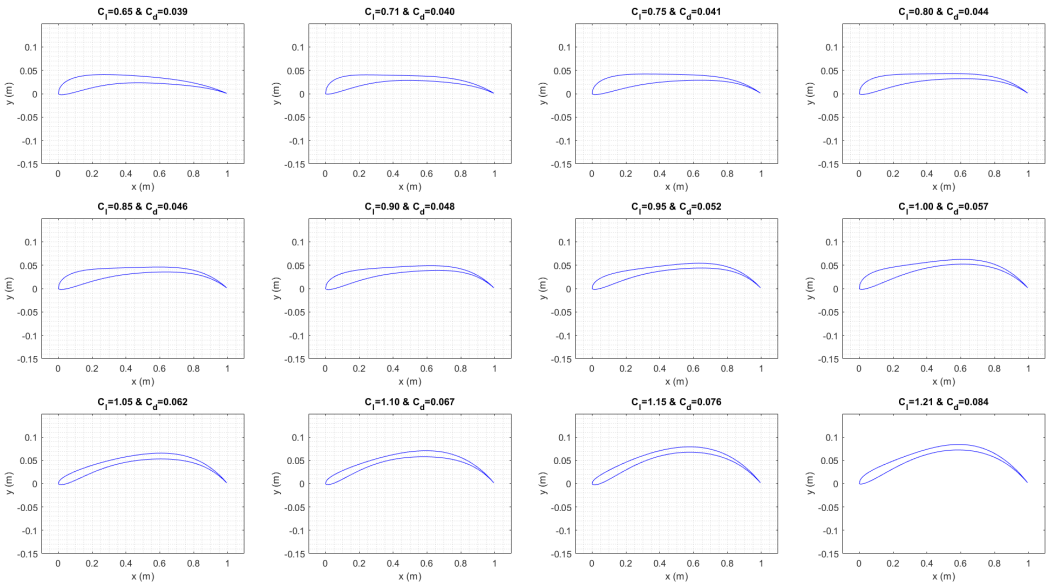

Fig. 3.46 Pareto optimal airfoil geometries for different lift coefficients.

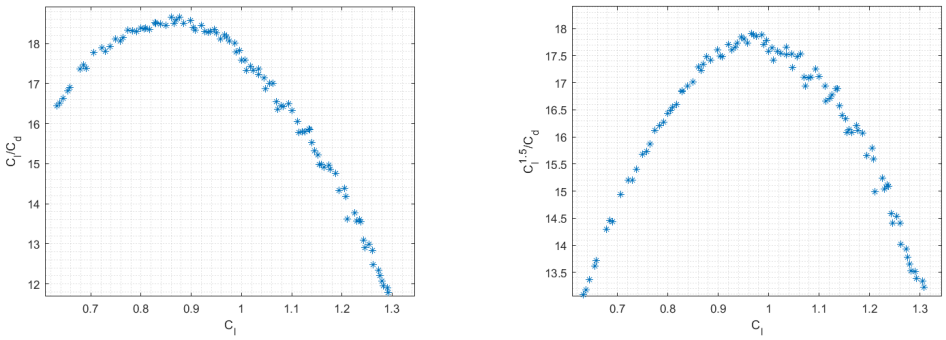

(a) Aerodynamic Efficiency. (b) Maximum Range Efficiency.

Fig. 3.47 Evaluation of Pareto Optimal airfoil maximum efficiencies.

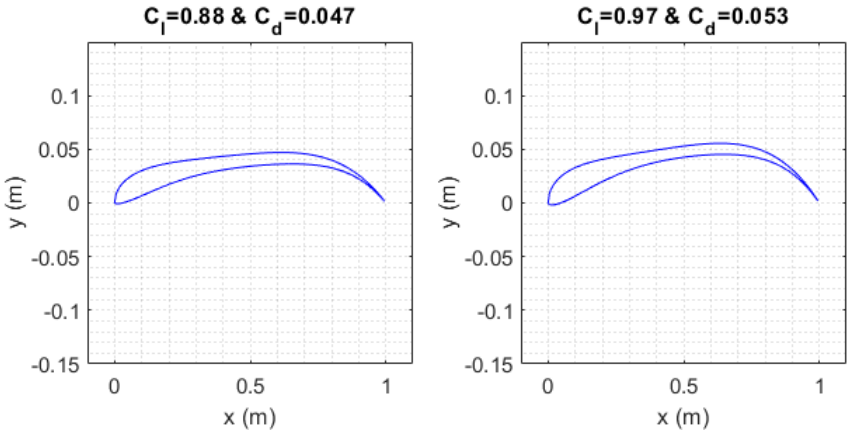

Fig. 3.48 Efficiency vs. lift coefficient for Pareto optimal airfoils and most performing NACA 4-digit series airfoils at Reynolds number of 10,000 using XFOIL with N=14.

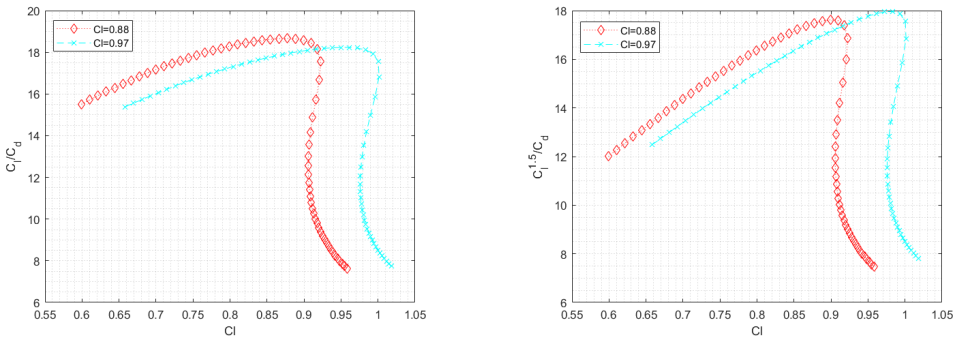

(a) Aerodynamic Efficiency. (b) Maximum Range Efficiency.

Fig. 3.49 Efficiency vs. lift coefficient for two selected Pareto optimal airfoils series airfoils at Reynolds number of 10,000 using XFOIL with N=14.

Table 3.17 Aerodynamic characteristics of the optimized airfoil for M=0.5, Re=3000, AOA=6°.

Adjoint Iteration	C_l	C_d	**L/D**
1(Flat plate)	0.49	0.083	5.9
50(PoliTO-1)	0.977	0.095	10.3

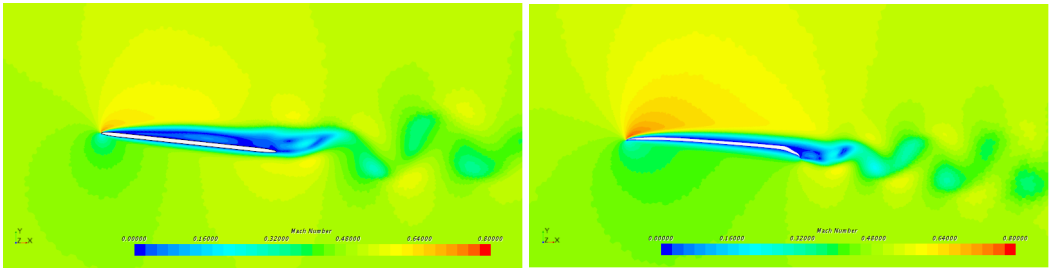

(a) Initial airfoil (Flat plate). (b) Final optimized airfoil (PoliTO-1)

Fig. 3.50 Instantaneous Mach number, AOA=6º, Re=3000 and M=0.5.

3.2.6.3 Adjoint-based CFD Optimization

PoliTO-1

We performed an initial optimization exercise using the adjoint solver in STAR-CCM+, described in Chapter 2. Using a flat plate with a thickness of 2% and rounded edges as the initial geometry, we obtained an airfoil that optimizes aerodynamic efficiency, defined as the ratio of lift to drag, for Re=3,000 and Mach=0.5.

The optimized airfoil has a flat suction side and concentrates the camber at the leading and trailing edges. The maximum camber is about 5.2%, very close to the trailing edge, and it shares some similarities with the NACA-6904 proposed in [233], shown in Figure 3.51. The average thickness is around 1.5%. We show the aerodynamic characteristics of the airfoil and a comparison with those of the initial flat plate in Table 3.17. The dramatic increase in efficiency can be justified by an attached flow at the PoliTO-1 suction side, compared with the flat plate, which presents leading-edge separation, as shown in Figure 3.50.

The airfoil is optimized for M=0.5 and Re=3000 but not necessarily for the rest of the polar. However, comparing its performance with those declared by other authors for an airfoil optimized for similar conditions [24], the result is promising, as shown

in Figure 3.53. The adjoint optimized airfoil is best for Reynolds numbers close to 3000, while for Re = 10000, its performance starts to degrade. The computing time was under 8 hours on an 8-core AMD RYZEN 7.

PoliTO-2

Our previous geometry, PoliTO-1, performs well at low Reynolds numbers and high angles of attack. That is because it results from an optimization process at an initial angle of attack of 6 degrees and a Reynolds number of 3,000. To improve performance at small and intermediate angles of attack and higher Reynolds conditions, we performed an adjoint optimization starting with the PoliTO-1 geometry rotated to 4 degrees and setting the Reynolds number at 10,000. The resultant geometry, PoliTO-2, is shown in Figure 3.51, compared with other efficient airfoils presented in the literature for ultra-low Reynolds number conditions. All the airfoils concentrate the maximum camber near the trailing edge, a very different characteristic from conventional airfoils. PoliTO-2 presents a more even curvature distribution than PoliTO-1 on the suction side. The point of maximum curvature is not so close to the trailing edge but around 60% of the chord. The maximum airfoil camber is 4.7%, and the mean thickness is 1.3%. These values relate well with the 5% cambered plate with a relative thickness of 1% presented by Koning [107] as a more performing geometry with respect to the clf5605 airfoil. Figure 3.51 shows how our airfoil is flatter compared to the cambered plate, possibly due to the maximum efficiency single-point optimization that attempts to avoid separation at the optimal angle of attack. Figure 3.51 also includes one of the sharp leading edge versions of the airfoils proposed by Koning [108], which has been selected as one of the airfoils for the Mars Science Helicopter (MSH) [101].

Figure 3.52 compares the instantaneous velocity fields for PoliTO-1 and PoliTO-2 airfoils. PoliTO-2 presents a slightly stronger expansion at the leading edge. Also, the strength of the vortex shedding is stronger for PoliTO-1 caused by the more aggressive flap geometry despite having a slightly smaller lift. The aerodynamic efficiency is increased by around 15% for the present condition.

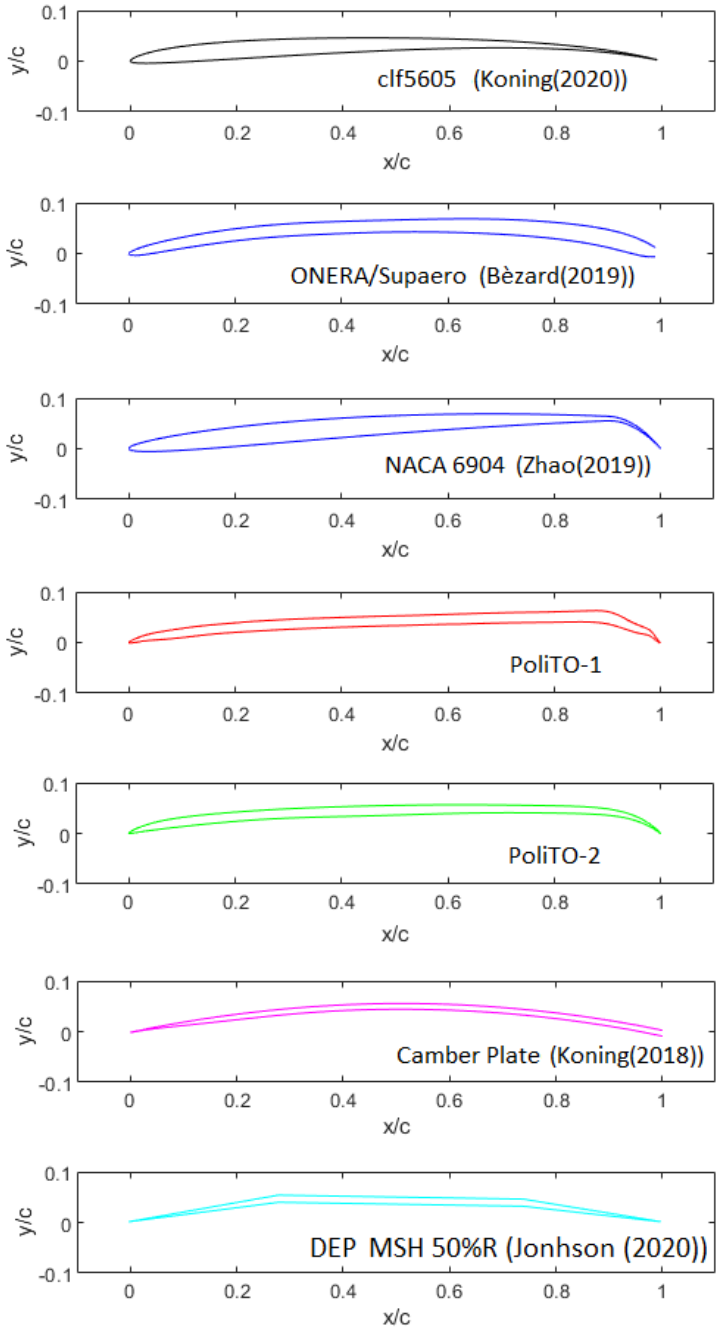

Fig. 3.51 Shapes of airfoils reported in the literature compared with the two PoliTO airfoils.

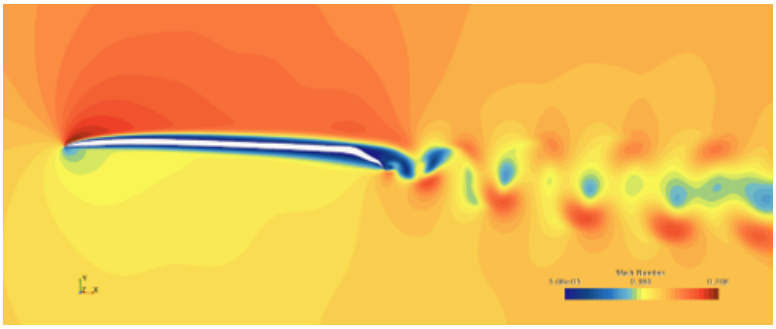

(a) PoliTO-1.

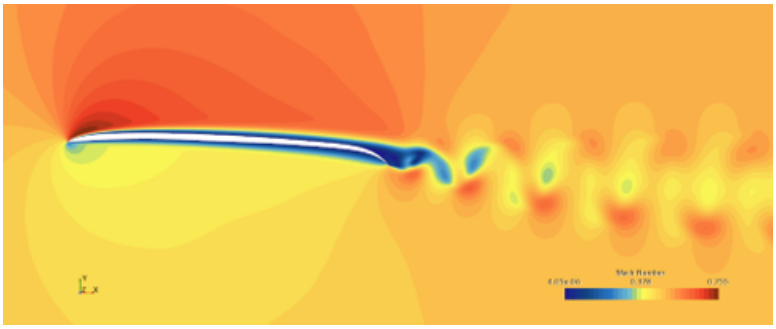

(b) PoliTO-2

Fig. 3.52 Instantaneous Mach number, AOA=4º, Re=10,000 and M=0.5.

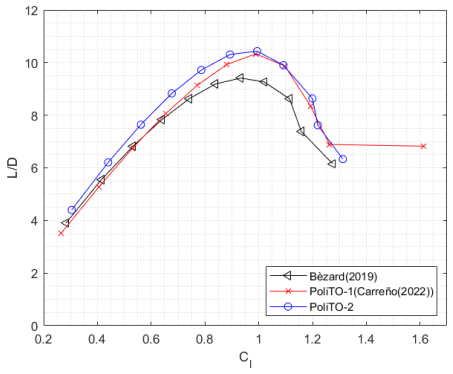

(a) Re=3000

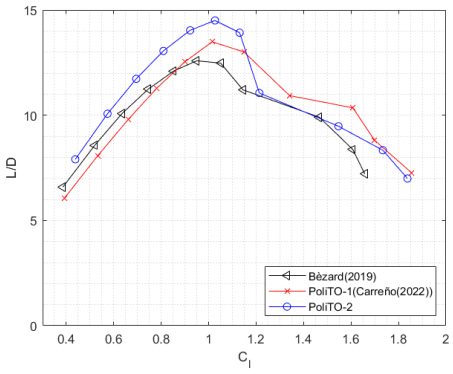

(b) Re=6000

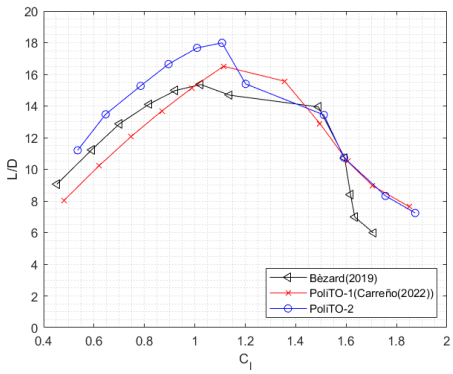

(c) Re=10000

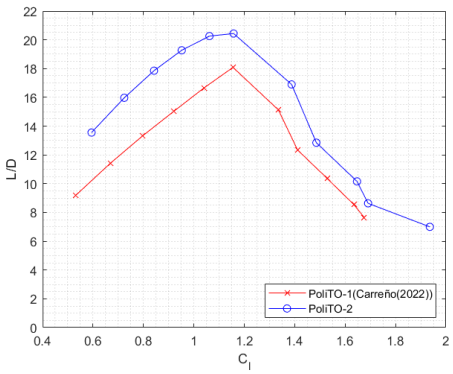

(d) Re=14000

Fig. 3.53 Comparison of aerodynamic efficiency at different Reynolds numbers: PoliTO-1 [46] vs Bézard (2019) [24] vs PoliTO-2. Data from [46] has been interpolated to the current Reynolds number.

Figure 3.53 shows the aerodynamic efficiency of the PoliTO-2 airfoil compared with PoliTO-1 and the airfoil proposed by Bézard [24]. The efficiency of the new airfoil seems to provide a better performance until a lift coefficient of 1.2 for all tested Reynolds number conditions. Since the local lift coefficients in efficient rotors rarely go above 1.2, the PoliTO-2 airfoil should enhance the rotor performance compared to PoliTO-1. However, we must mention that the differences are subtle and could be due to potential discrepancies of our numerical approach compared to Bézard's [24]. It is also worth noting that Bézard's [24] optimization arises from a single objective function combining Cl/Cd and $Cl^{1.5}/Cd$ for four angles of attack around the optimum and three Reynolds numbers: 2000, 6000 and 10,000. The adoption of the $Cl^{1.5}/Cd$ term is possibly the reason for the higher efficiency at large values of the lift coefficient. Also, lower Reynolds numbers typically have larger optimal cambers [111]. PoliTO-2 airfoil will be used for the rotor optimization presented in Chapter 5.

3.2.7 CFD Simulation of Optimal Airfoils

Figure 3.54 presents the efficiencies for different airfoils computed using unsteady compressible Navier-Stokes simulations at Reynolds 10,000 and a Mach number 0.5. In particular, we compare 3 of the most efficient airfoils from the NACA family, three Pareto optimal airfoils obtained at different lift coefficients, and the airfoil PoliTO-2 optimized using an adjoint-based optimization. We can appreciate how the behavior before leading edge separation is congruent with that obtained with XFOIL increasing the efficiency of the airfoils with smaller camber at low angles of attack. The separated regime can be identified by the sudden increase in the lift coefficient between two consecutive angles of attack caused by the low-pressure cores of the vortices being shed above the suction side of the airfoil. The peak efficiency in the NACA airfoils is smaller compared to the rest. Interestingly, all Pareto airfoils present peak efficiencies around 18. However, we must distinguish between the first two airfoils and the one obtained for the highest lift coefficient airfoil ($C_l = 1.056$). The peak efficiency is obtained for the attached flow regime in the first two airfoils, whereas the peak efficiency for the third airfoil occurs after leading-edge separation. In both NACA and Pareto optimal airfoils, we can appreciate that higher cambers have better efficiency after leading-edge separation. The high and delayed maximum camber position allows the large-scale vortices

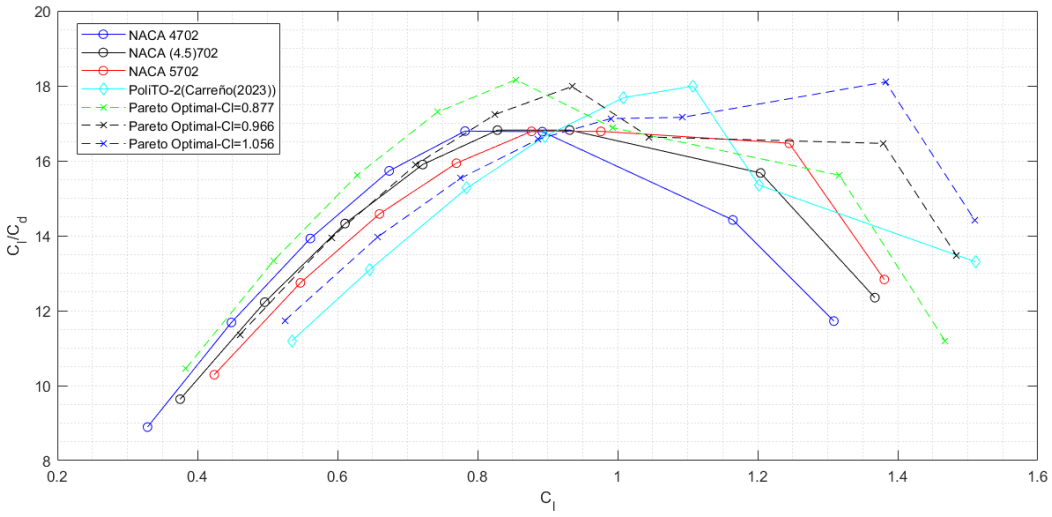

Fig. 3.54 Efficiency vs. lift coefficient for Pareto optimal airfoils and most performing NACA 4-digit series airfoils at Reynolds number of 10,000 using Navier-Stokes simulations.

emitted from the leading edge to remain closer to the airfoil surface, enhancing the lift without a large drag penalization. We can also see how the peak efficiencies are comparable to PoliTO-2, obtained with the adjoint approach. This evidences that the XFOIL approach can generate efficient geometries for attached flow conditions. However, XFOIL cannot provide valuable information for the separated regime. Regarding the performance of the airfoil PoliTO-2, we can see how the optimal value is obtained at a higher lift coefficient. The adjoint solution can adapt the surface of the airfoil to ensure an attached flow with maximum efficiency. Adjoint optimization is gradient-based and, therefore, dependent on the initial condition as it converges towards local optima. In this case, the adjoint solver was used to explore how efficient Martian airfoils would be, but they are typically used for refining an already good-performing geometry defining the region of the design space where your local optimum is found and using the adjoint methodology to exploit it. This approach is followed in the three-dimensional adjoint optimization shown in Chapter 5 to refine a baseline sub-optimal design. In any case, the maximum efficiency exceeds the other optimal efficiencies in its range of lift coefficients, showing how the adjoint approach can find optimal airfoil solutions for attached flow conditions at a contained computational cost. Due to the steady nature of the adjoint approach employed in this work, the analysis could not be extended to the optimal design of unsteady configurations, including leading-edge separation.

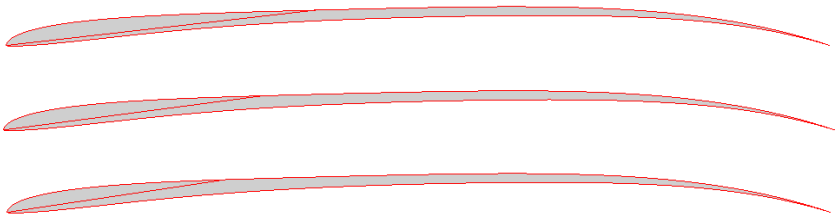

Fig. 3.55 Sharp leading edge geometry. 6.5^o (top), 7.5^o (middle) and 8.5^o (bottom).

3.2.8 Sharp Leading Edge Airfoils

Recently, the ROAMX project researchers decided to use sharp double-edged plate airfoils in the blades of the Mars Science Helicopter. They show how these geometries outperform conventional airfoil shapes, increasing the peak lift-to-drag ratio between 17% and 41% [108]. We want to clarify that in this section, by conventional, we refer to continuous parametrizations without sharp edges that are typically optimal for attached flow conditions. They associate the enhanced performance of these airfoils with large-scale vortex shedding caused by the forced leading edge separation. This effect has been well studied in literature [24, 23]. However, for several airfoils studied in literature [24, 45], this high lift regime due to the low-pressure vortex cores present in the suction side of the airfoil is not necessarily associated with an increase in the lift-to-drag ratio.

We believe the real reason for the enhanced performance of sharp leading-edge airfoils is associated with the mean laminar separation bubble characteristics. The sharp leading edge triggers a laminar separation bubble, which can be steady or unsteady depending on Reynolds number and angle of attack. This separation bubble creates an effective curvature equivalent to a conventional airfoil but with reduced skin friction and, thus, a higher lift-to-drag ratio. The behavior of the flow over a rotor composed of these sharp geometries is yet unknown. The spanwise pressure gradient and three-dimensional effects could cause differences compared with this two-dimensional analysis. In any case, a better understanding of the behavior of these sharp geometries is necessary to exploit their potential.

This section studies the sharp leading-edge versions of the maximum lift-to-drag ratio airfoil obtained using multiobjective optimization combined with XFOIL.

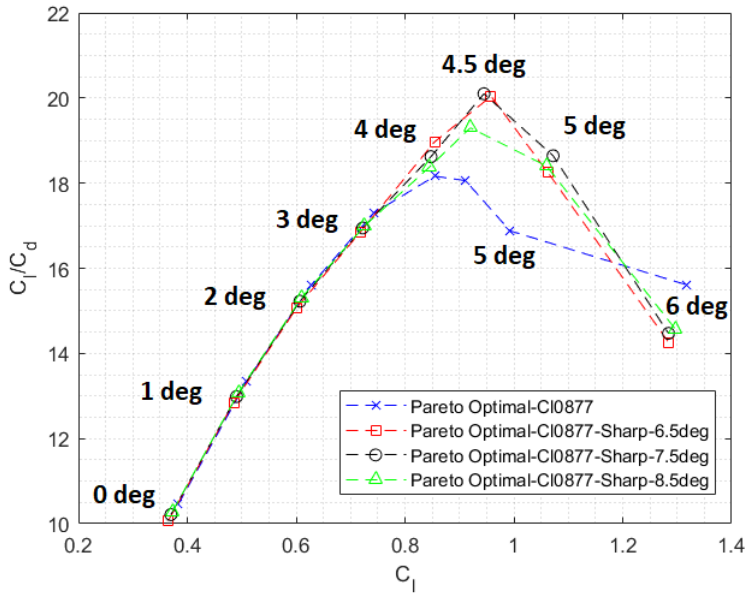

Fig. 3.56 Efficiency vs. lift coefficient for Pareto optimal airfoils with and without sharp leading edges.

The modified geometry is obtained by slicing the airfoil with planes at different inclinations with the horizontal as shown in Figure 3.55. These airfoils combine sharp leading edges and conventional airfoil characteristics. The rationale behind this approach is that XFOIL generates high-performing attached flow geometries. Therefore, if we can maintain the external flow, the pressure distribution will be conserved with reduced skin friction. The flat region in the suction side acts as a cavity for the separation bubble to settle. It is important to mention that these geometries with a sharp leading edge are difficult to manufacture. However, even if the sharp leading edges were substituted with a small radius of curvature, the separation would still be fixed at the leading edge, creating comparable separation bubbles.

Figure 3.56 shows how, for low angles of attack, the efficiency against lift coefficient for sharp airfoils collapses with the rounded leading edge geometry. This collapse shows how, even with these thick boundary layers, the maximum camber, which remains constant, still dominates the airfoil efficiency, despite differences in the local camber distributions, which affect the velocity field. This behavior is corroborated by sharp leading-edge versions of the Pareto Optimal geometry selected for maximum range efficiency shown in Figure 3.57. We can appreciate how the

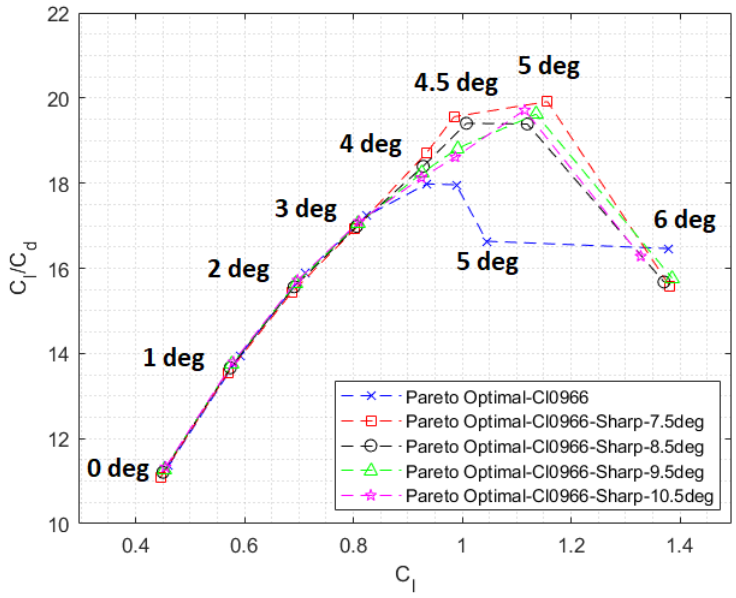

Fig. 3.57 Efficiency vs. lift coefficient for Pareto optimal airfoils with and without sharp leading edges.

lift coefficient is reduced for a given angle of attack as we decrease the slicing plane angle. However, the aerodynamic efficiency is insensitive to this parameter. It is very interesting from a design point of view as airfoils can be optimized using computationally efficient approaches such as XFOIL or steady CFD that work well for attached flow conditions and then enhance the airfoils' characteristics converting it into a sharp leading-edge version. When we increase the angle of attack to 4 degrees, we can see how the lift coefficient is virtually the same for all the airfoils. However, the efficiency increases with the inverse of the slicing angle. This trend is caused because the bubble now occupies virtually the whole cavity creating a local shear thrust that reduces the overall drag coefficient for the same lift coefficient. The longer the flat section, the higher the reduction in friction drag. This effect is exacerbated for larger angles of attack where the mean separation bubble grows beyond the apex caused by the slicing. Figures 3.58, 3.59 and 3.60 show the velocity fields averaged for 20 turnovers for different angles of attack, where we can appreciate the evolution of the separation bubbles for the different airfoils.

The instantaneous flow shows how a vortex is emitted from the apex and travels close to the airfoil's surface, creating a high-lift regime caused by the low-pressure vortex core that remains close to the airfoil's suction side as shown in Figure 3.61.

The increase in efficiency is associated with the overall reduction of the skin friction caused by a separation bubble on the suction side, as shown in Figure 3.60 that compensates the increase in pressure drag associated with the larger effective camber created by the separation bubble.

For slicing plane angles around 6.5 and 7.5 degrees, an optimal separation bubble can be found that trades off the effective camber for the external flow while maintaining low levels of skin friction. Drela [74], and Selig [183] studied the concept of optimal separation bubbles for airfoils at low Reynolds numbers concluding that usually, optimal separation bubbles are flat and short to avoid an excessive increase in pressure drag with the benefit of reduced skin friction. However, they studied bubbles typically formed by the transition to turbulence in the separated shear layer, increasing momentum near the wall. They usually have a 'dead zone' with almost zero friction coefficient as shown by [84, 206] using Implicit Large Eddy Simulations (ILES) for Reynolds numbers around 60,000. Our bubbles are caused by geometrical separation at the leading edge and present laminar reattachment. In these cases, the skin friction is negative and strong in magnitude, as seen in Figure 3.62. We can see how this skin friction distribution will result in a negative viscous drag for the suction side. Due to the ultra-low Reynolds numbers, the weight of viscous drag in total drag increases, and thus, the positive effect of having a separation bubble on the airfoil's suction side. We can also appreciate how the pressure distribution shown in Figure 3.63 shows high suction values due to the low-pressure vortex cores.

The peak efficiency we found for both cases is around 20, higher than our airfoils designed for attached flow conditions, which presented a peak value of 18. Our sharp airfoils efficiency is slightly higher than the value of around 18 reported by Koning [108] for his double-edged plate, at Reynolds 10,117 and Mach 0.5, using unsteady Navier-Stokes simulations with the solver OVERFLOW. Bézard [24] shows how their airfoil has a peak aerodynamic efficiency of around 15.5 for the same Mach and Reynolds number conditions, also using unsteady Navier-Stokes simulations with the solver `elsa`. This comparison must be made carefully as these geometries are highly sensitive to the numerical model. Nevertheless, the results show that these airfoils, obtained at a very low computational cost, can generate state-of-the-art performances.

(a) Pareto Optimal Geometry $C_l = 0.877$.

(b) Pareto Optimal Geometry $C_l = 0.877$. Sliced with plane at 6.5º

(c) Pareto Optimal Geometry $C_l = 0.877$. Sliced with plane at 7.5º

(d) Pareto Optimal Geometry $C_l = 0.877$. Sliced with plane at 8.5º

Fig. 3.58 Mean velocity field around sharp and round versions of maximum efficiency airfoil, AOA=3°.

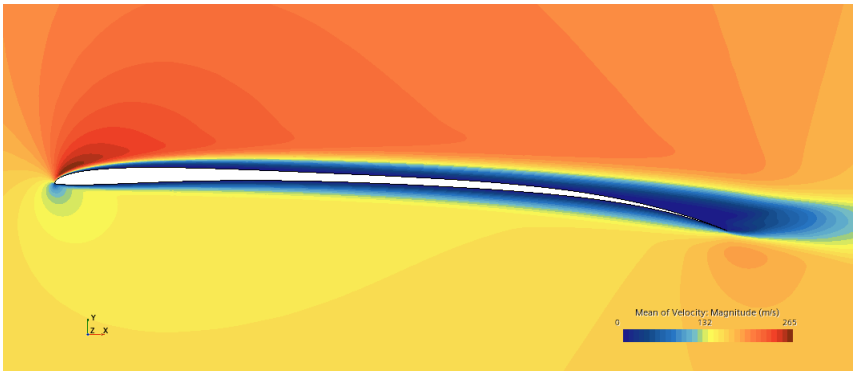

(a) Pareto Optimal Geometry $C_l = 0.877$.

(b) Pareto Optimal Geometry $C_l = 0.877$. Sliced with plane at 6.5º

(c) Pareto Optimal Geometry $C_l = 0.877$. Sliced with plane at 7.5º

(d) Pareto Optimal Geometry $C_l = 0.877$. Sliced with plane at 8.5º

Fig. 3.59 Mean velocity field around sharp and round versions of maximum efficiency airfoil, AOA=4°.

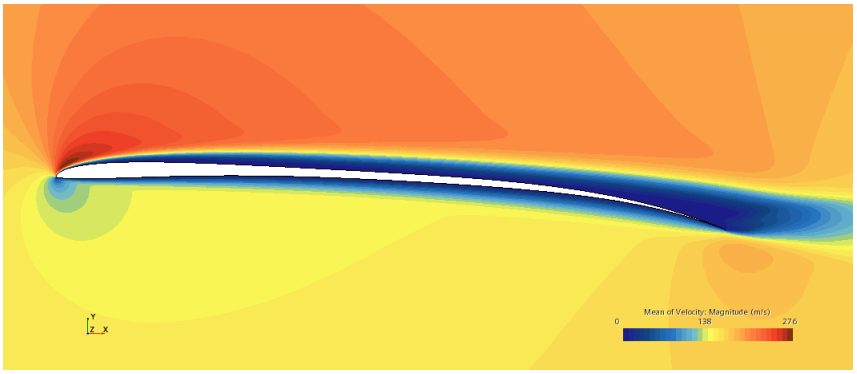

(a) Pareto Optimal Geometry $C_l = 0.877$.

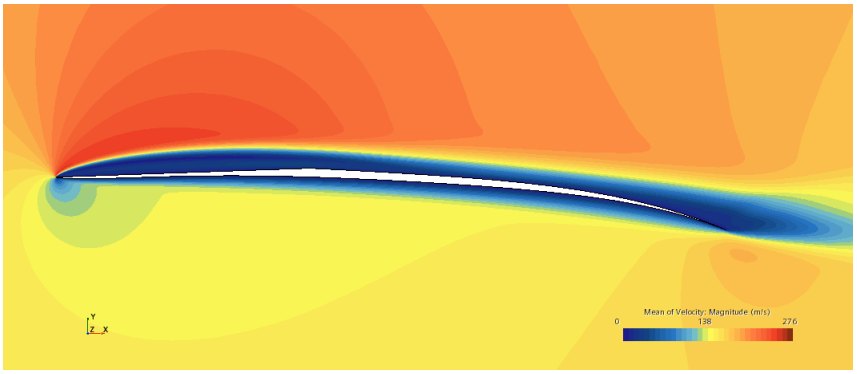

(b) Pareto Optimal Geometry $C_l = 0.877$. Sliced with plane at 6.5º

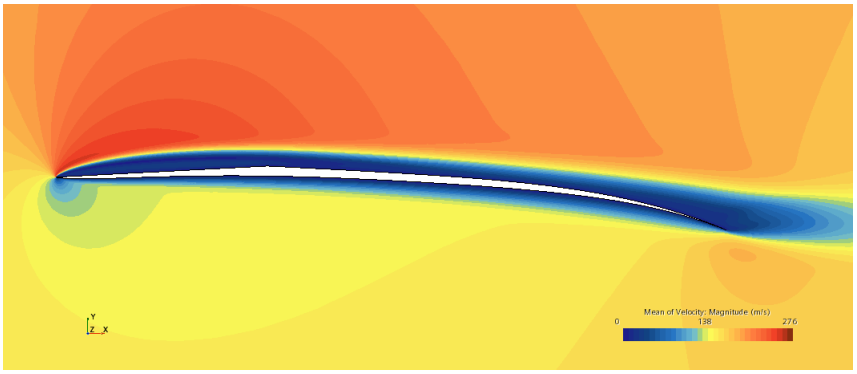

(c) Pareto Optimal Geometry $C_l = 0.877$. Sliced with plane at 7.5º

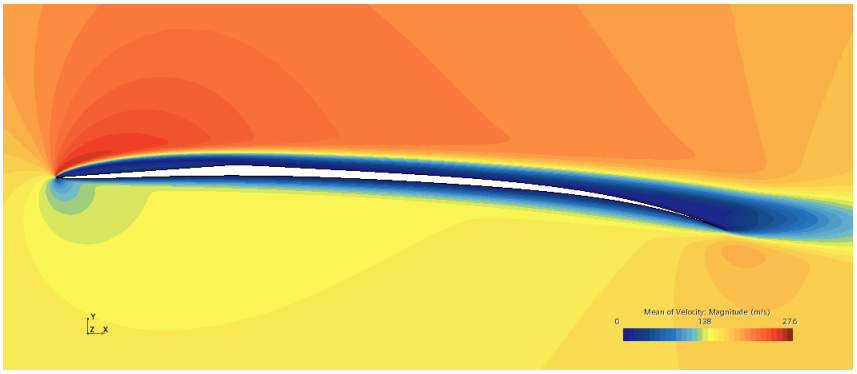

(d) Pareto Optimal Geometry $C_l = 0.877$. Sliced with plane at 8.5º

Fig. 3.60 Mean velocity field around sharp and round versions of maximum efficiency airfoil, AOA=4.5°.

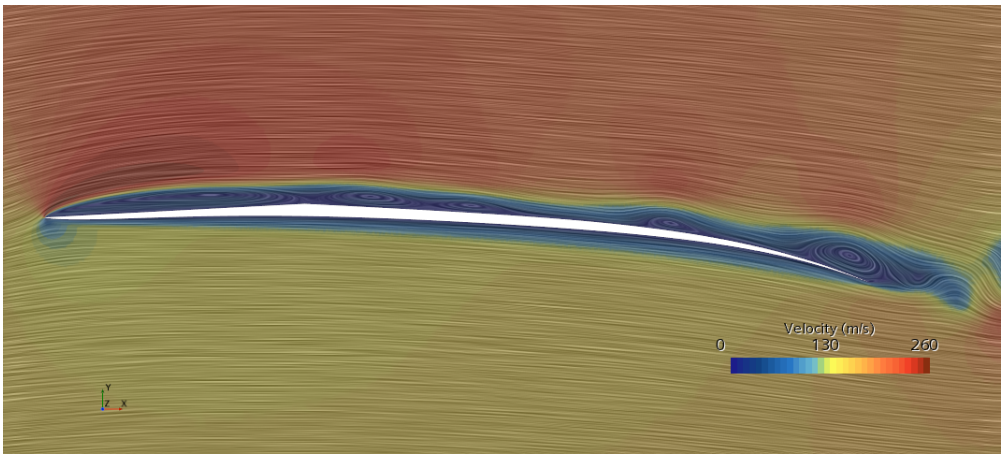

Fig. 3.61 Instantaneous velocity field around the sharp versions of the $C_l = 0.877$ airfoil, with a slicing plane of 7.5 degrees. AOA=4.5°.

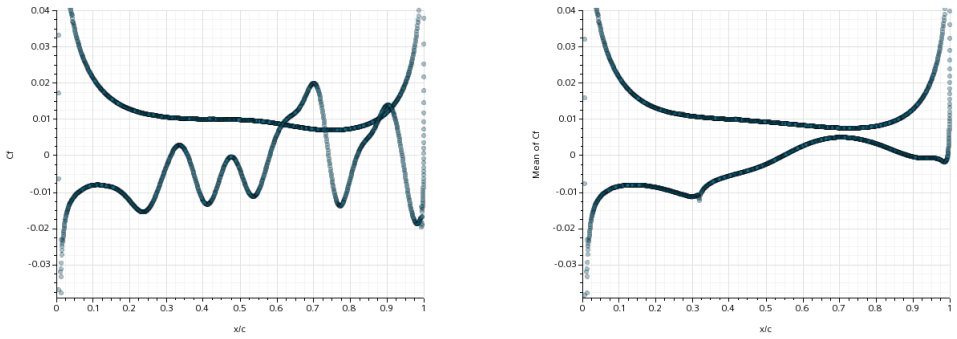

(a) Instantaneous Friction Coefficient. (b) Time-Averaged Friction Coefficient

Fig. 3.62 Friction Coefficient for Pareto Optimal Airfoil at $C_l = 0.877$. Sliced with a plane at 7.5º, AOA=4.5°.

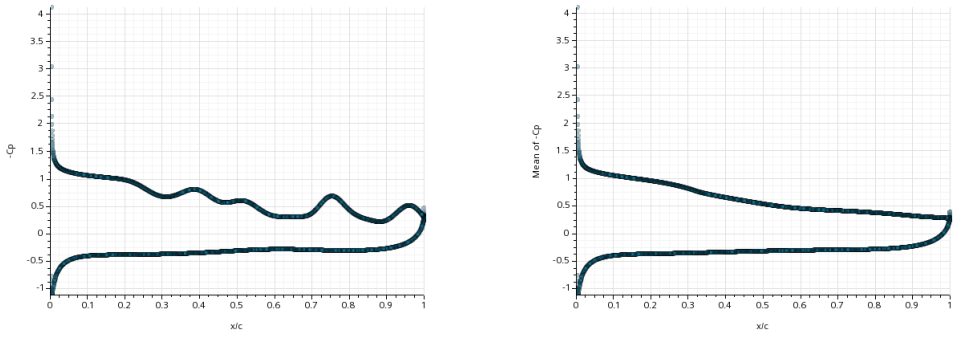

(a) Instantaneous Pressure Coefficient. (b) Time-Averaged Pressure Coefficient

Fig. 3.63 Pressure Coefficient for Pareto Optimal Airfoil at $C_l = 0.877$. Sliced with a plane at 7.5º, AOA=4.5°.

3.2.8.1 3D Simulations: LES and Navier-Stokes

The sharp leading-edge geometry obtained in the previous section for a Cl of 0.877 and sliced with a plane at 7.5 degrees at an angle of attack of 4.5 degrees was simulated using a quasi-2D domain extruded normal two the airfoil for 0.2 chords to identify eventual three-dimensional structures or transition to turbulence. The Navier-Stokes solution was performed using the hybrid MUSCL/third-order central difference scheme used for 2D simulations, also setting the upwind blending factor at 0.15. This was run for around 90 turnovers using the same time-step as in 2D simulations. Then, it was run for an additional 10 turnovers in which we resolved each convective turnover with 500 time steps, increasing by a factor of 5, the temporal resolution shown for the 2D airfoils in case smaller structures were to develop. A congruent behavior compared to that obtained with the 2D simulations was obtained. The leading edge bubble was slightly smaller. The slightly closer boundary conditions probably cause this by reducing the effective angle of attack. In any case, the interesting outcome of this study was that no three-dimensional instabilities were captured, and the flow remained 2D. A Q-criterion visualization is shown in Figure 3.64, showing a large-scale vortex shedding over the suction side of the airfoil, maintaining a two-dimensional structure.

Dimensioning a grid for LES in this regime is not trivial due to the lack of a realistic turbulence scale. Therefore, we will use a grid coherent to that shown to capture separation-induced transition at Reynolds 60,000. The cell size was slightly increased to maintain the cell count below 20,000,000 cells, as the SD7003 airfoil span was only 0.1 chords. The sub-grid stress model selected was the dynamic Smagorinsky proposed by Germano [88] using Lilly's modification [121]. The simulation used the aforementioned laminar solution as an initial condition and used the same computational grid. After five turnovers, the flow remained two-dimensional over the suction side, and the subgrid-scale turbulent kinetic energy production was minimal. Also, force and drag coefficient mean values and characteristic frequencies did not vary with respect to the solutions obtained with the Navier-Stokes model.

The fact that the flow remains laminar despite the intense vortex-shedding regime supports the use of Navier-Stokes simulations for this regime. However, care must be taken when extending this assumption to rotors, which present an important radial pressure gradient that may affect the transition to turbulence.

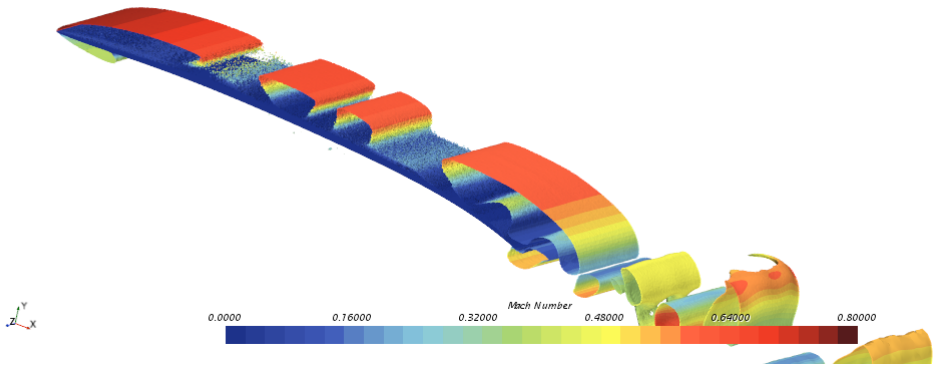

Fig. 3.64 Q-Criterion=500 isosurface around the $C_l = 0.877$ airfoil, with a slicing plane of 7.5 degrees. AOA=4.5°.

3.2.9 Discussion

This section presents a numerical investigation into airfoil optimality at ultra-low Reynolds numbers. Under the assumption of laminar flow, we perform different analyses using XFOIL and compressible Navier-Stokes simulations. We prove that XFOIL and CFD predictions are comparable when the flow is attached, but XFOIL predicts the airfoil stall when the flow separates. CFD simulations, on the other hand, predict a high lift regime associated with low-pressure vortex cores emitted from the leading edge traveling downstream near the suction side of the airfoil.

A preliminary exploration of the space of design was performed using the NACA XX02 family. We show how, for attached flow conditions, the optimal camber to maximize aerodynamic efficiency is between 3% and 5%. On the other hand, considering the maximum range efficiency, slightly larger cambers are required, between 4% and 6%. The optimal value for maximum camber position is found to have an equal performance for positions between 70%-80%.

An adjoint-based optimization is presented. Initially, we perform an optimization starting from a flat plate at Reynolds 3000 to prove this approach's ability to create efficient geometries. However, typically adjoint-based approaches are used to refine an adequate baseline solution as it is a gradient-based approach subject to getting trapped at local optima. Therefore, a second airfoil is presented using the previous airfoil as an initial condition and increasing the Reynolds number to 10,000. This airfoil has a high maximum aerodynamic efficiency obtained at a relatively high lift coefficient. The aerodynamic efficiency of around 18 is comparable with other

airfoils presented in literature at this Reynolds number. A limitation of this approach is the application of geometrical restrictions and the inability to test airfoils presenting leading-edge separations due to the steady nature of the adjoint algorithm employed. This approach is reasonably cheap, considering that simulations are two-dimensional and the employed adjoint step is small. So, the initial condition is already an excellent approximation of the final solution at each adjoint iteration.

An alternative approach employing a multiobjective optimization using XFOIL and a CST airfoil parametrization is also presented. The airfoil that optimizes aerodynamic efficiency has a camber of 4% and the airfoil that optimizes the maximum range efficiency of 5%. Beyond these two airfoils, the multiobjective optimization provides us with a family of optimal airfoils for different lift coefficients. This is a critical aspect as we show how, for rotor applications, using a constant fitness function to optimize airfoils at other radial coordinates is insufficient to obtain globally optimal designs.

Performing time-accurate Navier-Stokes simulations of the previously discussed airfoils, we show how the adjoint-based geometry and those optimized using XFOIL present maximum aerodynamic efficiencies of around 18 for different lift coefficients. This number seems to be a limit for an airfoil presenting an attached boundary layer at this combination of Reynolds and Mach numbers.

Regarding the airfoil performances after leading-edge separation, we show how airfoils with smaller camber present deteriorated performance because the large-scale vortices emitted from the leading edge travel further away from the airfoil surface compared to those with higher camber. We observed how one of the high-cambered Pareto optimal airfoils presented a peak just before the flow separated and a more prominent efficiency peak when the flow presented leading-edge separation. Studying the fluid flow around this airfoil, we noticed that large-scale vortices emitted from the leading edge remained close to the airfoil surface, and the mean flow showed a closed separation bubble. The increase in the pressure drag was compensated by an even more significant drop in shear drag as the flow was separated for a large portion of the suction side.

Following the finding of separated geometries with high efficiencies, we proposed geometries derived from those calculated with XFOIL, modified to have a sharp leading edge to force separation and a cavity for the separation bubble to settle, enhancing the reduction in shear drag. We show how sharp geometries derived from

the previously optimized airfoils improve the peak performance by around 10%, achieving aerodynamic efficiency values of about 20. This improvement is obtained for a narrow window of angles of attack of about 2 degrees. However, we show that the proposed slicing methodology does not affect the aerodynamic efficiency for lower angles of attack. Therefore, for a given lift coefficient, sharp geometries perform at least as well as rounded leading-edge geometries, except for large angles of attack. The improved efficiency is associated with the presence of mean separation bubbles on the suction side of the airfoils, creating a slightly larger camber while drastically reducing the shear drag. Optimal separation bubbles are more extensive than those found at higher Reynolds numbers due to the greater importance of the shear drag on the total drag.

The proposed passive flow control solution is really interesting. We could design airfoils for attached flow with the previously discussed computationally affordable methodologies and then force the presence of laminar separation bubbles to obtain state-of-the-art performances. The only alternative in the literature addressing this problem performs a multiobjective optimization using URANS or time-accurate Navier-Stokes solutions, and this approach is computationally very demanding. Depending on the genetic algorithm settings, this approach could be between 3-4 orders of magnitude more expensive than ours. Furthermore, these approaches only guarantee good peak performances without guaranteeing high performance for lower angles of attack.

Finally, we present 3D simulations of one of the sharp leading-edge optimal geometries. Initially, we performed a Navier-Stokes simulation of the blade, showing a fully 2D unsteady behavior congruent with the vortex shedding regime found in the two-dimensional simulations. Even though the 2D behavior could prove the laminarity of the flow, we performed an LES to ensure this fact. The subgrid stress model remained dormant in the simulation, providing further evidence that these airfoils remain laminar despite the strong vortex shedding regime until their angles of maximum efficiency at Reynolds number 10,000 and Mach number 0.5. This finding must be extended with care to other geometries or flow conditions. Nevertheless, it increases the confidence and reliability of the performance predictions found by our 2D models.

Chapter 4

Experimental Validation of Hovering Rotor Performance prediction

This chapter includes the partial content of the paper:

- M. Carreño Ruiz, M. Scanavino, D. D'Ambrosio, G. Guglieri, and A. Vilardi. Experimental and numerical analysis of hovering multicopter performance in low-Reynolds number conditions. *Aerospace Science and Technology*, 128:107777, 2022

4.1 Introduction

The main objective of the following study is to develop numerical models to precisely describe the flow around rotors, providing performance predictions at different computational costs. We will rely on experimental campaign data obtained at different operating conditions to validate these models. Section 4.2 will briefly describe the experimental activity in a climate-controlled laboratory performed by Scanavino [179]. The measured data include thrust, torque, and power coefficients for different Reynolds numbers considering unconventional atmospheric conditions, i.e., low temperature and high altitude, which generate very low rotor Reynolds numbers and allow the study of the performance deterioration shown in [13]. Section 4.3 describes the CFD model and its results, including comparisons with experimental

data. The rotor in this validation activity is the T-Motor 15x5 rotor, typical of conventional multicopters, such as the SUI endurance. Section 4.4 discusses the application of the ROMs described in Chapter 2 to this particular rotor. Section 4.5 presents a Machine Learning (ML) model trained with experimental data to predict rotor performance. In section, 4.6, we focus on extending the validation of the CFD model with experimental data collected on a complete small UAS, the Q4L (MAVTech S.r.l), by Scanavino [177].

4.2 Experimental Data

The experimental campaign was performed in the climatic chamber terraXcube, managed by EURAC Research [81, 34, 146]. Scanavino [177] performed aerodynamics experiments on rotary-wing vehicles in the Large Cube chamber, where it is possible to simulate the most extreme environmental conditions on the Earth's surface. He measured the aerodynamic performance of small-scale UAS on both an isolated rotor and the complete vehicle, considering combinations of temperature and altitude to explore their effects on thrust and power coefficients.

4.2.1 Test matrix

The test matrix's three independent variables are throttle, temperature, and altitude (via pressure). According to the dimensional analysis, the Mach and Reynolds numbers are the only independent variables that can affect the thrust and torque coefficients of the hovering rotor. In any case, the tip Mach number's small variation range and proximity to the incompressible limit reduces its expected influence relative to the Reynolds number. Using the Mach number at the tip, one could apply the Prandtl-Glauert correction [89] to determine the impact of compressibility effects on thrust and torque coefficients. The range of Mach numbers shown in table 4.1 yields maximum differences of 3%. However, the estimated value would be conservative given the radial thrust and torque distributions for this rotor shown in Section 4.4 and considering a linear dependence of Mach number with the radial coordinate. Integrating the radial distributions adjusted with Prandtl-Glauert's correction yields a more precise estimation. With this method, the maximum Mach number differences between the largest and smallest Mach numbers shown in table 4.1 are around 1.5%.

As a result, the Mach number effect is roughly an order of magnitude smaller than the Reynolds number effect, which is in charge of variations in the thrust coefficient of more than 10% in the ranges under consideration. The experimental matrix consists of five temperature levels ranging from 40°C to -40°C in 20°C intervals, four throttle levels (50, 66, 86, and 100%), and six altitude conditions (from sea level to 6000 m in intervals of 1500 m with a final test at 9000 m). This test matrix yields 120 cases with Reynolds numbers ranging from 24,099 to 186,670. As shown in table 4.1, we selected three representative conditions to compare and validate numerical simulations in hovering.

Table 4.1 Experimental conditions selected for comparison with numerical simulations.

Reynolds number	**Pressure(Pa)**	**Temperature(ºC)**	**RPM**	**Tip Mach number**
24,099	30,900	40.05	3293	0.19
61,539	58,000	19.91	3979	0.23
186,670	98,450	-40.85	4683	0.31

4.2.2 Experimental setup for small scale UAS testing

The test bench consists of a welded steel construction with a sand-filled hollow tube in the center to dampen mechanical vibrations. The upper-end cap is detachable to gather data on force and torque and can house a six-axes load cell. Precision shunt resistors measure electrical currents, and optical tachometers measure motor speeds. The experimental setup used to test a quadrotor vehicle is shown in Figure 4.1, along with a plot of the combined thrust coefficient of the four rotors against the Reynolds number and Mach number. With Reynolds numbers up to about 120,000, we can see a linear increase in the thrust coefficient. It is then possible to appreciate an asymptotic behavior. However, there is no discernible trend for this range of Mach numbers. The following section shows how this setup is rearranged to perform measurements on an isolated rotor.

4.2.3 Experimental tests on an isolated rotor

The thrust coefficient C_T versus the Reynolds number is displayed in the experimental results of rotor performance tests conducted following the methodology described

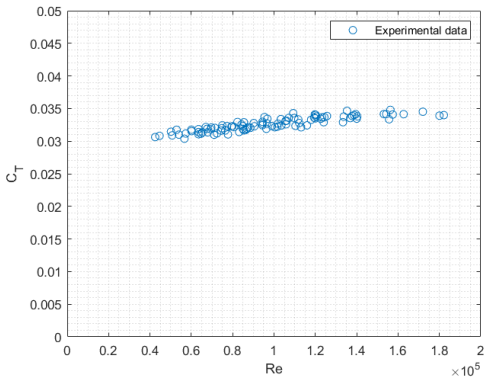

(a) Thrust coefficient vs Reynolds number (quad-rotor tests)

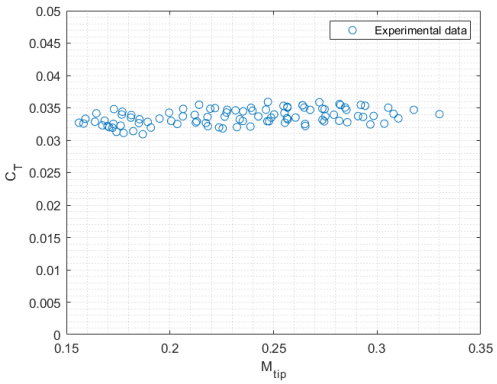

(b) Thrust coefficient vs Mach number (quad-rotor tests)

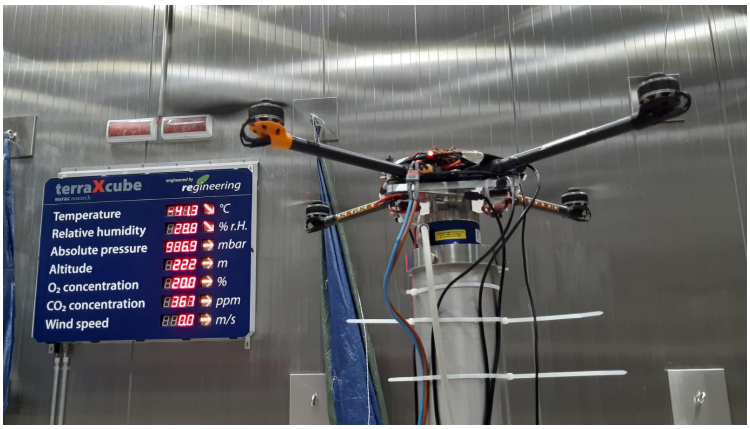

(c) Quad-rotor testing in terraXcube

Fig. 4.1 Experimental testing in terraXcube laboratory

in [178, 177]. Our analyses focus on a T-Motor 15'x5' carbon fiber rotor. The experimental results shown in Figure 4.2 reveal a linear relationship between C_T and the Reynolds number, with the thrust coefficient degrading as the Reynolds number decreases. At the highest Reynolds number values, it appears that C_T is getting close to asymptotic behavior. The thrust coefficient deterioration might arise due to delayed transition, causing important separated regions without reattachment of the boundary layer and the formation of separation bubbles. Another factor that must be considered is that even for attached flows, for very low Reynolds numbers, the relative importance of the torque due to drag starts to be non-negligible. This causes an increased torque that further deteriorates the performance of the rotor. Previous research [13] has noted a critical Reynolds number of 120,000, below which the effects of laminar separation become significant and highly susceptible to operating

conditions that might affect transition. Rotor performance exhibits an asymptotic behavior above these limits. This observation is consistent with the outcomes of our experiments, as seen in Figure 4.2d, where the figure of merit exhibits an almost linear increase with rising Reynolds numbers up to Re=120,000, at which point an asymptotic evolution begins. The trends of the non-dimensional coefficients that describe the performance of rotors are consistent with the CFD results we obtained using a transition model. In section 4.3, there will be a thorough explanation of the CFD model used to generate these results and a quantitative comparison of the numerical and experimental results. The asymptotic value of thrust and torque also appears to agree with the experimental data provided by Russel et al. [170]. However, there is a minor overestimation of the rotor loads for the lowest Reynolds numbers. Regardless of these differences, the performance deterioration is again in satisfactory agreement, observing the figure of merit. The observed discrepancies could be caused by slight differences in the experimental approach and the remarkably high sensitivity of laminar separation bubbles to free stream conditions as shown in [133], which report significant differences comparing results obtained in different facilities. For hovering tests, the size of the laboratory could also create different recirculation patterns influencing the performance.

4.3 CFD simulations: Tmotor 15"x5"

4.3.1 Blade geometry

Obtaining an accurate simulation geometry is challenging, especially for thin and small-scale blades. There are several ways to approach blade geometry generation. The first would be to use a commercial rotor and attempt to reproduce the geometry. This may be done using a 3D scanning technique (laser or optical) or image-based software to approximate the geometry as shown in [40] using PropellerScanner by Martin Hepperle. The second approach is accurate for the chord distribution but lacks the required resolution for the twist distributions with errors of the order of 1 degree [71] and, therefore, must be used only to perform preliminary calculations. The other methodology would be manufacturing a geometry using a CAD model. However, it is not trivial to accurately manufacture a complex blade geometry. For example, most 3D printing approaches do not provide the required accuracy, the rigidity is

(a) Isolated T-Motor 15x5 rotor test in terraXcube

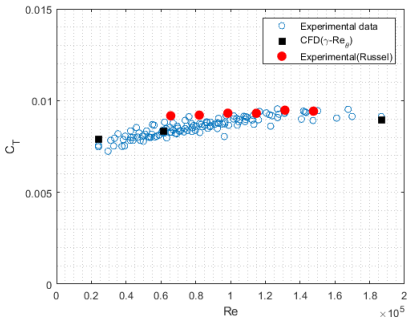

(b) Experimental and numerical $C_T\,(Re)$ data.

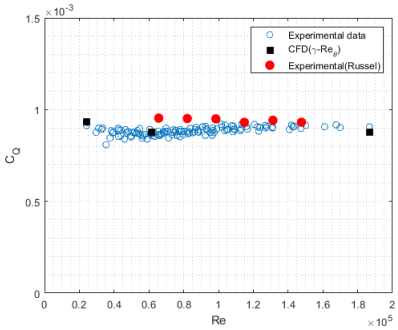

(c) Experimental and numerical $C_Q\,(Re)$ data.

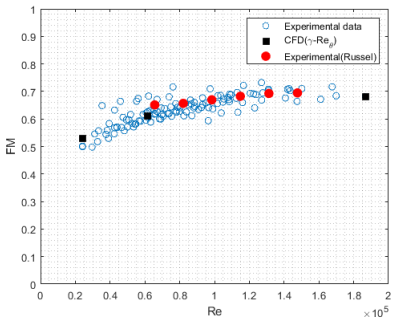

(d) Experimental and numerical figure of merit.

Fig. 4.2 Experimental measurements (terraXcube and [170]) and numerical results for an isolated rotor.

insufficient, or the surface finishing is inadequate. A safe but expensive solution is to use a CNC technique performed. Casalino et. al. [53] used this approach to manufacture the TU Delft Aeroacoustic benchmark blade.

The T-motor 15x5 CF two-bladed rotor used in the experimental campaign was scanned using an optical precision measuring machine (OPMM) to create a precise three-dimensional model for CFD simulations. The blade's outer surface is defined by a cloud of points produced by the 3D scan. To replicate an accurate geometry, we cut the point cloud with planes normal to the radial direction with a step of 1 cm. Using the points defining the leading edge, we created a guiding curve by interpolating the intersection points with a smooth spline. This procedure enables the creation of smooth manifold surfaces adequate for CFD simulations. Figure 4.3 compares images of the original rotor (left) with the top and front views of the reconstructed geometries (right).

Fig. 4.3 Comparison of top and front views of the original (left) and digitally reconstructed (right) blade.

4.3.2 Reynolds Averaged Navier-Stokes

4.3.2.1 Model description and assumptions

There are different ways to simulate the rotational motion of a rotor, and these can be divided into two big groups, static and dynamic approaches. Static approaches model rotation by solving the RANS equations in a rotating reference frame. This methodology is usually called the Moving Reference Frame technique (MRF). This method includes a source term into the RANS equations to model centripetal and Coriolis accelerations. The dynamic grid approaches move the grid every time step to fix the no-slip boundary condition on the rotor. Different grid motion techniques exist, and the sliding grid approach and the overset Chimera method are two of the most popular. In this work, we use the sliding grid technique, which uses an Arbitrary Mesh Interface (AMI) protocol to map the faces of an inner domain sliding inside an outer static domain.

Several researchers have validated the MRF approach [155, 220, 160, 125, 21], presenting a good overlapping between results obtained with the sliding grid methodology. The MRF approach is well suited to steady-state solution methods, which usually reduce the computational cost significantly compared to time-accurate analyses. Unfortunately, the approach is only accurate when the flow on the side surface of the cylinder defining the rotating region is nearly tangent to it [40], and one must, therefore, be cautious in defining and meshing these areas. In the case of hovering simulations, the inflow pattern does not correspond with the characteristic stream tube expected in the case of propellers, and defining boundary conditions is challenging to enable a fast and robust convergence. Two approaches are typically used to

override this problem and allow the convergence of steady solution algorithms. The most common is to use a small axial velocity in combination with a large domain. The alternative to this approach is to use sink-source boundary conditions [195]. In this work, we use the former approach.

The dynamic approach is more versatile compared to the MRF methodology. When transient effects are essential, and symmetry conditions are inapplicable, the dynamic approach is the way to go. It is also helpful when the rotating domain cannot be large enough to reduce the artificial fluxes at the interface or boundaries in the MRF method or when the influence of non-axisymmetric boundary conditions needs to be considered.

This transition model has been previously used to capture transition in rotating flows, namely in a wind turbine [112] and in a marine propeller [220]. The γ-Re_θ model is highly empirical and depends upon three correlations that have been published in slightly different forms by various authors [114, 124]. This section uses the correlations provided in [114] thoroughly assessed in Chapter 3.

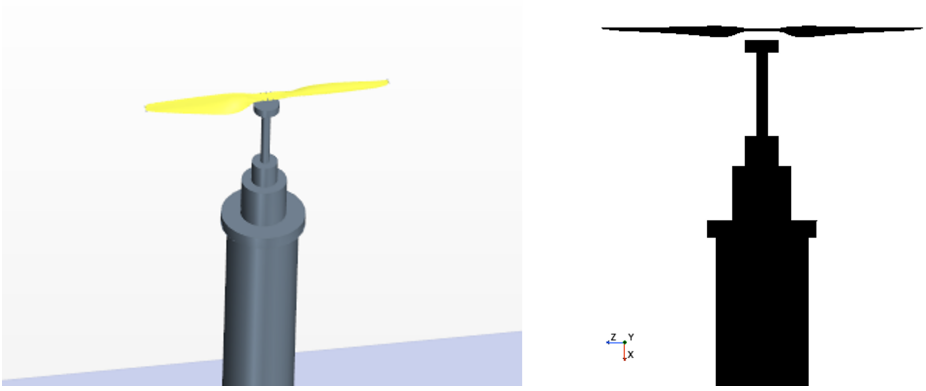

Fig. 4.4 Numerical setup. Perspective view (Left) and parallel scaled view (Right)

The simulated geometry reproduces in a simplified yet representative manner, the experimental setup in an attempt to account for a possible blocking effect of the pole, which has a diameter comparable to that of the rotor, as shown in Figure 4.4. Previous work by Andrea Manavella during his MSc Thesis in our department [125] suggests that similarly sized experimental equipment can produce significant increases in thrust and torque of up to 5% and 2%, respectively, due to the blockage effect. Table 4.2 shows how, for the highest Reynolds number, we found just an additional 1.5%

Table 4.2 Numerical results on the effect of support on the rotor thrust and torque coefficients (MRF approach and Adaptive Mesh Refinement).

	Isolated Rotor		**Experimental fixture**	
Reynolds number	**T [N]**	**Q [Nm]**	**T [N]**	**Q [Nm]**
186,670	12.85	0.243	13.04	0.244

and 0.5% in the thrust and torque values, respectively. The limited increase in thrust and torque is due to an extra rod present in our simulations (Figs. 4.1c and 4.2a) that was not present in the simulations reported in [125].

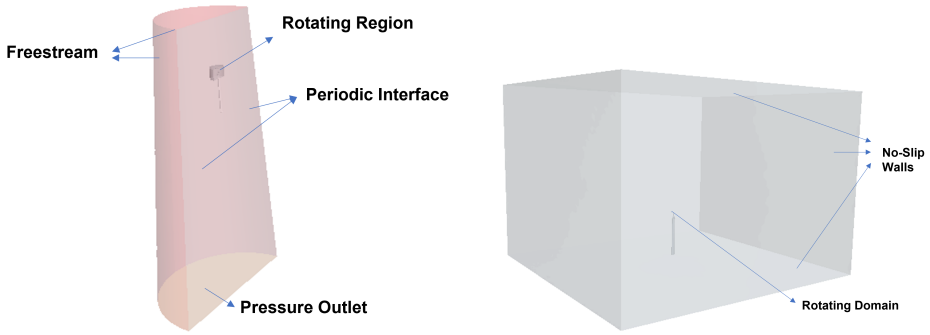

(a) Static approach (b) Dynamic approach

Fig. 4.5 Boundary conditions

As shown in Figure 4.5, the definition of the boundary conditions varies between static and dynamic approaches. The dynamic approach uses the actual dimensions of the experimental facility using no-slip wall boundary conditions as a domain. In the MRF approach, we defined a truncated cone geometry as a domain with free stream conditions characterized by a minimal axial velocity (0.1 m/s) to speed up convergence and a pressure outlet. The rotor is located 2 meters (>5 diameters) above the ground, and so we may consider it out of ground effect [177]. This fact renders both approaches comparable.

4.3.2.2 Turbulence and transition modeling

During this validation activity, we utilized SST $k-\omega$ turbulence. This model is possibly the most popular for external aerodynamics and has been proven effective in propeller simulations by several authors [155, 221, 40]. Furthermore, it allows

the coupling with the γ-Re$_\theta$ transition model, which is essential to capture potential laminar separation bubbles as shown in Chapter 3 and reference [39]. Including a transition model is necessary as differences in the boundary layer states create different wall shear stresses and friction torque coefficients. These differences' impact on torque estimations is more critical with decreasing Reynolds numbers. Furthermore, the creation of separation bubbles affects the blade's effective camber and may impact both thrust and torque estimations. We applied a laminar flow model for the lowest Reynolds numbers, as the pressure side will be laminar, and the inboard sections will too. Turbulence, if occurring, will be confined to the suction side outer radial stations. There is also no guarantee that transition models will work adequately in these regimes. Perez Perez [158] presents the same approach to calculate an aerodynamic database to be used in a reduced-order model. Table 4.3 shows how the thrust prediction is enhanced when the transition model is used. The following section describes how including the transition model allows for two transition mechanisms: natural transition and separation-induced transition. In this way, the near-blade flow field is qualitatively more accurate than using a standard turbulence model for these very low Reynolds numbers. It is interesting to note that the torque is unaffected by the transition modeling in this case. However, this is due to increased pressure and decreased shear torque, producing an exact cancellation.

Table 4.3 Experimental vs numerical results. MRF approach, Adaptive Mesh Refinement, SST $k-\omega$ turbulence model with and without transition model

	CFD simulation		**CFD vs. Experimental data**	
Turbulence model	**T [N]**	**Q [Nm]**	ΔT **(%)**	ΔQ **(%)**
$k-\omega$	12.74	0.244	-5.00	-3.71
$k-\omega+\gamma$-Re$_\theta$	13.04	0.244	-2.76	-3.71

4.3.2.3 Grid independence study

Accurately resolving tip vortices, at least until they first interact with the blade, is crucial, especially in hovering cases where the vortices are very close to the rotor, and the velocity they induce on the rotor is relevant [97]. Vortex cores require a much smaller cell size than the rest of the flow field. A standard refinement strategy involving the entire computational domain, or even the wake region only, increases

the number of cells prohibitively before achieving grid convergence. Here, we adopted various mesh refinement strategies starting from a baseline grid (Figure 4.6) and increasing the number of cells where we expect strong gradients, as in tip

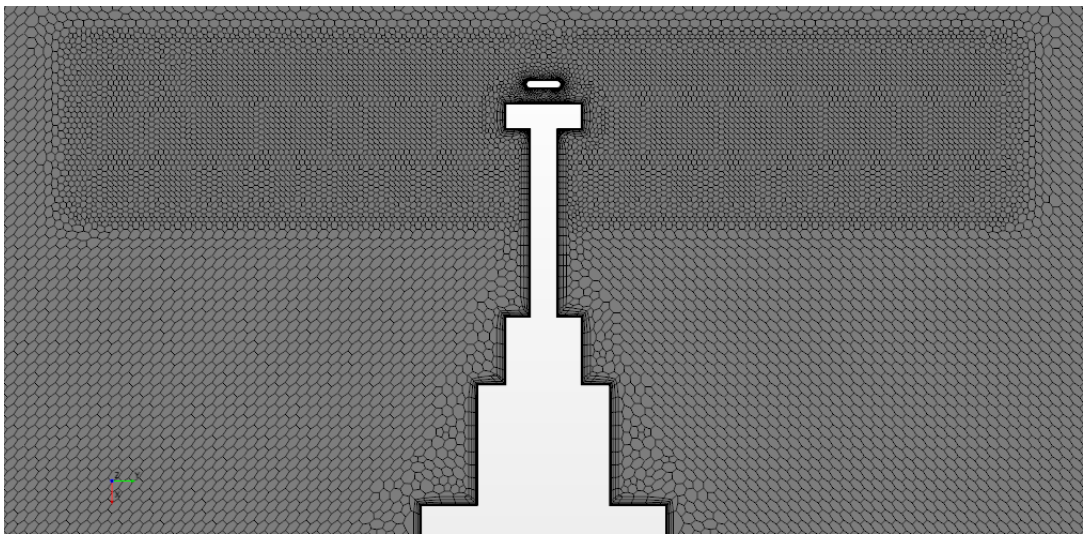

Fig. 4.6 Baseline Grid.

vortices and the rotors' near wake. Using the MRF approach, we applied an adaptive grid refinement based on the Q-criterion to correctly track and resolve tip vortices, as shown in Figure 4.7. Based on this experience, in the dynamic approach, we

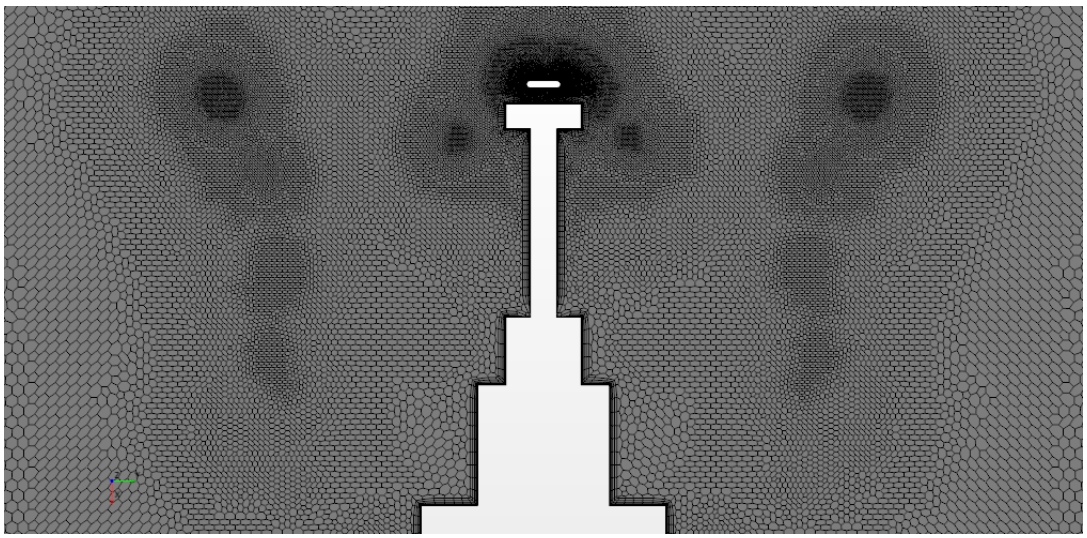

Fig. 4.7 Adaptative Mesh Refinement (AMR) based on the Q-criterion. MRF approach.

axisymmetrically refined those regions where we expect to see tip vortices, as shown

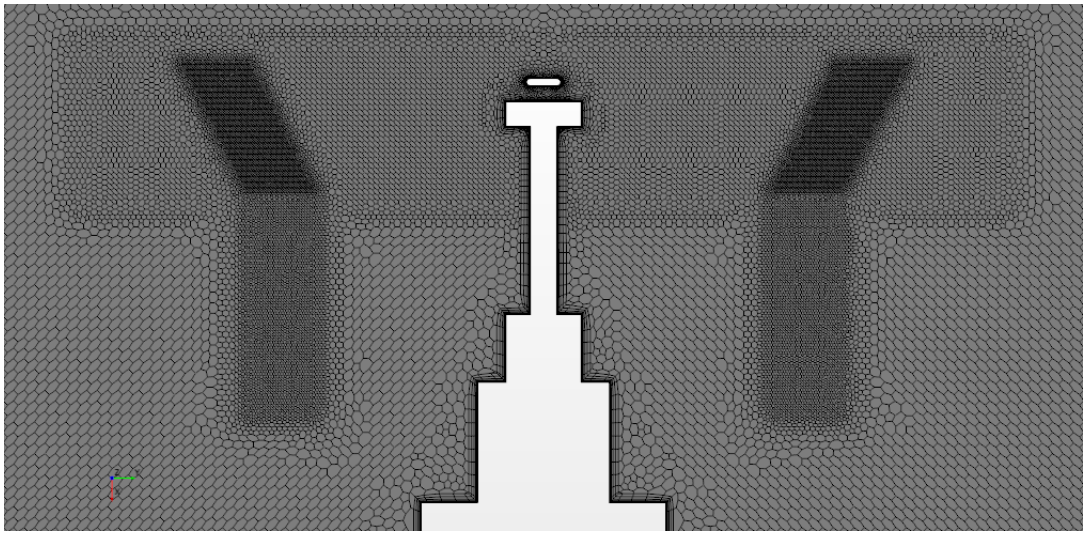

Fig. 4.8 Baseline Grid with tip vortex refinement.

in Figure 4.8. We further refined the grid by reducing the target cell size on the rotor surface, increasing the number of prism layers, and adding a wake refinement near the trailing edge of the blades, as shown in Figure 4.9.

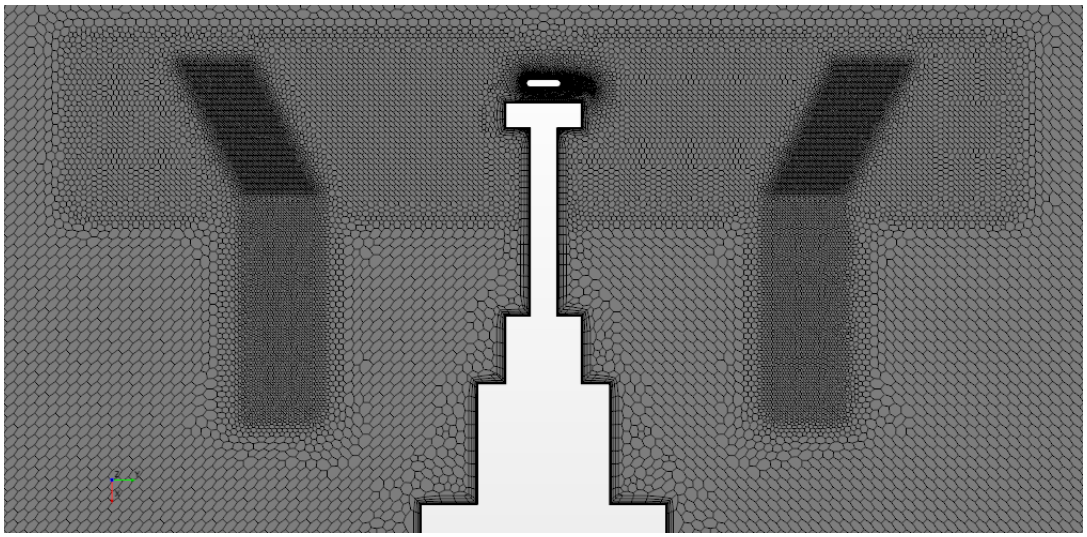

Fig. 4.9 Baseline Grid with tip vortex and near rotor refinement.

Table 5.4 shows the performance predictions of the blade using different grid generation strategies for the highest Reynolds number. The grid size would have easily reached 100 million cells had we used a global refinement strategy instead of targeting the area where tip vortices are present. In these simulations, showing a traditional

grid convergence study based on systematic global mesh refinement/coarsening is impossible due to our limited computing capabilities. However, the intense, localized refinement and the reasonably small distance from the experimental measurements suggest that grid convergence is not far. Previous studies by Bergmann [21] find grid independence for around 40 million cells for propellers with a diameter over 1 meter and Schenk [180] at around 20 million for small-scale propellers. These further support our proximity to grid independence. The results presented in the following section will use the finest grid.

Table 4.4 Grid refinement study using the dynamic approach at Re=186,670

		CFD simulation		**CFD vs. Experimental**	
Grid	**Nº Cells**	**T [N]**	**Q [Nm]**	ΔT (%)	ΔQ (%)
Baseline	8.6×10^6	13.03	0.238	-2.83	-5.29
Tip vortex	14.1×10^6	13.13	0.241	-2.09	-4.89
Tip vortex & Rotor	17.0×10^6	13.16	0.246	-1.86	-2.92

4.3.2.4 Comparison between the MRF and the dynamic approaches

We compared the performance prediction capabilities and computational cost of the static (MRF) and dynamic approaches in the highest Reynolds number case. Both simulations use the baseline grid settings shown in Figure 4.6. The two meshes cannot be identical as the computational domains differ. However, the grid generation strategies in regions close to the rotor are similar and should allow a realistic contrast of the results of the two approaches. Table 4.5 presents performance results predicted by both approaches, using the same turbulence modeling and the baseline grid. We can appreciate how both thrust and torque values are very close. This finding indicates that the unsteadiness in the averaged flow is low; therefore, the steady

Table 4.5 Comparison between static and dynamic approaches using baseline grids

	Static approach		**Dynamic approach**	
Reynolds number	**T [N]**	**Q [Nm]**	**T [N]**	**Q [Nm]**
186,670	13.14	0.238	13.03	0.240

MRF approach can accurately model the rotor's motion. Care must be taken when setting up these simulations, as adding source terms in momentum equations might render the equations stiff, causing convergence issues. In the static procedure, we evaluate just one blade employing a periodic boundary condition; thus, the cell count is split in two. We must point out that the use of periodic boundary condition limits the maximum allowable CFL. Therefore, the reduction in CPU time compared to simulating the whole domain might not scale linearly with the number of cells. In any case, the steady approach reduces the computational cost by around a factor of 6 compared to the unsteady approach and also an important reduction in memory requirements. We used a conservative time step matching to a rotation of 0.5° to provide time accuracy even though different studies use larger values [180] compared to ours. In particular, this reference finds an error of 1.6%, increasing the angular advance per time step from 0.5° to 3°.

Finally, we also compare the results obtained with both methodologies, using the grids that provided the closest predictions to the experimental data. Table 4.6 presents differences below 1% for two operating conditions. This finding is remarkable, considering that the mesh was changed, the solver settings were different, and the rotation modeling approach varied.

The enhanced computational efficiency of the AMR grid combined with a periodic interface is also evident from our results. This approach provides comparable results with a threefold reduction in cell count. The total computational cost of this approach is around ten times cheaper compared to the dynamic approach with the finest grid.

Table 4.6 Static (AMR mesh) vs dynamic (baseline grid with tip vortex and near rotor refinement) approach

	Static approach		**Dynamic approach**	
Reynolds number	**T [N]**	**Q [Nm]**	**T [N]**	**Q [Nm]**
61,539	4.08	0.0830	4.12	0.0828
186,670	13.04	0.244	13.16	0.246

4.3.2.5 Results

We compare our experimental measurements and numerical results using the dynamic approach and the 17 million cell grid for three representative Reynolds number conditions in Table 4.7. We discuss the main flow features in the following subsections.

Table 4.7 Experimental data vs CFD simulations. Dynamic approach, 17 million cells.

	CFD simulation			**CFD/Experimental**	
Reynolds number	**Turb. model**	**T [N]**	**Q [Nm]**	ΔT (%)	ΔQ (%)
24,099	Laminar	1.21	0.0280	-4.27	-4.76
24,099	$k-\omega+\gamma$-Re$_\theta$	1.33	0.0299	5.22	1.70
61,539	$k-\omega+\gamma$-Re$_\theta$	4.12	0.0828	-0.96	0.98
186,670	$k-\omega+\gamma$-Re$_\theta$	13.16	0.246	-1.86	-2.92

Re=24,099

For the lowest Reynolds number, we initially performed a laminar simulation. Figure 4.10 shows a Q-criterion iso-surface that reveals, apart from the expected rotor vortex system formed by pairs of root and tip vortices, vortex shedding towards the tip of the blade. Table 4.7 shows that the laminar solver underestimates thrust and torque values by under 5%. The results look promising, considering the absence of turbulence models. At these Reynolds numbers, the vortex shedding pattern is likely to become turbulent, so we rerun the simulation using the γ-Re$_\theta$ transition model, even though it was not clear if the transition model would work adequately for Reynolds numbers as low as 24,000, as discussed in the previous chapter. The results show that the separated boundary layer undergoes transition, but the production of turbulent kinetic energy is not fast enough to produce boundary layer reattachment before the trailing edge. However, since the transition model calibration arises from two-dimensional boundary layer simulations, the reliability of the transition process predicted after the trailing edge is at least doubtful. Using the γ-Re$_\theta$ transition model, thrust and torque are overpredicted by 5% and 2%, respectively. Even though the difference with the experimental measurement is limited, the validity of this empirical transition model could be compromised for these and especially for lower Reynolds numbers,

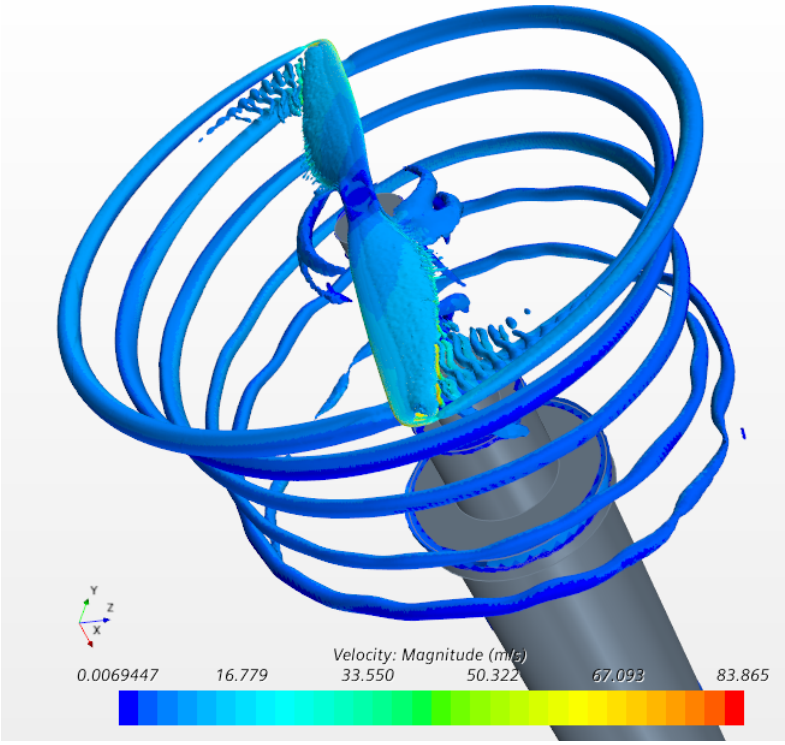

Fig. 4.10 Q-criterion iso-surface coloured with velocity magnitude. Re=24,099.

as this model has been designed, tuned, and tested mainly for flat plate cases at higher Reynolds numbers [112, 114]. The spatial and temporal resolution required to accurately resolve the vortex-shedding and eventual transition to turbulence would require a prohibitive cell count and time step dimension. However, the laminar solver could become an attractive option to compute the performance of blades in the lower range of the very-low-Reynolds number regime ($10^4 - 10^5$), as, in these conditions, the effects of turbulence in the averaged flow are modest and confined to the suction side of the outboard sections of the blade presenting the highest Reynolds numbers. As shown in Chapter 3, at Reynolds numbers 23,000, the performance computed with the laminar solver matches well experimental data below angles of attack of 5 degrees. Reduced order models shown in the following section predict angles of attack below this value for all the blade span, supporting Navier-Stokes evaluations at this Reynolds number falling between the ultra-low and very-low Reynolds number regimes.

Re=61,539

We chose to perform a numerical experiment at this Reynolds number because we expected to find a laminar behavior in the inner region of the blade and transition toward the tip. Transition models such as the γ-Re_θ model are highly empirical, and their calibration relies mainly on 2D boundary layer simulations. Nevertheless, they should identify the main transition mechanisms. Separation usually triggers the transition at these Reynolds numbers, as shown by [206, 83] for the SD7003 airfoil using scale-resolving simulations. If separation-induced transition is captured, they should also detect the separation bubbles formed after the reattachment of the boundary layer due to the increased near-wall momentum of the now turbulent boundary layer. Figures 4.11a and 4.11b show different wall quantities that could help identify the presence of a separation bubble on the suction side of the blade. The separated flow region followed by a rise in intermittency suggests the formation of a separation bubble as corroborated by the streamlines shown in Figure 4.11c, which we computed using the velocity expressed in the rotating reference frame. Apart from the expected recirculation, one can notice a velocity component directed toward the blade tip. That is due to the lack of centripetal forces when the wall shear stress is low, and its effect is producing a spiral motion towards the blade tip in the streamlines trapped inside the separation bubble.

Re=186,670

This value of the Reynolds number is the largest in the experimental matrix. In this case, transition is expected, though it is not necessarily separation-induced but likely also natural, as the local Reynolds number is almost 200,000 in the outer part of the blade. Figure 4.12 shows a separated region with posterior transition, characterized by a rise in the wall intermittency, between 50% and 60% of the blade span. Separation is no longer present for larger radial coordinates, but natural transition still occurs due to the higher Reynolds numbers. It is clear how when transition is separation-induced, the rise in wall intermittency is much more vigorous than when transition occurs through the natural mechanism. Furthermore, towards the tip, possibly due to the large relative thickness of the airfoil's leading edge and the influence of the rolling tip vortices, we can notice a separation again, followed by

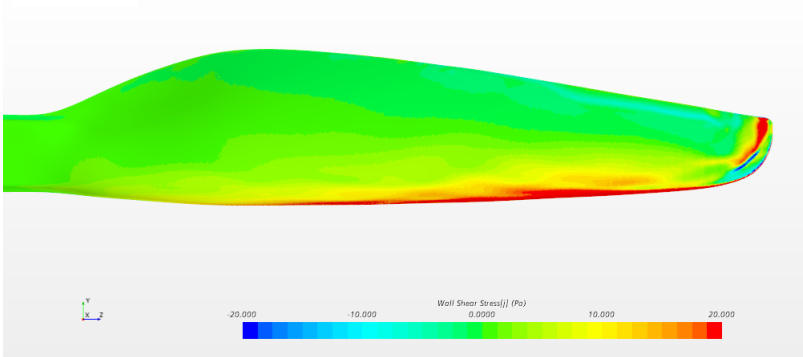

(a) Chordwise component of the Wall shear stress

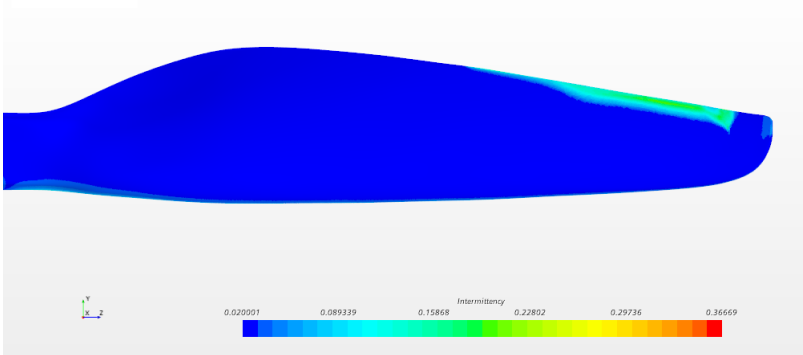

(b) Wall intermittency

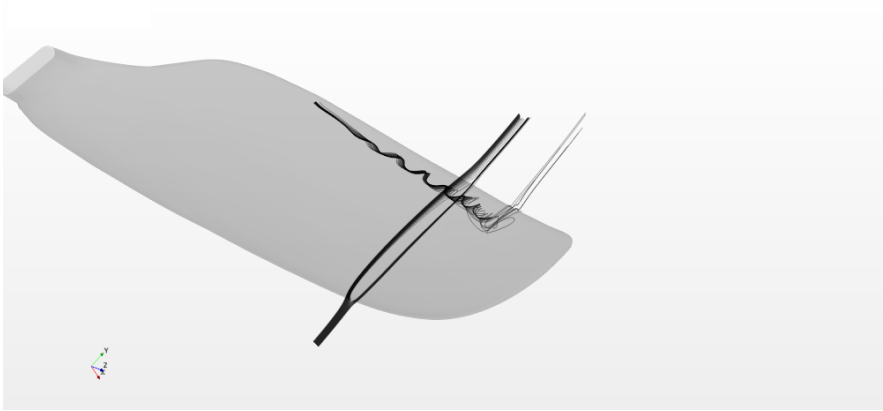

(c) Streamlines illustrating the separation bubble.

Fig. 4.11 Near blade fluid flow characteristics. Re=61,539

a noticeable increase in wall shear stress indicating a short, leading-edge separation bubble.

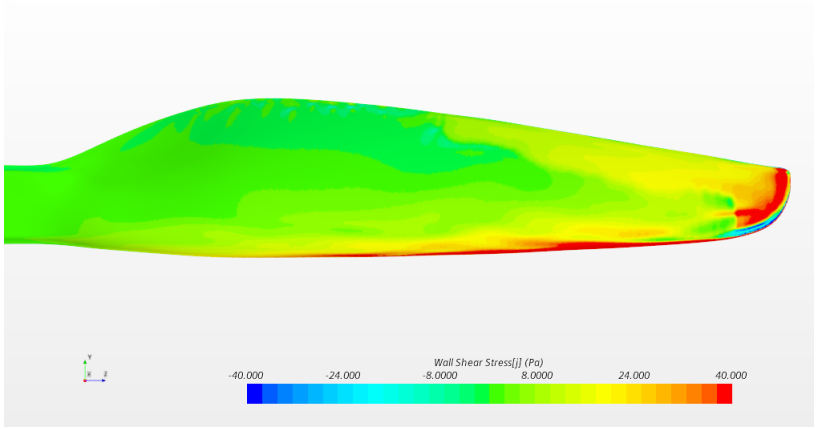

(a) Chordwise component of the Wall shear stress

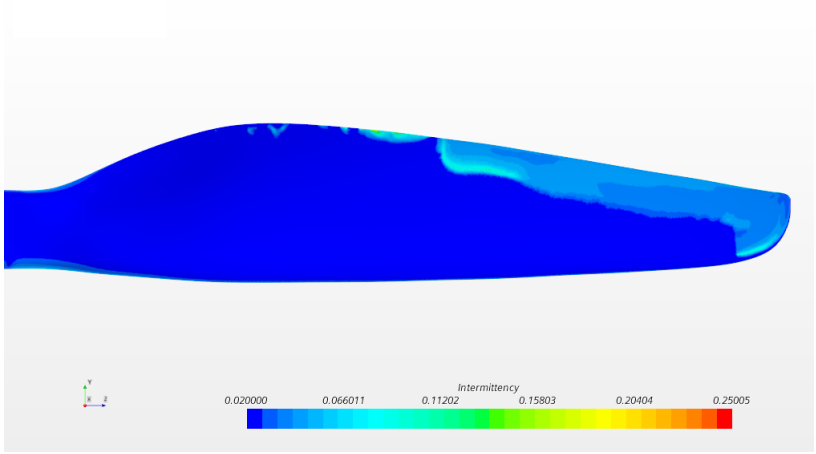

(b) Wall intermittency

Fig. 4.12 Near blade fluid flow characteristics. Re=186,670

4.3.3 Dettached Eddy Simulations

This section presents Delayed Detached Eddy Simulations (DDES) for the highest Reynolds number conditions to confirm the numerical results obtained with the RANS methodology. Attempts were made to include the transition model. However, the simulation presented instabilities that possibly are related to the interaction of the subgrid-scale model and the transition model in regions with insufficient grid resolution. We performed two DDES simulations using the hybrid third-order CD/MUSCL with a blending factor 0.15.

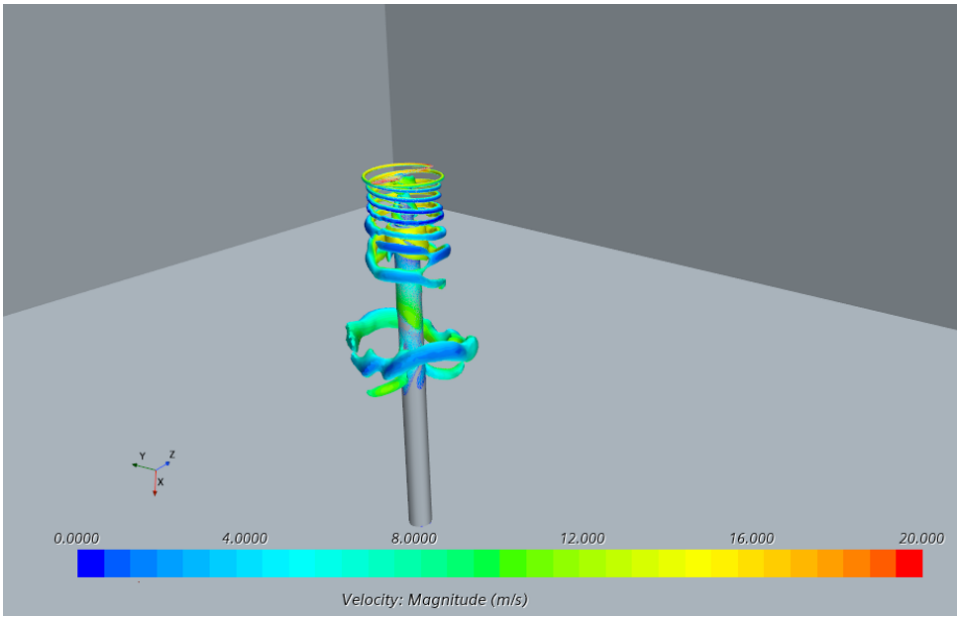

Fig. 4.13 Q-criterion iso-surface colored with velocity magnitude. Re=186,860.

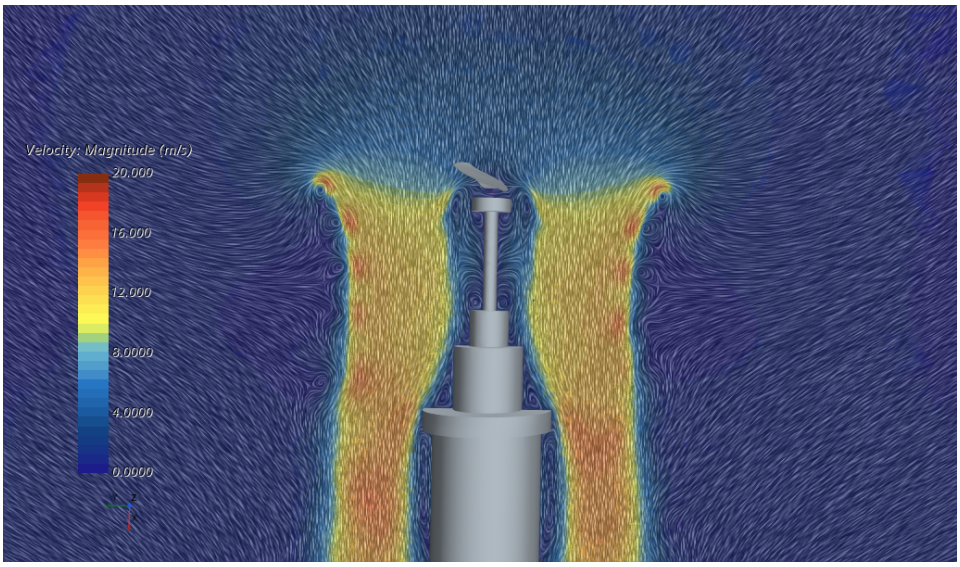

Fig. 4.14 velocity magnitude with line convolution integrals of the velocity direction projected on the plane z=0. Re=186,670.

An initial simulation was performed using a 15 million grid similar to that used for the RANS simulations. In this simulation, the $k-\omega$ DDES model [136] was used to objectively compare the effects of resolving scales. We initialized the solution with 8 revolutions with a time-step equivalent to 2.5 degrees per iteration and then

performed another 8 revolutions with a time step that allows a 0.5 degrees rotation per temporal iteration. Dual time stepping is performed with 10 inner iterations.

A second DDES was performed following some of the guidelines presented by Ventura Díaz and Yoon [212, 213] validated for several rotor flows using DDES Spalart-Allmaras [193] turbulence. The near-body grid was maintained, but the wake region was refined to achieve a global cell count of 32 million. The time-stepping strategy was maintained, but the last revolutions were performed with a time step equivalent to 0.3 degrees per temporal iteration to increase time resolution. In this case, the dual time stepping is performed with an adaptive number of inner iterations, ensuring the continuity residual drops at least two orders of magnitude.

Table 4.8 Integral loads on the rotor predicted by Detached Eddy Simulations. Re=186,870.

DES Approach	**Mean Thrust (N)**	**Mean Torque (Nm)**
$k-\omega$ SST DDES	12.92	0.2414
SA DDES	13.08	0.2437

Table 4.8 presents the integral loads on the rotor predicted by the aforementioned DDES approaches. Differences are around 1% and close to the values predicted in section 4.3.2 with the RANS approach. On the other hand, Figures 4.15, 4.16, 4.17 and 4.18 show how the wake region is drastically different from that obtained in a RANS simulation shown in Figures 4.13 and 4.14 with well defined helical tip and root vortex structures. Also, the velocity field is symmetric and coherent, radically different from both scale-resolving simulations. DES simulations show how secondary braids start to coil around the main vortices. The results are qualitatively in line with those shown by Ventura-Díaz [212] for a small-scale DJI Phantom 3. The SA turbulence DDES has a finer grid resolution, and therefore, more structures are being resolved, as shown in Figure 4.18.

4.4 Reduced Order Models: Tmotor 15"x5"

This section presents the application of the reduced order models implemented in the code *ROT8*, described in Chapter 2, to the Tmotor 15"x5" in the conditions previously analyzed with the CFD model. These models require an airfoil aerodynamic database

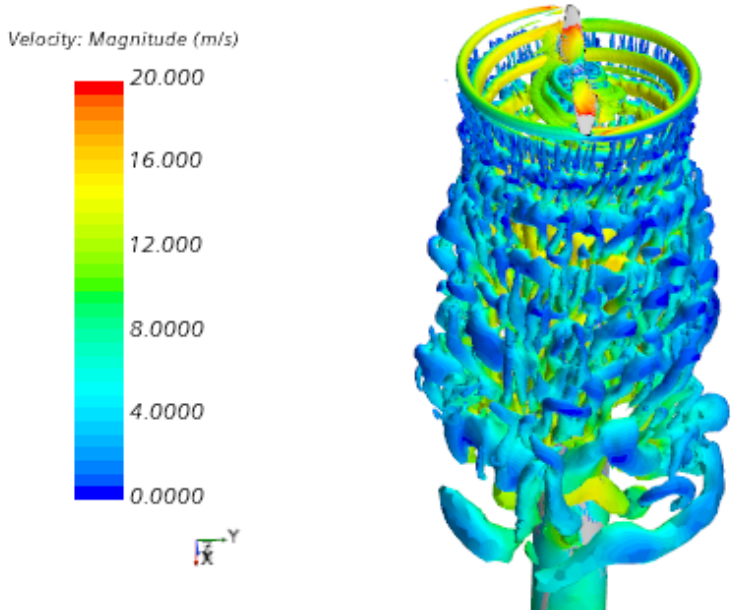

Fig. 4.15 Q-criterion iso-surface colored with velocity magnitude. Re=186,670. DDES $k-\omega$.

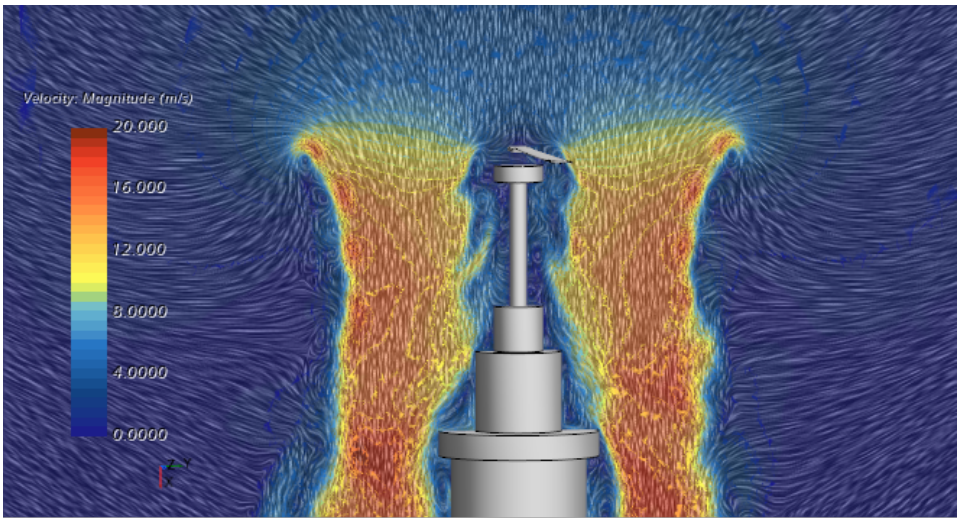

Fig. 4.16 velocity magnitude with line convolution integrals of the velocity direction projected on the plane z=0. Re=186,670. DDES $k-\omega$.

to compute the rotor loads. Different polars have been calculated using XFOIL and CFD, following the guidelines presented and validated in Chapter 3.

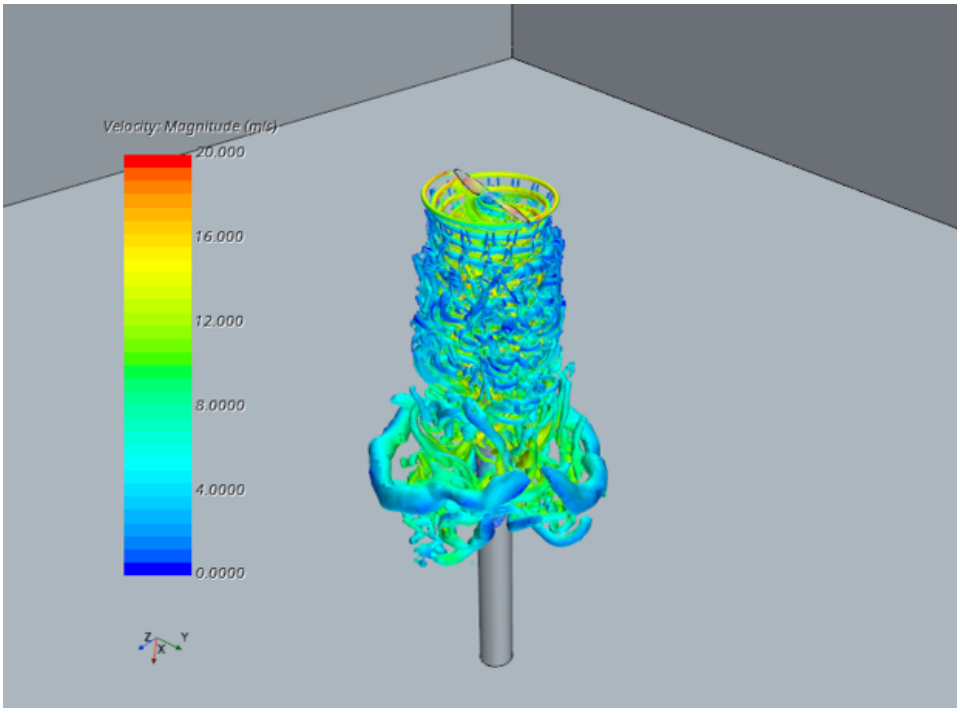

Fig. 4.17 Q-criterion iso-surface colored with velocity magnitude. Re=186,670. DDES Spalart-Allmaras.

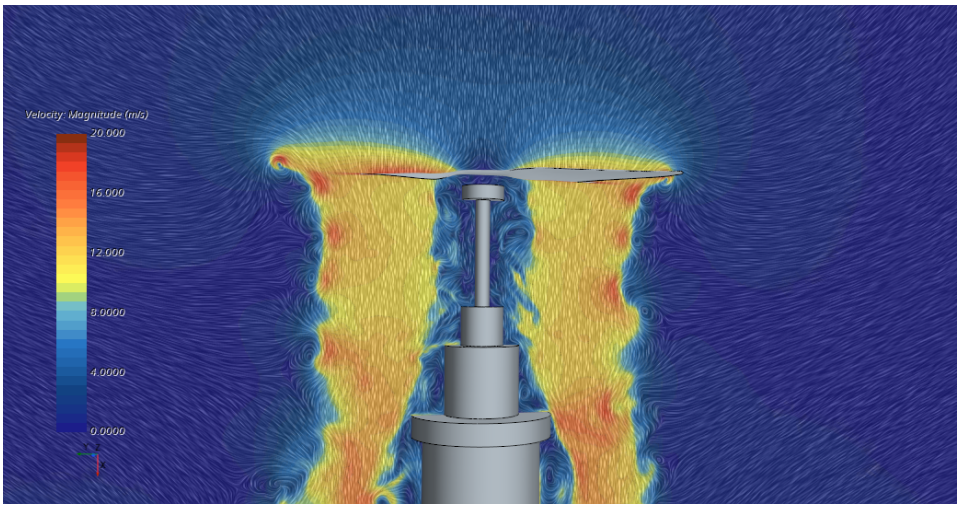

Fig. 4.18 velocity magnitude with line convolution integrals of the velocity direction projected on the plane z=0. Re=186,670. DDES Spalart-Allmaras.

4.4.1 Airfoil Database

The radial discretization must be fine enough to capture variations in camber and thickness distributions to ensure reasonably accurate interpolation. Therefore, we propose discretizing the blade geometry using five sections at a normalized radial position of 0.28, 0.53, 0.78, 0.91, and 0.99. Table 4.9 shows the interpolation strategies between these stations.

Table 4.9 Interpolation strategy between airfoil polars in the aerodynamic database.

r/R	Initial Airfoil	Final Airfoil	Interpolation
0.15<r/R<0.28	28%	28%	Constant
0.28<r/R<0.53	28%	53%	Linear
0.53<r/R<0.78	53%	78%	Linear
0.78<r/R<0.91	78%	91%	Linear
0.91<r/R<99	91%	99%	Linear
0.99<r/R<1	99%	99%	Constant

Figure 4.19 demonstrates clear non-linearities in the aerodynamic efficiency of the airfoils, which arise from the reattachment of the flow forming a separation bubble. It is also evident that the efficiency drops by one order of magnitude between the highest and lowest Reynolds numbers.

Figure 4.20 illustrates that the airfoils' camber decreases as the radial coordinate increases, and thickness initially decreases before growing again near the tip. This trend is consistent with the value of aerodynamic efficiency, which drops by a factor of three when comparing the inboard and tip airfoils. Figure 4.21 shows an example of a separation bubble forming on the suction side of the airfoil. The capability to reproduce these separation bubbles is crucial, as their presence generates a transitional ramp in the polar of the airfoils, as described in [183]. The ramp causes the drag coefficient to scale linearly with the lift coefficient instead of the typical parabolic scaling observed at higher Reynolds numbers. Such a behavior highlights the importance of including a transition model capable of capturing separation bubbles, as demonstrated in [125, 39]. Reduced-order models, such as the blade element method, use aerodynamic databases in the literature that mostly employ XFOIL [75] or similar codes based on the panel method to compute airfoil polars. Considering their computational cost, those codes can achieve impressive accuracy, as shown in [84, 206], which contain comparisons of XFOIL calculations with

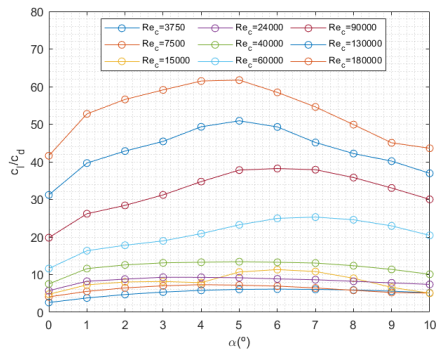

(a) r/R=0.28

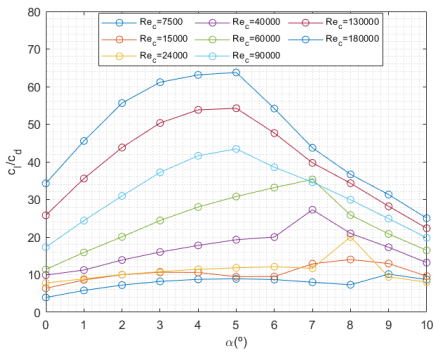

(b) r/R=0.53

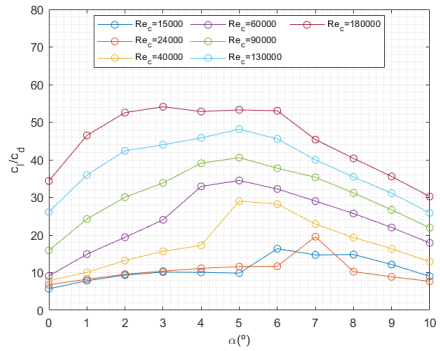

(c) r/R=0.78

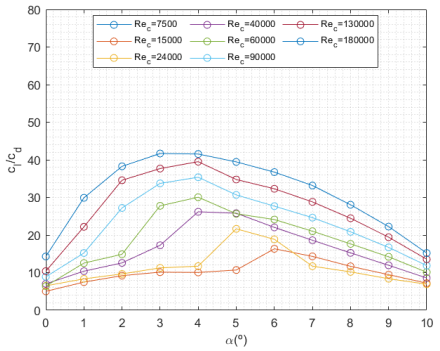

(d) r/R=0.91

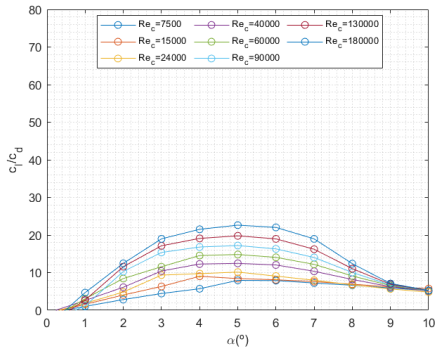

(e) r/R=0.99

Fig. 4.19 Aerodynamic efficiency at different radial stations, Reynolds number and angles of attack calculated using CFD.

implicit large-eddy simulations. CFD and XFOIL results will be similar if the flow is attached and steady. Both include a transition model, and the integral boundary layer method embedded in XFOIL is accurate in these cases. However, XFOIL and CFD calculations may differ significantly if the flow separates without reattaching in the form of an LSB. This scenario is typical at very-low and ultra-low Reynolds numbers,

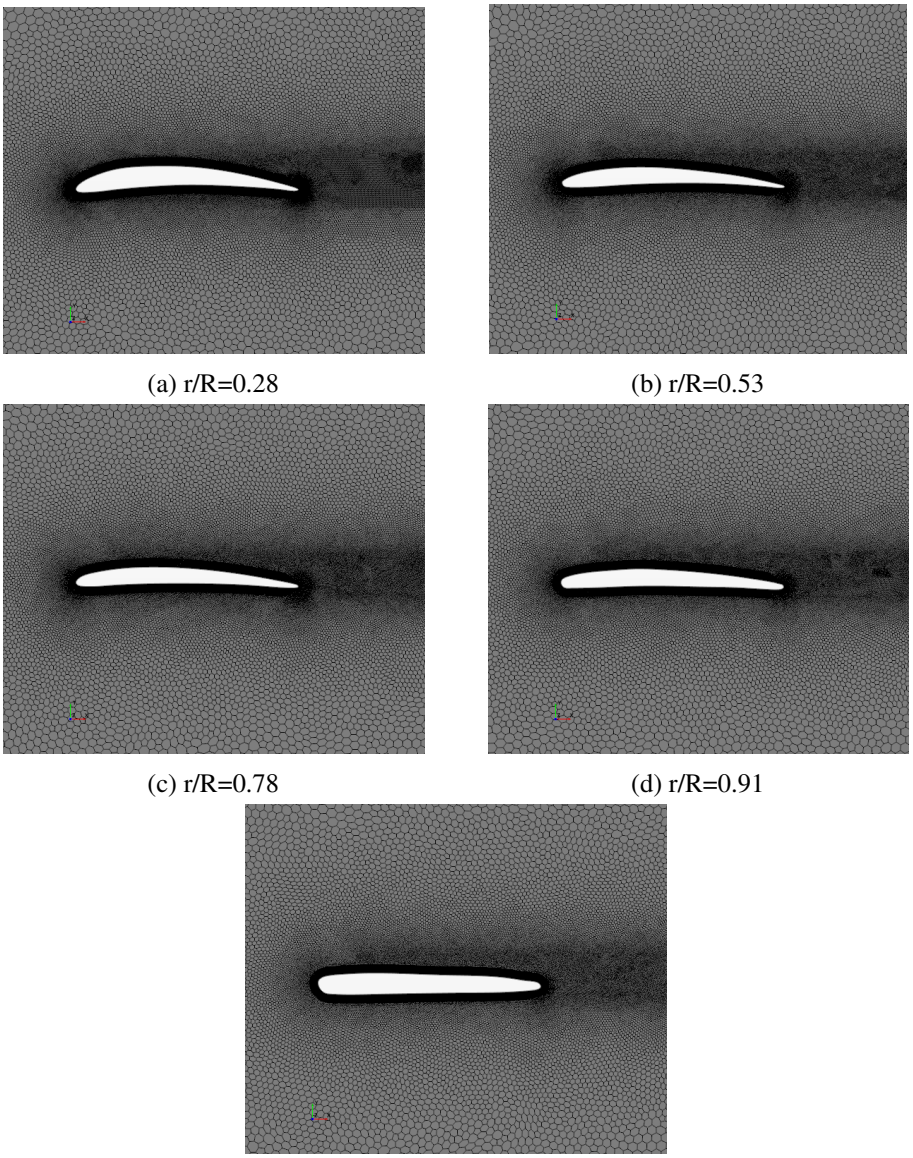

(a) r/R=0.28 (b) r/R=0.53

(c) r/R=0.78 (d) r/R=0.91

(e) r/R=0.99

Fig. 4.20 Airfoil shape and mesh at 0º angle of attack for polar computation on the five selected blade sections.

as shown in [70]. For Reynolds numbers below 15,000, we used a laminar model. Above this value, we adopted the $k-\omega$ SST turbulence model [135] in combination with the γ-Re$_\theta$ transition model [114]. The decision to perform laminar simulations for the lowest Reynolds numbers is because, for ultra-low Reynolds numbers, a laminar, separated, unstable regime arises that generate high lift due to the reduced pressure connected with the high velocities associated with vortex emission as shown

in the previous Chapter. The transition model may dampen or not capture this regime, especially for higher angles of attack, where this highly empirical model predicts an early transition for Reynolds numbers as low as 3000. Figure 4.20 shows refined grids around the airfoils that combine a polyhedral grid with a prism layer grid near the airfoil to capture the strong wall-normal gradients present in the boundary layer. The y+ has been maintained below 0.1 to ensure the adequate performance of the transition model. Time-accurate simulations have been performed to capture unsteady flow features such as vortex shedding, typically present at low Reynolds numbers. The time-step has been set to 0.01 convective turnovers sufficient to capture vortex shedding in ultra-low Reynolds number flows, and an ambient turbulence production term is used to prevent the freestream turbulence intensity from dropping below 0.0003, as discussed in Chapter 3. The Mach number is fixed at 0.2. The computational approach follows the rest of the guidelines presented in Chapter 3.

We have also computed an aerodynamic database using XFOIL to assess if the extra computational cost required to compute the CFD airfoil database is justified. Figure 4.22 shows the aerodynamic efficiency for different angles of attack obtained using XFOIL. We selected a critical exponent for the e^N transition model of 8 following the analysis performed by [84]. We can appreciate how the major trends in the effect of the Reynolds numbers found in CFD simulations are also captured with XFOIL. However, noticeable differences exist, especially in the outer and innermost stations. For higher Reynolds numbers, XFOIL overpredicts the efficiency of the airfoils. This discrepancy may be associated with the finite trailing edge generating a separated region that XFOIL cannot accurately model. On the other hand, for the lowest Reynolds numbers, XFOIL predicts very low efficiencies. This is associated with a laminar separation of the boundary layer without reattachment. In these cases, unsteady Navier-Stokes simulations capture a vortex-shedding regime over the airfoil's suction side, improving the aerodynamic efficiency. As discussed in the previous Chapter, XFOIL cannot model this phenomenon accurately.

4.4.2 ROM Performance comparison

Figure 4.23 illustrates a local comparison between the thrust and torque per unit length predicted by the reduced-order models (ROMs) using the CFD-based polar and the rotor CFD simulations. Table 4.10 includes the integral values of thrust and

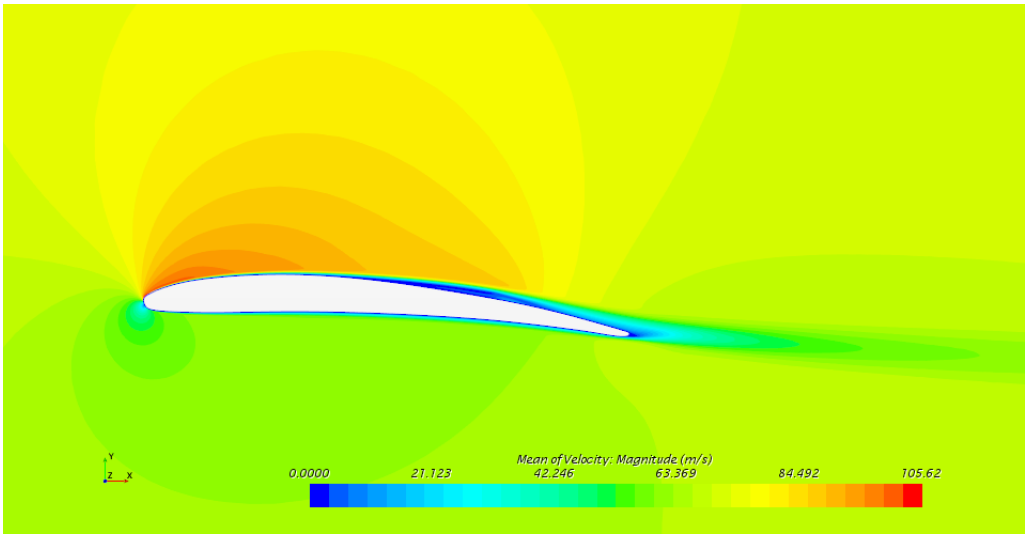

Fig. 4.21 Velocity magnitude of the flow around the airfoil at 53% of the radial coordinate at a Reynolds number of 90,000 at an angle of attack of 4º.

torque and the experimental results reported in [177]. The numerical data agree with the measured values, with errors below 10% for all fidelity approaches.

When comparing the results along the radial coordinate, it is observed that the blade element method (BEM) tends to overestimate the local thrust for intermediate blade positions, which may be associated with underestimated inflow angles. On the other hand, the Free Vortex Wake (FVW) approach shows a better local agreement but still overestimates the thrust and torque toward the tip region compared to the CFD results. The Vortex Particle Method (VPM) shows less overestimation in the tip region compared to the free vortex wake approach. This is likely due to the particulate nature of the VPM, which allows a better representation of the induced flow near the tip. In addition, the VPM approach provides improved performance predictions, particularly at lower Reynolds numbers, making it a valuable option for MAV's propulsive systems. In the FVW and VPM models, an inflection point in the local thrust distribution is found at around 80% of the radial coordinate. This inflection point relates to the tip vortex emitted from the opposite blade, passing under the original blade for the first time. Only CFD, NLL-FVW, and VPM, which model the evolution of the wake, can capture this feature. This capability is significant in hovering simulations, where the passage of the first vortex is much closer to the blade than in cases with high inflow velocities. We can also appreciate how the

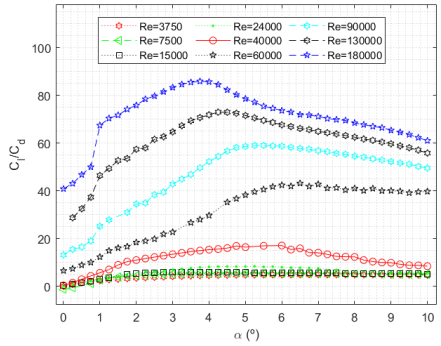

(a) r/R=0.28

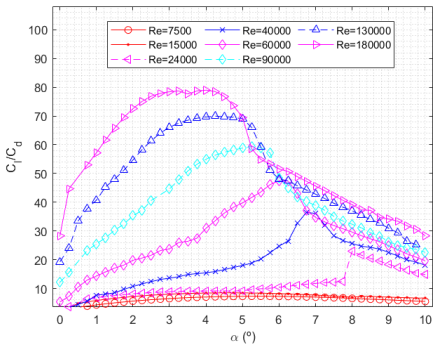

(b) r/R=0.53

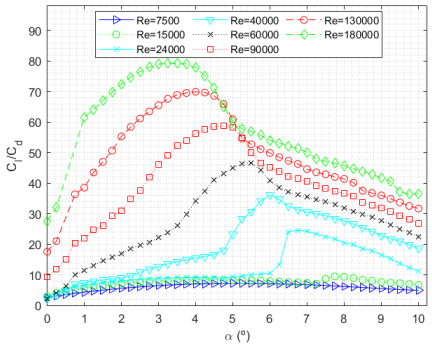

(c) r/R=0.78

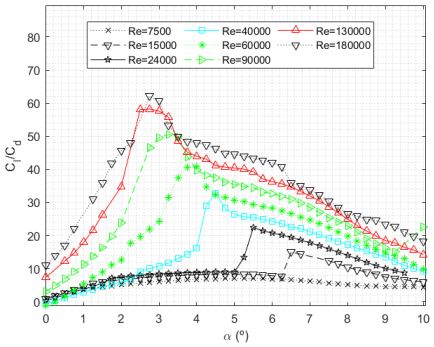

(d) r/R=0.91

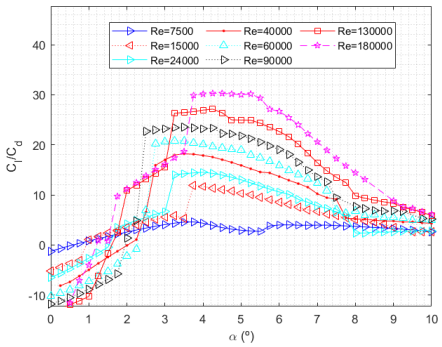

(e) r/R=0.99

Fig. 4.22 Aerodynamic efficiency at different radial stations, Reynolds number and angles of attack calculated using XFOIL.

tip-loss correction is slightly too aggressive near the tip, decreasing the local thrust and torque compared to CFD data.

It is also worth noting that Table 4.10 illustrates that the computational cost of the performance calculation increases significantly as the fidelity of the approach is improved. On the other hand, enhancing the accuracy of the integral performance of

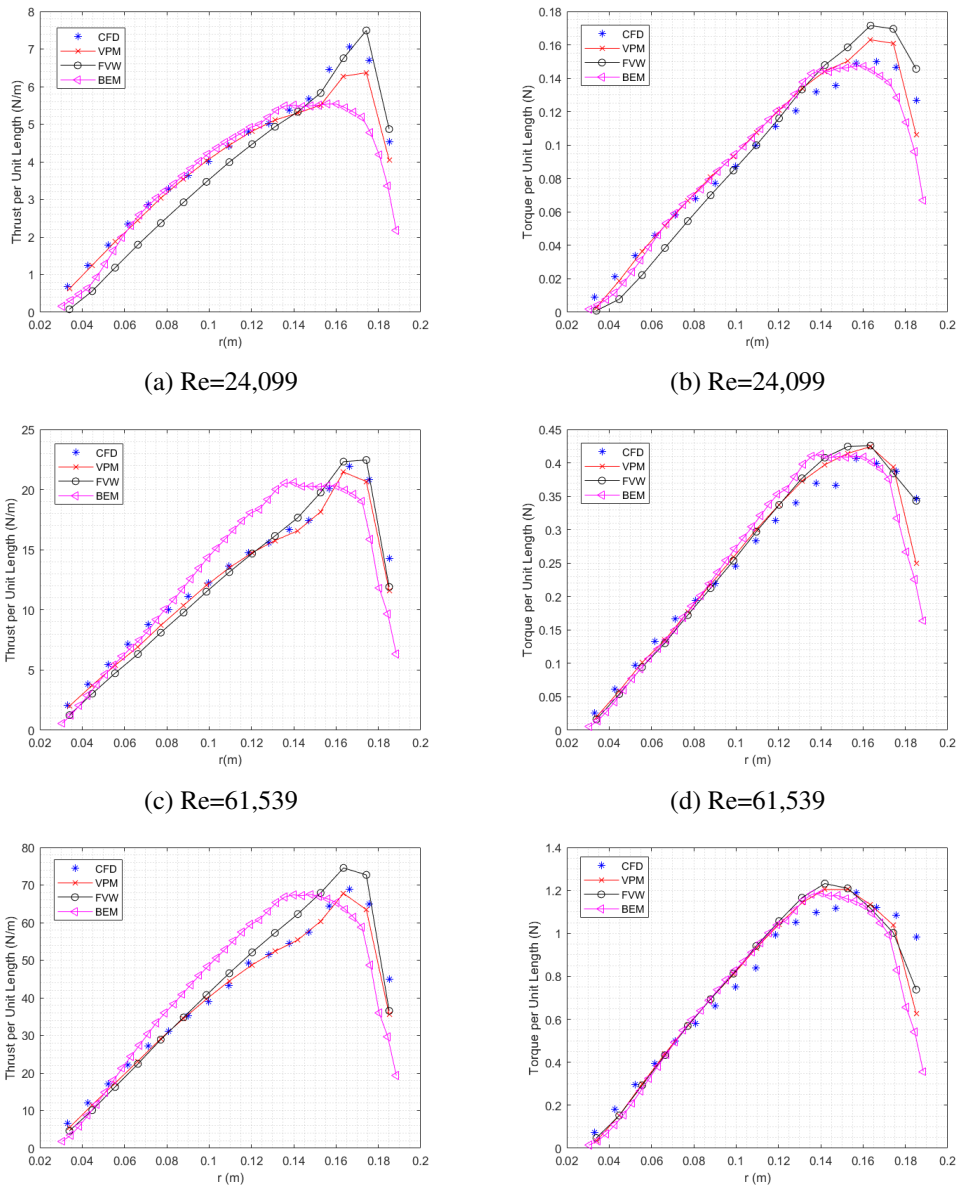

(a) Re=24,099 (b) Re=24,099

(c) Re=61,539 (d) Re=61,539

(e) Re=186,670 (f) Re=186,670

Fig. 4.23 Thrust and torque radial distributions for different Reynolds numbers using the CFD-based polar for the Reduced Order Models.

the blade is relatively limited. However, this should not be taken as an indication of an overall trend as the cancellation of errors seen in Figure 4.23 for the BEM might not extend to other geometries or operating conditions.

Table 4.10 Comparison of numerical approaches to compute rotor performance at different Reynolds numbers.

	BEM		**NLL-FVW**		**VPM**		**CFD**		**Experimental**	
Re	**T [N]**	**Q [Nm]**	**T [N]**	**Q [Nm]**	**T [N]**	**Q [Nm]**	**T [N]**	**Q [Nm]**	**T [N]**	**Q [Nm]**
24,099	1.19	0.029	1.21	0.0307	1.27	0.0310	1.33	0.030	1.26	0.029
61,539	4.18	0.082	3.95	0.0848	3.92	0.083	4.12	0.083	4.16	0.082
186,670	13.80	0.236	13.55	0.248	12.71	0.245	13.16	0.0246	13.41	0.253
CPU-h	0.0003		0.5		28		2000		-	

4.4.3 Influence of the 2D airfoil aerodynamic database

In section 4.4.1, we presented two aerodynamic databases for different airfoils sections forming the Tmotor 15"x5" blade. Table 4.11 compares thrust and torque relative to the experimental values using both aerodynamic databases. We can appreciate that for the highest Reynolds numbers, the thrust and torque are slightly higher using all ROMs, but the BEM seems more affected by the change in Polar. The results at a Reynolds number of 61,539 are almost identical, with no clear trends. On the other hand, for the lowest Reynolds number, we can appreciate an evident underestimation of thrust and torque values using all three ROMs. This is a consequence of the drop in the lift coefficient due to laminar separation without reattachment discussed in section 4.4.1. Compared to the experimental data, the mean discrepancies using a CFD polar seem less sensitive to the Reynolds numbers than XFOIL. Morgado [141] did not appreciate a significant improvement in using CFD to compute the polars compared to XFOIL for a Reynolds number of 200,000. For our highest Reynolds number, around 200,000, we detect slight overestimations of the thrust, possibly associated with the thick trailing edges of the airfoils composing this blade, but the overall trends are captured adequately. For lower Reynolds numbers, when separation regions become important, using a time-accurate transitional URANS approach becomes advantageous to improve small-scale rotor performance predictions.

Figure 4.24 shows the local thrust and torque per unit length comparing the Vortex Particle Method using XFOIL-based and CFD-based polars with 3D rotor CFD simulations. For the highest Reynolds number, 187,000, we can appreciate how, in the tip region where the chord-based local Reynolds number is high, the XFOIL-based polar overestimates the CFD-based one. At around 50% of the radial

coordinate, both predictions are equal, and for the innermost stations, the XFOIL-based polar underestimates the CFD-based polar. For Reynolds 62,000, the local thrust per unit length is underestimated with the XFOIL-based polar for the whole span of the blade, and this effect is exacerbated for the lowest Reynolds numbers. Overall, the CFD-based polars seem to adequately capture the local thrust distributions obtained in the 3D CFD simulations for all Reynolds numbers, improving the predictions done with the XFOIL-based polar for all the tested conditions.

Table 4.11 Comparison of ROMs performance predictions with respect to experimental data [177] using different airfoil aerodynamic databases.

	BEM		**NLL-FVW**		**VPM**		**Mean Values**	
Re-Polar	**Δ T [%]**	**ΔQ [%]**	**ΔT [%]**	**ΔQ [%]**	**ΔT [%]**	**ΔQ [%]**	**ΔT [%]**	**ΔQ [%]**
24,099-CFD	-5.5	0.0	-4.0	5.9	0.8	6.9	-2.9	4.3
24,099-XFOIL	-24.9	-10.3	-24.1	-7.6	-19.0	-8.3	-22.7	-8.7
61,539-CFD	0.5	0.0	-5.0	3.4	-5.8	1.2	-3.4	1.5
61,539-XFOIL	-1.2	1.2	-6.0	0.6	-9.5	-0.5	-5.6	0.4
186,670-CFD	2.9	-6.7	1.0	-2.0	-5.1	-3.2	-0.4	-4.0
186,670-XFOIL	12.2	2.4	5.4	2.0	-3.4	0.0	4.73	1.5

Figure 4.25 shows the pressure coefficient obtained at the 78% radial station in the CFD simulation at the highest Reynolds number, compared with those obtained with the CFD-based polar and XFOIL-based polar at an angle of attack of 2 degrees. This value was selected to match the suction peak in the CFD simulation looking at the CFD-based polar. We can observe how the agreement between the CFD-based 2D polar and the 3D pressure distributions is satisfactory, apart from a delayed transition of the 2D simulations characterized by the pressure recovery. On the other hand, we can see how XFOIL is slightly overpredicting the suction and pressure distributions, which will increase the lift coefficient overall. This is possibly related to the rounded and finite trailing edges these airfoils possess. XFOIL predicts transition at a congruent position compared with the CFD-based polar. The earlier transition observed in the CFD simulation is associated with higher freestream turbulence intensity near the rotor leading edge. We can appreciate how a 2D CFD polar, computed at a higher freestream turbulence intensity, allows the correct prediction of the pressure distribution revealed by the 3D rotor CFD simulation. Figure 4.26 shows how these higher values are induced by the close passage of the tip vortices generated by the opposite blade. Apart from this effect, we can appreciate how with an accurate 2D database and precise induction predictions, lifting-line-based

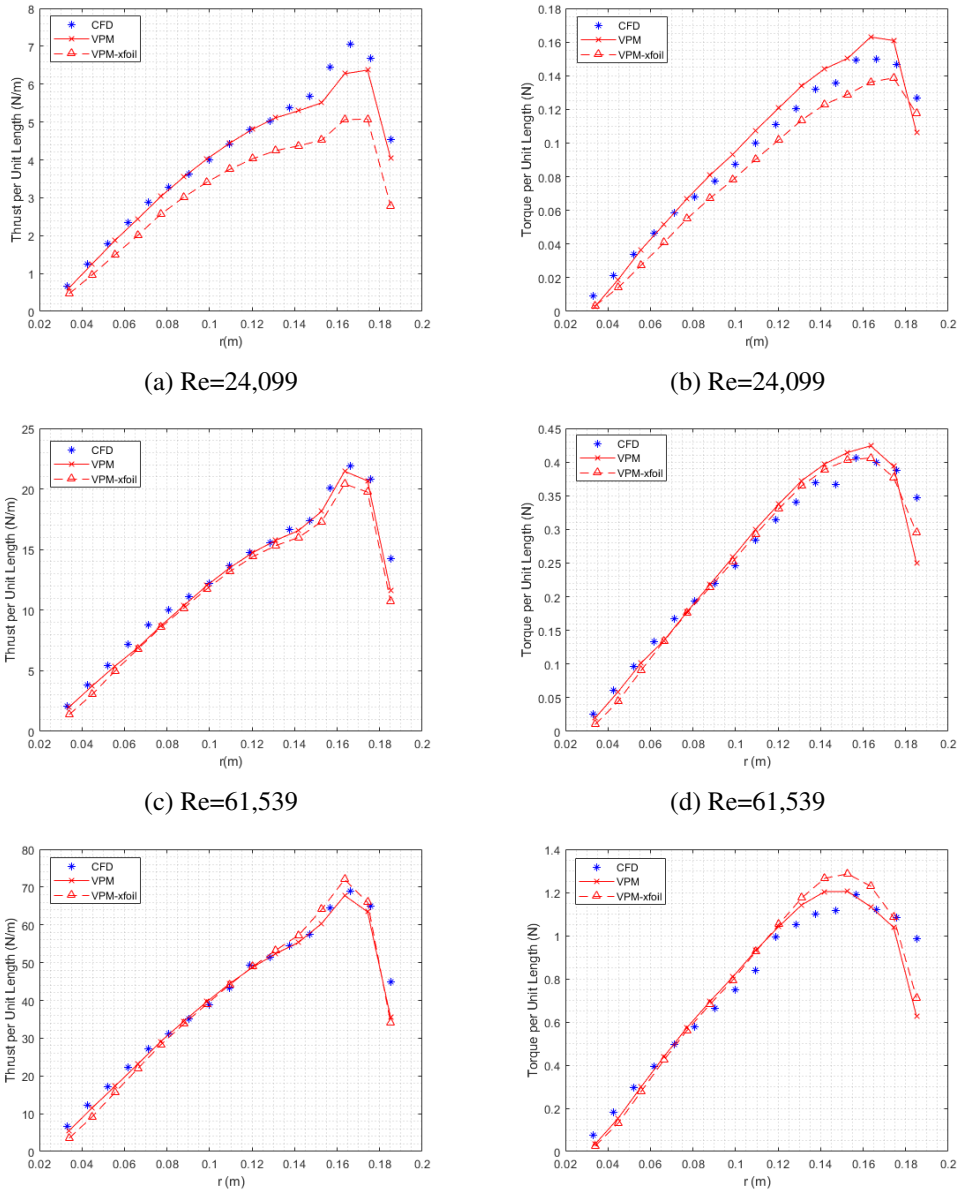

(a) Re=24,099 (b) Re=24,099

(c) Re=61,539 (d) Re=61,539

(e) Re=186,670 (f) Re=186,670

Fig. 4.24 Thrust and torque radial distributions for different Reynolds numbers comparing the Vortex Particle Method using CFD-based and XFOIL-based polars with CFD simulations.

reduced order models can accurately predict loads locally and integrally and local blade surface characteristics.

Regarding computational cost, an XFOIL computed polar takes around 10 minutes on a standard laptop. This is negligible compared to a time-accurate CFD-based

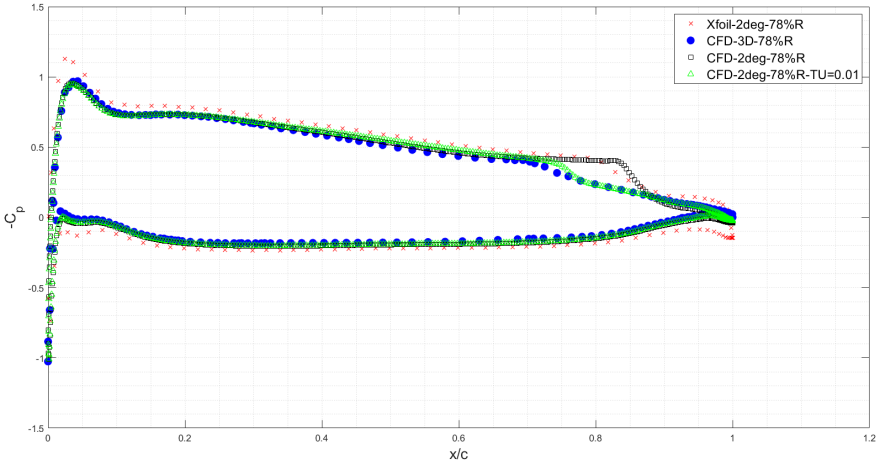

Fig. 4.25 Pressure coefficient at Reynolds 180,000 from CFD-based polar and XFOIL polar compared with the 78% radial station in the 3D CFD simulation.

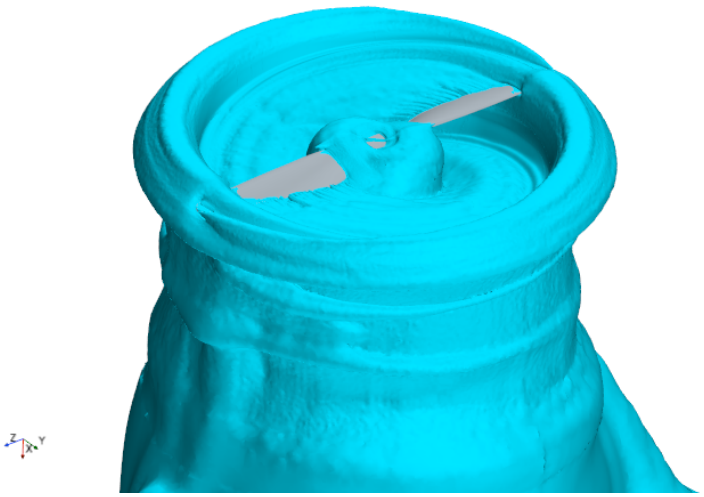

Fig. 4.26 Turbulence intensity isosurface at Tu=0.01. Reynolds number 186,670.

polar, which takes around 4,000 CPU hours using 32 cores of an Intel Xeon Scalable Processors Gold 6130 2.10 GHz. It is worth mentioning that the computational cost of the polar is comparable to a full 3D rotor simulation. This cost would be higher if the effects of compressibility were included in the polar by computing all airfoil sections for different Mach numbers.

4.5 Machine Learning Model for rotor performance estimation

The aim of this model is to obtain a preliminary rotor performance using input front and top images of rotors. For this purpose, the propeller database of the University of Illinois at Urbana-Champaign (UIUC) [33] was used. Around 120 propellers were experimentally tested and precisely photographed in its two first volumes. A Machine Learning (ML) model was trained using as inputs post-processed data from the original rotor images present in the database to match thrust and torque coefficients.

Propeller performance depends on several operational and geometrical parameters, among which the most important are the chord and twist distributions, airfoil employed, diameter, sweep, surface roughness, and angular velocity. Performing a simplified dimensional analysis neglecting sweep and roughness, the thrust and torque coefficient results to depend only on the Reynolds number, Mach number, non-dimensional twist, chord distributions, and the airfoil employed at each radial station. In fact, at the scale of propellers and rotors that we are dealing with, of only a few inches in diameter, the Mach number effects are typically negligible, and the Reynolds number will be relevant, especially for the smaller propellers. These simplifications imply that the coefficient mainly depends on the chord, twist, and airfoil radial distribution. It is possible to perform an approximation of chord and twist distributions using as an input the front and top views of the propellers, as done, for example, by the open-source software PropellerScanner by Martin Hepperle. Unfortunately, no information can be obtained from the images regarding the airfoil distribution. This is the biggest limitation of this approach. Figure 4.27 summarizes the methodology employed to extract the relevant features from the images and the use of these to train the model.

Propeller images were post-processed to estimate the chord and twist in 17 different radial positions, and this was considered our input data. The variables predicted by the ML model are the thrust and torque coefficients obtained from the UIUC propeller database. The Gaussian Process Regression models provided the best validation metrics using k-fold validation, which we employed to avoid data loss considering the small database. The most performing GPR model, employing a 5/2 Matern kernel, obtained an R-squared value of 0.88 and a root-mean-square

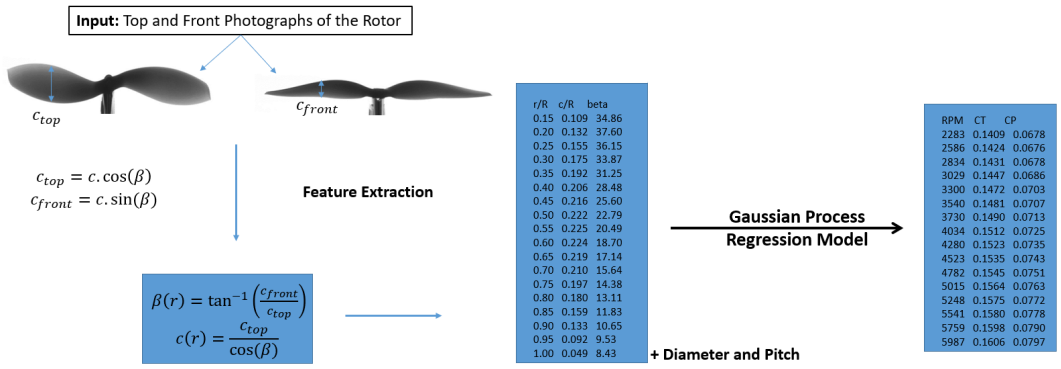

Fig. 4.27 Machine Learning approach to compute thrust and torque coefficients.

error of 0.0072. A plot showing the validation predicted against the actual value is shown in 4.28 for the thrust coefficients.

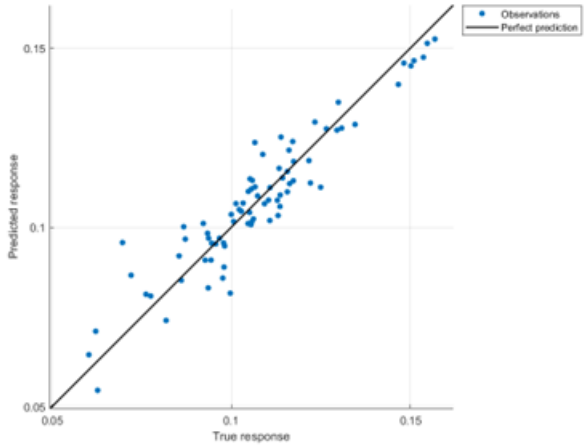

Fig. 4.28 Thrust coefficient (using UIUC's definition) validation of a Matern 5/2 Kernel GPR model using k-fold validation for volume-1 propellers.

This module offers the possibility of performing almost instant thrust and torque coefficient predictions simply by uploading front and side view images of the rotor.

Two random rotors that were not part of the training set and that have associated experimental and numerical work have been tested to analyze the fidelity of the predictions. These are the Tmotor 15"x5" rotor and Delft Aerocoustic Benchmark blades shown in Figure 4.29. These blades have been extensively studied experimentally and numerically in the previous section and in [53] respectively. Table 4.12 compares the GPR predictions of the thrust and power coefficients for these blades hovering at 4000 rpm with the available experimental and numerical data.

It is interesting how, starting from an image, this machine-learning technique can predict the order of magnitude of the performance coefficients of the blade with maximum errors below 20% compared to experiments and around 10 % if we consider numerical results.

(a) Tmotor 15"x5" cf (b) TU Delft Aeroacoustic Benchmark [53]

Fig. 4.29 Input geometries for Gaussian Process Regression model predictions.

Table 4.12 GPR model predictions of Tmotor 15"x5" and Delft Benchmark blades compared to CFD and experimental data. CFD and experimental data obtained is obtained from [49] for the Tmotor 15"x5" blade and from [53] for the Delft Benchmark blades.

	CFD		**Experimental**		**GPR model**	
Blade	C_T	C_P	C_T	C_P	C_T	C_P
Tmotor 15"x5"	0.00895	0.000879	0.00919	0.000912	0.01019	0.000838
TU Delft	0.0165	0.00232	0.0148	0.00206	0.0166	0.00246

4.6 CFD simulations: Q4L UAS

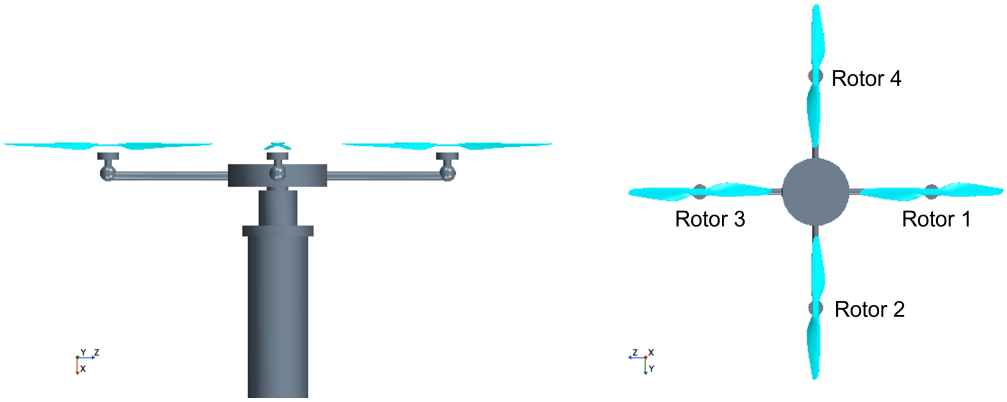

Fig. 4.30 Numerical setup of the complete quadcopter.

We have already confirmed the accuracy of the rotation model and are now utilizing it to run simulations on the quadrotor. To evaluate the impact on the

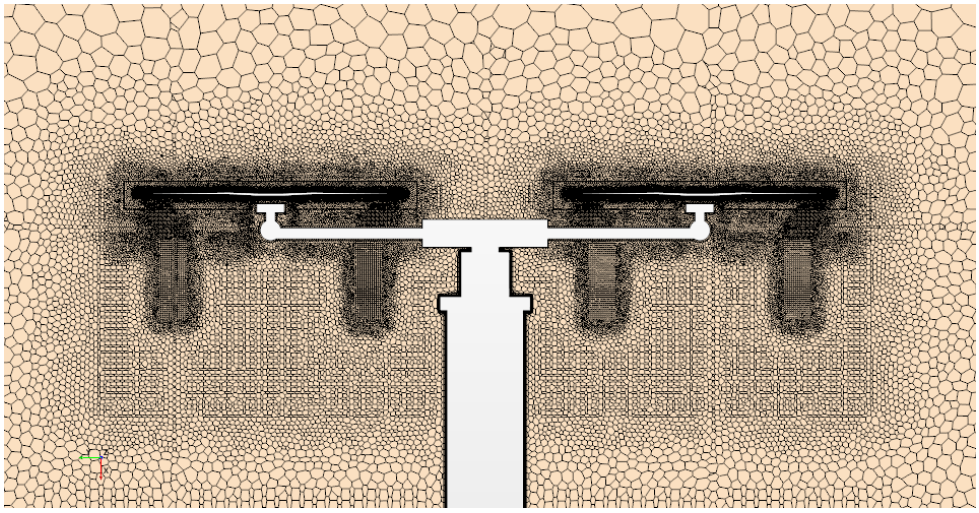

Fig. 4.31 Grid around the complete quadcopter.

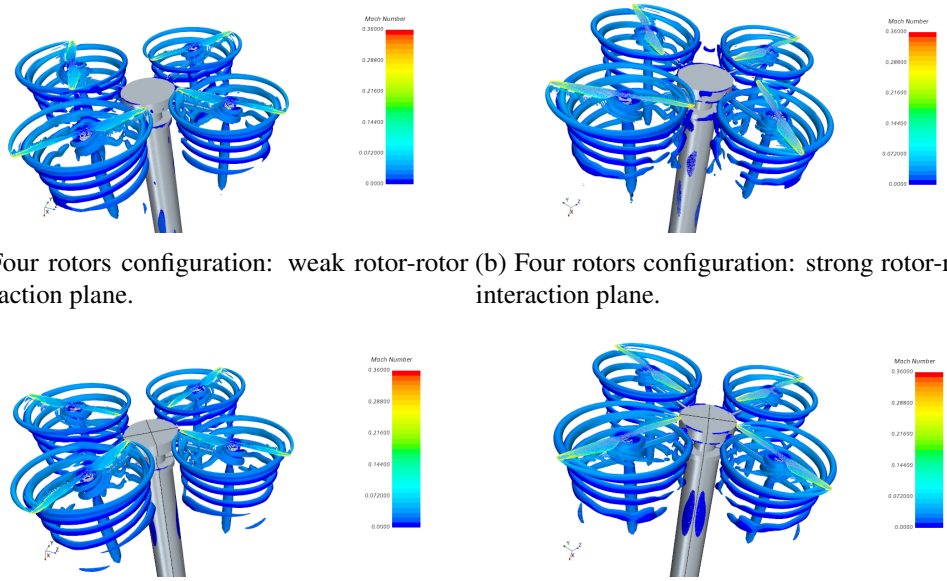

(a) Four rotors configuration: weak rotor-rotor interaction plane.

(b) Four rotors configuration: strong rotor-rotor interaction plane.

(c) Symmetry boundary conditions: weak rotor-rotor interaction plane.

(d) Symmetry boundary conditions: strong rotor-rotor interaction plane.

Fig. 4.32 Q-criterion coloured with Mach number around the quadcopter including experimental fixture.

thrust coefficient due to rotor-rotor interactions, we created a basic CAD model that aligns with the Q4L quadcopter. This UAS has four Tmotor 15'x5' rotors tested in the previous section. The numerical setup is illustrated in Figure 4.30. For the highest Reynolds number case (Re=181,410,Figure 4.1a), we conducted a simulation

using four rotors, each with its own experimentally measured rotation speed. This Reynolds number is determined by combining the average RPM from Table 4.13 with a temperature of 233.8 K and a pressure of 98,280 Pa. Our results serve as a reference solution, which we will compare with results obtained using a single rotor with symmetry boundary conditions.

In simulations where symmetry boundary conditions are used, the rotation speed of the single rotor is determined by taking the root-mean-square of the four rotation rates listed in Table 4.13. The mesh surrounding the entire quadcopter, which consists of 46 million cells, is shown in Figure 4.31. The simulation that uses symmetry boundary conditions has a grid with only one-quarter the number of cells as the four-rotor case. This simulation setup is similar to the isolated rotor simulations discussed in the previous chapter.

This study observed that the symmetry boundary condition simulations produced almost identical results, as shown in Table 4.14 and Figure 4.32. This was observed even though the physical problem was not the same due to slightly different rotation rates. Our findings suggest that the symmetry boundary condition slightly dampens rotor-rotor interactions at this separation distance, reducing vortex breakdown. However, it did not significantly affect the thrust value, and using the symmetry boundary conditions resulted in a 4x reduction in simulation time and memory requirements.

Notably, the rotor-rotor interactions are stronger in the inter-rotor regions when the blade tip rotates from the vehicle's center outwards, as shown in Figure 4.32. The flow visualizations presented in Figures 4.32b and 4.32d represent the same situation as Figures 4.32a and 4.32c, respectively, but rotated by 90° to emphasize the different planes of interaction. Figure 4.33 depicts how counter-rotating vertical vortices are created in the inter-rotor region near the smallest tip clearance location.

It is interesting to note that these vortices only appear in the previously defined strong rotor-rotor interaction planes. Notably, these vortices are responsible for the enhanced breakdown of the rotor tip vortices seen in Figure 4.32. Based on Schenk's observations, as mentioned in [180], two counter-rotating isolated rotors induce a local upwash current in the inter-rotor regions following the direction the tips move. The four rotors on a quadcopter create a vortex system that generates a current toward the center of the device. These currents move in the same direction when the rotors move toward the body, but when they move away from the body, the induced

currents oppose each other. We suggest that this is what causes the formation of vortices. However, more research is needed to understand this instability fully.

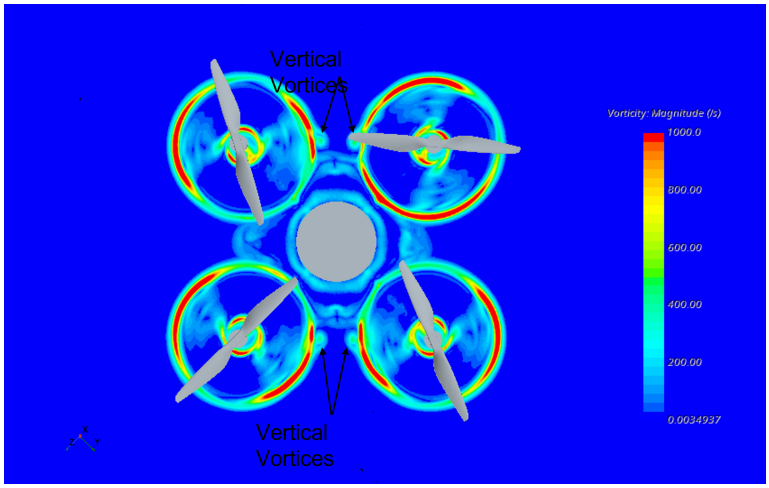

Fig. 4.33 Vorticity magnitude in a horizontal plane x=0.02m.

To assess the effects of rotor-rotor and rotor-body interactions on the integral vertical force on the quadrotor, we computed the thrust coefficient using the average rotation speed for the complete vehicle. Then, we compare it to the corresponding isolated rotor at the closest Reynolds number. Equation (4.1) shows the relation to calculate the download factor, which considers the overall decrease in the axial force of a quadcopter due to the interaction between rotors and airframe.

Table 4.13 Rotation rates of the four rotors in the full quadcopter configuration.

RPM Rotor 1	**RPM Rotor 2**	**RPM Rotor 3**	**RPM Rotor 4**	**Mean RPM**	**RMS RPM**
4338	4310	4388	4316	4338	4338

$$DL = \frac{4C_{T_{rotor}} - C_{T_{UAS}}}{4C_{T_{rotor}}} \tag{4.1}$$

The Reynolds number conditions for the isolated rotor (Re=186,670) and quadcopter (Re=181,410) are similar, making it possible to compare their thrust coefficients. The numerically computed download factor is 4.5%, slightly higher than the experimental value of 3%, which could be due to the lack of resolution in the boundary layer and wake behind the quadcopter's arms and body, or the difficulty

Table 4.14 Comparison between experimental and numerical approaches to compute the quadcopter thrust.

	Symmetry Condition	**Full Quadcopter**	**Experimental**
Mean RPM	**4 x Thrust [N]**	**Thrust [N]**	**Thrust [N]**
4338	42.72	42.65	44.2

in accurately predicting drag values in separated flows using RANS turbulence modeling. Other possible reasons for the discrepancies include minor geometrical simplifications in the numerical model, particularly in some airframe details.

4.7 Discussion

We conducted a study that assessed the effectiveness of various methods in calculating rotor performance during hovering conditions. These methods range from Blade Element Momentum calculations to Detached Eddy Simulations. Our findings indicate that the cost of these methods can vary greatly, with relatively minor improvements in the prediction of experimental results. Depending on the intended use, more expensive models may be necessary.

We used CFD simulations to develop a protocol that accurately describes low Reynolds number effects. Our simulations showed that the γ-Re_θ transition model, calibrated according to [114], produced satisfactory results for Reynolds numbers between 60,000 and 200,000. However, for Reynolds numbers 20,000, the performance predictions with the transition model started to deviate from the experimental results. Using a laminar solver to compute rotor performances may be beneficial in such cases.

We validated CFD simulations using experimental data and found that they agreed well across all Reynolds numbers. Our accurate replication of the experimental results was made possible by using localized meshing strategies, incorporating the experimental device into the geometric model, and obtaining precise blade geometry through 3D optical scanning. Although the differences caused by these aspects were individually minor, they could accumulate and result in errors when assessed integrally.

The Moving Reference Frame approach has been validated for rotor simulation during hovering. It is an interesting approach because it reduces computational costs by about ten times compared to the dynamic approach while maintaining reasonable accuracy. Reducing computational costs can enable CFD simulation in optimization and design activities. As a result, it would be possible to design rotor geometries that maximize performance and minimize the negative impact of low Reynolds number effects.

We assessed the impact of performing Delayed Detached Eddy (DDES) Simulations at the highest Reynolds number conditions. The wake disposition presented differs, showing much smaller braids coiling around the original tip and hub vortices. Two different DDES were performed, one using a $k-\omega$ SST turbulence model on a grid with similar resolutions as used in the RANS simulations and another using a Spalart-Allmaras DDES approach with a finer resolution. Despite the different wake structures, the differences in the performance coefficients are below 1%.

We conducted full rotorcraft simulations, agreeing satisfactorily with the experimentally measured thrust values. We noted a slight overestimate of the download factor compared to the experimentally computed value, possibly due to a lack of grid resolution in the wake of the UAS arms and the loss of fidelity of RANS turbulence models when dealing with large flow separations.

Regarding reduced-order models, we assessed the effect of the aerodynamic database. The XFOIL-based polar errors are more sensitive to the Reynolds number for this rotor, producing large underestimations of thrust and torque for the lowest Reynolds numbers. XFOIL is unable to reproduce accurately flows with moderately separated regions. This is especially critical for finite trailing edge airfoils, typically employed in small-scale blades for manufacturing limitations. For the highest Reynolds numbers, the lift coefficient is slightly overestimated. This effect is not fully translated into the thrust predictions as the Reynolds numbers towards the root are still relatively small, and the thrust is underpredicted. The CFD-based polar provides consistent local and integral performance predictions for a wide range of Reynolds numbers for the tested rotor and operating conditions. Furthermore, the CFD-based polar has proven able to predict the pressure distributions recovered in the rotor CFD simulation, supporting the use of strip theory for the load calculations. Differences in the boundary layer state between 2D and 3D simulations are caused by the increased levels of leading-edge turbulence intensity due to the effect of the

wake and tip vortex. This influence on the pressure distribution is also a reminder of the importance of using transition modeling in CFD simulations to compute rotor loads in this range of Reynolds numbers accurately.

Regarding the performance predictions of the reduced order models, the FVW and VPM techniques appear to be a reasonable compromise between accuracy and computational cost, as they provide a better agreement in the local distribution of the thrust compared to the Blade Element Momentum Method due to their explicit wake modeling. Both codes have the advantage of being meshless and not suffering from Courant-Friedrichs-Lewy (CFL) restrictions, significantly reducing the computational cost. In particular, the VPM is preferable when it is necessary to account for wake mixing or when the connectivity of vortex structures is difficult to afford. In addition, it can be used with variable fidelity as the number of vortex particles can be adjusted, making it a valuable tool for design applications. Furthermore, the VPM approach seems to capture better the low Reynolds number effects on the wake due to accurate modeling of vortex particle strength diffusion compared with the simplified Lamb-Oseen approach to model this phenomenon in the FVW approach.

A data-driven model has been developed to obtain fast reduced fidelity estimation of rotor performance. We used a Gaussian process regression model trained with experimental data from the UIUC database, including over-rotor 120 geometries. The inputs of our model are frontal and lateral images of the rotor, and the output is the thrust and torque predictions. We tested this approach in two rotors not present in the database showing maximum errors between 10 and 20%.

While CFD is quite expensive for design applications, it is a powerful tool for validation activities where the experimental setup's influence must be considered. It also allows us to understand the physical phenomena behind rotor performance and provide the necessary information to develop corrections for the previously mentioned ROMs. Its use is mandatory when investigating exotic design conditions, such as those on Mars or high-altitude aerodynamics, where three-dimensional and compressibility effects can become significant due to the unique combination of low Reynolds and high Mach numbers. Even though compressibility effects on the loading can partially be considered through the airfoil polar, the incompressible formulation of the vortex methods will limit the fidelity of these approaches at high Mach numbers.

Chapter 5

Ultra-Low Reynolds Number Rotor Aerodynamics: Design and Optimization

This chapter includes the partial content of the papers:

- M. Carreño Ruiz and D. D'Ambrosio. Aerodynamic optimization and analysis of quadrotor blades operating in the Martian atmosphere. *Aerospace Science and Technology*, 132:108047, 2023
- M. Carreño Ruiz and D. D'Ambrosio. Hybrid Fidelity Optimization of Efficient Airfoils and Rotors in Ultra-Low Reynolds Numbers Conditions. In *AIAA SciTech 2023 Forum*, National Harbor, MD, January 2023. AIAA-2023-0652

Martian aerodynamics is a current topic, and many space agencies aim to achieve Martian flight. However, it is rare to find well-documented efficient blade geometries and the optimization procedures employed to obtain them due to the recent interest in this topic since the announcement of Ingenuity. In this work, we discuss an efficient optimization strategy and obtain blade geometries that generate a thrust of 1.1 N with minimal power consumption. This thrust level is approximately equivalent to 300g on Mars and thus would result in a quadcopter (4 rotors) with a mass budget of around 1.2 kg. We also analyze the fact that, due to the reduced density, the weight of the blades might not be negligible and, therefore, should be considered.

Initially, we obtained the best-performing 2-bladed geometries using a multiobjective Genetic Algorithm (GA) using the Blade Element Momentum method as a solver aiming to maximize efficiency and minimize weight while maintaining a thrust level of 1.1 N. The BEM model uses as an airfoil the geometry PoliTO-2, shown in Chapter 3. Reduced-order models are necessary, as optimizations employing full Navier-Stokes CFD simulations are computationally expensive. Using the lessons learned with the multiobjective optimization, we defined a single objective function to allow a less computationally intensive optimization approach, in this case, to find an optimal 3-bladed geometry. We perform Navier-Stokes simulations of both optimal blades. Here, we also compare forces and moments with those obtained with an in-house reduced-order model based on the BEM method to assess its prediction capabilities. Then, we present a further refinement of the blade geometry obtained in the previous Section using a 3D adjoint-based CFD optimization to enhance the blade performance. Finally, we performed a Large Eddy Simulation (LES) of the final blade geometry to assess the potential effects of turbulence on the performance of these blades.

5.1 Methodology

5.1.1 BEM Blade optimization

The blade optimization uses a reduced order model, the BEM method described in Chapter 2, looped into a genetic algorithm. The optimization is subject to a fixed diameter of 0.4 m and a minimum thrust generation of 1.1 N. The atmospheric conditions for our simulations are the average Mars atmospheric conditions reported in Bézard [23], corresponding to a temperature of -63ºC and a pressure of 660 Pa. The atmosphere is idealized as pure carbon dioxide. Such a choice affects the gas constant value in BEM simulations and the fluid characteristics in CFD simulations.

5.1.1.1 Blade Parametrization

We parametrized both chord and twist distributions using an Akima spline interpolation [4] with four degrees of freedom along the radial coordinate. The definition of the control stations for the interpolation appears in Fig. 5.1. The fixed rotor diameter

is 0.4 m. The chord at the root, $c_{15\%}$, located at 15% of the radial coordinate, has been determined according to a non-overlapping condition, with a 25% margin, as shown in equation 5.1.

$$c_{15\%} = 0.75 \cdot 0.15R\,sin(\frac{2\pi}{2N}) \tag{5.1}$$

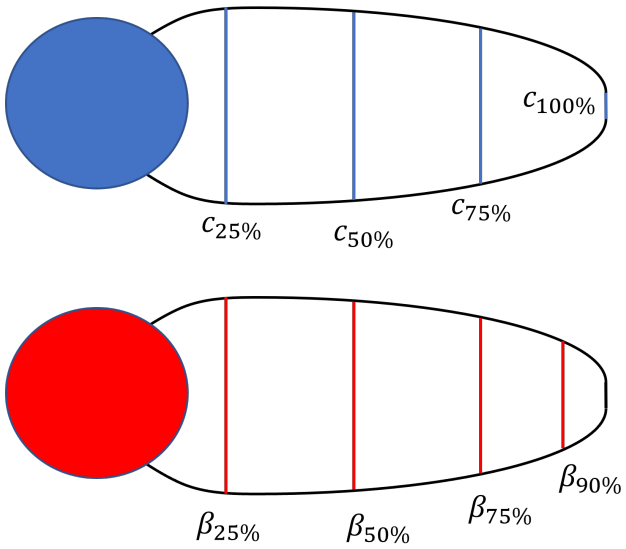

Fig. 5.1 Control stations on the blade for chord and twist distribution.

This choice is necessary so that optimization does not generate too wide chords at the root to compensate for the small Reynolds number. The first three radial stations allow chords ranging from $c_{15\%}$ to $c_{15\%}$ plus 10cm. None of the Pareto front solutions shown in the following section reached the upper limit. The chord at the tip allows values between 0 and $c_{15\%}$. It is worth noting that there are no explicit limitations on manufacturing requirements, such as minimum thickness or maximum solidities. However, except for the near-tip region that can achieve unrealistically small thicknesses, they are implicitly considered in the parametrization in the rest of the blade. This is caused by the fact that we consider a unique airfoil for the whole blade. Realistic designs tend to present increased relative thicknesses towards the tip to avoid structural and manufacturing issues. In this work, we focus on the aerodynamic end of rotor design, but the developed approach is sufficiently general to allow the inclusion of structural and manufacturing constraints.

In the twist distribution, we added a station at 90 percent of the radius to increase the near-tip region resolution, where most of the blade thrust resides. In this case,

we set the twist at the root at 5 degrees to have a flat suction side and allow a smooth transition to the other blade, which occurs through a circular hub. The twist at the tip has been fixed at 6 degrees, as it has shown to be an insensitive parameter in the BEM optimization due to the tip loss correction introduced in the following section. The 6-degree value is chosen because this is the value of the optimal angle of attack of the airfoil at the tip Reynolds number. As the induction at the tip will drop to zero, the local angle of attack and twist angle will be equivalent. The rest of the radial stations are allowed to present a twist between 0 and 45 degrees.

5.1.1.2 BEM Solver Specifications

The BEM solver embedded in *ROT8*, described in Chapter 2, was used for this optimization. The solver requires geometrical inputs to define the blade. These inputs consist of the chord and twist radial distributions, with 8 degrees of freedom. In this optimization activity, we also provide the rotation rate as a design parameter so that the total number of design variables is nine. The rotation rate can vary between 5000 to 8500 RPM. The upper limit is selected to keep the tip Mach number below 0.8. The BEM performance is the fastest within the rotor design tools with a computational cost of around 10^{-5} CPU hours. The speed and simplicity of this code make it one of the most used for design applications. As we will show in the next section, the introduced modifications in the code allow a satisfactory agreement between CFD and BEM predictions, which is very interesting for design purposes, considering the extremely cheap computational cost.

5.1.1.3 Genetic Algorithm: Single-objective and Multi-objective Optimization

We showed in a previous publication [46] that on Mars, it is necessary to consider the mass of the blades in the optimization algorithm, as if the latter is not penalized, large chord generation occurs near the root to compensate for the low Reynolds numbers. This fact deteriorates the performance of the blades, whose weight is not negligible compared to the thrust, and reduces the available mass budget. To compute the mass of the blades, we assume Carbon Fiber as a material with a density of 1600 kg/m^3, and we evaluate the volume integrating the airfoils in the radial direction. The calculation of the weight of the blades considers Martian gravity (3.72 m/s^2). Initially, we propose a Multi-Objective Optimization (MOO) using a Genetic

Algorithm (GA) with the objectives of power loading and blade weight on Mars. The rationale for using a multi-objective approach in the first place is to understand the morphology of the Pareto front and decide the trade-off between the objectives after the optimization has been performed. The employed algorithm is `gamultiobj` embedded in MATLAB [130]. This solver adopts an elitist genetic algorithm, a variant of NSGA-II [68]. It selects 35% Pareto points from a total population of 2000 and evolved for 1000 generations. Table 5.1 summarizes the parameters and settings that characterize the genetic algorithm.

Table 5.1 Multi-objective Genetic algorithm parameters.

Setting	**Value**
Number of Variables	9
Population	2000
Mutation	Adaptive Feasible
Cross-Over Rate	0.8
Pareto set Fraction	0.35
Generations	1000

Based on the multi-objective optimization results, we defined a single objective function that allows a sweep of the Pareto front based on one parameter σ_w.

$$L = \frac{T - \sigma_w W_{Mars}}{P} \tag{5.2}$$

Using the net thrust power loading ($\sigma_w = 1$) prevents the rotor from having too large solidities that would be counterproductive because of their weight. However, Ref.[46] shows how this correction results in large aspect ratios and very thin blades, which could compromise the blade structurally. Selecting $\sigma_w = 0$ is equivalent to performing a purely aerodynamic optimization resulting in large solidities. Section 5.2.2 shows how selecting $\sigma_w = 0.5$ trades off both effects, obtaining a balanced geometry. The aforementioned single objective optimization approach, using the genetic algorithm (*ga*) embedded in Matlab, is followed to design a three-bladed rotor. Table 5.2 specifies the genetic algorithm settings. In this case, we used a smaller population and number of generations. The result was used as an initial condition for a gradient-based optimization to ensure the local optimality of the solution. The algorithm employed was *fmincon* embedded in Matlab's Optimization toolbox.

Table 5.2 Single-objective Genetic algorithm parameters.

Setting	Value
Number of Variables	9
Population	200
Mutation	Adaptive Feasible
Cross-Over Rate	0.8
Generations	100
Elite count	10

5.1.2 Navier-Stokes Evaluations

The mathematical model used in this simulation is the unsteady and compressible Navier Stokes (NS) equations. The calculation of inviscid fluxes adopts a second-order upwind reconstruction scheme combined with Roe's scheme, while the evaluation of viscous fluxes uses a second-order approximation detailed in Chapter 2. The simulations presented in this paper employ a second-order implicit time integration scheme. Rotor rotation modeling follows the sliding mesh approach, in which a rotating inner region flows within a static outer region. This approach uses an AMI (Arbitrary Mesh Interface) algorithm. We initially performed ten revolutions with a time step equivalent to 2.5 degrees per temporal iteration and four revolutions with a time step corresponding to 0.25 degrees per temporal iteration. The latter time step was used in [58, 229, 213] for Detached Eddy Simulations (DES) of several rotors. It allows a reduction of the residual by more than three orders of magnitude in 5 iterations of the internal solver per time step. The first revolutions with a larger time step allow the flow to develop.

Figure 5.2 shows the computational domain of CFD simulations. The domain is a cube with a lateral dimension of 25 rotor diameters and is large enough to avoid wall interference for the simulated physical time.

5.1.2.1 Mesh

Figure 5.3 shows the computational grid. Refinement in the wake region allows the capture of tip vortices and shear layers. This well-resolved region extends axially for a diameter along the wake. The mesh resolution in this region is critical to capture Blade Vortex Interactions (BVI), especially under hovering conditions, as

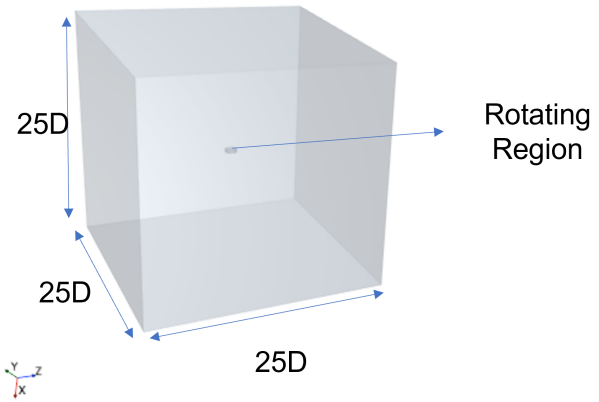

Fig. 5.2 Computational setup for the unsteady simulations.

evidenced in [97, 49]. A secondary wake refinement is also present for the following five diameters, with four times lower resolution. A prismatic layer near the blade surface allows the accurate capturing of the strong gradients near the wall. However, the boundary layer is relatively thick at these low Reynolds numbers and requires less intense mesh stretching. The grid has 15.6 million cells and corresponds to the grid settings used to generate the medium grid shown in Sec. 5.1.2.2, where we demonstrate the grid independence for the final blade simulations. Typical mesh sizes appear in Table 5.3 for three different grids we used in the mesh independence analysis presented in the following section.

Table 5.3 Rotor Grid settings.

Setting	Coarse Grid	Medium Grid	Fine Grid
Target Surface Size (mm)	3.08	1.68	1.4
Minimum Surface Size (mm)	0.11	0.06	0.05
Volumetric Refinement (mm)	4.4	2.4	2
Prism Layers	16	16	16
Wall thickness (mm)	0.01	0.01	0.01
Prism Layer Thickness (mm)	6.6	3.6	3.0

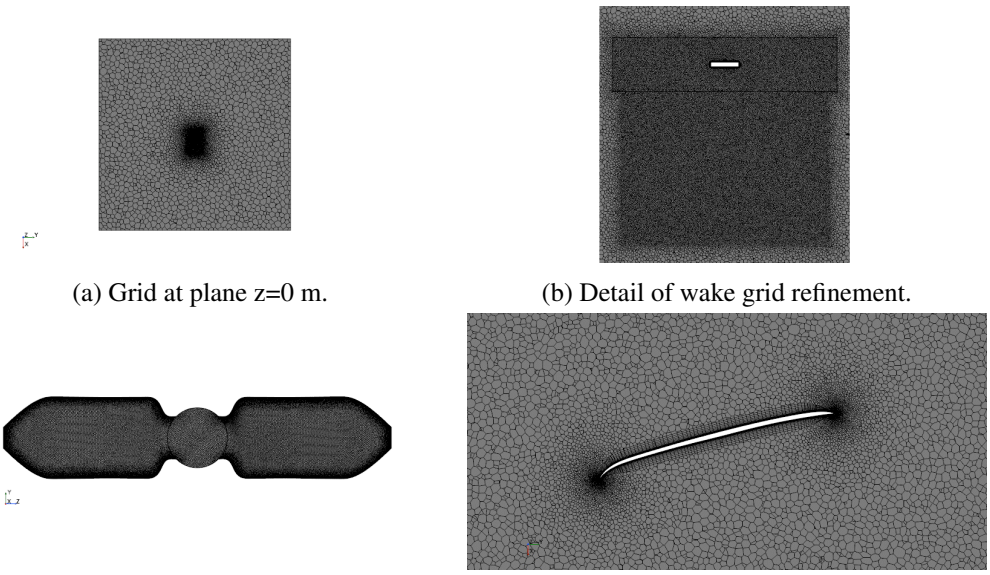

(a) Grid at plane z=0 m.

(b) Detail of wake grid refinement.

(c) Blade surface grid.

(d) Detail of the near-body grid at plane z=0.1 m.

Fig. 5.3 Computational Grid employed for the medium refinement.

5.1.2.2 Mesh Refinement Study

To prove the reliability of the numerical results, we present a grid-independence study for the final adjoint refined 2-bladed rotor. We defined three grid levels: coarse, medium, and fine. To obtain the second and third ones, we consistently reduced the cell size in all settings starting from the coarse level. Table 5.4 reports a difference of about 2% in the thrust between the coarse and medium levels. The difference between the medium and fine levels is less than 0.3% for both thrust and torque.

Table 5.4 Grid refinement study using the Navier-Stokes solver at 7115 rpm.

Grid	Nº Cells	Thrust [N]	Torque [Nm]	T/P [N/W]
Coarse	7.1 Million	1.101	0.0408	0.0362
Medium	15.3 Million	1.123	0.0411	0.0367
Fine	21 Million	1.120	0.0410	0.0367

5.1.2.3 Large Eddy Simulation

In this ultra-low Reynolds number context, we may consider Navier-Stokes solutions as scale-resolving simulations, which could approach Direct Numerical Simulations

(DNS) with an adequate grid resolution. However, the default Navier-Stokes solver embedded in STAR-CCM+ is just second-order accurate, which is inaccurate compared with typical DNS solvers. In addition, the grid resolution is insufficient to capture the small structures in the case transition to turbulence occurs. The solver's capability of precisely predicting rotor performance is closely related to the boundary layer resolution and the flowfield organization during the first revolutions of the wake due to the BVI. At these low Reynolds numbers (<14000), if the flow is attached, it seems reasonable to work under the hypothesis that the boundary layer will remain laminar as a separation-induced transition triggered by Kelvin-Helmholtz (K-H) instabilities developing in the separated shear layer is the only transition mechanism expected in the boundary layer. However, it is unclear if transition to turbulence in the wake could affect the blade performance. For this purpose, we performed an LES with a third-order central difference solver with a 15% upwind blending to stabilize the solution, as shown in Chapter 3 for the airfoil case. This LES can be interpreted as a Detached Eddy Simulation (DES), meaning that we are only attempting to have an adequate grid resolution to capture transition in the wake as the boundary layer on the designed blades is attached (Fig. 5.19) and, therefore, laminar. The selected Sub-Grid Scale (SGS) model used is the Dynamic Smagorinsky model [88] applying the modifications proposed by Lilly [121]. The LES simulations use a 21 million cells grid with the same time-step settings as the Navier-Stokes simulations. We chose these settings in agreement with the DES simulations of rotor flows presented in [213, 229] and should allow a sufficient temporal resolution to capture eventual vortical structures occurring on the wake.

5.1.3 Navier-Stokes Adjoint Rotor optimization

The steady adjoint solver settings are similar to those used for the airfoil optimization presented in Chapter 3. Exceptions are the definition of the control points, shown in Fig. 5.13, which have an offset of 5 mm from the surface, and the definition of the objective function, which is defined as follows:

$$X = \frac{T^{3/2}}{Q} \tag{5.3}$$

This function allows simulations with constant rotation rates, ensuring that even if the blade thrust decreases, the rotation rate can be increased, improving the blades'

power consumption. This approach noticeably accelerates the convergence of the Navier-Stokes equations solutions without the need to adjust the rotation rate at each iteration. Control points are free to move in the tangential and axial directions but not in the radial direction to avoid rotors with larger diameters. This way, airfoil geometry, twist distribution, and chord distribution can change.

The unsteady simulation shown in the previous section reveals that the flow on the blade is attached and stable in a reference frame that rotates with it. The only source of instability is a vortex shedding downstream of the trailing edge. Therefore, the Navier-Stokes (primal) simulation adopts the Moving Reference Frame (MRF) approach described in Chapter 4, where the Navier-Stokes equations frame of reference rotates with the blade. Despite the technique's steady-state nature and the flowfield's imperfect resolution at the trailing edge, it is possible to reproduce the boundary layers and initial tip vortex revolutions with acceptable accuracy, as corroborated in Chapter 4 for the T-motor 15"x5" blade. The general consistency between steady-state and unsteady solutions suggests that an optimal shape obtained through the steady-state approach will also improve performance in time-accurate simulations. As shown in Chapter 4, the computational cost of the MRF approach is about an order of magnitude lower than the unsteady sliding-grid approach. That is due to using a periodic boundary condition, which allows the simulation of only one blade, thus halving the number of cells in the case of the 2-bladed simulation and dividing the cell count by a factor of 3 in the 3-bladed simulations. Also, since we keep the adjoint step at 0.5 mm, the converged solution of one adjoint iteration is a good initial condition for the next adjoint iteration.

These steady-state calculations adopt a simplified domain that takes advantage of the periodic symmetry of the problem. The outer static region has the shape of a halved truncated cone. The solution of the Navier-Stokes equations in the rotating reference frame takes place in an inner cylindrical domain to model the rotation of the blade. In this second computational domain, the formulation of the governing equations of fluid dynamics contains the centrifugal and Coriolis accelerations as source terms, as explained in Chapter 4. We insert a free stream in the axial direction with a velocity of 0.25 m/s. Figure 5.4 shows the boundary conditions and periodic interfaces that define the problem. It is clear that the periodicity boundaries are set at 180 degrees for the two-bladed geometry, and for the three-bladed geometry, it goes down to 120.

The grid used for these simulations is equivalent to the medium grid shown in the previous section in the region near the blades. The wake region is slightly less refined to promote convergence by damping the instability observed downstream of the trailing edge. The number of cells for these simulations is around 6.5 million cells.

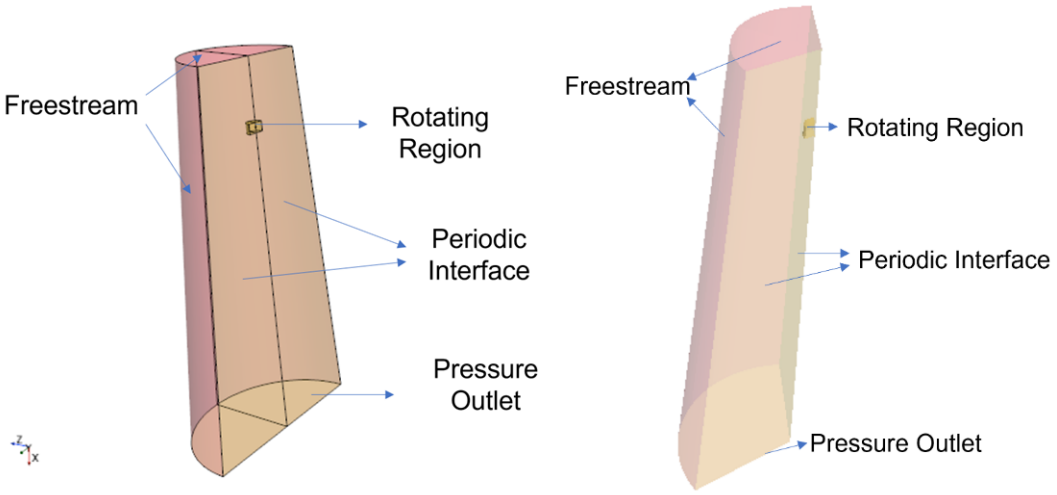

Fig. 5.4 Boundary conditions and computational setup for MRF simulations. 2-bladed rotor (left) and 3-bladed rotor (right),

5.2 Results

5.2.1 Aerodynamic Database

The airfoil PoliTO-2 discussed in Chapter 3 was used as our baseline geometry to construct our rotor. We computed the polar curve for a Mach number of 0.5, which is the Mach number expected in the radial stations comprising 75%-90% of the blade, the most relevant region regarding thrust generation and power consumption. We extrapolated the polar to the remaining radial stations using the Prandtl-Glauert transformation [89]. Such a correction will provide a first-order estimation of compressibility effects. The transformation scales up the incompressible pressure coefficient, which one can extend directly to lift and drag coefficients at high Reynolds numbers, as the shear drag component will be negligible. At lower

Reynolds numbers, boundary layers become thicker, and the shear drag becomes of the same magnitude as the pressure drag. Furthermore, compressibility will affect the boundary layer behavior, as can be deduced from Karman's equation [75], creating uncertainties regarding drag predictions. However, Bézard [24] shows that the lift-to-drag ratio of the tested airfoil is almost insensitive to the Mach number up to M=0.5, while the flow does not present leading edge separation. Table 5.5 shows how Prandtl-Glauert's transformation predicts lift and drag coefficient values within 5% of CFD's obtained values. Keeping in mind that this transformation derives from the potential flow equation, it approximates relatively well the variation in the lift and drag coefficients induced by compressibility. Therefore, it seems unnecessary to compute a full Polar for different Mach numbers, especially considering that the final 3D adjoint-based optimization will perform a final tuning of the blade.

Table 5.5 Compressibility effects assessment. PoliTO-2, AOA=4 degrees and Re=10,000.

Mach Number	**Calculation**	C_l	C_d	**L/D**
0.5	CFD	1.01	0.0568	17.78
0.1	CFD	0.92	0.0512	17.96
0.1	Prandtl-Glauert	0.88	0.0494	17.78

5.2.2 BEM-based multiobjective optimization

We adopted the PoliTO-2 airfoil for the whole blade due to its high efficiency at different Reynolds numbers. This study was performed before deriving all the airfoils reported in Chapter 3; therefore, the choice was evident compared to PoliTO-1. The optimization could benefit from changing airfoils with radial stations due to the noticeable variations in the Reynolds and Mach numbers. However, as we will refine the geometry with a 3D adjoint optimization, using a single airfoil for this preliminary BEM optimization seems reasonable. Sec. 5.1.3 presents the airfoils of the morphed blade showing how these are considerably different depending on the radial station. The computing time was around 24 hours on an 8-core AMD RYZEN 7. Figure 5.5 shows the Pareto front (blue) and highlights how, by loosening the weight limit, the aerodynamic efficiency of the blades increases up to a weight of about 0.24 N, where the Pareto front ends. This point represents the blade with maximum power loading and would be close to the value obtained from a single objective optimization that

does not consider the weight of the blades. The other end of the Pareto front depends on the minimum chord allowed by the parameterization. To perform a relevant comparison of the blades forming the Pareto front, we increased the rotation rate of all the optimal blades until the produced net thrust equals 1.1 N. The red plot in Fig. 5.5 shows the power loading obtained at the required net thrust level. We can appreciate that the corrected power loading function is relatively flat between 0.1 and 0.195 N, with a peak around 0.13 N. These points do not represent blade designs that optimize net thrust, but they show how, in the Martian context, the mass of the blades may not be negligible to maximize a mass budget. Figures 5.6 and 5.7 display the chord and twist radial distributions of 15 representative blades from the Pareto front, obtained for different weight values. It is noteworthy that unlike chord variations along the radius combined with an adequate twist distribution can provide quite similarly performing blades. This fact is interesting as structural and manufacturing reasons may constrain the chord and thickness distributions, but the twist distribution could still optimize the performance for that particular chord distribution. Another aspect arising from Fig. 5.6 concerns how the chord distribution varies in the radial direction as we increase the available mass budget for the blade. First, the chord near the tip responsible for most of the thrust generation increases. Then, as more weight is allowed, the chords near the hub increase to compensate for the reduced Reynolds numbers. In addition, the optimal rotation rate drops with increased chords to maintain the desired thrust level.

Among the 700 Pareto solutions available, we selected the blade configuration with a weight of 0.18 N. This blade maximizes the single objective function defined in equation 5.2 using $\sigma_w = 0.5$. This geometry is in the range where the corrected power load has a flat trend close to the maximum. In addition, the rotation rate is not the fastest, which is interesting from a structural point of view and provides some margin before the onset of transonic effects due to the lower tip Mach number. Finally, the blade has high solidity, which reduces its loading, potentially producing a structural advantage.

Figure 5.8 shows the resultant two-bladed rotor. The chord distribution is almost constant, up to 80% of the radius. Figure 5.9 shows the distribution of torsion and other quantities predicted by the BEM solver. Interestingly, the angle of attack is inversely proportional to the Reynolds number, and the lift coefficient remains close to 1 along most of the radial coordinates, except in the tip region, where it increases. We expected the decrease of the angle of attack with the Reynolds number, as the

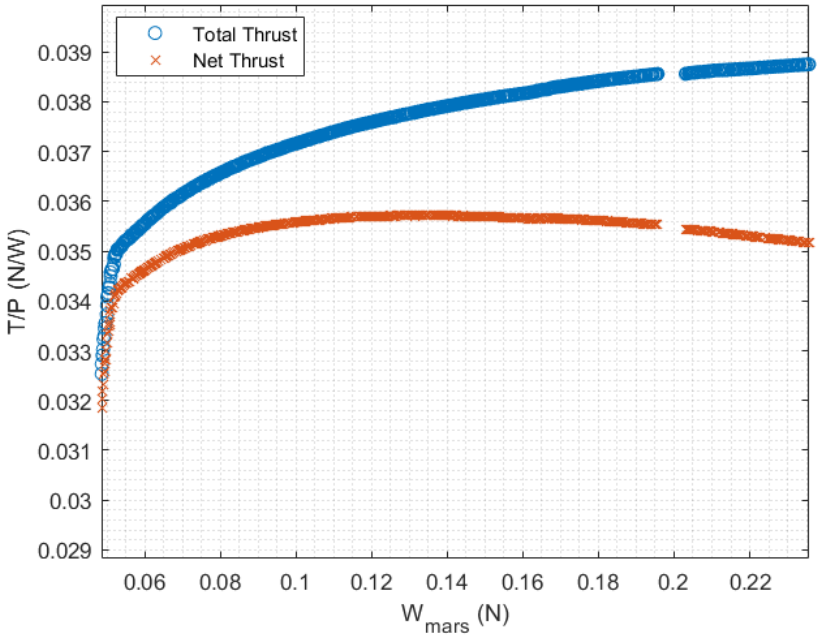

Fig. 5.5 Pareto front and net thrust correction.

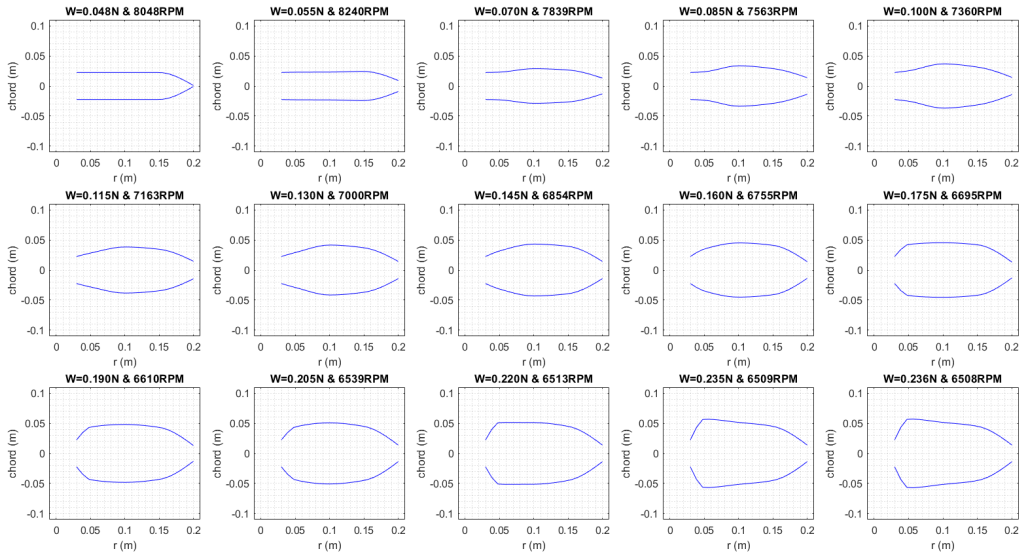

Fig. 5.6 Chord distributions for different Pareto optimal solutions.

optimizer tries to profit from the maximum efficiency angle of the airfoil, which decreases with the Reynolds number as shown in Fig. 3.53. That is also why the lift coefficient remains close to one, as this value corresponds to the maximum efficiency.

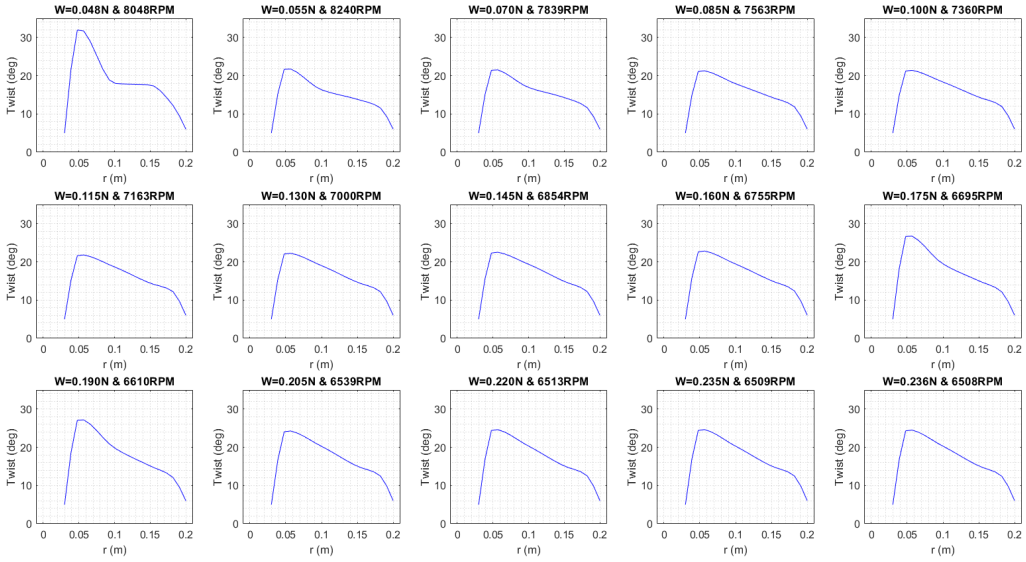

Fig. 5.7 Twist distributions for different Pareto optimal solutions.

The most efficient part of the blade is the region near the tip, while the area near the hub performs less well and becomes a candidate region for weight reduction. Table 5.6 reports the blade performance predictions according to the BEM model.

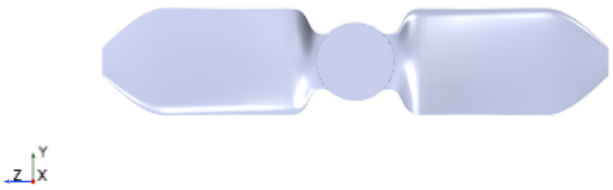

Fig. 5.8 BEM: optimal 2-bladed geometry.

5.2.3 BEM-based single-objective optimization

A single objective optimization using a genetic algorithm was followed to compute an optimal three-bladed geometry using $\sigma_w = 0.5$. The algorithm evaluated around 20,000 geometries before it converged. A very small number compared to the around 1,000,000 geometries evaluated in the multiobjective optimization. It is fair to note that the initial settings of the multiobjective approach are different and could probably

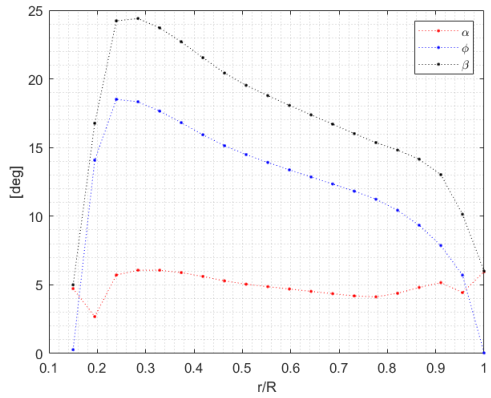

(a) Geometric (β), inflow (ϕ) and attack (α) angles

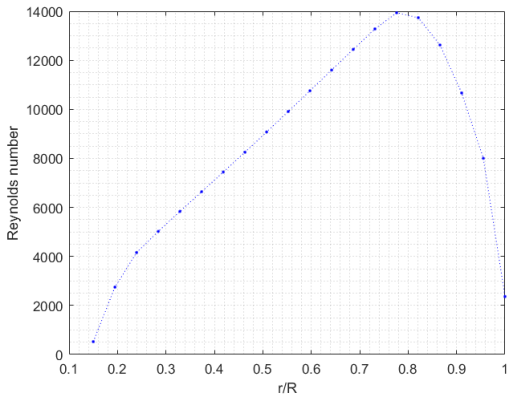

(b) Reynolds number.

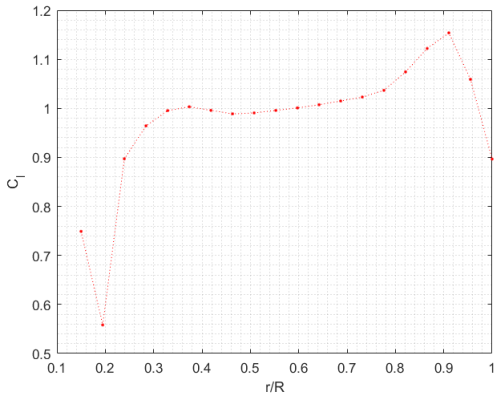

(c) Lift Coefficient.

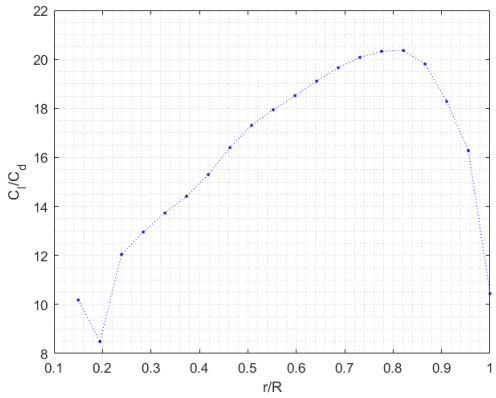

(d) Lift-to-drag ratio.

Fig. 5.9 BEM: local results on the optimal geometry.

be improved. Nevertheless, the computational cost would inevitably be higher than that obtained for the single objective optimization. This approach took less than an hour on an 8-core AMD RYZEN 7. The multiobjective optimization using the BEM approach takes around 24 hours which is affordable. However, if we switch the solver to a vortex method, the hour would easily transform into days, and 24 hours would transform into months running in the same machine. In these cases, a single-objective optimization penalizing mass could be a more reasonable option.

This geometry presents noticeable differences from its two-bladed counterpart. The chord is not constant and reaches its maximum at around 75% of the radial coordinate, as shown in Figure 5.10. Figure 5.11 shows the distribution of the blade twist and other quantities predicted by the BEM solver. The Reynolds number is

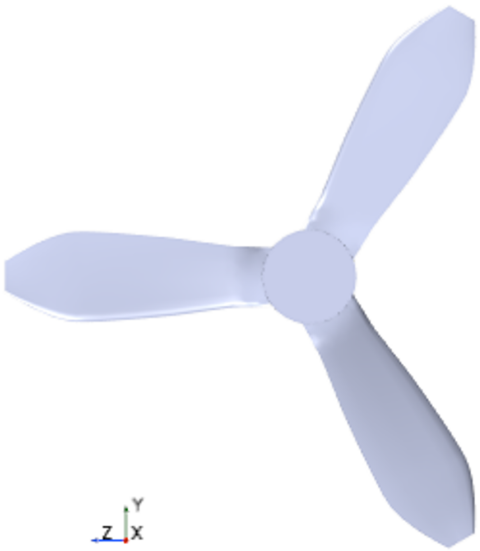

Fig. 5.10 BEM: optimal 3-bladed geometry.

globally smaller in all radial stations since an almost identical solidity is divided into more blades, and the lift coefficient is below the optimal. It seems that as the number of blades increases, the optimizer prefers to concentrate the solidity and thrust generation in the most efficient region of the blade. It is possible that as the number of blades increases, the value of the weighing parameter σ_w should be relaxed to avoid too thin geometries towards the hub.

5.2.4 Blade Element Momentum Method and Navier-Stokes performance prediction comparison

Table 5.6 shows that BEM over-predicts thrust by approximately 3% and under-predicts torque by 4%, reducing the power loading by about 7% for the 2-bladed geometry. Similar results are obtained for the 3-bladed geometry, in which a 4% overestimation of thrust and a 2% reduction in torque is obtained. This trend is compatible with an over-prediction of the lift coefficient. These results are satisfactory considering the substantial simplifications incorporated in a two-dimensional lifting-line-based theory, such as the BEM method and its speed compared to CFD simulations.

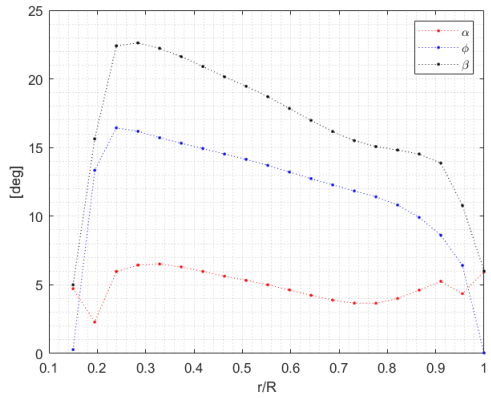

(a) Geometric (β), inflow (ϕ) and attack (α) angles

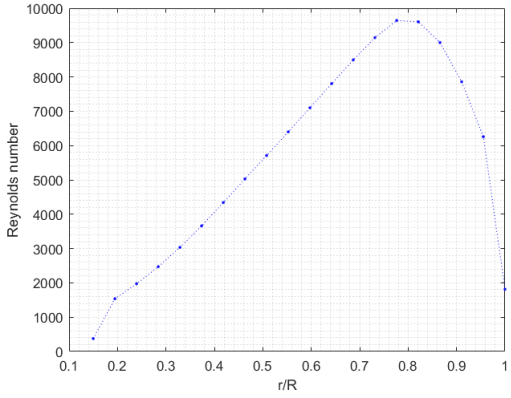

(b) Reynolds number.

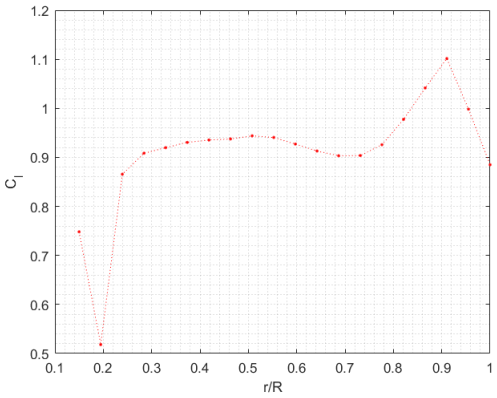

(c) Lift Coefficient.

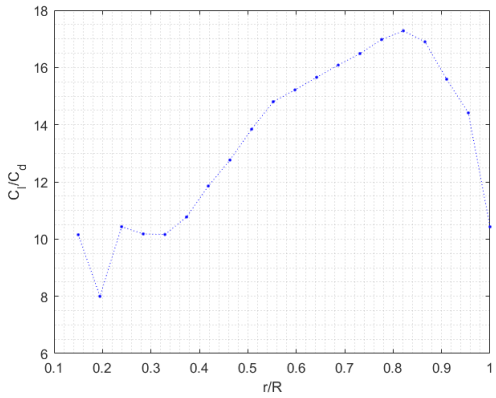

(d) Lift-to-drag ratio.

Fig. 5.11 BEM: local results on the 3-bladed optimal geometry.

We can see that the employed rotation rate cannot fulfill the thrust requirement. The simplest way to match the thrust constraint is to increase the rotation rate with the square root of the ratio between the desired and actual thrust. Dimensional analysis shows that such a relationship only holds when the Reynolds and the Mach numbers are constant. In our case, the required variation is so slight that Reynolds and Mach numbers do not change significantly, and the relationship holds. We demonstrate this fact in [46]. Therefore, Table 5.6 shows the results of an additional CFD simulation at an adjusted rotation rate that provides the required thrust level for a realistic comparison of power loadings.

Figure 5.12 compares the radial thrust and torque distributions obtained with CFD and BEM solvers for the two-bladed geometry. It shows an overall satisfactory

Table 5.6 Optimal BEM geometries.

Blade-Solver	Omega(rpm)	Thrust(N)	Torque(Nm)	T/P (N/W)
2 Blades-BEM	6596	1.10	0.0414	0.0385
2 Blades-CFD	6596	1.073	0.0433	0.0359
2 Blades-CFD	6678	1.10	0.0444	0.0354
3 Blades-BEM	6518	1.10	0.0432	0.0373
3 Blades-CFD	6518	1.057	0.0440	0.0352
3 Blades-CFD	6649	1.10	0.0458	0.0345

agreement of torque and thrust radial distributions between both solvers with the BEM method that slightly overestimates the maximum thrust and torque values. Considering that the computational cost of one blade evaluation using the BEM code (10^{-5} CPU hours) is several orders of magnitude lower compared to the CFD approach (10^{3} CPU hours) and the relatively good performance estimation obtained, the BEM solver seems an adequate solver to embed in the optimization algorithm. That is especially true considering that the adjoint optimization step discussed in the following section corrects the inaccuracies in the induction prediction introduced by the reduced-order model.

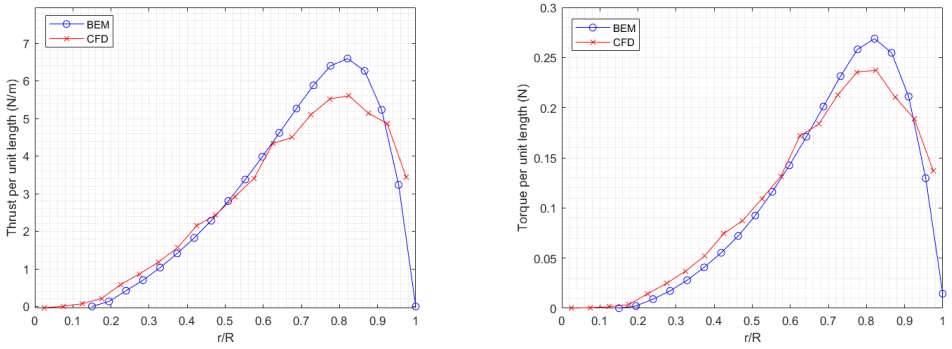

(a) Thrust radial distribution

(b) Torque radial distribution.

Fig. 5.12 Local forces and moments on the 2-blade rotor as predicted by different solvers.

5.2.5 Navier-Stokes Adjoint Rotor optimization

In order to perform an ulterior refinement of both BEM optimal geometries, an adjoint-based optimization is performed as explained in Section 5.1.3. Figure 5.13

shows the lattice of points that the morpher uses to deform the grid. After optimization, adjoint sensitivities to the objective function suggest reducing the curvature at the trailing edge and the angle of attack in the 75%-90% radial coordinate region. Figure 5.14 displays the final shape of the blade after 16 adjoint iterations. Figs. 5.15 and 5.16 shows the airfoil geometry at different radial stations for both blades. We notice that the airfoil geometry has a reduced camber towards the tip, where the Reynolds number is the largest and is evenly distributed throughout the chord. It is also noticeable how the maximum camber position moves towards the leading edge as the Reynolds number increases. The angle of attack got smaller along most of the blade span except in the vicinity of the tip region. It is interesting to see how the modifications introduced by the adjoint solver move in the same direction for both blades, even for very different planforms and rotation rates.

Table 5.7 Comparison between BEM and CFD-Adjoint optimal geometries.

Geometry-Solver	**Omega(rpm)**	**Thrust(N)**	**Torque(Nm)**	**Power (W)**
2B-BEM-CFD	6678	1.10	0.0444	31.07
2B-Adjoint-CFD	7042	1.10	0.0403	29.72
2B-Difference(%)	5.5	0	-9.2	-4.4
3B-BEM-CFD	6649	1.10	0.0458	31.89
3B-Adjoint-CFD	6504	1.10	0.0433	29.91
3B-Difference(%)	-2.2	0	-5.5	-6.2

To compare the performance of the final blade geometry with others, we performed a full unsteady Navier-Stokes simulation with the same grid settings that we used to evaluate the optimal BEM geometry. Table 5.7 shows that the adjoint method improves the performance of two and three-bladed rotors. In the case of the two-bladed rotor, we can appreciate a reduction in power consumption of 4.4% in comparison with the BEM optimal blade. Interestingly, the new geometry tends towards a lower torque configuration operating at a higher rotational speed. However, due to the choice of the objective function, the result is a decrease in energy consumption. Similarly, the three-bladed design has a slightly more significant improvement in power consumption than the BEM baseline design achieving a 6.2% reduction. In this case, the optimization converts the geometry into a slightly lower torque configuration with a slight decrease in rotation rate, further improving the blade's efficiency.

Both rotors present a figure of merit around 0.60. This result is consistent with the experimental and numerical values that Koning [106] show for the Martian Helicopter rotor for an equivalent blade loading of 0.11. Considering that our radius is limited to 0.2 m compared with the 0.605 m of the Martian rotor blade, the results look promising as increasing the rotor diameter could potentially improve the performance due to the increase in the Reynolds number, reducing the rotation rate and chord distribution for a constant tip velocity. The blade geometry proposed by Bézard [23] for the upper rotor of the 300 g coaxial helicopter configuration has a figure of merit of 0.55, 10% lower compared to our rotors. However, they limit the radius to 0.15 m, and thus the results may not be comparable. In any case, we can conclude that the proposed blade design procedure generates rotor geometries that are at least as performing as those designed using other techniques based on vortex methods.

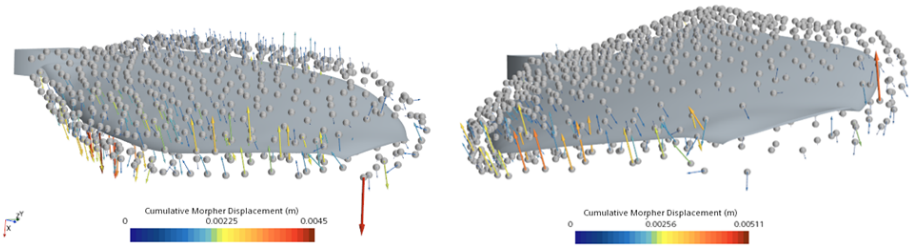

Fig. 5.13 Morpher control point displacements after the adjoint optimization process for the two-bladed rotor (left) and three-bladed rotor (right).

5.2.6 Navier Stokes evaluations and Large Eddy Simulations

We performed an LES of the two-bladed adjoint optimal geometry to further strengthen the confidence in the numerical approach. We show thrust and torque instantaneous temporal histories for LES simulations in Figs. 5.17 and 5.18. We can appreciate a good convergence with 14 revolutions for both thrust and torque. The loads are unsteady, but the peak-to-peak oscillation is below 1% of the total value. These results align with Bézard's[23] research which finds statistically converged results in 15 revolutions. Such a value is approximately half of the convergence requirement for DES found by some authors [229, 58] for the XV-15 Rotor. The fact could be related to the small influence of turbulence in our blade loading or the higher

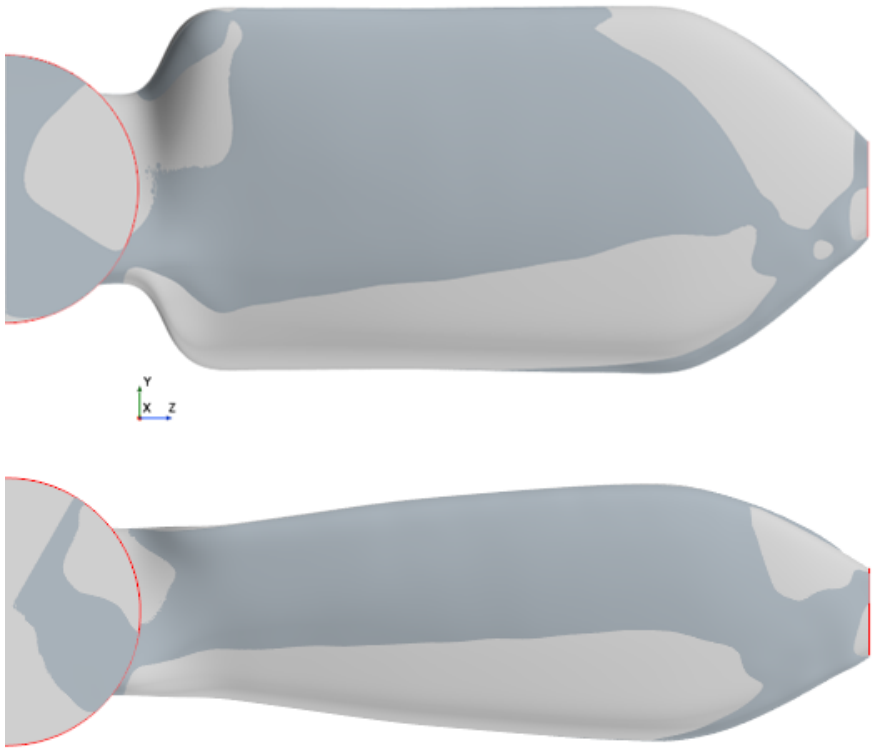

Fig. 5.14 Comparison between the original (light grey) and final morphed surface (dark grey) for the two-bladed rotor (left) and three-bladed rotor (right).

thrust coefficient that allows faster convergence of the induced velocity. Table 5.8 compares the performance predictions between Navier-Stokes solutions and LES. These values have been computed by averaging the thrust and torque values over one revolution. The values are almost identical. However, Figs. 5.20 and 5.21 show that the vorticity distribution is not the same. The first difference is that the Navier-Stokes second-order accurate solution is far more dissipative than the LES solution. The second one is that the shear layer in the LES is breaking down into smaller vortices. Figures 5.22 and 5.23 display the Q-criterion isosurfaces for both simulations. Even though the Navier-Stokes solver starts to capture the vortex breakdown due to its scale-resolving nature, only LES can capture accurately the full wake breakdown into smaller structures. The third-order scheme used for LES is also related to the enhanced vortex breakdown, probably even more than the influence of the actual subgrid stress model. In this regard, Ref. [196] shows how higher-order schemes

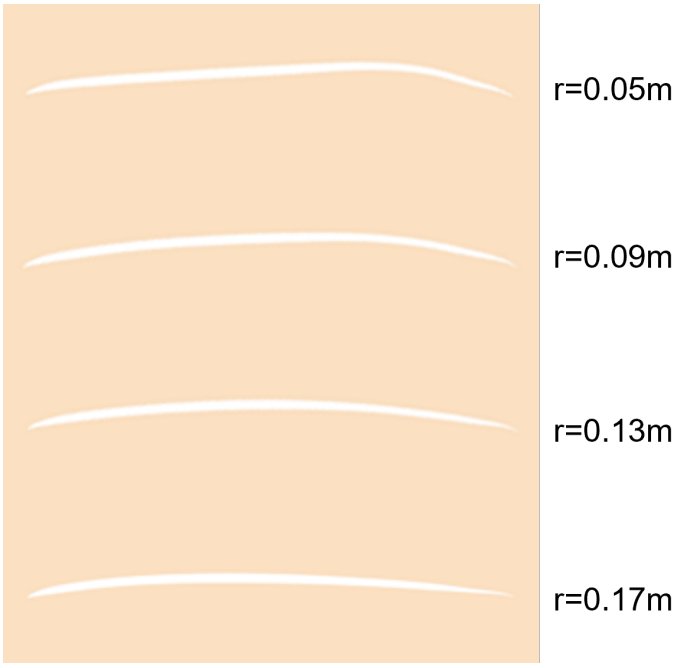

Fig. 5.15 Normalized airfoil sections at different radial stations after adjoint optimization. Two-bladed rotor.

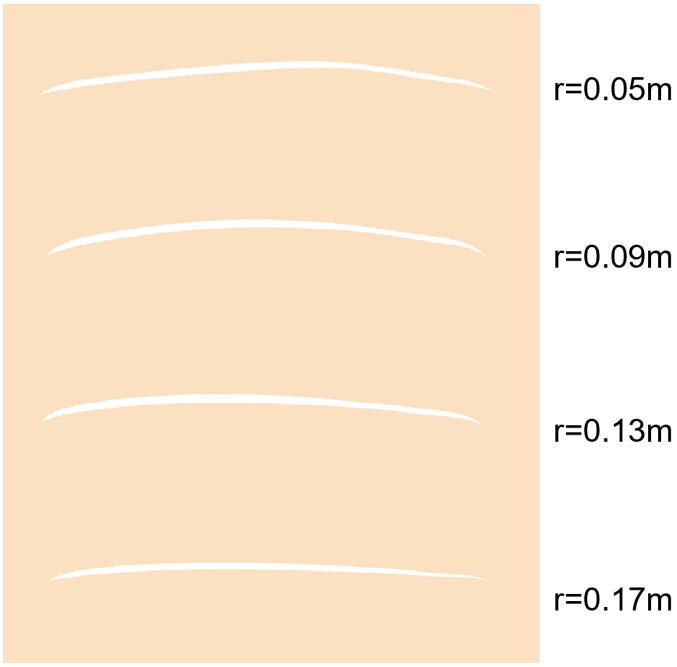

Fig. 5.16 Normalized airfoil sections at different radial stations after adjoint optimization. Three-bladed rotor.

can capture vortex breakdown in the rotor wake even using RANS. Despite the differences in the wake structure, the impact on performance is minimal, which brings us to the conclusion that Navier-Stokes solutions are a sound choice for predicting rotor performance in the Martian atmosphere. Figure 5.19 shows friction lines on the suction side of the blade's surface. One can see that the flow remains attached until the trailing edge, where the streamlines align with the radial direction due to the absence of the centripetal acceleration caused by the skin friction.

Table 5.8 LES and Navier-Stokes solver comparison using the 21 Million grid at 7115 rpm.

Solver	Thrust [N]	Torque [Nm]	T/P [N/W]
Navier-Stokes	1.120	0.0410	0.0367
LES	1.121	0.0410	0.0367

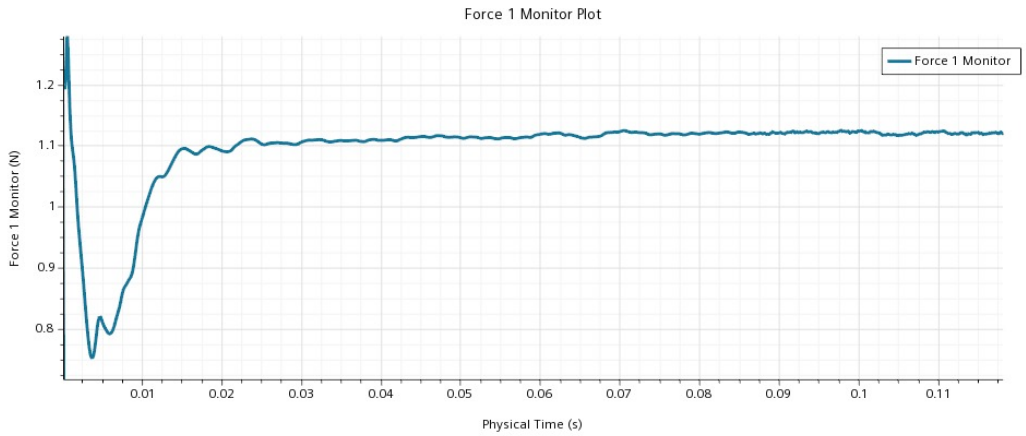

Fig. 5.17 Instantaneous thrust temporal evolution.

5.3 Discussion

The multi-fidelity optimization procedure described in this Chapter provides aerodynamically efficient blades comparable with other state-of-the-art rotor designs in the literature. The overall computational cost for an optimized blade generation is around one week using the 32 cores of an Intel Xeon Scalable Processors Gold 6130 2.10 GHz. This technique represents a computationally affordable alternative to the typically employed rotor design strategies using reduced-order models. We combine

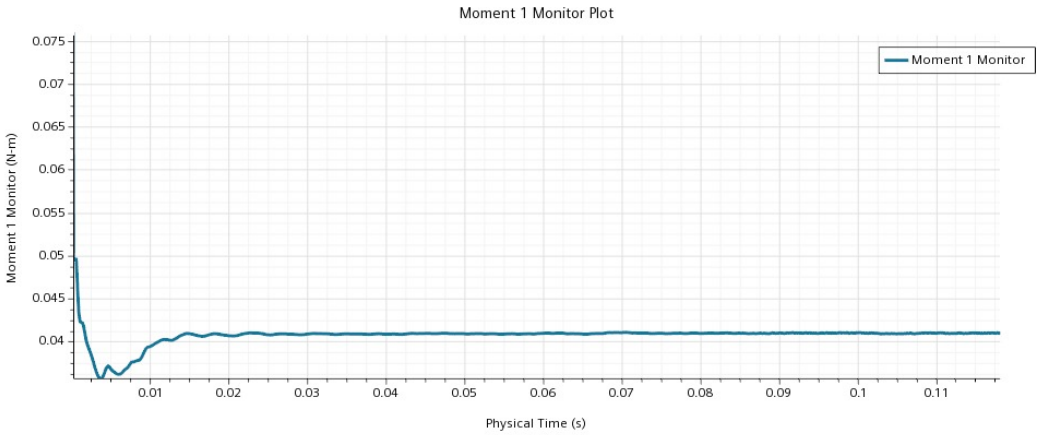

Fig. 5.18 Instantaneous torque temporal evolution.

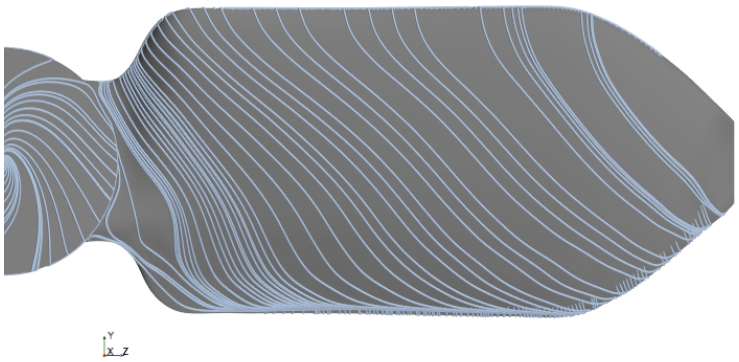

Fig. 5.19 Friction lines over the suction side of the optimal rotor for LES simulation.

global optimization algorithms (Evolutionary Algorithm) with local gradient-based optimization (CFD-Adjoint) to individuate maximal blade performance.

Two genetic algorithms were assessed. Initially, we performed a multiobjective optimization to understand the influence of considering the mass of the weight in the optimization process for a two-bladed rotor. The lessons learned from this approach allowed us to define a single objective function that trades off aerodynamic efficiency and the mass of the blades in a weighted manner avoiding geometries with too large aspect ratios in a three-bladed rotor. The single-objective algorithm required 50 times fewer rotor evaluations (20,000 vs. 1,000,000) to converge, rendering it computationally cheaper. On the other hand, multiobjective optimization provides

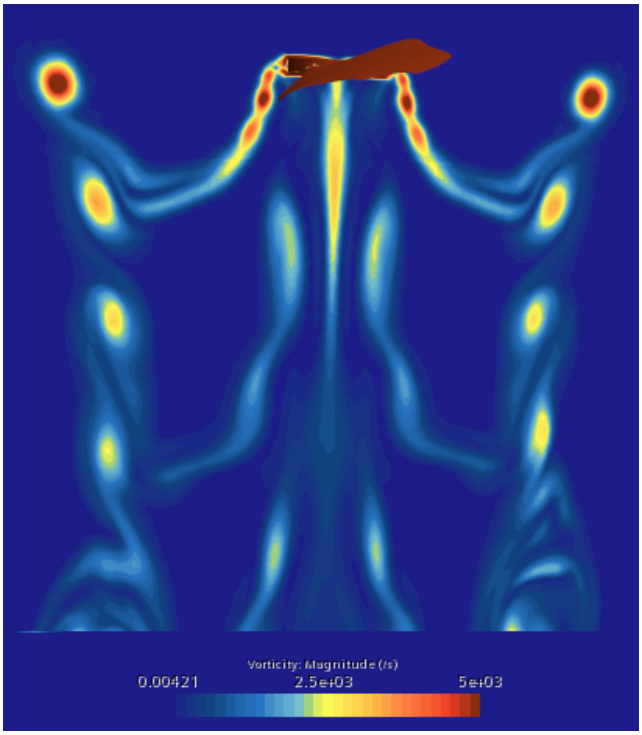

Fig. 5.20 Vorticity magnitude field for the Navier-Stokes simulation at plane z=0.

the decision maker with a set of geometries from which to select, which is very interesting as no decisions have to be made before the optimization process.

The adjoint optimization has proven reliable in obtaining well-performing geometries even though it uses the steady Navier-Stokes equations formulated in a rotating reference frame for the 3D case. Such a result is not a foregone conclusion because the flowfield around 2D airfoils and 3D blades showed some unsteadiness in time-dependent simulations. The 3D adjoint optimization maintained chord distribution revealing a preference to modify twist and airfoil distributions. The two- and three-bladed geometries optimized via the adjoint method present very similar performances obtaining a figure of merit of 0.60. It is remarkable how, despite the very different initial conditions and number of blades, the adjoint solver can morph the blades in such a way as to obtain almost identical performances. This observation suggests that the global optimum is reasonably flat. Therefore, sub-optimal geometries for a given chord condition can be obtained with performances close to the global maximum.

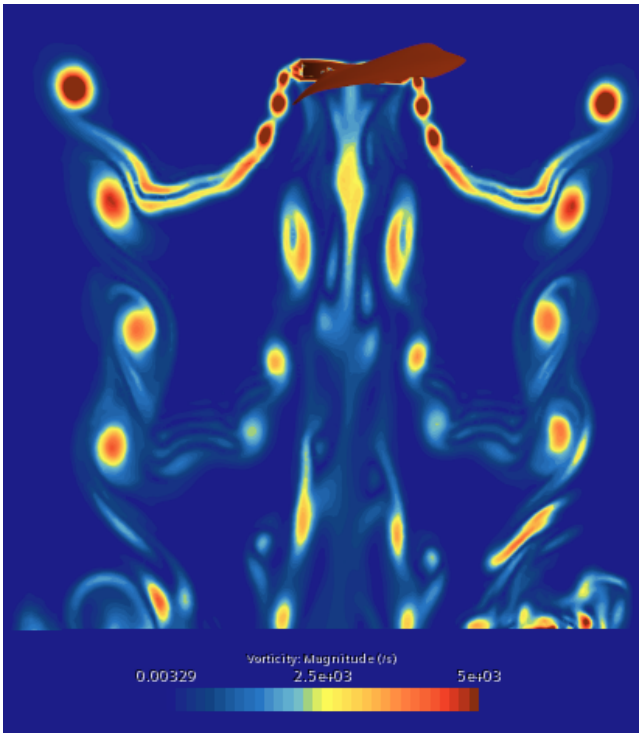

Fig. 5.21 Vorticity magnitude field for the LES simulation at plane z=0.

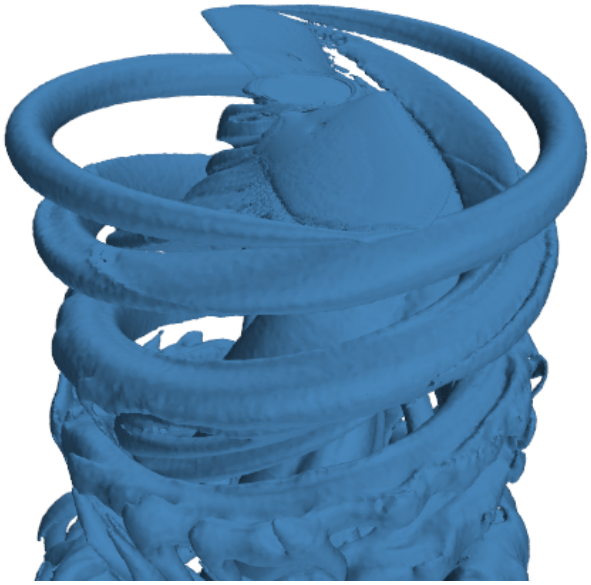

Fig. 5.22 Q-criterion isosurface for the Navier-Stokes simulation

We demonstrated grid convergence for Navier-Stokes simulations in the case of the two-bladed rotor. Second-order accurate Navier-Stokes simulations and third-

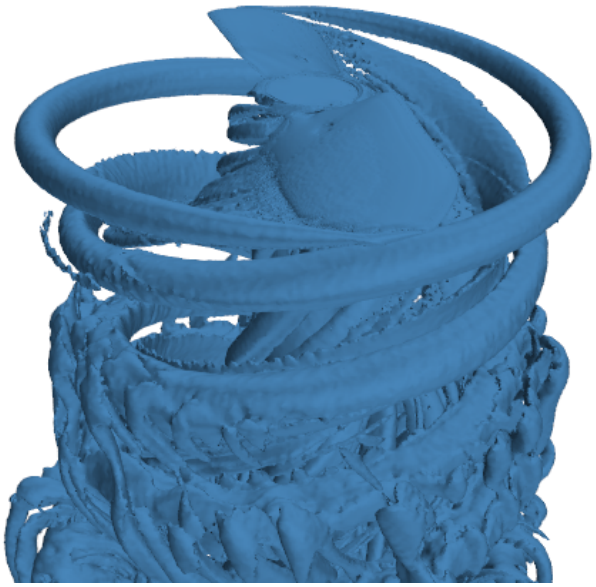

Fig. 5.23 Q-criterion isosurface for the LES simulation.

order accurate Large Eddy Simulations (LES) provide very similar rotor performance predictions despite the differences in the flow field in the wake region, which in the case of LES shows the breakdown of vortices and shear layer into smaller structures. As the angles of attack for efficient blades are usually moderate where the boundary layer is attached, we expect Navier-Stokes simulations to be sufficiently accurate to predict rotor performance in this Reynolds number regime. It is worth mentioning that recent designs of Martian blades include sharp leading edges that trigger separation. These cases require a dedicated analysis as the vortex shedding regime created on the suction side will probably anticipate the onset of transition to lower Reynolds numbers.

Chapter 6

Numerical Modelling of Swashplateless Rotors

This Chapter presents a numerical investigation of the passive swashplateless rotor concept using Computational Fluid Dynamics and the 6 degrees of freedom solver embedded in the commercial software STAR-CCM+. The main difference between active and passive pitch control strategies from a numerical point of view is the prior knowledge of the trajectory of the aerodynamic surfaces in the simulation in the case of active solutions. In this case, CFD simulations can calculate aerodynamic forces as a response to a prescribed motion [103]. In the case of passive pitch control strategies, a prescribed motion is applied to the hub, but the presence of a hinge uncouples the pitch-lag degree of freedom from the motion around the main rotation axis of the rotor. This is a challenge from a numerical point of view and is probably one of the aspects because of which this very interesting swashplateless solution has not been assessed numerically until now. We developed a time-efficient azimuthally resolved BEM approach to evaluate the forces and moments generated by these rotors. The results of this model show a good agreement with the higher fidelity 6-DOF-CFD approach with a computational cost several orders of magnitude smaller.

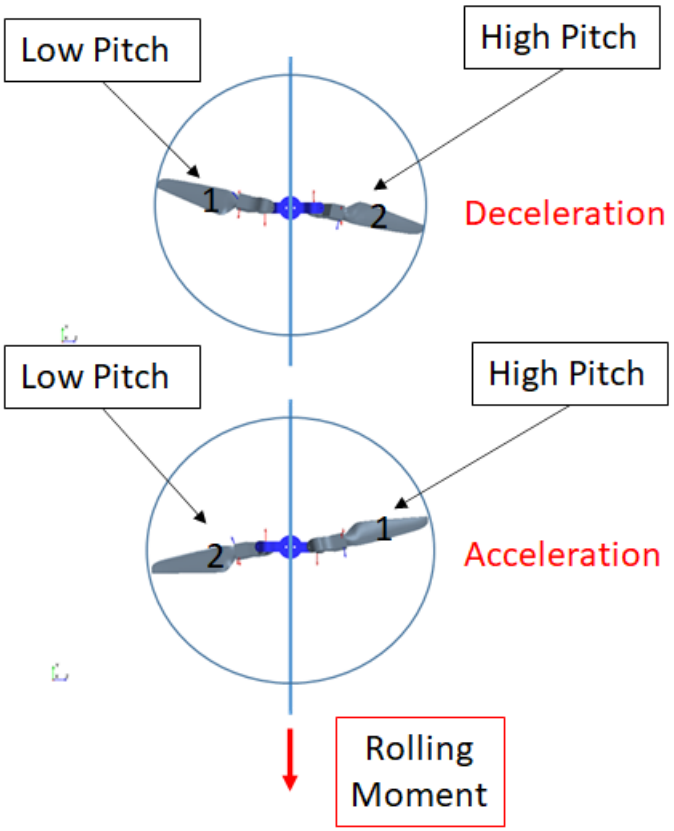

Fig. 6.1 Swashplateless Rotor pitch-lag coupling control.

6.1 Preliminary Swashplateless Rotor

The partially articulated rotor provides cyclic control replacing the swashplate and its associated actuators. This innovative concept couples asymmetrically lag and pitch to obtain, allowing the MAV to change the roll and pitch, employing the passive blade response. The two antisymmetric hinges have the axis on the same plane as the motor's shaft, but both axes are inclined at a certain angle by which the proportion of lag-pitch coupling can be controlled [152]. This angle, θ, is fixed with respect to the horizontal.

The antisymmetric disposition of the hinges creates one blade with positive lag-pitch coupling and the other with negative lag-pitch coupling. This means that the blade that presents a positive coupling increases its pitch when it lags forward, and the blade with a negative coupling decreases its pitch when the blade lags forward. For instance, when the motor is accelerating, both blades lag behind. This creates a

higher thrust on the negatively coupled blade than the positively coupled one. Figure 6.1 shows how if the accelerations and decelerations are adequately synchronized, you can maintain a higher pitch when blades move in one half of the disk and a low pitch for the other half. These differential thrusts create a control moment around an axis contained in the disk's plane that may be adjusted based on the motor input signal's phase. The signal's frequency must be the same as the average rotation rate to maintain the generated moment's constant orientation. In other words, in the time the blades complete one full revolution, the motor needs to create an acceleration for half of this period and a deceleration for the other half. A simple way to achieve this is to vary the motor speed over time in a sinusoidal way through a function like the following:

$$\omega = \omega_0 + \Delta\omega sin(\omega_0 t + \Phi) \tag{6.1}$$

where ω_0 is the average rotation rate and Φ controls the phase of the input signal. The oscillation period is a full rotor revolution, allowing the motor to accelerate over 180° while decelerating for the remaining 180°, ensuring that the blade 'sees' an equivalent relative pitch in every azimuthal position.

Carlotta Manca performed the rotor and hinge design and manufacturing during the MSc Thesis [126] in our department. In the lines below, we can find a brief description of these. For further details on the design process, the reader is referred to the aforementioned MSc Thesis.

6.1.1 Hinge design

The design is characterized by a central hub that can be screwed to the engine and two hinges coupling the hub and the blades. The hinges must be anti-symmetric to create non-zero control moments. To achieve the coupling of lag and pitch, the two hinges are screwed onto the hub with a 45-degree inclined axis on the same plane of the engine shaft. To make anti-symmetric their passive behavior, the hinges' axes are inclined in the same direction shown in Figure 6.2. Figure 6.3 shows how the hinges are possibly over-dimensioned for the selected blades. The reason for this is that they were designed to allow the testing of larger blades, and also, we

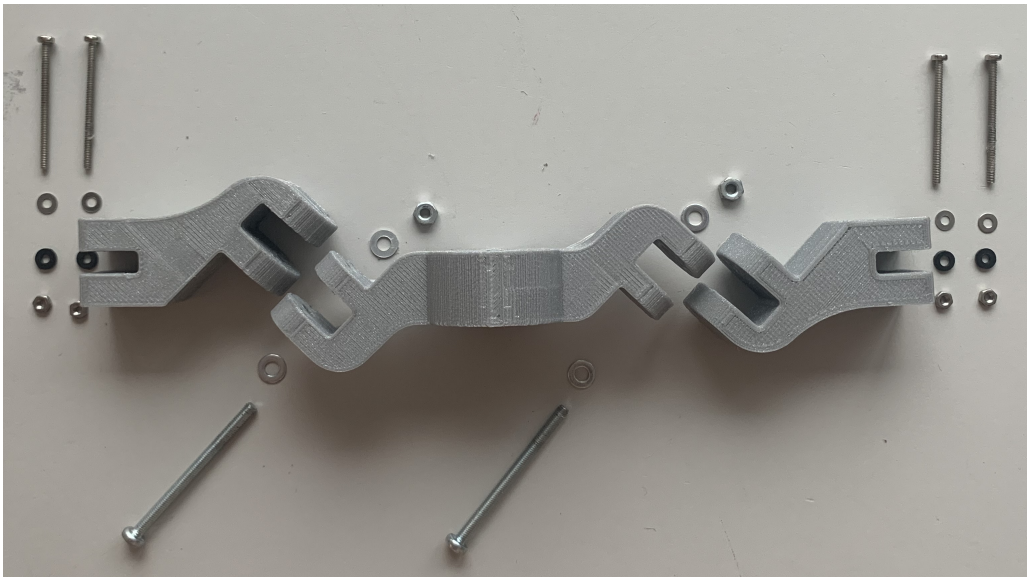

Fig. 6.2 Hinge Image.

are expecting non-negligible vibrations on the system so a more robust design was favored to ensure mechanical integrity.

6.1.2 Blade design

The blade was derived from a commercially available rotor: the T-Motor 15"x5". Some blade design modifications were necessary since the system requires a central hub and a pair of hinges between the blades that occupy 100 mm and 58 mm in the radial direction, respectively. The total diameter of the hub with the hinge mounted is 158 mm. To carry out our study, since the hub and hinge lengths are not insignificant, it was necessary to reduce the radius of the blades so that the distance between the two blade tips remained around 15". The original blade design outboard stations were preserved to keep the aerodynamic properties of the commercially available blade as unchanged as possible. We then lofted this outboard section with the innermost sections in a reduced radial distance, obtaining a rotor of 16" nominal diameter.

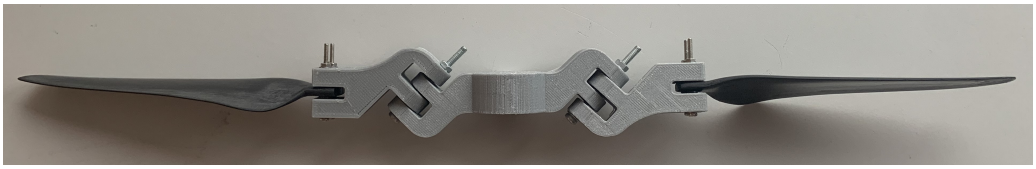

Fig. 6.3 Mounted blades.

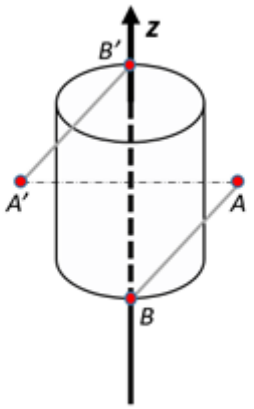

Fig. 6.4 Sketch of both hinges

6.2 Dynamical Model

Swashplateless rotor dynamics couples for each instant of time two motions: a rotation around the motor shaft and the lag-pitching rotation around the hinges. Figure 6.4 illustrates schematically the hub cylinder and the two inclined hinges axis. Points A and A' represent the actual position of the hinges. Points B and B' are two stationary points in all reference frames, as they are found in the intersection of both rotation axis. A free rigid motion has 6 degrees of freedom that can be determined by integrating the linear and angular momentum fundamental laws expressed in equation 6.2.

$$\begin{aligned} \left.\frac{d\vec{C}}{dt}\right|_1 &= \vec{F} + \vec{R} \\ \left.\frac{d\vec{\Gamma}_0}{dt}\right|_1 &= \vec{M}_0 + \vec{M}_R \end{aligned} \tag{6.2}$$

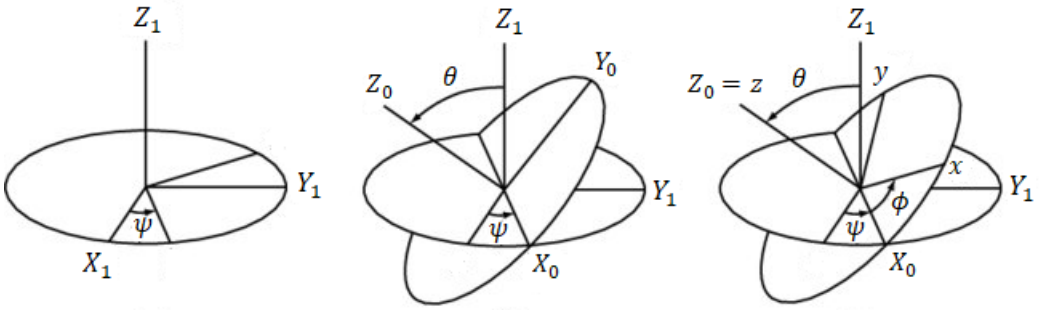

Fig. 6.5 Euler angles notation.

However, the motion of a solid with a fixed point can be defined with only 3 degrees of freedom. A convenient definition of these 3 degrees of freedom is the so-called Euler angles. Our definition of the Euler angles is shown in Figure 6.5. Let us define three sets of axis, inertial axis ($OX_1Y_1Z_1$ also referred to as 1), intermediate axis ($OX_0Y_0Z_0$ also referred to as 0), and body axis ($Oxyz$ also referred to as 2). The three rotations that map the inertial and body axis can be defined chronologically:

- A rotation around the axis Z_1 of angle ψ called precession.
- A rotation around the axis X_0 of angle θ called nutation.
- A rotation around the axis z of angle ϕ called rotation.

Using this notation, the angular velocity in the body reference frame can be expressed as shown in equations 6.3. A convenient choice is to align the z-axis with the hinge ($\theta = 45\,\text{deg}$). In this way, ψ becomes the angle driven by the motor and ϕ the angle around the hinge, completely defining the motion of the Swashplateless rotor.

$$\begin{aligned} \omega_x &= \dot{\psi} sin(\theta) sin(\phi) + \dot{\theta} cos(\phi) \\ \omega_y &= \dot{\psi} sin(\theta) cos(\phi) - \dot{\theta} sin(\phi) \\ \omega_z &= \dot{\psi} + \dot{\phi} cos(\theta) \end{aligned} \tag{6.3}$$

As we define the origin of our reference systems in stationary points B and B', the angular momentum in this point can be expressed as shown in equation 6.4.

$$\Gamma_0 = \overleftrightarrow{I}\ \vec{\omega} \tag{6.4}$$

The conservation law of angular momentum shown in equation 6.2 is referred to as the inertial reference frame, sub-index 1. We can express the variation of angular momentum with respect to the body reference frame, sub-index 2, using Poisson's formula. This is shown in equation 6.5.

$$\left.\frac{d\vec{\Gamma_0}}{dt}\right|_1 = \left.\frac{d\vec{\Gamma_0}}{dt}\right|_2 + \vec{\omega} \times \Gamma_0 = \vec{M_0} + \vec{M_R} \tag{6.5}$$

Expressing the angular momentum theorem in the body frame is convenient as the body's inertia would be time-dependent in any other frame. Equation 6.6 shows how developing the cross-product and projecting equation 6.5 into the hinge axis, we can obtain the second-order scalar differential equation for the evolution of the angle around the hinge, ϕ. This angle is the only unknown of our problem as the hinge tilting, θ, is fixed, and, the shaft angle, ψ, is driven by the motor. The axial component of the external moment, $\vec{M_0}$, applied along the hinge is zero. However, due to the friction at the hinge inside the reactive moment term, we have a component, $\vec{M_R}$.

$$\ddot{\phi} = \frac{\omega_y \vec{\Gamma_0} \cdot \vec{i_2} - \omega_x \vec{\Gamma_0} \cdot \vec{j_2} - I_{21}\dot{\omega}_x - I_{32}\dot{\omega}_y + \vec{M_R} \cdot \vec{k_2} + \vec{M_0} \cdot \vec{k_2}}{I_{33}} - \ddot{\psi} cos(\theta) \tag{6.6}$$

The vectors $\vec{i_2}, \vec{j_2}$ and $\vec{k_2}$ represent unitary vectors along the x, y, and z axis in the body reference frame. The friction at the hinge is essential to capture swashplateless rotor dynamics. Therefore, we implemented the simplified hinge model shown in equation 6.7.

$$M_R = -sign(\dot{\phi})\mu_f |F_N| r_{hinge} \tag{6.7}$$

$$F_N = m\sqrt{(\vec{R} \cdot \vec{i_2})^2 + (\vec{R} \cdot \vec{j_2})^2} \tag{6.8}$$

Moment $\vec{M_R}$ is a function of the reactions at the hinge, which renders the problem non-linear, as the reactions are related to the variation of linear momentum shown in expression 6.2, which can be simplified to equations 6.9.

$$
\begin{aligned}
m(\frac{dV_1^G}{dt} + \omega_y.v_3^G - \omega_z.v_2^G) &= \vec{R}\cdot\vec{i_2} + \vec{F}\cdot\vec{i_2} \\
m(\frac{dV_2^G}{dt} + \omega_z.v_1^G - \omega_x.v_3^G) &= \vec{R}\cdot\vec{j_2} + \vec{F}\cdot\vec{j_2} \\
m(\frac{dV_3^G}{dt} + \omega_x.v_2^G - \omega_y.v_1^G) &= \vec{R}\cdot\vec{k_2} + \vec{F}\cdot\vec{k_2}
\end{aligned}
\tag{6.9}
$$

The external forces, $\vec{F}$, include the aerodynamic forces on the blade. These also contribute to the external moment, $\vec{M_0}$, shown in equation 6.6.

The developed framework performs a second-order temporal integration using a predictor-corrector scheme. Every time-step the nonlinear equation solver available in MATLAB, *fzero* solves equation 6.6. To reduce the computational cost of the approach, it is possible to linearize the equation by using the angular acceleration of the previous time step.

6.3 Aerodynamic Model

6.3.1 Reduced Order Model

In this work, we use an azimuthally resolved version of the Blade Element Momentum model presented in Chapter 2 to compute the transient aerodynamic loading on the blade. The model includes corrections to the inflow and tangential velocities that consider the effective angle of attack. To compute this, we change the local pitch according to the dynamic equations and calculate the effective wind velocity relative to the actual motion of the blade. However, the model does not include pure unsteady aerodynamic models such as the one developed by Theodorsen [202], which allow the capturing of non-linear hysteresis effects and the tilting of the lift curve for a pitching airfoil. By isolating the pitching component of our motion, we can estimate the reduced frequency and oscillation amplitude of a representative radial station situated at 80% of the radius. The angular frequency of the pitching motion coincides with the rotor's rotation rate set at 300 rad/s. The resultant pitching motion presented an amplitude of approximately 2 degrees for the applied condition. The angle of attack predicted by the BEM method at this station was 3.25 degrees. Even though the 2-degree amplitude will not directly affect the effective angle of

attack, as this will be damped by an increase in induction, it would represent a conservative estimate. The airfoil's angle of attack will range between 1 and 5 degrees. The Reynolds number that this station sees is around 60,000. Except for the lowest angles of attack, where the flow could be separated at the trailing edge, we expect the lift distribution to be approximately linear in this range. On the other hand, the reduced frequency will be around 0.06. This value is close to 0.05, the upper value until which Leishman [119] considers the quasi-steady aerodynamics valid. Considering that at this low reduced frequencies, non-circulatory effects are generally negligible and that the range of angles of attack falls in a regime where the flow is expected to be attached, we believe that the quasi-steady aerodynamic model is sufficient to verify the developed ROM with the higher fidelity CFD model.

A BEM approach in this context is justified by the approximately time-independent azimuthal distribution of induced velocities on the disk due to the blade's synchronized rotation and pitch-lag motion. In this approximation, we are neglecting that both blades generate different inductions. Each blade's induced velocities are calculated assuming the opposite blade is identical. In this way, the code runs independently for each blade.

To consider the non-negligible torque contribution associated with the hinges' drag, we will add an extra term, assuming the drag coefficient of a square, the effective tangential velocity at the center of mass of the hinge, and its frontal area.

$$Q = \frac{1}{2}\rho(\Omega r_{cm} + \phi(r_{cm} - r_e)cos(\theta))^2 SC_{d_{sq}} + \int dQ_{BEM} \tag{6.10}$$

Using this approach, the computational cost of a two-bladed simulation for 17 revolutions is around 1 CPU hour using 8 cores of an AMD Ryzen-7. The simulation used a time step of 10^{-4} and a second-order temporal integration.

6.3.2 6-DOF CFD model

The commercial CFD software STARCCM+ [188] was used to develop a 6-DOF computational model of the swashplateless rotor presented in section 6.1. The multibody solver described in Chapter 2 was used to model the motions of both blades and the hub.

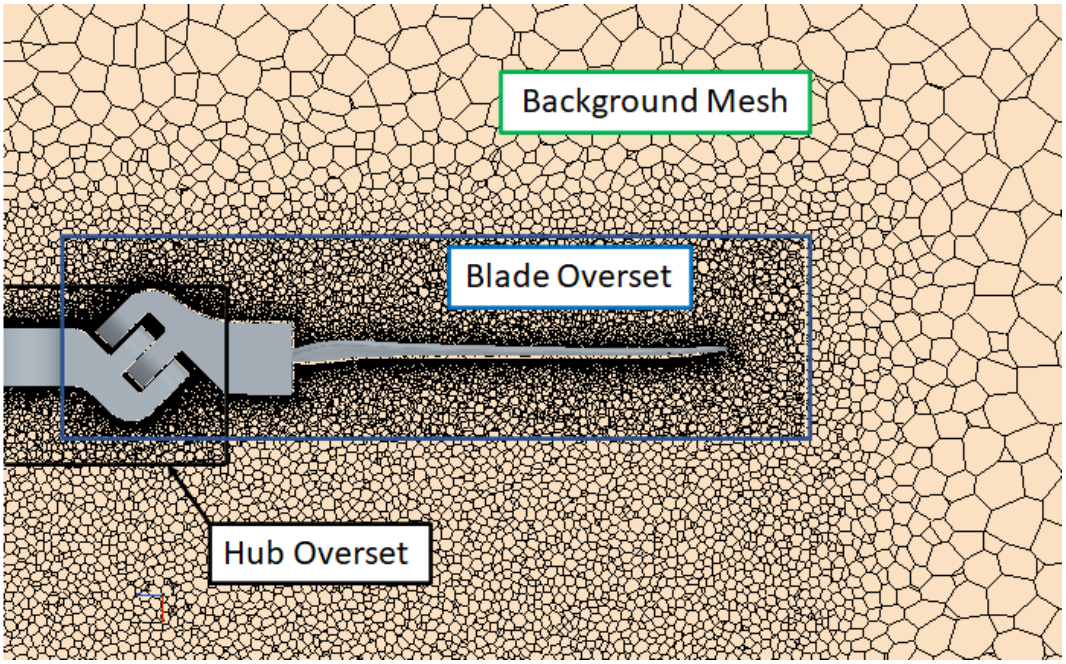

Fig. 6.6 Overset Mesh Layout.

We have created an overset grid for each blade and one for the hub to move over a background grid. Figure 6.6 shows the layout of these grids. Three 6-DOF bodies were created in STAR-CCM+ to model the motions of the aforementioned overset grids. The motion of the hub is driven by the sinusoidal signal shown in equation 6.1. The inertial forces, the aerodynamic forces, and the reactions drive the motion of the blades. Each blade is coupled to the hub by a hinge joint. The time step is defined to allow a rotation angle of the hub of 1^o per temporal iteration. This time step is fixed to $5.10^{-5}s$, so the simulated physical time is limited depending on the computational resources. The adopted time-integration scheme is implicit and second-order accurate, and the spatial discretization is a third-order hybrid CD/MUSCL scheme. Using high-order spatial discretizations has been found computationally advantageous to capture rotor performance [196] even on coarser grids compared to second-order spatial discretizations. Furthermore, it allows to better capture vortex breakdown in the rotors wake. As a turbulence model, we use the URANS SST $k-\omega$ model [135]. The grid adopted in this work follows the meshing guidelines presented in Chapter 4 but with a uniform wake refinement to capture vortex structures in the wake of the hub and blade. The employed grids comprise a cell count of around 10 Million cells.

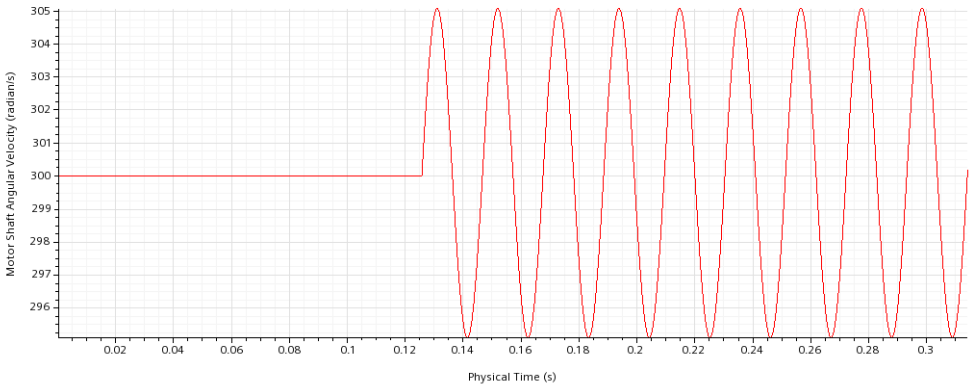

Fig. 6.7 Angular velocity applied to the hub.

We conducted the simulations using the 64 cores of two Intel Xeon Scalable Processors Gold 6130 2.10 GHz. The computational cost of the simulations presented in this paper, with a duration of 0.31 seconds, is around 10,000 CPU hours. Approximately 15 full revolutions of the rotor were simulated.

6.4 Results and Comparison

A test was performed in which the angular velocity of the motor was maintained constant for the first 6 revolutions, and then a sinusoidal rotation rate, with a $\Delta\omega$ of 5 rad/s, was applied to the hub to generate the desired passive response of the blades. As we detailed in equation 6.1, the angular velocity of the sinusoidal signal is equal to the mean rotation rate to synchronize the dynamic response of the blades with its azimuthal position. This signal is shown in Figure 6.7. We can appreciate a mean value of 300 radian/s.

Figure 6.8a shows the angular velocity of the blades around the axis of the hinges. We can appreciate how the blade presents negligible angular velocities when the motor input provides a constant angular velocity. This is caused by the friction model explained in the previous section. This model causes high frequency and very small amplitude oscillations associated with the changes of sign of the angular velocity, causing a discontinuity in the friction moment. Once the sinusoidal input becomes active, the blade's angular velocity undergoes a transient phase, and about 4 revolutions later, a persistent oscillatory regime with almost constant amplitude is achieved. We can appreciate a good agreement between CFD and our reduced order

model. It is interesting to note that both models predict a larger amplitude for the left blade. This is associated with the fact that both blades' inertia along the hinge axes are slightly different due to the anti-symmetric disposition of these.

Figure 6.8b shows the thrust of the blades computed with both models. We can appreciate how, overall, the BEM overestimates thrust compared to CFD asymptotic values. This difference of around 10% is not rare within BEM models, as shown in Chapter 4. Figure 6.9 shows the impact of the anti-symmetric disposition of the hinge in the velocity field, clearly showing an increased induced velocity when the azimuthal position of the blade coincides with that of maximum thrust. We can see how the left blade presents a relatively higher maximum thrust than the right blade. This is due to the center of mass of the blade not being aligned with the radial axis, and the centrifugal forces tend to align these two. In one blade, this alignment results in a small positive angle, and in the other, a negative angle due to the anti-symmetric disposition of the hinge. After the sinusoidal input is activated, the thrust follows the same overall sinusoidal trend in both models, but we can point out several differences. The first and most evident is the presence of higher frequency oscillations. These are probably caused by vortices emitted in the wake of the massive hub impinging the blade. Figure 6.10 reveals how, apart from the classical tip vortices, we can see large-scale structures emitted on the wake of the hub. Some differences could be associated to unsteady phenomena that our simplified quasi-steady airfoil polar model cannot consider. Nevertheless, we can see how this tool accurately predicts the differential thrusts created on both blades, which is related to the generated control moment. It is interesting to note how this problem is highly dominated by the forcing dynamic term in the hub, and the aerodynamic interactions are mild. This is revealed by the satisfactory agreement in the hinge dynamics despite the differences in amplitude in the forces acting on the blades.

6.5 Discussion

This Chapter presents the numerical modeling of an innovative UAS concept that enables cyclic control using a synchronized motor input signal in phase and amplitude. A CFD model was developed to understand these systems' potential dynamic-aerodynamic interactions. We use a 6-DOF multibody solver to model the blade lag-pitch motion around the hinges and the coupling of this with the hub.

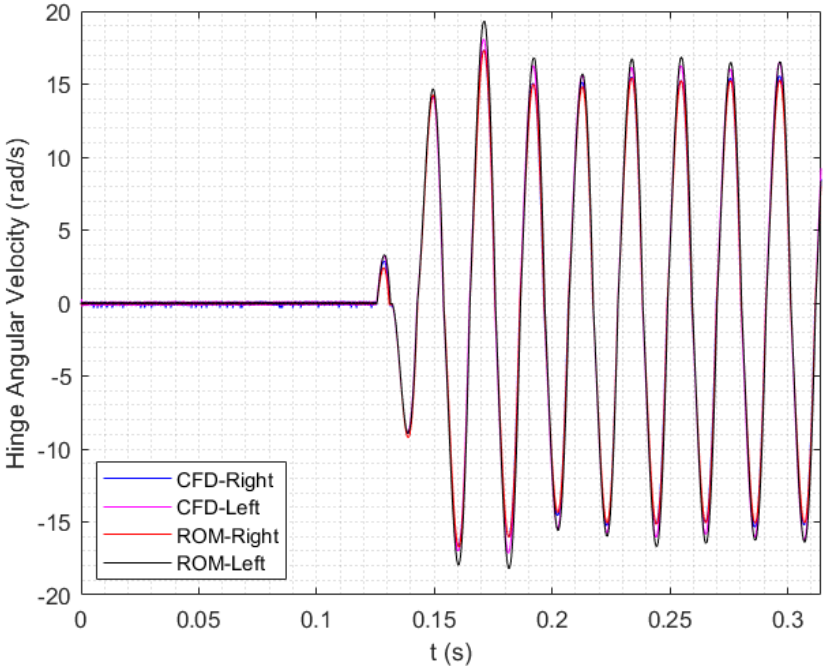

(a) Blade Angular Velocity around the hinge.

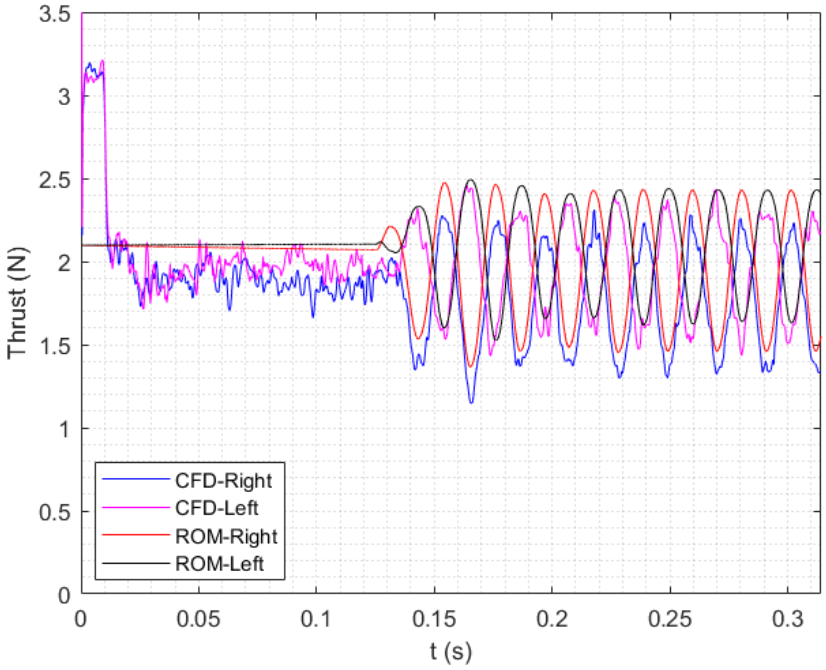

(b) Thrust generated.

Fig. 6.8 Comparison of both models predictions for right and left blades.

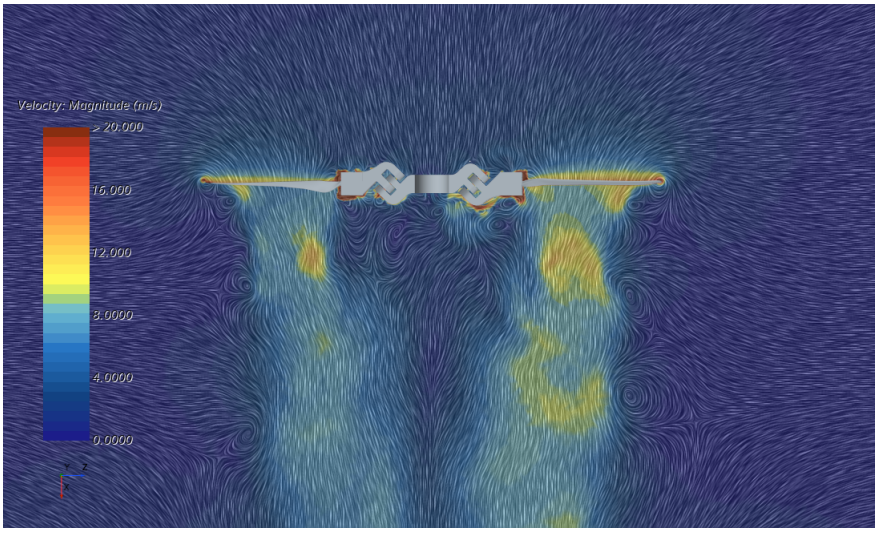

Fig. 6.9 Velocity magnitude with line convolution integrals of the velocity direction projected on the plane y=0 after 12 Rotor Revolutions.

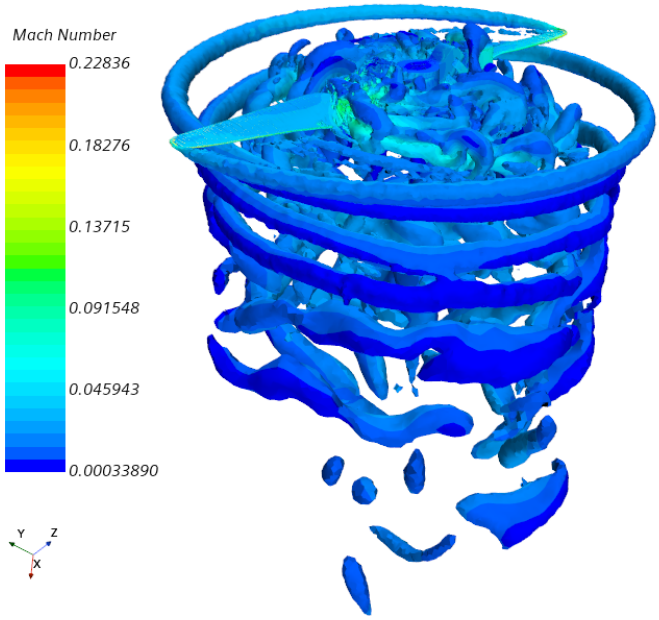

Fig. 6.10 Q-criterion colored by velocity magnitude after 12 Rotor Revolutions.

The CFD results provided us with invaluable insight into the complex interactions that play a part in this dynamic system. The dynamic forcing term resulting from the sinusoidal motor input dominates the aerodynamic term, but this is not negligible. We also noticed how the dynamics of both blades differ due to their slightly different

inertia around the axis of the hinge. Previous work on this subject assumed both blades had identical behavior and scaled the result with the number of blades. Having slightly different dynamics has design implications, as these differences will induce imbalances in the system resulting in vibrations. On these lines, our rotor presents very subtle misalignments (<1mm) of the center of mass of the blade with the radial direction. This creates a non-zero equilibrium angle as the centrifugal term attempts to align these. Also, introducing hinge friction is instrumental in maintaining stable dynamics. The model we employed is simplified, and its validity will require validation and possibly tuning with experimental data. As we anticipated, the hinge is too massive, both in inertial and aerodynamic terms. The mass of the mobile part of the hinge is larger than the blade's, shifting the center of mass close to the hinge. Also, aerodynamically, it creates an undesirable torque, and its wake impinges on the blades, possibly deteriorating the performance.

The aforementioned discoveries informed the development of a reduced order model that allows the estimation of the forces created by the pitch-lag motion of the blades with errors around 10% compared to CFD. Its formulation uses classical rigid body mechanics to derive a second-order equation of motion that is solved numerically. The synchronized motion of these rotors creates a disk induction that varies in space but not in time. This allows the implementation of an efficient azimuthally resolved BEM model to calculate the force and moments on the blade. This model has a computational cost of about 1 CPU hour using eight cores of an AMD Ryzen-7, considerably less than 10,000 CPU hours required for the CFD simulation using 64 cores of two Intel Xeon Scalable Processors Gold 6130 2.10 GHz at the high-performance computing facility HPC@PoliTO.

Chapter 7

Numerical Analysis of UASs Maneuvers.

This chapter includes the partial content of the paper:

- M. Carreño Ruiz, N. Bloise, E. Capello, D. D'Ambrosio, and G. Guglieri. Assessment of Quadrotor PID Control Algorithms using six-Degrees of Freedom CFD simulations. In *2022 61st IEEE Conference on Decision and Control (CDC)*, 2022
- M. Carreño Ruiz, N. Bloise, E. Capello, D. D'Ambrosio, and G. Guglieri. Assessment of Quadrotor Near-Wall behaviour using six-Degrees of Freedom CFD simulations. In *AIAA SciTech 2023 Forum*, National Harbor, MD, January 2023. AIAA-2023-2272

The main objective of this Chapter is to present an innovative approach to accurately reproduce maneuvers with a higher fidelity model compared to the simplified propulsive models typically used in control applications, such as constant thrust and torque coefficients models. The numerical model combines a PID control system and Computational Fluid Dynamics, providing insight into critical scenarios, including ground/wall effect near obstacles or wind gust disturbances. We aim to create a virtual testing environment that allows the reproduction of maneuvers that may potentially fail without the risk and cost that the experimental approach has. This approach is useful in running preliminary simulations to help design experiments and test environments that are difficult to accomplish in a controlled experimental facility,

such as testing low-density environments, including the Martian scenario. This case, in particular, poses an additional challenge due to the different gravitational accelerations making experimental dynamic testing very complex and limited.

This Chapter is divided into two main sections. Section 7.1 proposes the methodology and tools, including a detailed UAS dynamic model, the PID control law, and the CFD modeling. It also contains a numerical verification exercise comparing our model with a simplified Simulink model to demonstrate the controller implementation. Our colleague Nicoletta Bloise, from the flight mechanics group at Politecnico di Torino, developed the Matlab/Simulink model. For more details on this model, please refer to [41]. Section 7.2 contains the simulation results of the quadcopter in wall effect. We present two studies, one in which the UAS is fixed and the forces and moments are computed at different wall distances and another in which the UAS uses a PID algorithm varying the angular rates of the rotors to maintain a hovering position at a fixed distance to the wall.

7.1 Methodology

This section illustrates the proposed methodology with the mathematical formulation and the underlying numerical tools. Initially, a simple horizontal translation is shown as a validation case. Then a critical maneuver, hovering in the neighborhood of the wall, is analyzed in detail. The challenge is to evaluate the ability of the discussed control algorithm to maintain a constant position, altitude, and attitude at different distances from the wall.

7.1.1 Quadrotor dynamics

This Chapter will focus on the dynamics of a quadrotor. This UAS represents an under-actuated system with four inputs, the angular velocities of four rotors. They are controllable in position and attitude dynamics through differential thrust and torque generation. The model of a multi-rotor is described in detail in [208]. In this research, the "+" (cross) quadrotor orientation is considered, where the drone has two rotors parallel to the body x-axis (rotors 1 and 3 with counterclockwise rotation) and two rotors parallel to the body y-axis (rotors 2 and 4 with clockwise rotation), as shown in Figure 7.1 with the main quadrotor parameters taken as a reference.

As mentioned before, four control inputs influence the quadrotor dynamics, u_1 the

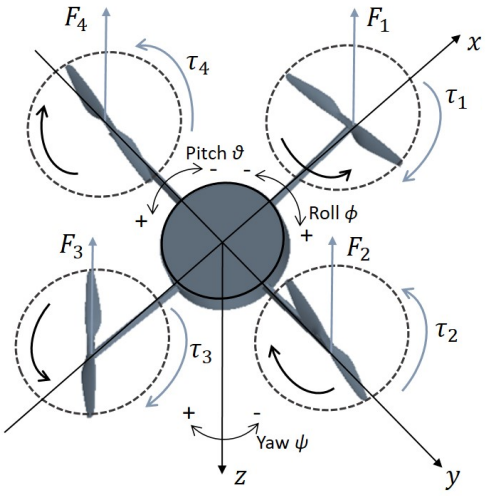

UAS model parameters			
Mass	2.45 kg	ω_{max}	523.6 rad/s
Ix	0.02 Kgm^2	ω_{min}	104.72 rad/s
Iy	0.02 Kgm^2	**r**	0.19 m
Iz	0.04 Kgm^2	k_T	4.51 10^{-5}
l	0.4 m	k_D	8.57 10^{-7}

Fig. 7.1 Forces and torques on the quadrotor in the body frame and parameters used in the simulation.

sum of all rotor thrusts, u_2 the rolling moment generated along y_b, u_3 the pitching moment generated along x_b, and u_4 the yaw moment around z_b. A propulsive model relating the thrust and torque of each rotor ($i = 1, ..., 4$) is introduced as a function of the rotation rate (ω_i) to obtain these forces and moments. A constant coefficient model for k_T and k_D, thrust, and a torque coefficient, respectively, is used as shown in Eqs.7.1 and 7.2.

$$F_i = k_T \ \omega_i^2 \tag{7.1}$$

$$\tau_i = (-1)^{i+1} k_D \ \omega_i^2 \tag{7.2}$$

Combining the rotor forces and moments as defined in Figure 7.1, the control algorithm, discussed in Section 7.1.2, provides four control inputs (u_1, u_2, u_3, u_4) and the rotor rotation rate required for each motor can be calculated using Eq. 7.3 that derive from a basic force and moments balance according to the definitions provided by 7.1. The rotors' rotation rates (ω_1, ω_2, ω_3, ω_4) will be the input values

of the CFD model.

$$\begin{bmatrix} \omega_1^2 \\ \omega_2^2 \\ \omega_3^2 \\ \omega_4^2 \end{bmatrix} = \begin{bmatrix} k_T & k_T & k_T & k_T \\ 0 & -lk_T & 0 & lk_T \\ lk_T & 0 & -lk_T & 0 \\ k_D & -k_D & k_D & -k_D \end{bmatrix}^{-1} \begin{bmatrix} u_1 \\ u_2 \\ u_3 \\ u_4 \end{bmatrix} \tag{7.3}$$

As thoroughly discussed in Chapter 4, the thrust and torque coefficients depend on other parameters, such as the Reynolds number, the Mach number in the hovering case, and the advance ratio when operating in propeller mode. This comes from a dimensional analysis in an isolated rotor case. Actually, there are many more factors, such as proximity to obstacles, forward flight velocity, rotor-rotor interactions, and rotor-body interactions, among many others. In our simulations, we can compute the influence of some of the aforementioned parameters in the coefficients as we can compute the thrust coefficient. However, this would not be realistic. Our simulations use the constant coefficient model to predict the updates in rotor angular velocities through the motor mixer shown in equation 7.3. The control is based only on the position and attitude of the UAS, as it is typically done in commercial autopilots. It must be mentioned, though, that we are not modeling the sensors. The states are obtained directly as the output of the 6-DOF solver.

7.1.2 PID control design

A Proportional-Integral-Derivative (PID) controller is implemented within the CFD framework. This control law is popular because of its simplicity, robustness, and effectiveness in forcing the controlled variable *y(t)* to follow as closely as possible a reference variable *r(t)* defined by the guiding law [19]. The system uses feedback control to stabilize itself by measuring the controlled variable. This helps to minimize the difference between the reference variable and the measured variable, also known as the error *e(t) = r(t) - y(t)*. The control signal *u(t)* becomes

$$u(t) = K_P e(t) + K_I \int e(\tau) d\tau + K_D \frac{d}{dt} e(t) \tag{7.4}$$

where K_P is the proportional gain, K_I is the integral gain, and K_D is the derivative gain. Moreover, adjusting these control parameters to reach the reference in a finite

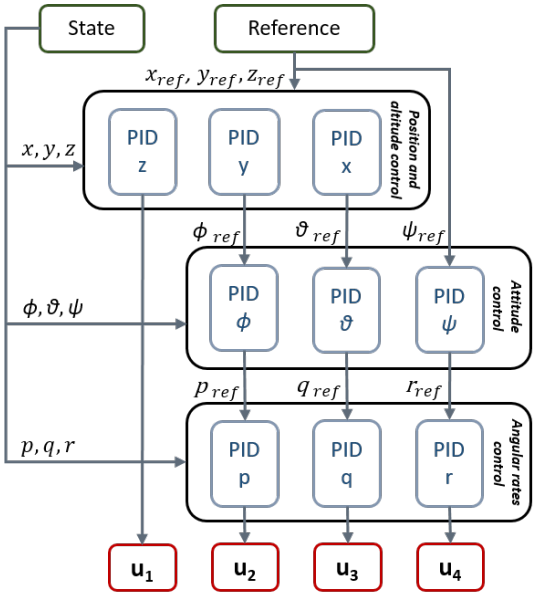

Fig. 7.2 Robust cascade PID position and attitude control.

time is relatively easy to accomplish the required performance in terms of stability, steady-state error, and convergence time.

A robust cascade PID control algorithm to track position and the yaw angle (x_{ref}, y_{ref}, z_{ref}, ψ_{ref}) has been developed, as shown in Figure 7.2. Inputs to the control logic are (x, y, z), (ϕ, θ, ψ) and (p, q, r) in body frame. For more details on the algorithm, please refer to [41].

7.1.3 CFD analysis

The commercial CFD software STARCCM+ [188] was used to develop a 6-DOF computational model of a quadrotor equipped with the PID controller previously described in Section 7.1.2. An overset grid interface strategy allows the UAS to move within a background grid. Simulations are executed in a closed cube environment with a height, width, and depth of 20 meters, as shown in Figure 7.3. Using such a large domain is possible without too many cells since the background mesh is very coarse. An automatic Adaptive Mesh Refinement (AMR) algorithm refines the background mesh using the interface with the body grid as a trigger function, which moves in solidarity with the quadcopter, as shown in Figure 7.3. The adaptive mesh refinement occurs every ten integration time steps to limit the computational cost. The

update frequency must be selected carefully, as the overset interface should always lay in the refined region. The grid cell size in this region matches the size on the overset body to enable a smooth transition of the flow variables, minimizing spurious fluxes at the interface. Figure 7.3 shows AMR using the polyhedral mesher. Typically the polyhedral mesher allows a reduced cell count compared to the hexahedral mesher (or trimmed cell meshes) and presents an advantage in non-aligned interfaces. However, the run time is slightly slower due to the higher number of faces. In some situations, the hexahedral mesh might be advantageous as faster AMR and solver time could compensate for an increased cell count. The simulation environment remains a cube for the wall effect simulations shown in Section 7.2. The UAS is moved towards a wall and oriented adequately depending on the desired configuration. In this case, avoiding the overhead of using an AMR strategy is preferable, and a volumetric refinement is performed around the UAS, as this has minimal variations.

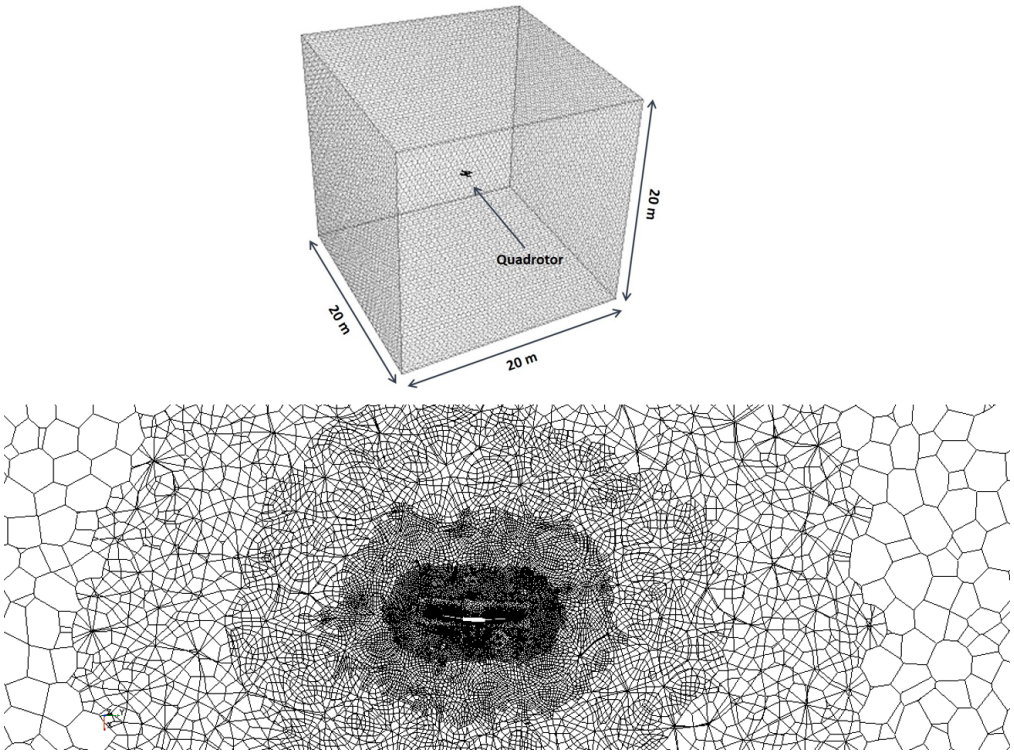

Fig. 7.3 Computational domain (top) and Computational grid with adaptive mesh refinement tracking the near-body grid (bottom).

As shown in chapter 4, a sliding grid approach models the rotors' motion inside the body overset grid. The time step is defined to allow a maximum rotation angle of 3^o per temporal iteration at the highest angular velocity defined in the table in

Figure 7.1. This time step is around $10^{-4}s$, so the simulated physical time is limited depending on the computational resources. The adopted time-integration scheme is implicit and second-order accurate, and the spatial discretization is also second-order. As a turbulence model, we use the URANS one-equation Spalart-Allmaras model [192]. The grid adopted in the horizontal maneuver is under-resolved (5 million points) to simulate aerodynamic rotor-rotor interactions or the wake breakdown in detail. However, its refinement is sufficient to describe the coupling between rotor aerodynamics and quadrotor dynamics. Such a capability gives our simulations a noticeable advantage compared to the simplified propulsive model usually employed in dynamic simulations, which relies on constant thrust and torque coefficients, as shown in Eq. 7.3. We verified the scalability of such an approach to larger grids by running the simulations on a 5 million and a 10 million cells grid. The results showed an approximately linear increase in CPU time, showing that this approach could be extended to grid refinement levels such as those reported in Chapter 4 for the Q4L quadcopter. The wall effect simulations have been performed with the 10 million cell grids. The link between the controller and the CFD model depends on the rotation rates at each time step, and the framework includes an input file that allows the definition of different waypoints.

Figure 7.4 illustrates our virtual control test strategy. In particular, the process controller, being a feedback system, computes the error between a reference signal and an actual state vector obtained from the CFD model. Its output, namely forces and torques, is converted in rotation rates according to Eq. 7.3 and enters directly into the virtual simulator.

We conducted the simulations using the 32 Intel Xeon Scalable Processors Gold 6130 2.10 GHz cores. The computational cost of the 6-DOF maneuvers presented, with a duration of 1.5 seconds, is around 5000 CPU hours. These simulations were performed with the 5 million grid. On the other hand, the static simulations are performed with the 10 million grid with a computational cost of around 9000 CPU hours.

These computational costs are already large, even with relatively coarse grids. The computational grid required to accurately resolve the blade aerodynamics using a RANS approach would be larger, as shown in Chapter 4 for the Q4L multicopter. Therefore, this technique might be used to study only specific cases where unsteady aerodynamic forces might be relevant for short simulation times. The computational

cost spike due to the time-step limitation that the sliding grid requires in combination with large physical time requirements. An alternative to this approach is to use a virtual disk model to reproduce the effect that the rotor would have on the flow. STAR-CCM+ offers a variety of virtual disk models, including the Blade Element method, the actuator disk model, and the body force method. Using these models becomes interesting when the problem under study is driven by the mean bulk flow created by the rotors, and resolving each revolution in time is unnecessary. An example of this could be low-speed maneuvers where induction angles barely vary within a revolution. The time step required to model the mean flow becomes much less restrictive due to the smaller speeds, as only induced velocities are modeled. Also, meshes do not require as much resolution as the rotor geometry is not resolved. An example using the body force propeller method is shown in the following section.

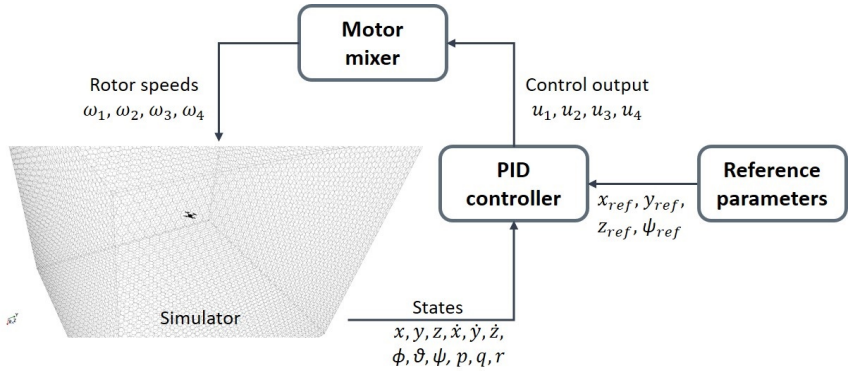

Fig. 7.4 Configuration of the virtual UAS control test system.

7.1.4 Numerical Verification: Quadcopter in horizontal translation

7.1.4.1 Sliding Grid Approach

Our CFD/PID simulation framework's results are compared with a simplified model implemented in Simulink for a simple test case. For details on this model, refer to reference [41]. In particular, a horizontal translation of 20 cm on the x-axis, maintaining altitude, is simulated. The active control must move the UAS to the desired position while compensating the gravity force. We compare the simplified Simulink model and the CFD simulation to evaluate seldom-captured non-linear aerodynamic and propulsion effects. To show the translation along the x-axis NED,

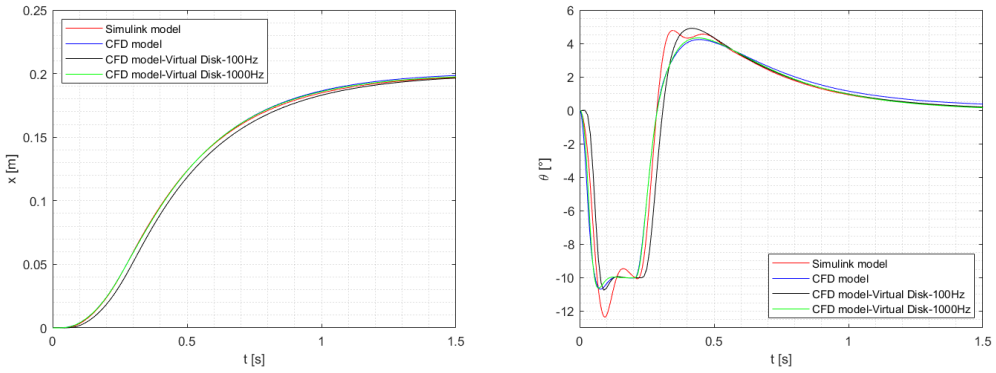

(a) x. (b) θ.

Fig. 7.5 Comparison of x-position and θ for the two models.

we present the relevant states x and θ, the pitch angle, in Figure 7.5. The two states are comparable in both models, and minor discrepancies are due to the transient of the rotors and the fact that the fluid force on the multicopter's frame is also computed.

Finally, we show some images from the CFD simulation in Figure 7.6, where one can see the simulated advancing maneuver of the quadcopter. It is possible to

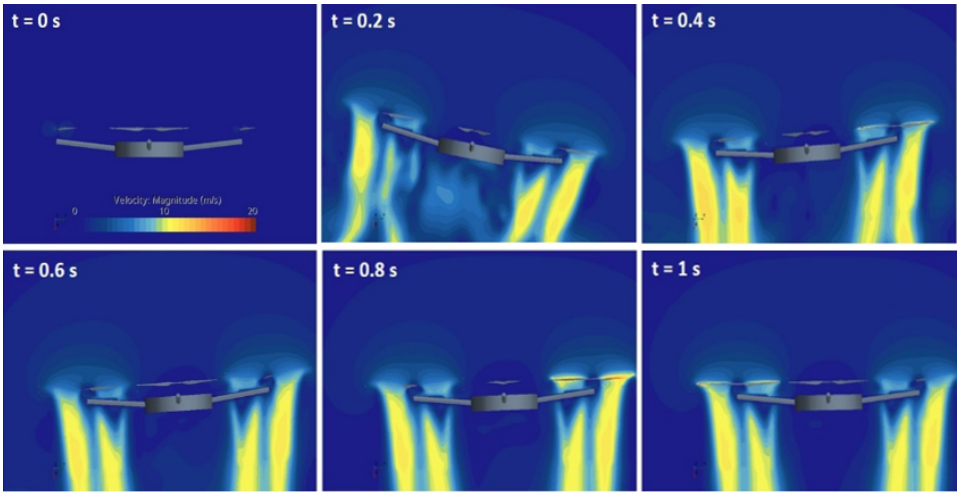

Fig. 7.6 Visualization of the velocity magnitude field obtained with CFD during the quadrotor maneuver using the sliding grid approach.

see the downwash velocities and the vehicle's attitude. Initially, the quadcopter has a negative pitch angle to accelerate the vehicle to the desired position. Then, a higher thrust, revealed by the increased downwash speeds in rotor 1, helps increment the

pitch angle to positive values, as shown in Figure 7.5, in an attempt to compensate for the positive velocity that the vehicle has acquired. The last images show that the UAS asymptotically regains a hovering position at an x coordinate of 20 cm. A detailed verification of this maneuver was presented in [41].

7.1.4.2 Body-Force Propeller Method.

The same mission is reproduced in this section using a body-force propeller method. This model adds a volume force in the virtual disk region that mimics the momentum generation produced by a rotor. The radial distribution of the axial and tangential can be set to match the actual distribution of the rotor under study. The model was fine-tuned using the radial thrust and torque distributions presented in Chapter 4 for the Tmotor 15"x5". Conversely, a theoretical distribution such as Goldstein's optimum expressions may be used. For more details on how these body forces are modeled, please refer to [189].

The grid requirements were approximately halved as the rotor geometry does not require to be resolved. The time step used is 0.01 s. This frequency allows a stable integration of fluid dynamics equations and represents a typical frequency at which autopilot controllers run. In this case, dynamics were also run at this frequency. However, a sub-stepping option is available to run dynamics at a higher frequency, as shown in the previous Chapter for the Swashplateless rotor. Figure 7.7 shows how this simplified model can reasonably reproduce the order of magnitude and distribution of the velocity field on the wake compared to the sliding grid approach. With this methodology, we cannot model unsteady wake effects such as blade vortex interaction, but we can reproduce the bulk velocity magnitudes on the wake while accurately modeling the propulsive forces with a 200-factor reduction in computational time. This model is ideal for simulations in the following Chapter, including a PID-controlled spraying mission in which Lagrangian particles are injected.

Figure 7.5 shows how both models perform similarly but with a small delay. This delay is caused by the lower frequency at which the control is performed. Figure 7.5 also includes simulations performed at 1000Hz, showing how this delay is not present anymore. It is also interesting how the virtual disk approach presents a behavior without the oscillations of the Simulink model more similar to the sliding grid approach. Both trends are comparable due to the inclusion of the fluid forces

acting on the body that dampen these oscillations. On the other hand, the asymptotic behavior is more in line with the Simulink model. This is because the thrust and torque coefficients required for the virtual disk approach have been set at the same value as the Simulink model. These values correspond to the experimental values obtained by Scanavino [177] shown in Chapter 4. In theory, the sliding grid approach should approximate those values, but, as we mentioned earlier, the grid resolution is insufficient to capture accurately the blade performance, presenting a reduction in thrust predictions.

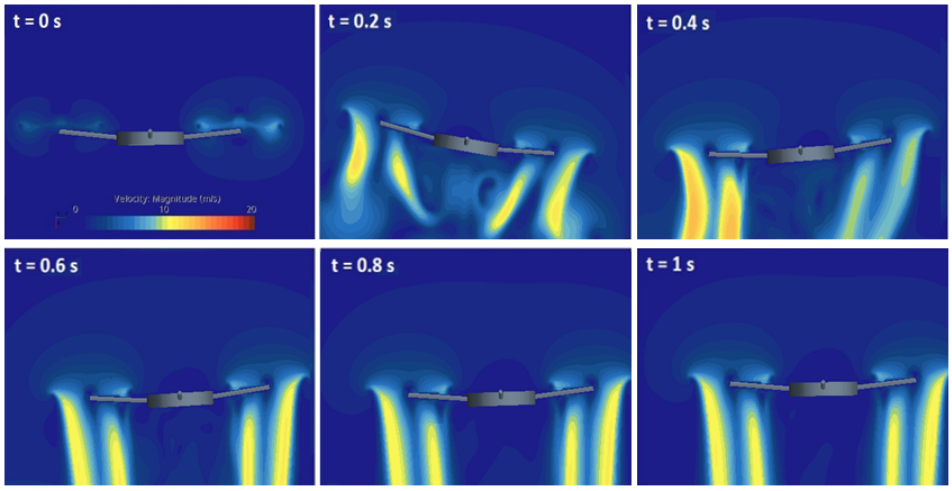

Fig. 7.7 Visualization of the velocity magnitude field obtained with CFD during the quadrotor maneuver using the virtual disk approach.

7.2 Quadcopter in Wall Effect

This section describes a numerical analysis of a quadcopter's performance in the wall effect through CFD simulations. Two types of analysis were conducted: static simulations at a fixed distance from the wall and 6-DOF simulations of the same quadcopter using a PID controller that compensates for the wall-induced disturbances. Figure 7.8 shows the UAS position relative to the wall used for the static simulations. This configuration maximizes the wall effects on the quadcopter [63].

Meanwhile, dynamic simulations were performed using the configuration described in Figure 7.9. In this case, the UAS was kept in a hover position while flying in a '+' configuration parallel to the wall. These maneuvers cannot be replicated with

a classical simplified propulsive model as it cannot consider the near-wall effects on the quadcopter dynamics. To address this, the sliding grid approach was used to resolve the transient loads in the blades caused by the small tip-wall clearance occurring twice per revolution. A virtual disk approach is also insufficient to capture transient loads due to the small tip clearance.

The CFD/PID framework proves essential in understanding this complex coupled aerodynamic/dynamic phenomenon since experimental testing poses the risk of losing the UAS, which can incur high costs. Using CFD simulations during the design of experiments can improve the campaign's safety.

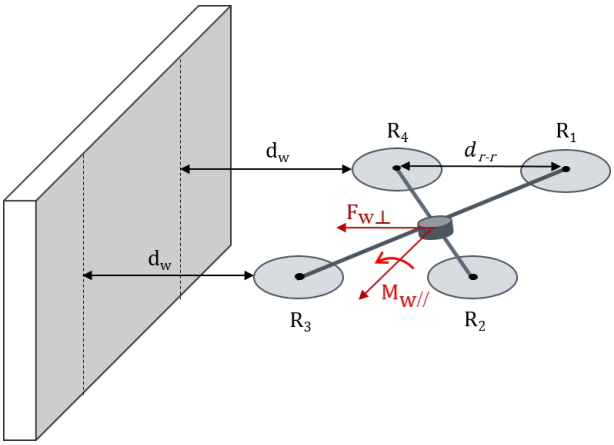

Fig. 7.8 Quadrotor near a wall in configuration 1.

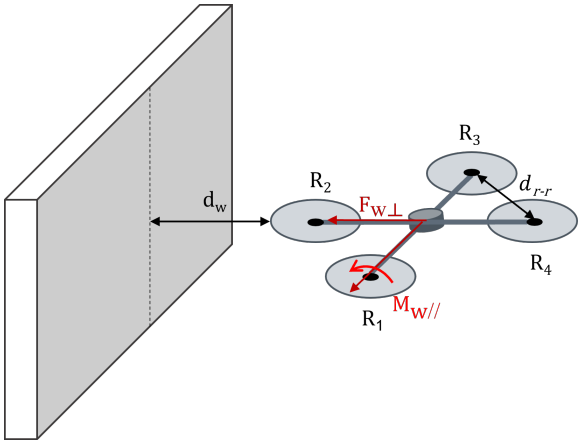

Fig. 7.9 Quadrotor near a wall in configuration 2.

7.2.0.1 Simulations with a Fixed UAS

In this section, we analyze the impact of different wall distances on the UAS, using simulations with a fixed UAS to predict future dynamic behavior. One of the main effects of operating a UAS near a wall is the wall-normal force that pulls the multicopter towards the wall, along with a roll moment that tilts the quadcopter towards the wall, as demonstrated in [63]. Table 7.1 displays the consequences of reducing the tip wall clearance, revealing how these forces and moments increase as the distance to the wall decreases. This instability generates a dynamic situation where the attraction force and tilt moments lead to a super-linear reduction in wall distance. Interestingly, simulations with a zero tilt angle indicate that the inherent coupling between the tilt angle and the thrust orientation is not responsible for the attraction force.

In order to better understand the forces and moments at play, we can refer to Figure 7.10, which depicts the velocity contours and streamlines in a vertical plane perpendicular to the wall containing two rotors. We can deduce how the flipping moment is generated by analyzing the differences in the flow field around the rotors. Precisely, the rotors near the wall experience an increased inflow velocity due to the wall's blockage, which decreases their effective angles of attack and slightly reduces their thrust compared to the rotor positioned further away from the wall. These slight differences in thrust can lead to significant moments, as shown in Table 7.1, especially when the wall clearance is reduced.

In contrast, the attraction force is caused by the reduced change in horizontal momentum across the rotor closer to the wall, thanks to the more vertical inflow direction, as seen in Figure 7.10.

It takes about 1.5 seconds for these simulations to reach a statistically converged solution, roughly equivalent to 100 rotor revolutions. This is ten times more than needed to achieve converged forces and moments in a single-rotor simulation. This suggests that while the wall effect can be risky for multicopter flights, its slow dynamics assist controllers in safely managing this type of operation.

Table 7.1 Influence of tip clearance in time-averaged forces and moments on the Quadcopter.

Tip-Wall Clearance	Wall-Normal force (N)	Roll Moment (Nm)
0.2 R	0.098	0.075
1.2 R	0.054	0.067
2.2 R	0.036	0.045

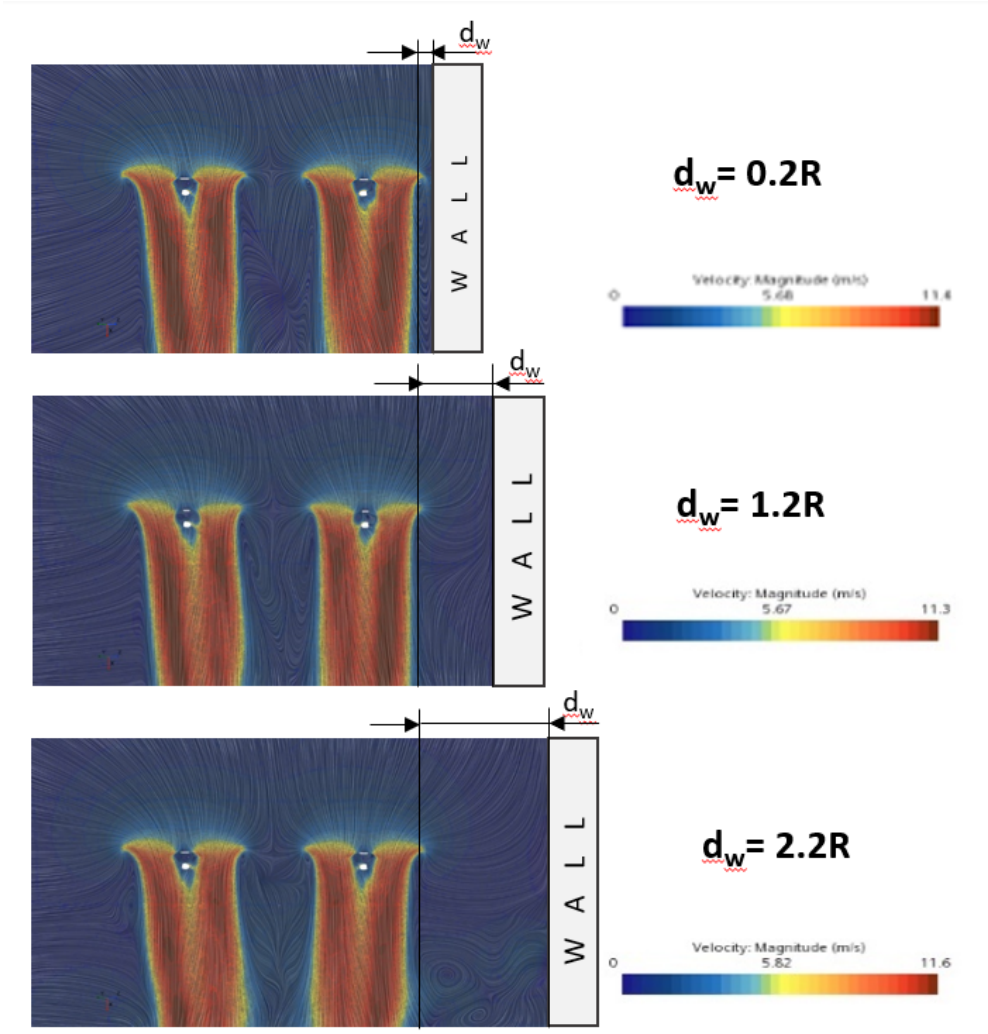

Fig. 7.10 Influence of tip clearance in the fluid flow around the quadcopter.

7.2.0.2 6-DOF UAS simulations

This section examines the behavior of a UAS near a wall when it hovers. When the control algorithm is not activated, the vehicle gradually moves closer to the wall. Simulations were conducted at various distances from the wall to study how sensitive the UAS is to this parameter. In both scenarios, the control algorithm stabilized the UAS by adjusting the roll angle to direct the positive normals of the rotors away from the wall. A slight thrust component also counteracts the suction effect that pulls the vehicle toward the wall.

We conducted two simulations placing the nearest rotor at 5 cm and 10 cm from the wall using configuration two, as depicted in Figure 7.9. Figure 7.11 displays the roll angles' progression during the mission. The roll angle is -0.38 degrees for a larger wall clearance, which decreases to -0.45 degrees for the smallest one. Despite the small absolute values, they suffice to compensate for the wall suction force explained in the previous section. A reduction in wall distance results in a 20% increase in the roll angle. Given that these angles are small, we can infer that the lateral force is proportional to the thrust and angle's product, so the wall suction force would have also increased around 20%. The PID controller compensates for the wall-induced roll moment by slightly elevating the rotation rate of the rotor closer to the wall (Rotor-2) compared to its opposite rotor (Rotor-4). This effect is visible in Figure 7.12.

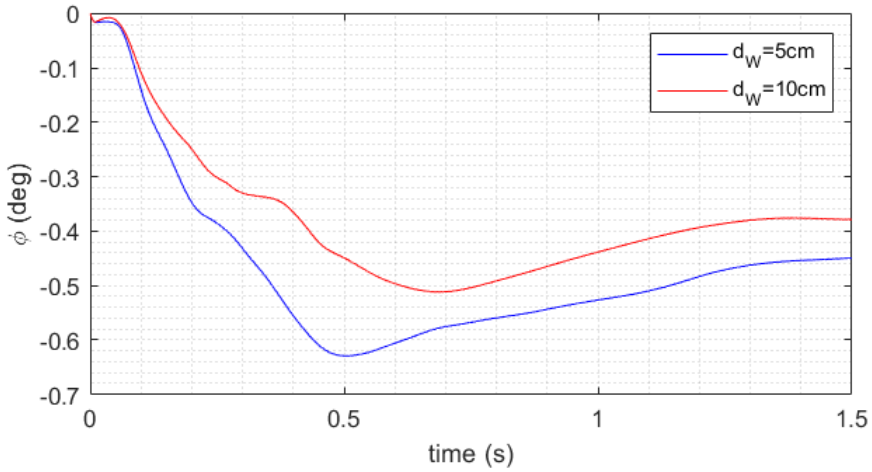

Fig. 7.11 Roll angle of the quadcopter hovering in configuration two at different wall distances.

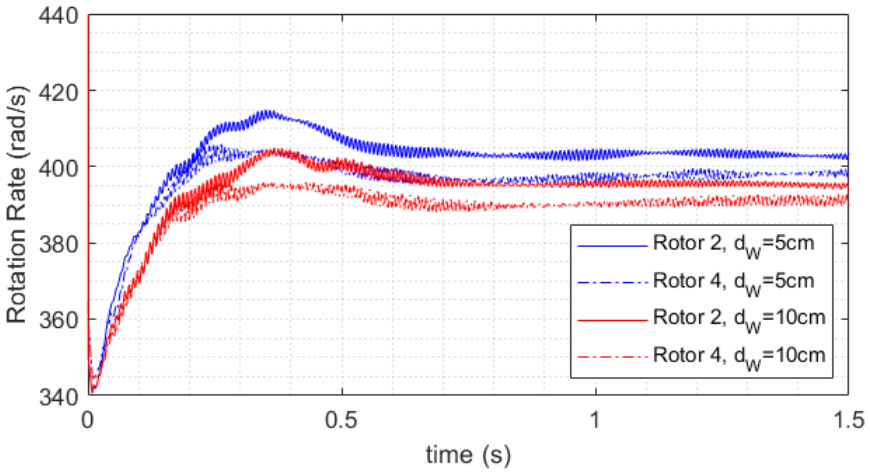

Fig. 7.12 Rotation rates of rotors 2 and 4 hovering in configuration two at different wall distances.

7.3 Discussion

This chapter outlines the development of a virtual simulation environment for a quadcopter, which combines CFD simulations with PID control. Two different approaches have been proposed to model the wake of the rotors. The sliding grid approach is a more general methodology that can resolve transient loads of the rotors. However, it is computationally expensive due to the time-step restrictions caused by high rotor tip velocities and the need to resolve blade geometry accurately. The simplified virtual disk approach is more computationally efficient and uses blade performance coefficients to model the rotor-induced velocities. Although it cannot resolve transient loads, the averaged induced velocities in the wake are comparable. An advantage of this approach is that the time step required for the stability and accuracy of the CFD solver is much larger as these models only reproduce induced velocities and do not consider high rotor tip speeds that typically limit the time step. The PID and dynamics implementation was verified by comparing results with a simplified Matlab/Simulink model for a simple horizontal translation.

The previously verified model employing the sliding grid approach was used to study the wall effect with a fixed quadcopter to understand the aerodynamic interaction of the flow generated by the rotors and the wall. The presence of the wall produces two primary disturbances: a suction force toward the wall and a rolling moment that tends to point the rotor normals toward the wall. The rolling moment

is likely associated with slightly reduced thrust caused by wall blockage, while the suction force is due to the reduction of lateral momentum across the disk. The simulations revealed that the controller could achieve a trimmed hovering position at a slight negative roll angle, pointing the rotor normals away from the wall and compensating for the suction force. An increase in the rotation rate of the near-wall rotor compensates for the wall-induced moment. The trim angle becomes more negative as the distance toward the wall is reduced to compensate for the suction force toward the wall.

These results demonstrate the benefits of CFD simulations in understanding the wall effect in which multicopters are obliged to work for several applications and the coupling with the UAS controller. Preliminary simulations have helped dimension an experimental campaign to study the wall effect in the climate-controlled terraXcube, the same facility used in Chapter 4 for the rotor and quadcopter characterization. The outcome of these tests will provide more insight into this phenomenon and will be a valuable database for validation purposes.

Chapter 8

Numerical Analysis of a UAS Spraying Operation

This chapter includes the partial content of the paper:

- M Carreño Ruiz, N. Bloise, G. Guglieri, and D. D'Ambrosio. Numerical Analysis and Wind Tunnel Validation of Droplet Distribution in the Wake of an Unmanned Aerial Spraying System in Forward Flight. *Drones*, 6(11), 2022

This Chapter begins with a discussion regarding the experimental testing of a hexarotor in a wind tunnel facility. This experimental campaign has two primary objectives. Firstly, we aim to gain a preliminary understanding of the impact on the spray distribution of placing the nozzles under the rotors. Secondly, we seek to validate a numerical model that can accurately predict droplet distributions. The first objective is critical as it enables us to quantify the spray cone angle of the hollow-cone nozzle. The spray cone angle is essential in determining the flight altitude that minimizes PPP deposition in vineyards' inter-row regions. The second objective is crucial in defining a general framework to virtually test any UAS flight configuration. By setting up this simulation environment, we can conduct complete simulations, specify flight conditions and spray system parameters, and evaluate the spray distribution before moving to the vineyard. This approach significantly reduces the number of field tests, which are costly in terms of time and money. Furthermore, the CFD simulation allows us to understand the underlying mechanisms leading to spray drift and attempt to propose solutions. We analyzed the results of the

experimental campaign to determine the effect of different variables involved in the spraying process, such as nozzle type, injection pressure, advance velocity, and rotor velocity. We used a LED backlighting technique to visualize the flow and capture some spray characteristics. These parameters will help us validate a numerical model. To this end, we present a CFD model that simulates the flow inside the wind tunnel, including the hexarotor. The droplets are modeled using spherical Lagrangian particles. We addressed the difficulties in determining the inputs of such models in [28]. In the present work, the model inputs have been estimated by fusing data provided by nozzle manufacturers, experimental observations, and simulations of the hollowcone nozzle using a Volume Of Fluid (VOF) approach as shown in [72, 116]. Once the spray model is validated, it can be used within the virtual simulation environment to reproduce a mission of the sprayer hexacopter in a vineyard.

8.1 Methodology

In this section, we will provide a detailed explanation of the materials and methods we used to achieve the goals of this project. We conducted an experimental campaign in a wind tunnel, utilizing a commercial drone with a specialized spray system. Meanwhile, we also performed numerical simulations of the same setup and conditions. By comparing the results of the experiment and simulations, we validated the CFD model's predictions of the spray distribution in a virtual environment, specifically for a hollow-cone nozzle.

8.1.1 Wind tunnel facility

The SEASTAR-WT (Sustainable Energy Applied Sciences, Technology, and Advanced Research Wind Tunnel) facility in Turin, Italy, is an open circuit wind tunnel called Sustainable Energy Applied Sciences, Technology, and Advanced Research Wind Tunnel. It uses ten fans with a total capacity of around 100 kW to draw air from outside the building through a convergent intake and expel it through a divergent outlet. The test section is 6.4 meters wide and 2.4 meters high, as described in [87]. We could conduct our testing campaign in this facility due to its sufficiently large dimensions and the ability to achieve wind speeds of up to 8 m/s.

Fig. 8.1 UASS and Camera Setup in the SEASTAR Wind Tunnel.

Fig. 8.2 DJI Matrice 600 with a customised spray system.

In particular, a structure was included in the experimental setup to hang the drone from the top of the test section to avoid disturbances in the free stream in the neighborhood of the drone, as shown in Figure 8.1.

8.1.2 Specifications of UASS

A customised standalone spray system is designed for a hexacopter DJI Matrice 600 (DJI, China) and integrated for the experimental test in the wind tunnel, as in Figure 8.2.

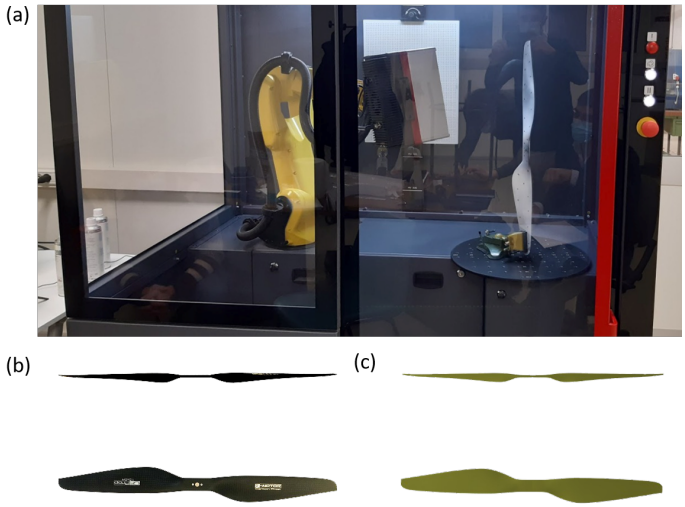

Fig. 8.3 (a) Optical Precision Measuring Machine, (b) Photo of T-Motor 15”x 5”, (c) CAD model.

For this purpose, the original blades are replaced with the smaller T-Motor 15”x 5” to reduce thrust generation and not compromise the structure supporting the drone. To properly validate the numerical model, a precise blade geometry was needed. An Optical Precision Measuring Machine (OPMM) was used to perform a 3D scan of the blade geometry, as shown in Figure 8.3. The procedure used to transform the cloud of points obtained from the 3D scan to a CAD model is explained in detail in Chapter 4.

8.1.2.1 DJI Matrice 600

The DJI Matrice 600 was chosen for the experimental testing campaign due to its recommended Maximum Take-Off Weight (MTOW) of 15.5 kg. The drone’s characteristics are reported in Figure 8.4 and Table 8.1. The drone is fixed to the supporting frame with its nose, represented with red motors (M1 - M2), rotated clockwise by 30° with respect to the wind direction, as shown in Figure 8.4. The UAS is in a horizontal position relative to the ground. In this study, we did not consider the effect of the tilt angle, a parameter that depends on the weight of the UASS, which decreases during the spray mission. It is challenging to measure this angle accurately, so instead of fixing the tilt angle at an arbitrary angle, as done in other studies, we decided to set the tilt angle to zero.

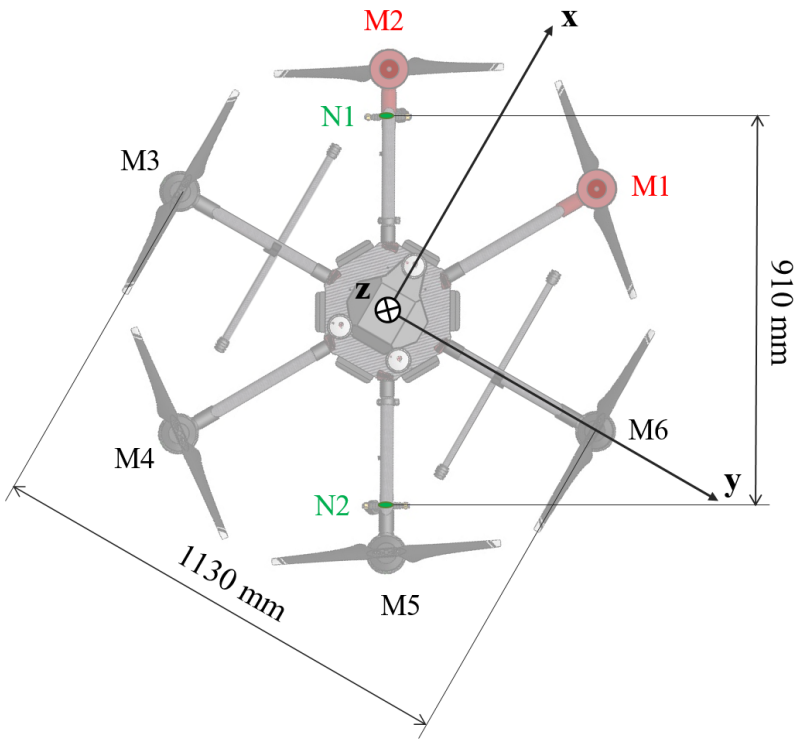

Fig. 8.4 Top view of DJI Matrice 600 (Body-Fixed axes) with nozzles aligned with wind direction.

Table 8.1 Main parameters of DJI Matrice 600.

Parameters description	**Value**
Wheelbase	1133 mm
Rotor diameter	381 mm
Rotor pitch	127 mm
Number of rotors	6
Brushless motor	DJI 6010

In the idle condition, the rotors' speed is 1590 RPM, whereas, in full throttle, the rotors turn at 5100 RPM. Furthermore, the rotor plane is inclined by 7° with respect to the ground, and this angle influences the spray distribution.

8.1.2.2 Spray system design

A dedicated spray system was manufactured according to the circuit presented in Figure 8.5 and includes a remote-control system to switch the pump on and off. The system contains a battery, a membrane pump, a pressure regulator, a pressure gauge, and two nozzles for a total weight of approximately 2.5 kg. In particular, the external battery powers the membrane pump to generate a flow rate of up to 6 l/min and can be switched on/off by a radio remote control. A manual pressure regulator is placed downstream of the pump. Finally, a vacuum pressure gauge measures the pressure level in real-time to guarantee the correct liquid flow rate of the nozzles. Two nozzles' holders (N1 and N2) are installed under the rotors M2 and M5, as evidenced in Figure 8.4, perpendicular to the rotor arms. Hollowcone (HCI8002, manufactured by ARAG Group) and anti-drift fan nozzles (AFC11002, manufactured by ARAG Group)) are tested to analyze relative spray characterization. This figure's coordinate system (x,y,z) represents the body axes, complying with the reference frame that the DJI company specifies for the flight controller. The UASS is rotated clockwise by 30° because, in this application, the nozzles must be precisely above the vine rows and therefore aligned with the wind direction.

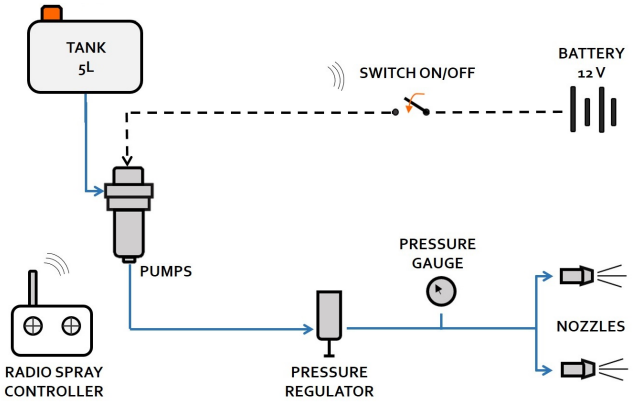

Fig. 8.5 Hydraulic circuit of spraying system.

8.1.3 Experimental Campaign

An experimental campaign was performed to analyze qualitatively the interaction of the droplets. Different parameters were assessed, including the wind tunnel velocity, the nozzle type, the motor speed, the nozzle location, and the injection pressure. In this Chapter, we only analyze a selection of these cases useful for validation purposes. Please refer to [28, 43] for details on the experimental procedure and complete set of results.

8.1.4 Numerical methods

8.1.4.1 Simulation of DJI Matrice 600 in SEASTAR

The numerical model simulating the wind tunnel's flow solves Unsteady Reynolds-Averaged Navier Stokes (URANS) equations embedded in the commercial CFD software STARCCM+ [188]. An accurate wind tunnel model was created to adequately reproduce the experimental setup. The rotational motion of the rotors is modeled with a dynamic mesh approach in which a portion of the grid embedding the rotor slides inside an outer static grid using an Arbitrary Mesh Interface (AMI) protocol. This approach has been validated and explained thoroughly in Chapter 4. The computational grid is formed of 10 million cells. The leading rotor and its wake have an enhanced grid resolution compared to the rest of the domain to adequately capture the region where most rotor-droplet interaction will occur, even though its resolution is still smaller compared to the analysis presented in Chapter 4. The time step is set to $10^{-4}s$ to limit the maximum rotation per temporal iteration of 3^o. Initially, the flow inside the wind tunnel is allowed to evolve for 60 seconds using a larger time-step which is possible as, during this time, the rotors are off. Then the rotors operate for a total time of 4 seconds. They operate 2 seconds before the particles are injected to allow the rotor wake to develop and an extra 2 seconds with the spray system on. The adopted time-integration scheme is implicit and second-order accurate. The inviscid fluxes are modeled with a second-order upwind reconstruction. We use the one-equation Spallart-Allmaras model as a turbulence model [192]. The generated grid has y^+ values lower than 1, in agreement with the turbulence model guidelines. The flow in the wind tunnel is driven by ten fans, as shown in Figure 8.1. These are modeled with a fan-type interface that assumes a finite pressure jump across a

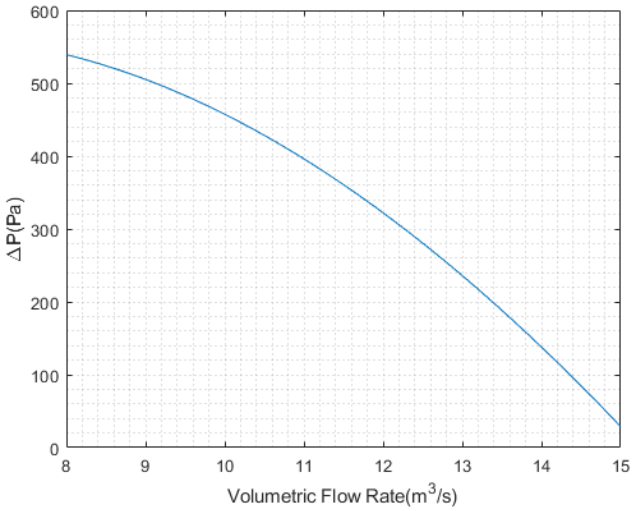

Fig. 8.6 Fan performance curve at 1700 RPM.

zero-thickness disk. The pressure jump is computed based on the fan performance curve supplied by manufacturers shown in Figure 8.6. The performance curve can be adjusted for different operating rotational velocities of the fans, which allows the adjustment of the velocity magnitude in the test section. The usual linear scaling for flow rate and quadratic scaling for pressure jumps, predicted by actuator disk theory, are used as shown in Equations 8.1 and 8.2.

$$\Delta P_2 = \Delta P_1 \frac{\Omega_2^2}{\Omega_1^2} \tag{8.1}$$

$$V_2 = V_1 \frac{\Omega_2}{\Omega_1} \tag{8.2}$$

Figure 8.7 shows the velocity field inside the wind tunnel driven by the fans, including the UAS operating at 5100 rpm. The wind velocity at the center of the test section inside the wind tunnel with the rotors off was measured to a value of 2.0 m/s. This value compares well with the velocity of 1.96 m/s revealed by the CFD simulation at the same position for the selected fan operating point.

Simulations are performed using 64 cores of 2 Intel Xeon Scalable Processors Gold 6130 2.10 GHz. The computational cost of one simulation was around 6000 CPU hours.

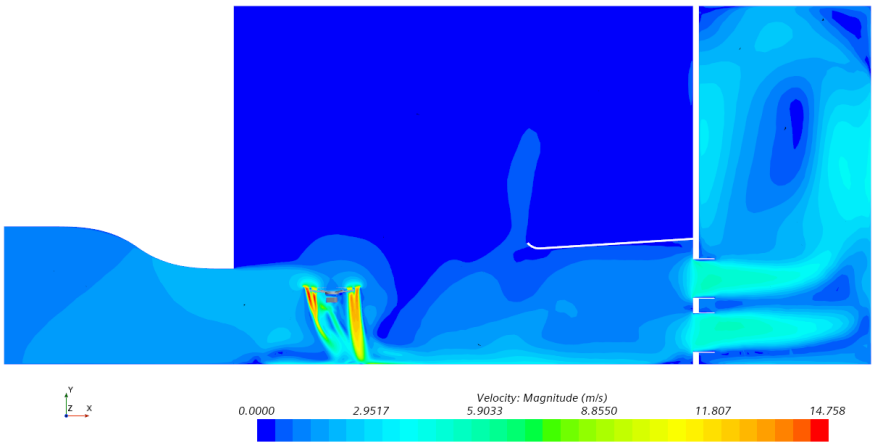

Fig. 8.7 Instantaneous velocity magnitude field inside the wind tunnel operating at 2 m/s and rotors operating at 5100 RPM.

8.1.4.2 VOF Simulation of the Hollowcone Nozzle

Our simulations use a Lagrangian spherical particle model to represent the spray droplets. Chapter 2 explains how Newton's second law defines particle dynamics. However, solving this equation requires integrating the initial position and velocities of the particles. While the initial position is defined at the nozzle location, determining the initial velocity is crucial, especially for larger particles with higher inertia.

The initial velocity conditions for integrating the dynamic equation for the particles have been computed using the multiphase high-resolution interphase capturing VOF method in a separate CFD simulation of the employed nozzle. This methodology has been followed by [116, 72] among others to compute spray characteristics. We used the VOF solver embedded in STAR-CCM+, described in detail in Chapter 2. For these simulations, 20 implicit sub-steps of the phase transport equation are combined with an adaptive time-stepping to avoid interface blurring. Despite this improvement, the global time-step must be kept around $10^{-6}s$. A $k-\omega$ SST turbulence model was used in these simulations. However, an in-depth study would be required to understand the ability of turbulence models to reproduce turbulent conditions combining internal flows and external boundary layers. A better approach would have been to use large eddy simulations as performed by Laurila [116], given that temporal and spatial resolutions are already very fine. In any case, this was

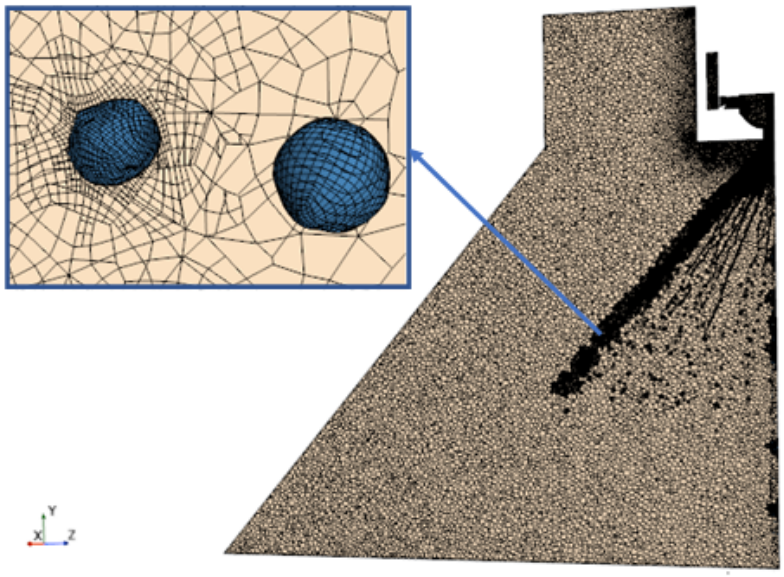

Fig. 8.8 Grid detail showing interphase triggered AMR.

out of the scope of this work, which aims to estimate the initial velocities of the droplets. An adaptive mesh refinement using a minimum refinement level of 10 μm was used to adequately track the interface. A grid detail is shown in Figure 8.8. The simulations used 64 cores of 2 Intel Xeon Scalable Processors Gold 6130 2.10 GHz. The computational cost was approximately 12,000 CPU hours per simulation.

8.2 Experimental Results

Figures 8.9 and 8.10 show the most significant lateral photos taken during testing campaign. Following the test matrix, the cases of hollowcone and fan nozzle are presented by varying RPM and wind velocities. Likewise, Figures 8.11 and 8.12 represent some results of frontal photos to evaluate the reduction of spray angle with increased RPM rotors or the pressure.

Based on the results presented, it is evident that the rotors' wake has a significant impact on droplet distribution. A higher rotor speed leads to better control and a more vertical spray distribution, which is highly beneficial in vineyards. Furthermore, the hollow cone nozzle is more significantly affected by wind velocity and rotation rate than the fan nozzle. This is because the droplets produced by the hollow cone nozzle are finer and more prone to drift with the flow. The following section uses

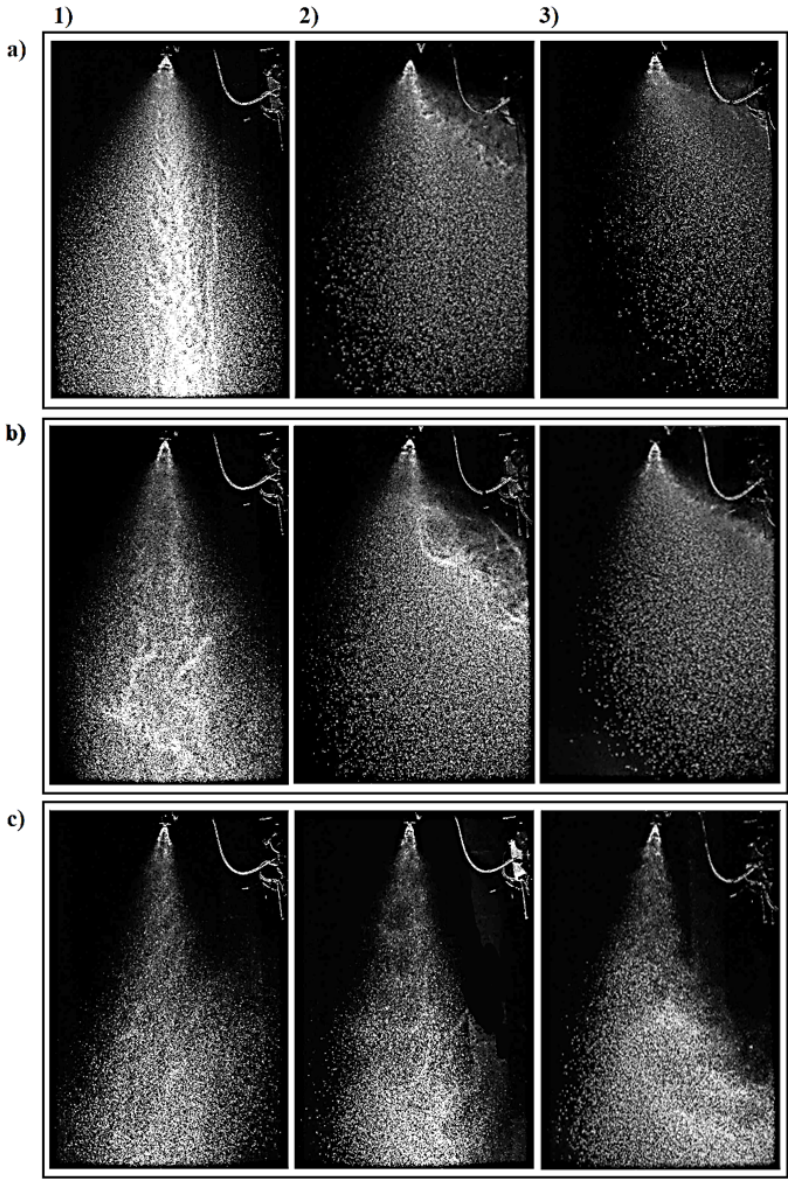

Fig. 8.9 Lateral view of spray with Hollowcone nozzle for a) no rotor, b) idle, and c) throttle condition in 1) hovering, 2) at wind speed = 2 m/s, and 3) at wind speed = 3 m/s.

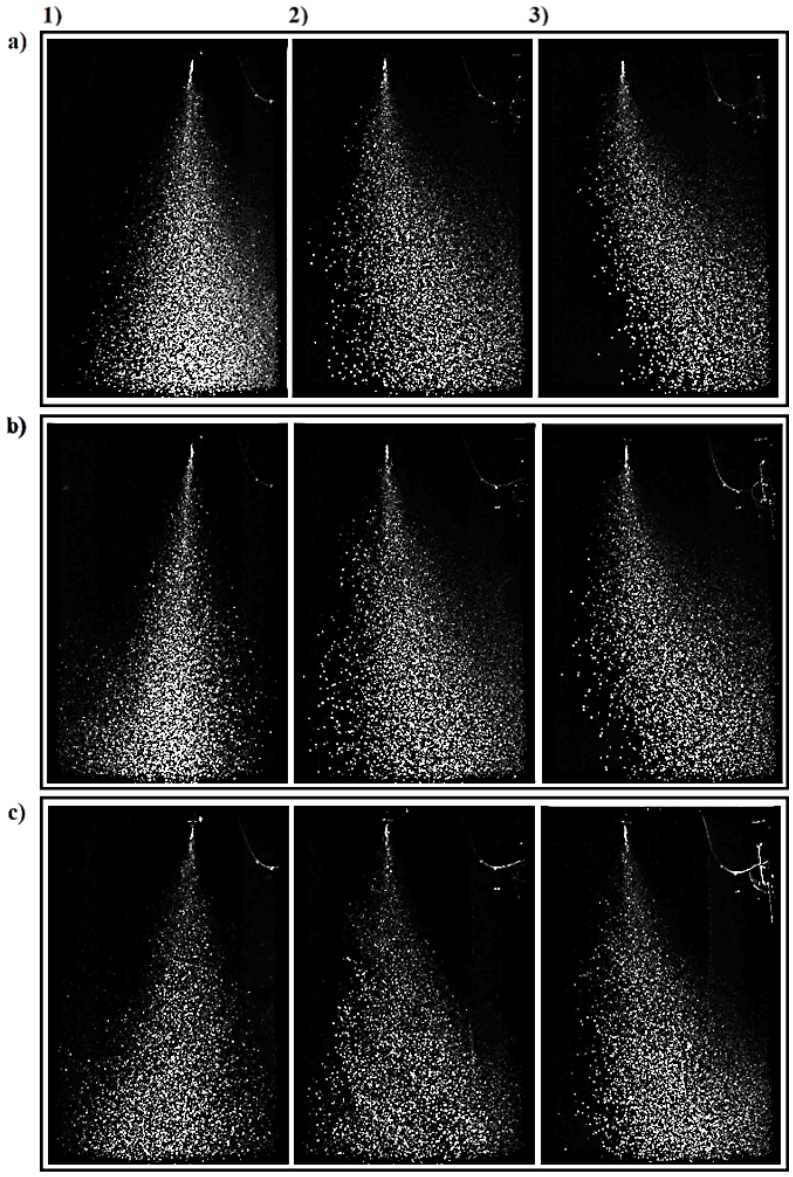

Fig. 8.10 Lateral view of spray with Fan nozzle for a) no rotor, b) idle, and c) throttle condition in 1) hovering, 2) at wind speed = 2 m/s, and 3) at wind speed = 3 m/s.

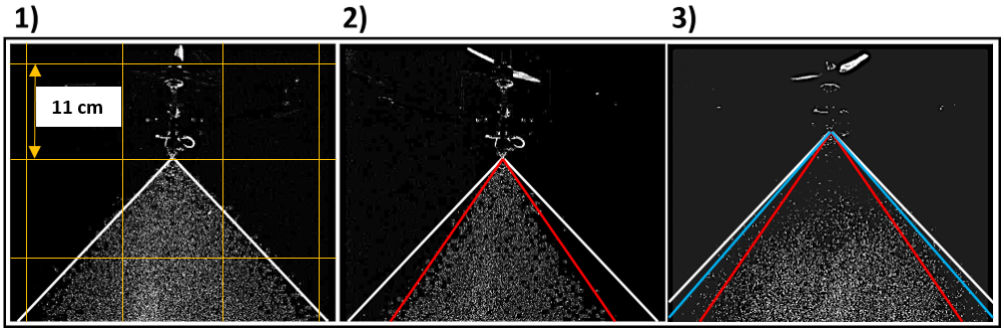

Fig. 8.11 Frontal view of spray with Fan nozzle for 1) no rotor at 2 bar, 2) throttle at 2 bar and 3) throttle at 3 bar.

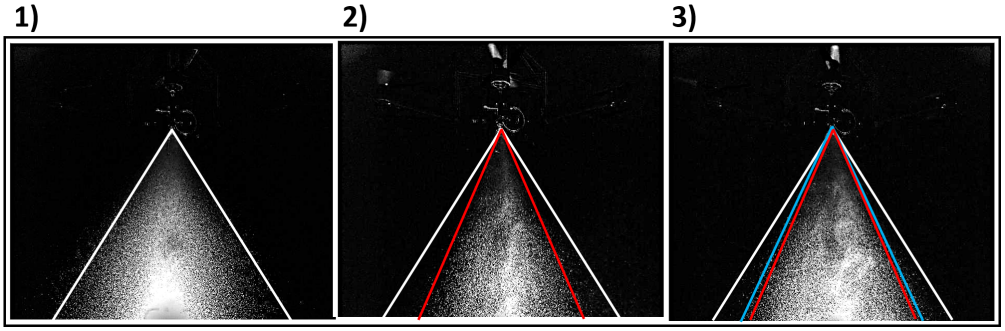

Fig. 8.12 Frontal view of spray with Hollowcone nozzle for 1) no rotor at 2 bar, 2) throttle at 2 bar and 3) throttle at 3 bar.

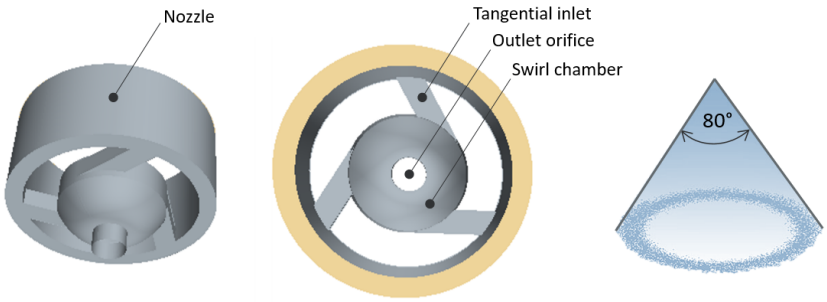

Fig. 8.13 CAD model and the hollowcone spray angle of the HCI8002 nozzle.

the research findings to validate the CFD model for predicting particle distribution. After validation, we could explore other conditions to avoid the time and economic costs associated with experimental campaigns.

8.3 CFD Simulation

8.3.1 Hollowcone Nozzle Characterization

The ARAG Group supplied the hollow cone nozzle, identified by the reference code HCI8002, for our experimental campaign. This type of nozzle is classified as a pressure-swirl nozzle because it creates a conical sheet of fluid at the nozzle exit through centrifugal forces acting on the rotating fluid in the swirl chamber. The breakdown of the conical sheet into droplets is highly complex and expensive to model numerically [118]. Some researchers [72, 116] have used interphase capturing methods to resolve it.

The four main characteristics of a hollow cone spray are particle diameter distribution, film velocity, film thickness, and cone angle. These characteristics are heavily influenced by the injection pressure/mass flow and the nozzle's geometry, particularly the exit orifice. Determining the hollow cone spray characteristics is crucial to model the interaction between the rotors and the spray. Figure 8.13 displays a simplified CAD model of the nozzle, and Table 8.2 lists its primary characteristics.

This model shows the inside of a nozzle and is designed to help with precise CFD modeling of the multiphase flow. The nozzle has three tangential inlets that enable the rotation of the flow around the swirl chamber's vertical axis. Due to centrifugal

Table 8.2 Main characteristics of the HCI8002 nozzle.

ARAG - HCI8002	
Pressure	3 bar
Volume flow rate	0.8 $lmin^{-1}$
Droplet size	fine

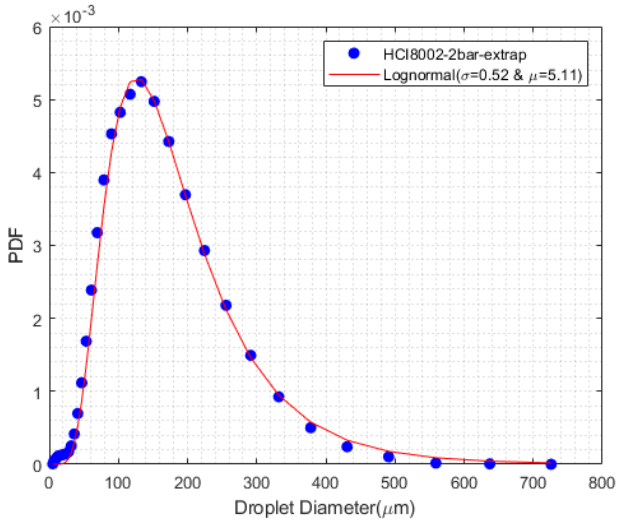

Fig. 8.14 Probability density function for the droplet diameter distribution.

forces, the fluid moves towards the wall, creating an air core in the nozzle. When pressure builds up, the rotating liquid film is pushed through the orifice, and the centrifugal forces expand the liquid film, forming a conical fluid film, as displayed in Figure 8.16.

8.3.1.1 Droplet diameter distribution

The nozzle manufacturers provided information about the size of particles at different injection pressures. In Figure 8.14, we can see the size distribution of particles at our working pressure of 2 bar, which has been extrapolated using a 3-point-based Akima algorithm for each droplet diameter. The particle size distribution follows a log-normal pattern with parameters $\mu = 5.11$ and $\sigma = 0.52$.

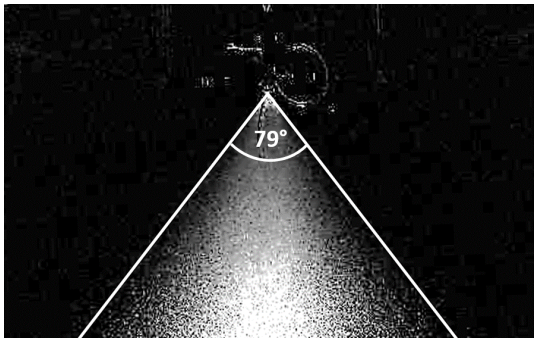

Fig. 8.15 Hollowcone angle for a pressure of 2 bar measured during the experimental campaign.

8.3.1.2 Cone angle

In [43], we explain how our visualization method can determine the angle of a conical sheet of liquid as it breaks down into droplets following initial instability. The hollow cone sheet breakdown simulation is discussed further in [72]. We measure the angle using frontal images, as illustrated in Figure 8.15. Our results show an angle of around 79 degrees.

Figure 8.16 shows the water-air interphase, which clearly shows a hollowcone shape, and this value agrees well with the cone angle found in the CFD simulation shown in Figure 8.17, where a half cone angle of 40 degrees is measured. The atomization process is reproduced and shows the breakdown of the conical fluid sheet first into ligaments, and then, these ligaments break down into droplets. This image is a detail of the near nozzle region. Figure 8.20 shows a much larger domain showing complete atomization.

8.3.1.3 Film velocity and tangential velocity

The film velocity is the non-tangential velocity component of the liquid contained in the conical sheet. Considering a cylindrical coordinate system (r, θ, z) centred on the exit orifice and with the z-axis coincident with the vertical axis, the film velocity (U_f) would be the result of combining the radial (U_r) and axial (U_z) components of velocity as shown in Equation 8.3.

$$U_f = \sqrt{U_r^2 + U_z^2} \tag{8.3}$$

Fig. 8.16 Water-air interphase in VOF CFD simulation showing the conical sheet of fluid produced by the pressure swirl nozzle at a pressure of 2 bar.

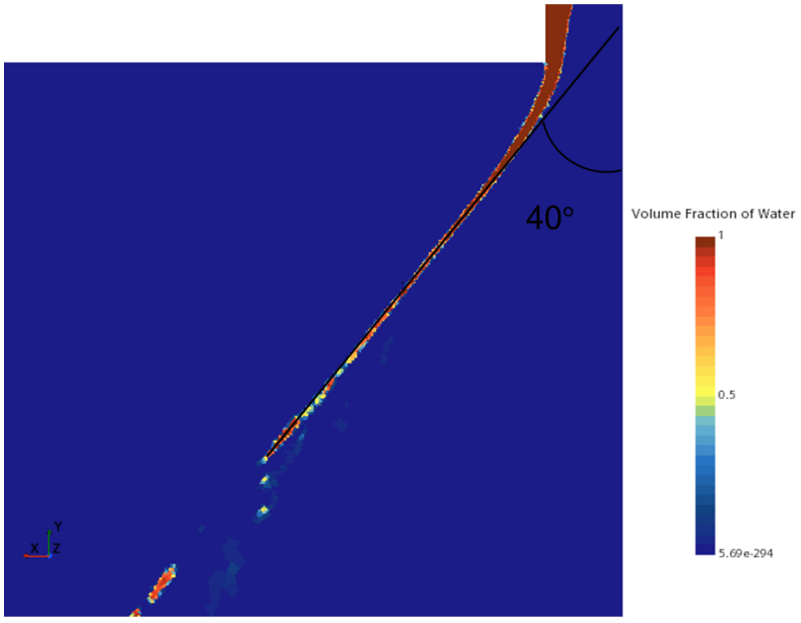

Fig. 8.17 Water volume fraction in VOF CFD simulation showing the conical sheet of fluid produced by the pressure swirl nozzle at a pressure of 2 bar.

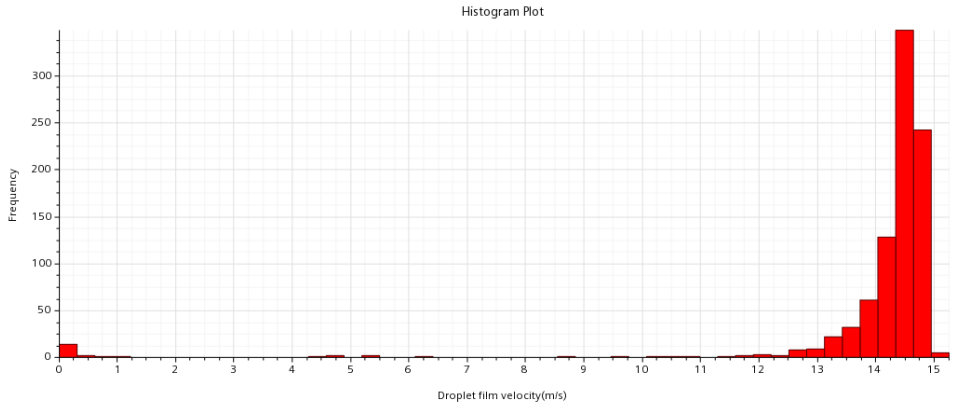

Fig. 8.18 Film velocity of the liquid droplets after the breakdown of the conical sheet of fluid produced by the pressure swirl nozzle at a pressure of 2 bar.

According to the CFD simulations, the film velocity of the conical sheet is approximately 14.5 m/s before it breaks down into ligaments and droplets due to instabilities. Although the simulation time and generated droplets may not be enough for statistical convergence, Figure 8.18 indicates that the droplets' initial velocity is nearly equal to the film velocity after the breakdown. Most droplets have a velocity ranging between 14 and 15 m/s. Therefore, we will use a constant injection velocity of 14.5 m/s for the Lagrangian particle model.

On the other hand, the tangential velocity (U_θ) is not constant as the fluid film evolves and decreases as the radial coordinate of the cone increases, as shown in Figure 8.19. We can appreciate how the generated droplets have a tangential velocity close to zero. Therefore, we will simulate Lagrangian particles without an initial tangential velocity.

8.3.2 Wind effects on the hollow cone spray

Based on simulations using an 80-degree cone angle to inject Lagrangian particles, it appears that droplet dispersion is much wider than the actual experimental measurements. This suggests that the conical sheet is deformed before the droplets detach from the ligaments due to the strong rotor induction. Therefore, the injection angle of the Lagrangian particles needs to be adjusted. To capture the rotor downwash's first-order effects on droplet formation, a multiphase simulation was conducted with a constant vertical wind. The simulation of the hexacopter at maximum throttle

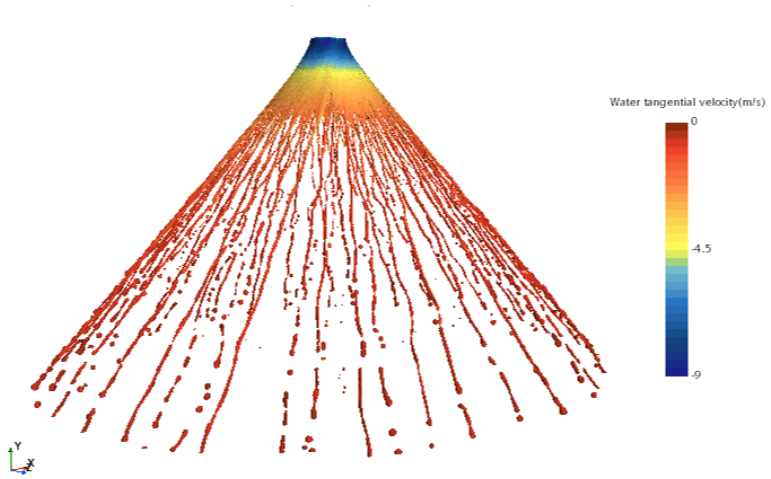

Fig. 8.19 Tangential velocity of the liquid phase forming a conical sheet of fluid produced by the pressure swirl nozzle at a pressure of 2 bar.

Table 8.3 Numerical Simulation Parameters.

Simulation	Wind speed [m/s]	Nozzle type	Motor speed	Pressure
1	2	HCI8002	0	2 bar
2	2	HCI8002	5100 rpm	2 bar

revealed that the induced axial velocity at the injection point is 12 m/s, which is used as the vertical velocity in the VOF simulations. Figure 8.20 displays a significant closure of the cone angle from 80° to 56°. Therefore, an angle of 56 degrees was used to model the hollowcone injector of Lagrangian particles.

8.3.3 Experimental Validation

In the previous sections, we explained how we determined the initial conditions (momentum, diameter, and cone angle) for the Lagrangian particle injection model. The mass flow rate we used was 0.67 liters per second, which matches the VOF simulation. To ensure that the diameters of the particles we injected were statistically representative, we used a random number generator that followed a lognormal distribution with $\mu = 5.11$ and $\sigma = 0.52$. We allowed the particles to be injected for 2 seconds to ensure that we had reliable statistics and to give them enough time to be carried by the flow.

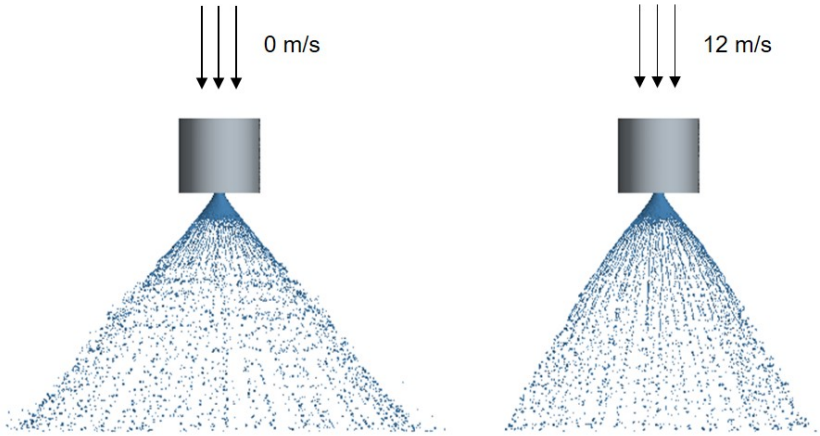

Fig. 8.20 Water-air interphase in VOF CFD simulation showing the conical sheet of fluid produced by the pressure swirl nozzle at a pressure of 2 bar with no axial velocity (left) and with an axial velocity of 12 m/s (right).

To assess the validity of the developed numerical model, we present a comparison between experimental LED visualization images and the distribution of Lagrangian particles. We have performed this validation with the wind tunnel operating at 2 m/s with the rotors off and operating at maximum throttle. The simulation parameters are summarized in Table 8.3. The comparison with experimental results is shown in Figure 8.21. We can appreciate how the lateral views are congruent, presenting similar cone angles, and the lateral wind-induced drift is evident. The contours of the spray have been highlighted in blue for the experimental images and red for the numerical prediction of droplet distributions. The minor deviations of the spray distributions are possibly caused by the fact that in Section 8.3.2 a fully vertical flow was considered, and indeed, a small component of cross-flow would be present that could eventually deform the hollowcone fluid sheet slightly, modifying injection parameters. Another possible source of error is a slight misalignment of the injector in the experimental campaign caused by the impulsive activation of the spray system. CFD simulations give additional information as we can track every particle in the 3-dimensional domain. In addition, it is appreciated how the drift is extremely sensitive to particle diameter. Large particles (red and orange) maintain the conical structure considerably due to their large inertia, making them much less sensitive to the velocity and pressure fields. On the other hand, the smaller particles (yellow, green, and blue) are affected by the flow, which convects the droplets upstream and downstream of the hexacopter. However, we appreciate how most of the particles are contained in the wake and how this directs the particles toward the ground, reducing

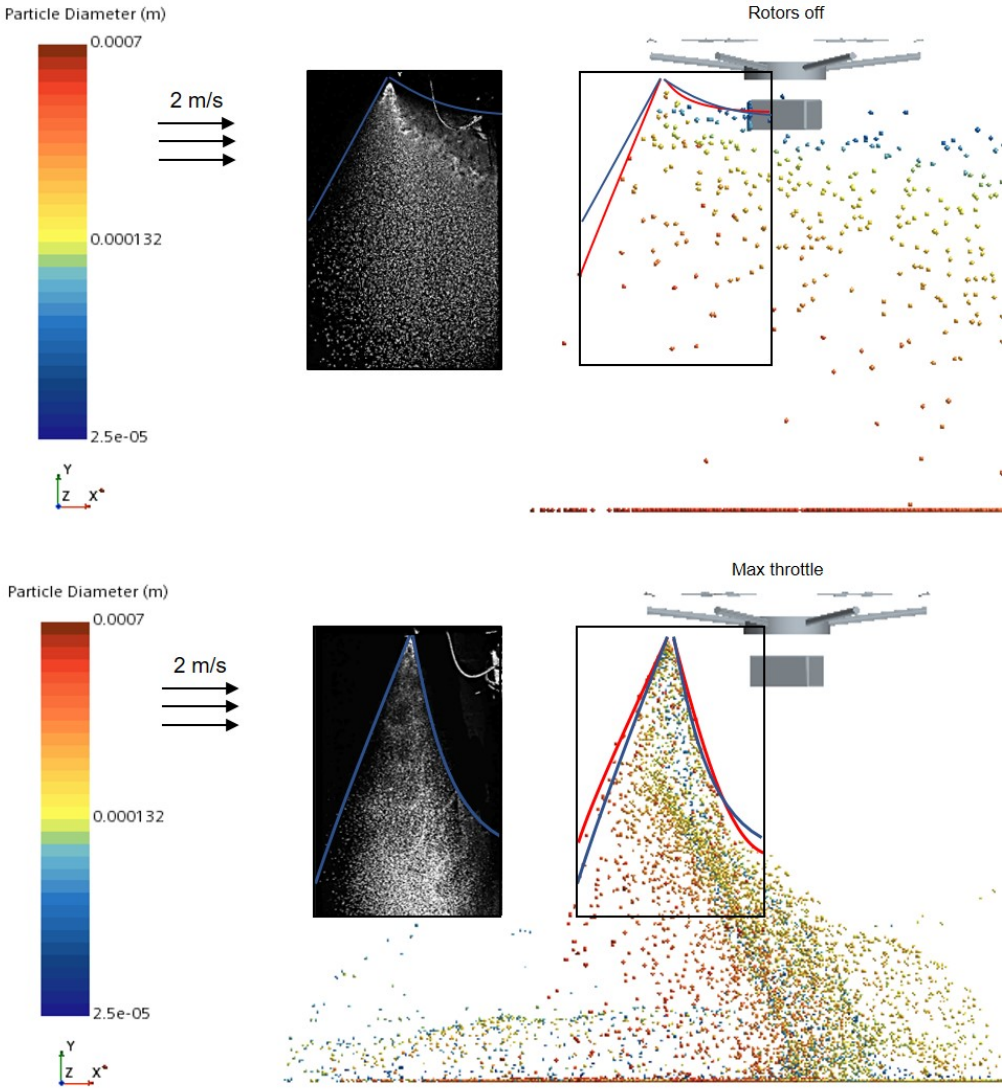

Fig. 8.21 Comparison between the lateral views of droplet LED visualization and CFD simulations with a wind tunnel speed of 2 m/s. Rotors off (top) and Rotors at full throttle (bottom).

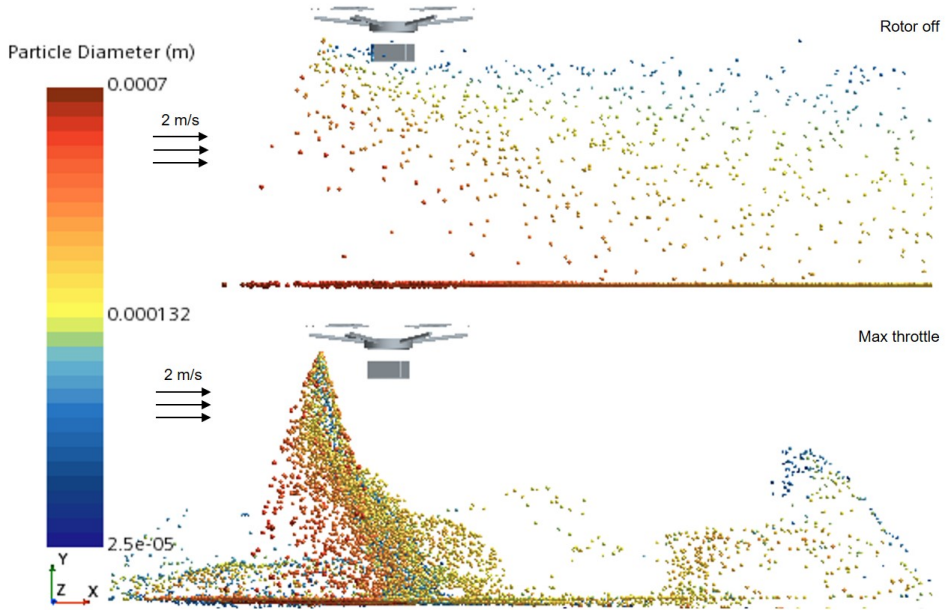

Fig. 8.22 Comparison between droplet distribution in CFD simulations at a wind speed of 2 m/s with Rotors off (top) and Rotors at full throttle (bottom).

drift. To show the beneficial effect of the rotor downwash, Figure 8.22 compares the droplet distributions obtained with and without the rotors operating at full speed.

The drift is minimized except for a lateral flow generated when the particles leave the downwash region. This is caused by the stream tube forming the wake deviating toward the negative Z direction. This is evident in Figure 8.23 presenting isosurfaces of the velocity magnitude at 10 m/s. This asymmetry is caused by the interaction of the swirling flow in the wake and the wind tunnel velocity. Acknowledging this asymmetry is important as it could impact the optimal nozzle positioning and the optimal trajectory of the vehicle, which could be potentially corrected to compensate for this effect. Figure 8.23 suggests that the rear rotor may be a more suitable location for the nozzles due to the much more uniform wake structure.

Reducing the cone angle could be beneficial to reduce this drift, allowing the droplets to remain in the high-velocity wake region until they are very close to the ground or the vine in a real application. Also, using cone nozzles instead of hollow-cone angles would be advantageous. Small particles ($<100\mu m$) represent a small fraction of the total volume of sprayed liquid due to the cubic relationship

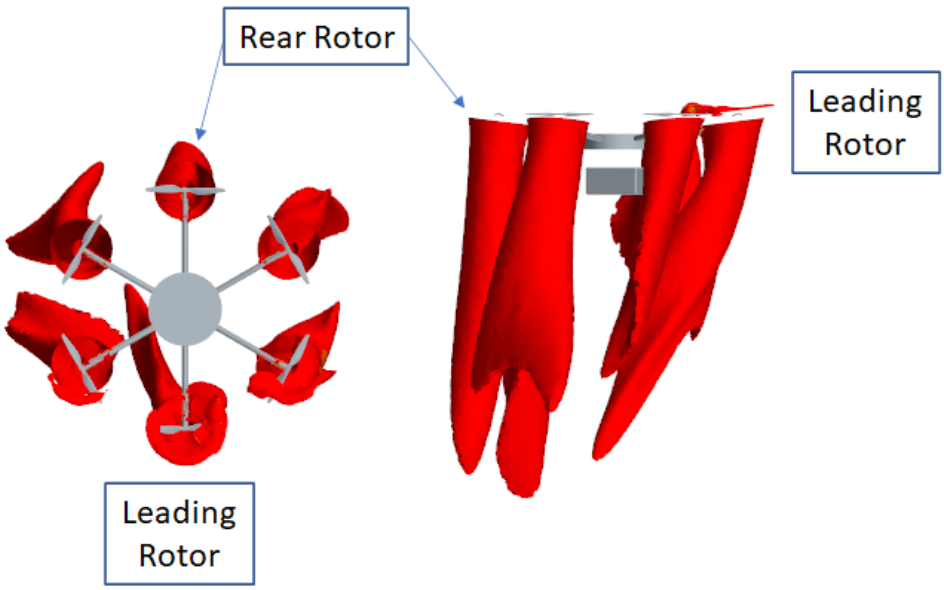

Fig. 8.23 Velocity magnitude 10 m/s Isosurface in the Wind Tunnel simulations at 2 m/s with rotors operating at 5100 rpm.

between diameter and volume. It is interesting to note that the different inertia of the particles cause the stratification by diameter when the rotors are not operating.

The improved droplet deposition obtained with the rotor-on configuration was expected as the particles with small inertia align with the streamlines of the flow, which in this case, are directed toward the ground. In the case of rotors-off, these are horizontal, and droplets may be drifted for long distances. In a real flight, this situation would be equivalent to placing the injectors in such a way as to avoid the hexacopter's wake. In this case, particles remain suspended in the air for a long time and could be transported very long distances, even by small wind gusts. This situation could pose health issues, as Plant Protection Products (PPPs) are often hazardous and should also be avoided from an efficiency point of view, as a reasonable amount of the product could miss the target. Both situations shown in Figure 8.22 are identical, with the only difference of the blades' rotation rate. This observation reinforces the critical role of this operation parameter in droplet deposition, which is especially important to study as the weight of UASS may vary significantly during their mission, with ratios of up to 40% comparing final and initial weight. Another comment is the need to avoid the formation of the so-called horseshoe vortices, also known as super tip vortices in the field of urban air mobility [213], typically formed in multirotors wakes operating at relatively high advance velocities [224, 27]. Otherwise, the spray

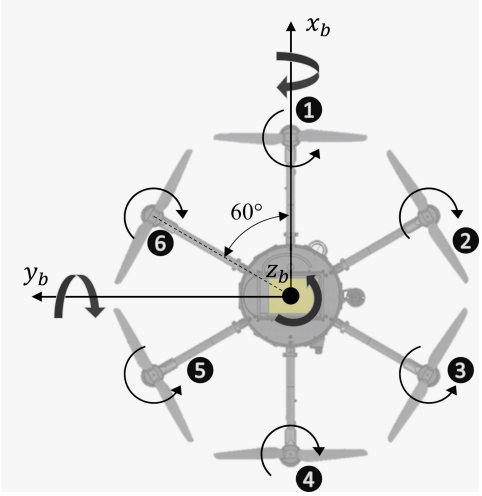

Fig. 8.24 Hexarotor sketch in the body frame.

imprint would become much more unpredictable and challenging to control, even though it could have some potential advantages, such as improved lateral penetration of the plant.

8.4 Simulation of a Spraying operation in a Vineyard

In this section, we apply the aforementioned spray model in a virtual spraying operation using the numerical setup described in Chapter 7. In this case, instead of testing a quadrotor, we will test an hexarotor, so small adjustments had to be made to the model to accurately correct the velocity of the six rotors using the same controller structure. The work shown in the previous section using the DJI Matrice 600 was vital in planning the field tests in an actual vineyard using our UAS and spray system. This experimental work is shown in [26]. We will use that spraying mission as a guideline to create our virtual testing environment.

8.4.1 Hexarotor Dynamics

Despite using the same control loop described in Chapter 7, the different dispositions and number of rotors of the DJI Matrice 600 require a modification in the motor mixer. The rotor positions, orientation and body axis are shown in Figure 8.24. This set of equations maps the control required force and moments with the rotational

speeds. Considering a planar configuration, these can be expressed as:

$$\begin{bmatrix} u_1 \\ \tau_2 \\ \tau_3 \\ \tau_4 \end{bmatrix} = \begin{bmatrix} K_T & K_T & K_T & K_T & K_T & K_T \\ 0 & -\frac{\sqrt{3}K_T l}{2} & -\frac{\sqrt{3}K_T l}{2} & 0 & \frac{\sqrt{3}K_T l}{2} & \frac{\sqrt{3}K_T l}{2} \\ -K_T l & -\frac{K_T l}{2} & \frac{K_T l}{2} & K_T l & \frac{K_T l}{2} & -\frac{K_T l}{2} \\ -K_D & K_D & -K_D & K_D & -K_D & K_D \end{bmatrix} \begin{bmatrix} \omega_1^2 \\ \omega_2^2 \\ \omega_3^2 \\ \omega_4^2 \\ \omega_5^2 \\ \omega_6^2 \end{bmatrix} \tag{8.4}$$

Apart from the additional rotors, this hexacopter presents the complication of not being planar. The arms, of length $l = 0.567m$, have an inclination, γ of around 7 degrees. This slightly complicates the rectangular matrix shown in equation 8.4. The new formulation of this matrix, **M**, is:

$$\begin{bmatrix} K_T c_\gamma & K_T c_\gamma & K_T c_\gamma & K_T c_\gamma & K_T c_\gamma & K_T c_\gamma \\ K_D s_\gamma & -\frac{\sqrt{3}K_T l}{2} - \frac{K_D s_\gamma l}{2} & -\frac{\sqrt{3}K_T l}{2} - \frac{K_D s_\gamma l}{2} & K_D s_\gamma & \frac{\sqrt{3}K_T l}{2} - \frac{K_D s_\gamma l}{2} & \frac{\sqrt{3}K_T l}{2} - \frac{K_D s_\gamma l}{2} \\ -K_T l & -\frac{K_T l}{2} + \frac{\sqrt{3}K_D s_\gamma}{2} & \frac{K_T l}{2} - \frac{\sqrt{3}K_D s_\gamma}{2} & K_T l & \frac{K_T l}{2} + \frac{\sqrt{3}K_D s_\gamma}{2} & -\frac{K_T l}{2} - \frac{\sqrt{3}K_D s_\gamma}{2} \\ -K_D c_\gamma & K_D c_\gamma & -K_D c_\gamma & K_D c_\gamma & -K_D c_\gamma & K_D c_\gamma \end{bmatrix} \tag{8.5}$$

where c_γ and s_γ represent the cosine and sine of the arms tilt angle. Furthermore, we can appreciate how our system is underdetermined. This system will have infinite combinations of the angular velocities that solve the problem. Of these solutions, we would like to select the minimum norm solution, as this would reduce the power employed in the control. Therefore, we can compute the square of the angular velocities as:

$$\omega_{\mathbf{S}} = [{\omega_1}^2, {\omega_2}^2, {\omega_3}^2, {\omega_4}^2, {\omega_5}^2, {\omega_6}^2]^T = \mathbf{M}^T(\mathbf{M}\mathbf{M}^T)^{-1}\mathbf{C} = \mathbf{M}^*\mathbf{C} \tag{8.6}$$

where $\mathbf{C}$ is a vector containing the control force and moments, and $\mathbf{M}^*$ denotes the Penrose-Moore Pseudoinverse of matrix $\mathbf{M}$ presented in equation 8.5.

Another subtle difference in the mission is linked to the required velocity. Chapter 7 shows a maneuver that attempts to arrive at a given point without controlling the velocity. In this case, we aim to spray at a constant velocity as this is a critical variable influencing spray drift and mission effectiveness. To this purpose, we control velocity instead of controlling position for the x direction (aligned with the row). Maintaining the same architecture, this modification can be done by setting the proportional term to 0, selecting a target velocity, and adding a derivative term for the error in velocity. These modifications will adjust the pitch angle to achieve a constant velocity in the direction of the row.

8.4.2 Virtual Vineyard and UAS model

Figure 8.25 shows the reference vineyard that will be used in this study. It must be noted that this is only one of the many configurations that can be found. These measures are coherent with the experimental study involving flight tests using our UAS and spray system presented by Biglia [26]. Figure 8.26 shows the geometry used in our numerical model, which respects the aforementioned configuration. We can see how the leaves forming the vine plant have different orientations, and their geometry is simplified and with an unrealistic thickness. Possibly, one of the biggest inaccuracies of the model resides in modeling leaves as rigid solids. The flapping of the leaves observed experimentally probably enhances the penetration of PPPs into the plant. Nevertheless, the model can distinguish the number of droplets deposited on the leaves from those in the inter-row region. These particles that end up in the inter-row region are actually the ones that we aim to minimize.

We can also appreciate how we are modeling the water tank as we did in the wind tunnel tests. The fluid inside the tank is not modeled, but the overall mass of the UAS decreases as the spray process starts. However, it is important to note that the variations in mass are limited due to the limited physical time performed in our mission. The initial mass is set to 14.05 kg. The aerodynamic modeling of the tank is important as the drag it generates causes an increase in the pitch angle to achieve the same velocity. This angle directly influences the wake direction and, therefore, its influence on droplet deposition. Our spray system is only active below the leading

rotor. However, future tests will include testing the spray system below the rear rotor, which possesses a slightly more uniform wake due to the flow blockage caused by the UAS body, as shown in the previous section.

The UAS mounted Tmotor 15"x5" blades in the wind tunnel test. However, these blades could not provide enough thrust for flight tests, and they were replaced with a DJI 21"x7" folding propeller (DJI 2170R). The thrust and torque coefficients of these blades are unknown. For simplicity, we scaled the coefficients (K_T and K_q) of the Tmotor to a higher diameter as the relative pitch is equivalent. For a detailed analysis, these should be accurately computed using CFD simulations as those shown in Chapter 4 or using manufacturer data. However, the author recommends using the latter with care, as they are not always accurate.

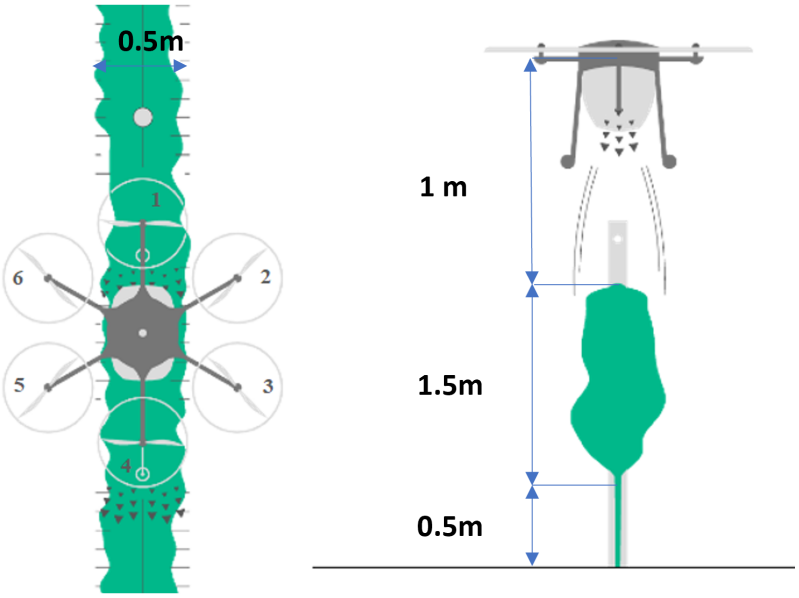

Fig. 8.25 Sketch of a standard vineyard in which we based our numerical model.

The rotors are modeled with the body force propeller method described in Chapter 7 for the quadcopter, only updating the thrust and torque coefficients as well as the area of the virtual disk. The simulation is done in a short vineyard section around 2 meters long. The objective is to assess the interaction of the fluid flow generated in the wake of the UAS and the injected lagrangian particles, as shown in the previous section. In this case, adaptive mesh refinement is not advantageous, as a decent resolution has to be maintained in the volume surrounding the vine row. Therefore, we opted for a generalized volumetric refinement adequate for a smooth transition in

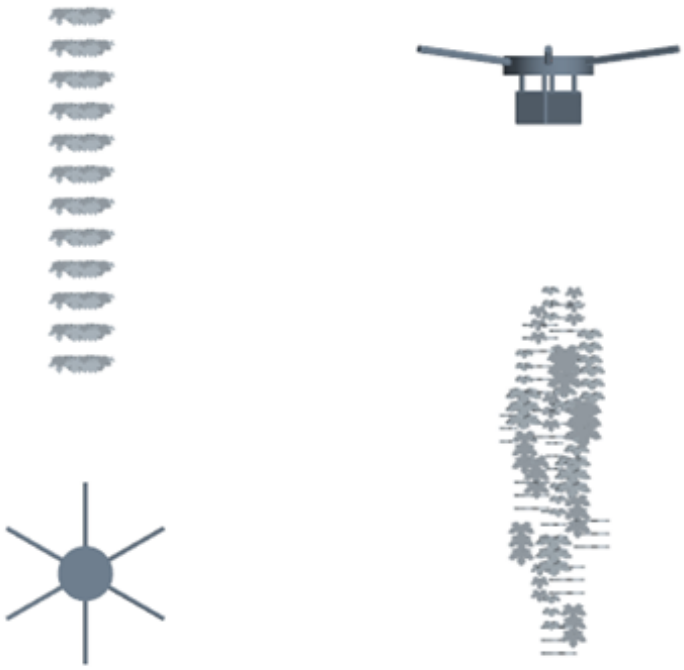

Fig. 8.26 Geometry used in our numerical model.

the overset grid. Figure 8.27 shows how our background grid uses a trimmed cell mesh, and our overset grid uses polyhedral cells to adequately resolve the vehicle geometry. A prism layer mesh is included around the UAS body and water tank to compute as the drag is relevant. We can also appreciate how the model includes a fine mesh around the vine region to model the blockage effect the vine plant would create on the wake. The regions containing the virtual disk are also refined to enable accurate results. This refinement, however, requires a small number of cells compared with that required when the blade is resolved.

8.4.3 Spraying Mission

A spraying mission has been performed to assess the influence of the cone angle on spray depositions. The duration of the mission is 4 seconds. The PID controller allows the UAS to reach its target speed of 2 meters per second before the start of

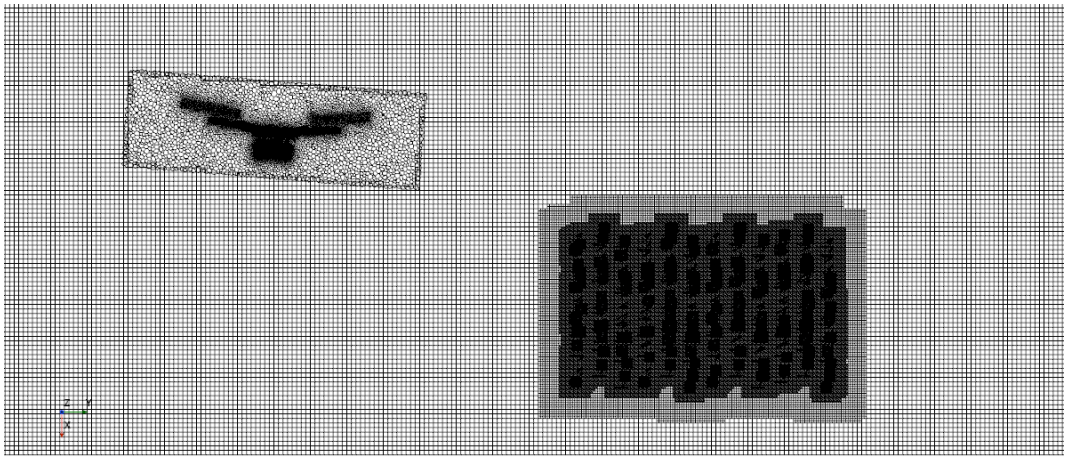

Fig. 8.27 Computational grid.

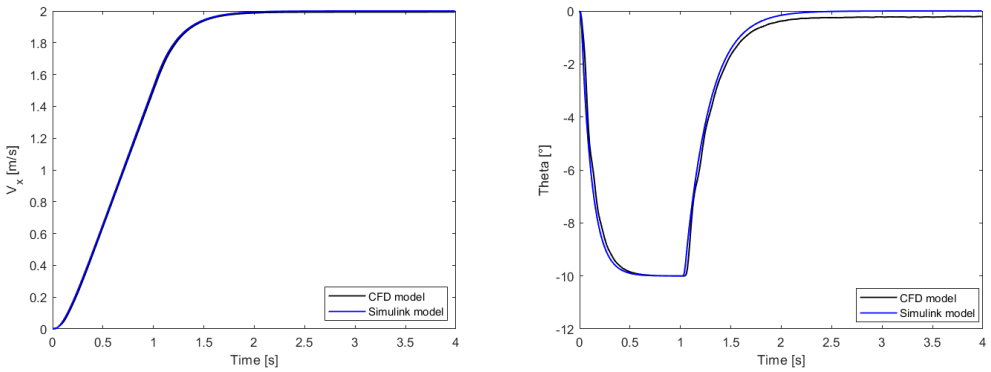

(a) x-velocity. (b) θ.

Fig. 8.28 Comparison of x-velocity and θ for the two models.

the vine row. The velocity component along the row and the pitch angle are shown in Figure 8.28. This Figure also includes a simplified Matlab/Simulink model. We can appreciate how both signals are equivalent except for the asymptotic value of the pitch angle that has to remain slightly negative in the CFD model to compensate for the drag force, which is not included in the Matlab/Simulink model.

The spray system is activated after 1 second. The droplets are modeled as spherical Lagrangian particles that don't interact with the Eulerian phase. This is a noticeable advantage as just one simulation allows studying as many spray system configurations as possible. The first phase uses the 80-degree hollow cone nozzle analyzed in the previous section to show how this angle is excessive and creates

substantial product waste, as commented in the previous section. A second phase is introduced using an injector with half of the cone angle.

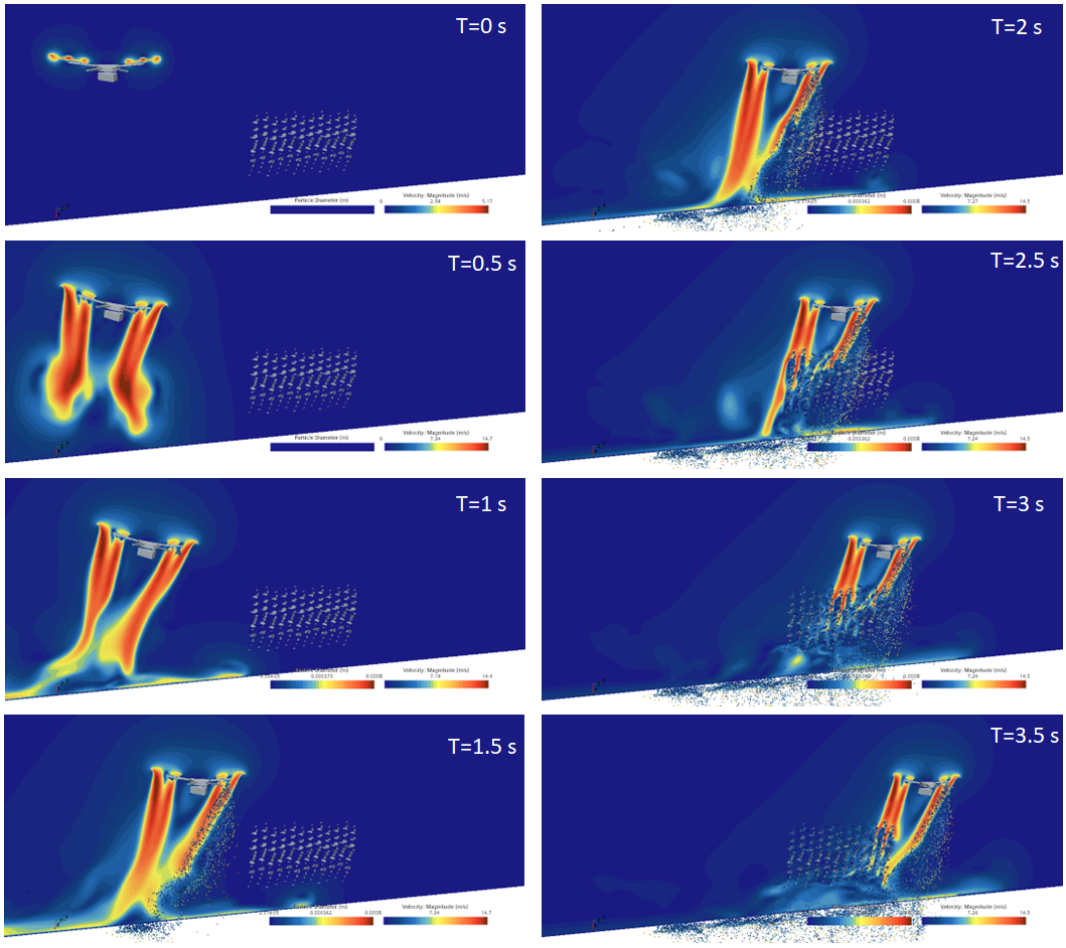

Fig. 8.29 Snapshots of the mission at different times. Velocity magnitude is shown on the UAS symmetry plane, and the particles are colored depending on their diameter.

Figure 8.29 presents snapshots at different times of the mission. We can see how the UAS starts with a horizontal position, tilts forward to achieve the desired velocity, and then progressively tilts back to the equilibrium position, which is not horizontal due to drag. We can also appreciate how the vine row produces a non-negligible blockage effect in the wake velocities.

Figure 8.30 shows how an important number of particles are drifting into the inter-row region due to the large cone angle. Figure 8.31 shows how the concentration of droplets on the top leaves of the row is more significant compared to those at lower leaves. However, as mentioned earlier, the fact that leaves are being modeled as rigid

Fig. 8.30 Top view of droplet distribution with 80^o hollow cone nozzle (Real cone angle set to 56^o). T=4.0 s.

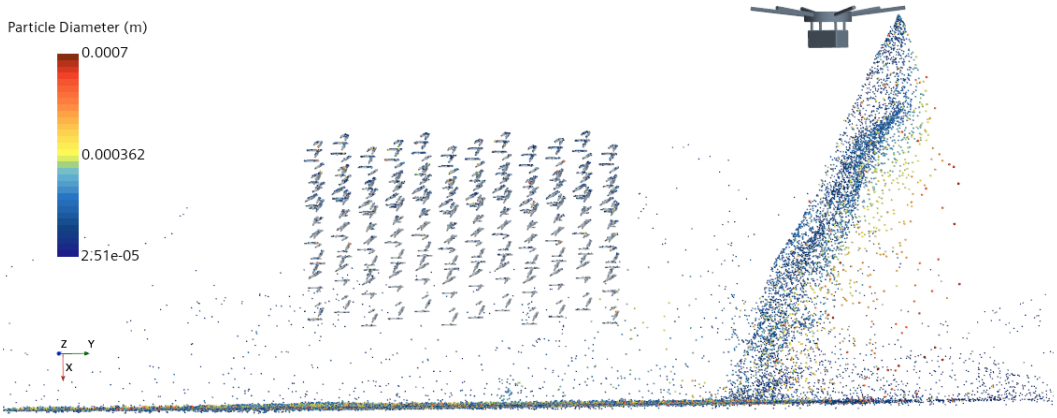

Fig. 8.31 Side view of droplet distribution with 80^o hollow cone nozzle (Real cone angle set to 56^o). T=4.0 s.

bodies probably biases the concentrations. Furthermore, not all the droplets will stick to the leaves, and they could rebound or slide. Another aspect that can be identified in this Figure is how small droplets (blue) coil into a helical structure caused by the interaction of the wake with the advance velocity. On the other hand, larger particles (Red) maintain the cone structure. In this case, as the cone is excessively wide, this causes PPPs losses. However, if a smaller cone aperture was used, this could decisively decrease the inter-row losses.

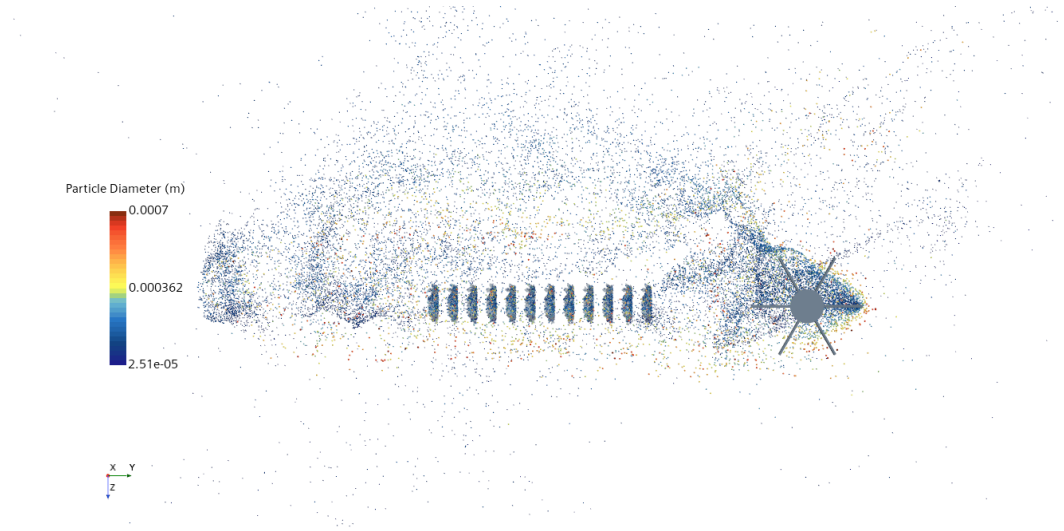

Fig. 8.32 Top view of droplet distribution with 40^o hollow cone nozzle (Real cone angle set to 28^o). T=4.0 s.

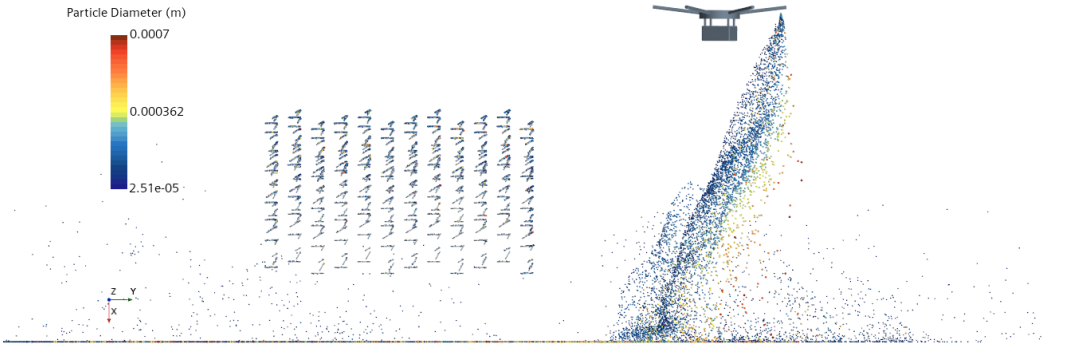

Fig. 8.33 Side view of droplet distribution with 40^o hollow cone nozzle (Real cone angle set to 28^o). T=4.0 s.

To test this hypothesis, we are going to analyze a 40-degree hollow cone nozzle, assuming that the closure of the cone would be proportional to that found for the 80-degree nozzle. This results in an effective angle of 28 degrees. Figure 8.32 shows how the number of droplets outside the target has been reduced due to the closure of the cone angle. Figure 8.33 shows how the cone presents an important reduction. We can appreciate again, in this case, the asymmetrical particle disposition noticed in the wind tunnel tests. In this case, the particle deviation is toward the left of the row

due to the change in the rotation rate of the forward rotor. The fact that this effect is also captured with the virtual disk model reinforces its validity for this application.

The proposed methodology also allows the quantification of droplet deposition on target. The amount of PPPs deposited on the plants was compared to the efficiency of the presented operations. Using the 80^o nozzle, the spray deposition was 0.0047 liters, whereas, for the 40^o nozzle, the deposition was 0.0083 liters. If we compare this value with the total amount of PPPs injected while the UAS was over the vine, we obtain a measure of the efficiency of the operation. The operation efficiency with an 80^o nozzle is around 0.30 and 0.52 for the 40^o nozzle. This represents a simple test case on how virtual testing may guide optimal spraying operations without the elevated costs of experimental testing regarding water-sensitive material to track particles and workforce to perform experiments and post-process the data.

8.5 Discussion

This study explores the effects of flight speed and rotation rate on spray distribution in the wake of a hexacopter. The experimental procedure uses lateral and frontal photographs to validate the spray pattern obtained from CFD simulations. While the methodology does not allow for individual droplet statistics, it provides spray contours for qualitative validation of the CFD model and evaluation of different operational parameters' effects on spray drift.

This work focuses on the benefits of positioning nozzles in the wake of rotors, which mitigate drift. The study demonstrates improved precision operations by comparing spray distributions at a flight speed of 2 m/s with and without rotors on. Increasing the rotation rate reduces spray drift for a given velocity, which is significant as UASS weight can decrease up to 40% due to spraying, during a single mission. Increasing flight velocity increases spray drift for a given rotation rate, making the non-dimensional ratio between flight and blade tip velocity a critical design parameter for efficient precision spray operations.

The study also reveals that droplet diameter significantly affects drift, with smaller particles being more susceptible to drift due to reduced inertia. Optimal nozzle positioning depends on flight speed and rotation rate, and nozzle location should aim to ensure droplet trajectories are immersed in high vertical velocity

regions for the longest possible distance to allow sufficient momentum injection toward the target. However, care must be taken as we have seen how the wakes deform and deviate due to the interaction with the freestream. The rear rotor seems to have a more vertical wake that would enhance precision applications.

The validation of the numerical model with wind tunnel data has informed the design of a virtual vineyard where several spray system configurations may be tested efficiently. Considering that the droplets' motion does not affect the bulk fluid flow allows us to use as many independent Lagrangian phases during the same simulation. This methodology enables the quantification of droplets drifting away. Also, due to the time-accurate particle tracking, we can understand why this drift is happening and attempt to propose an alternative location. Conversely, the model could be used to design adaptive path-planning strategies to enhance plant deposition.

Chapter 9

Conclusions and Future Work

9.1 Summary and Conclusions

This dissertation addresses the challenges in the numerical simulation of small-scale rotary-wing typically used in unmanned aerial systems in Terrestrial and Martian applications. Airfoil and rotor aerodynamic simulations were performed with very different fidelity analyses, ranging from simple and fast reduced order models to high-fidelity Computational Fluid Dynamics. High-fidelity approaches cannot be considered for design and optimization applications due to their prohibitive computational cost. It is, therefore, imperative to understand what fidelity reduced order models can provide and at which computational cost. After adequate validation, higher fidelity approaches are extremely valuable to understand complex aerodynamic phenomena and to inform the development of reduced-order models. It is also important to note that the fidelity of a computational tool may vary. For instance, a CFD simulation solving the RANS equations, depending on the grid resolution, the turbulence and transition models, temporal discretization, and application of symmetries in the problem may vary over an order of magnitude. This is also true for the vortex particle method that allows variable fidelity simulations as the number of particles increases. Depending on the user objectives, more complex approaches may not pay off in fidelity. Our work, summarized in the following lines, follows the aforementioned philosophy in which we validate our higher fidelity models with experiments, which inform the development of reduced-order models. However, it is also interesting to mention that CFD approaches can be instrumental in planning

experiments. Examples of this are the wind tunnel simulations, the quadcopter in wall effect, and the spraying operations used to inform the design of experiments.

During this research, we aimed to understand the complex aerodynamics that small-scale multicopters encounter during their missions in standard and low-density conditions. Given the remarkably low Reynolds number conditions (1,000-100,000), we studied airfoil aerodynamics in this regime (Chapter 3). We can distinguish two regimes in this range of Reynolds numbers: ultra-low (1,000-10,000) and very-low (10,000-100,000) Reynolds number regimes. The former is characterized by a laminar boundary layer and a high lift regime after leading-edge separation, defying the classical stall definition. Therefore, several airfoils were proposed to enhance ultra-low Reynolds number regime performance. The latter presents the challenges of combining non-negligible laminar and turbulent boundary layer regions. Furthermore, transition is usually triggered by the separation of the laminar boundary layer, typically forming laminar separation bubbles.

Once the behavior of airfoils was understood, we explored the numerical simulation of rotors in the very-low Reynolds number regime (Chapter 4). We assessed a transition model's ability to capture the separation bubbles and discussed different modeling approaches for rotating flows within a commercial CFD framework. This numerical model was validated with experimental data obtained in a climatic chamber that allows the reproduction of these conditions. The validated model informed the development of several reduced-order methodologies to assess rotor performance, including a data-driven approach, a blade element momentum method, a free vortex wake method, and a vortex particle method. The CFD model was also validated for a full quadcopter to check on the scalability of the proposed methodology to real scenarios. Rotor simulations were extended to the ultra-low Reynolds number regime (Chapter 5), assuming a laminar flow. Different optimization approaches are proposed based on both reduced-order models and CFD.

The lessons learned regarding rotor simulation and a 6-DOF solver were used to simulate the dynamic fluid body interactions in UAS applications. We used this approach to simulate an innovative passive swashplateless rotor (Chapter 6), including a coupled lag-pitch hinge that enables cyclic control by applying a sinusoidal torque at the hub. Initially, we simulated this rotor concept by combining a multi-body dynamic solver and a RANS CFD approach. These simulations allowed us to understand the complex dynamic/aerodynamic interactions and informed the

development of a reduced order model that couples an azimuthally resolved blade element method and a dynamic solver. The dynamic solver was also used to model multirotor maneuvers (Chapter 7). We implemented a PID controller that allows the virtual testing of different maneuvers. A simplified Simulink model was used to verify our virtual testing environment combining 6-DOF motion, PID control, and RANS-CFD using a quadcopter. In this case, we introduced the reduced order model within the CFD framework to reduce the computational cost and enable longer missions, modeling the flow and forces induced by the rotor with a virtual disk approach.

The last application investigated in this dissertation is rotor-droplet interaction in agricultural applications using unmanned aerial systems (Chapter 8). In this case, we used Lagrangian models to simulate the droplets in combination with the multicopter simulations developed in Chapter 7. A Volume of fluid interface capturing method was used to simulate the atomization process in a hollow cone nozzle necessary to determine the necessary initial conditions for the Lagrangian model. Due to the complexity of the approach and the lack of reliable data in literature, we performed an experimental campaign in a wind tunnel to assess the interaction of the droplets with the wake of a hexacopter and the freestream velocity. The spray dispersion patterns obtained experimentally were used to validate the numerical predictions. The validated spray model was used to develop a simulation environment similar to Chapter 7 but using a hexacopter and a virtual vineyard to assess droplet deposition and quantify the particles that drift away.

9.2 Research Contributions

The following lines highlight the main contributions presented in this dissertation.

- **Investigation of the γ-Re_θ transition model in the very low Reynolds number regime.**

  A thorough validation of applying the γ-Re_θ transition model to different airfoils in this regime was performed. We assessed different calibrations of the model and proposed a simple fine-tuning methodology. After the transition to turbulence, we show a deficit of turbulent kinetic energy production near the wall that creates low skin friction levels resulting in thicker boundary layers

and premature stall. The problem is enhanced for lower Reynolds numbers and higher angles of attack. We also show how the model fidelity is reduced for higher-camber airfoils that present separated regimes at intermediate angles of attack. This is the case with the airfoil e-387.

- **Ultra-low Reynolds number airfoil optimization using an adjoint-CFD approach.**

  We propose an alternative optimization procedure to those presented in the literature that typically uses either XFOIL or RANS equations within optimization algorithms. In this case, we use Navier-Stokes simulations coupled with an adjoint-based optimization to morph the airfoil geometry to reduce a user-defined cost function using a steepest descent approach. This computationally efficient approach allows good-performing geometries that present an attached flow.

- **Ultra-low Reynolds number airfoil optimization for airfoils presenting separated flow combining a panel method and passive flow control.**

  We propose an extremely efficient methodology in which we define an optimal airfoil designed to present an attached boundary layer using XFOIL. Then, we create sharp leading-edge versions of this airfoil by slicing the airfoil with planes. This slicing generates a cavity for a separation bubble to settle, significantly reducing the shear drag. We show for two different airfoils that this geometrical modification does not affect aerodynamic efficiency for a given lift coefficient, rendering it an extremely useful design technique that generates airfoils with state-of-the-art maximum efficiencies and guarantees high-performance levels before leading edge separation.

- **Large eddy simulations of sharp leading edge geometries.**

  We performed three-dimensional Navier-Stokes and large eddy simulations of the sharp geometries for the maximum efficiency angle of attack, showing that the flow remains two-dimensional and laminar. This finding justifies using two-dimensional Navier-Stokes solutions for airfoil design and optimization up to Reynolds 10,000.

- **Experimental validation and comparison of multiple fidelity numerical models for rotary wing considering an eventual transition to turbulence.**

We validated different fidelity numerical models for Reynolds numbers ranging from 20,000 to 200,000, sweeping the whole very-low Reynolds number regime. Our reduced-order models used a 2D aerodynamic database with a transition model. We show how a CFD-based airfoil aerodynamic database performs better than one obtained with XFOIL, especially for the lowest Reynolds numbers. We show how transition models in three-dimensional CFD simulations allow enhanced boundary layer characterization to distinguish laminar and turbulent regions and laminar separation bubbles.

- **Hybrid fidelity optimization for Martian rotor design.**

  We present an alternative methodology to those proposed in the literature that typically uses the vortex method to optimize rotor performance. We perform a baseline optimization with a genetic algorithm using the Blade Element Momentum method as a solver with posterior adjoint-CFD morphing of the 3D geometry. This hybrid fidelity approach is computationally efficient and allows the creation of state-of-the-art rotor performance with figures of merit above 0.6. We also consider the impact of blade weight in rotor optimization in low-density conditions.

- **Numerical simulation of a Passive Swashplateless rotor.**

  This work is among the first to present precise numerical simulations of this innovative UAS rotor concept that allows cyclic control using a sinusoidal torque input at the hub. We used a multi-body 6-DOF solver in combination with well-resolved RANS simulations to model the pitching-lagging motion of the blades. The developed reduced-order model showed satisfactory aerodynamic loads and dynamic response agreement compared to the higher-fidelity CFD approach. This approach reduces the computational cost by a factor of 10,000.

- **Development of a virtual testing environment for multicopters combining CFD, 6-DOF motion, and PID control.**

  We proposed a virtual testing environment that allows us to reproduce a broad selection of multirotor. The framework is general as it couples 6-DOF motion and PID control within a CFD environment. We created digital twins of a quadrotor and a hexarotor that we used for the experimental tests. Two rotor modeling fidelities are allowed; one uses a sliding grid approach, and the

other a virtual disk method. This framework was used to understand the dangerous situation that UASs face when approaching a wall in static and dynamic configurations.

- **Numerical assessment of an unmanned aerial spraying system (UASS) operation on a vineyard coupling CFD, 6-DOF motion, PID control, and Lagrangian particle injection.**

  An experimental campaign was performed in a wind tunnel facility to obtain preliminary droplet distributions in the wake of a sprayer hexarotor. We validated a Lagrangian particle model with this data and then coupled it within the aforementioned simulation framework. To the author's knowledge, this is the first droplet deposition prediction tool for an hexarotor spraying mission coupling CFD, 6-DOF motion, PID control, and multiphase flow modeling. Its generality allows the study of spray deposition in real situations, including lateral wind gusts and variable flight speed, and can capture the increase in pitch angle as the UAS's mass reduces.

9.3 Future Work

This dissertation presents numerical approaches to tackle very diverse applications involving rotary-wing UAS. Most of these applications are rapidly evolving, and this work proposes different methodologies to tackle these problems. However, for many of the addressed issues, our proposed methodology has been validated but not applied to actual missions or design activities. For instance, we have validated various reduced order models in different conditions, but only the Blade Element method has been applied to design applications. This is also the case with the swashplateless rotor reduced-order approach. Furthermore, some of the proposed approaches were performed with under-resolved grids due to our limited computational resources. However, approaches that seem unfeasible today will soon be standard due to the exponential growth of available computational resources, especially with the rapid growth of GPU acceleration in our field.

A special mention goes to the Martian flight. The presented rotor design activity started before any UAS had previously operated on Mars. Therefore, we opted for a small payload conservative design of quadcopter blades with a total budget

of 1.2 kg. After the great success of Ingenuity, the Martian flight community is quickly evolving towards larger-scale designs. Therefore, applying our proposed design and optimization methodologies for larger-scale UAS will be something to work on soon. Furthermore, the experimental validation of both our airfoils and rotor simulations will be a priority. Considering the extremely economical and technological complexity of testing Martian conditions on Earth, having a validated framework where rotor/UAS performance could be evaluated will definitely be an advantage.

There is a lot of work ahead regarding transition modeling in rotor flows. The very-low Reynolds number regime needs transition modeling due to the coexistence of laminar and turbulent regions. LES performed with the adequate resolution to capture transition is too expensive, and it will still be out of our reach for at least the next decade, reinforcing the need for accurate transition models. We have validated our numerical model using integral forces and moments. However, more detailed measurements are required to adequately assess the predictions of the boundary layer state over the rotor surface. Therefore another pending job is to compare our boundary layer state predictions with experimental measurements, which may include pressure-sensitive paint and oil visualization.

Another future activity is thoroughly validating our virtual simulation environment, comparing our simulated missions with actual flight logs performing the same operation. An experimental campaign to validate the operations in the wall effect is currently being conducted, as well as a validation of our spraying operation simulation. In the future, these multiphysics simulations could include other disciplines, such as aeroelasticity and aeroacoustics. Particularly interesting would be the interaction with control algorithms that could mitigate the problems associated with the aforementioned disciplines. This would allow us to perform virtual tests on digital twins with very high reliability. As we mentioned earlier, this concept would be beneficial to virtually test actual Martian missions, which are very difficult to reproduce due to the atmospheric conditions and the reduced gravitational acceleration.

References

[1] J. Abras, R. Narducci, and N.S. Hariharan. Impact of high-fidelity simulation variations on wake breakdown of a rotor in hover. In *AIAA Scitech 2020 Forum*, page 0531, 2020.

[2] B. J. Abu-Ghannam and R. Shaw. Natural Transition of Boundary Layers—The Effects of Turbulence, Pressure Gradient, and Flow History. *Journal of Mechanical Engineering Science*, 22(5):213–228, 1980.

[3] F. Ahmad, B. Qiu, X. Dong, J. Ma, X. Huang, S. Ahmed, and Farman A. C. Effect of operational parameters of UAV sprayer on spray deposition pattern in target and off-target zones during outer field weed control application. *Computers and Electronics in Agriculture*, 172:105350, 2020.

[4] H. Akima. A new method of interpolation and smooth curve fitting based on local procedures. *Journal of the ACM (JACM)*, 17(4):589–602, 1970.

[5] E. J. Alvarez. *Reformulated Vortex Particle Method and Meshless Large Eddy Simulation of Multirotor Aircraft*. PhD thesis, Brigham Young University, 2022. https://scholarsarchive.byu.edu/etd/9589.

[6] M. Alì. Development and validation of a reduced order method for the study of flow on a rotor. Master's thesis, Politecnico di Torino, 2021. https://webthesis.biblio.polito.it/18369/.

[7] A. F. Antoniadis, D. Drikakis, P. S. Farmakis, L. Fu, I. Kokkinakis, X. Nogueira, P. Silva, M. Skote, V. Titarev, and P. Tsoutsanis. UCNS3D: An open-source high-order finite-volume unstructured CFD solver. *Computer Physics Communications*, 279:108453, 2022.

[8] M. Anyoji and D. Hamada. High-Performance Airfoil with Low Reynolds-Number Dependence on Aerodynamic Characteristics. *Fluid Mechanics Research International Journal*, 3(2):76–80, 2019.

[9] M. Anyoji, H. Nagai, and K. Asai. Development of low density wind tunnel to simulate atmospheric flight on Mars. In *47th AIAA Aerospace Sciences Meeting including The New Horizons Forum and Aerospace Exposition*, Orlando, FL, January 2009. AIAA-2009-1517.

[10] M. Anyoji, T. Nonomura, H. Aono, A. Oyama, K. Fujii, H. Nagai, and K. Asai. Computational and Experimental Analysis of a High-Performance Airfoil Under Low-Reynolds-Number Flow Condition. *Journal of Aircraft*, 51(6):1864–1872, 2014.

[11] M. Anyoji, K. Nose, S. Ida, D. Numata, H. Nagai, and K. Asai. Low Reynolds Number Airfoil Testing in a Mars Wind Tunnel. Chicago, Illinois, USA, Jun. 28 – Jul. 1 2010. AIAA.

[12] H. Aono, M. Anyoji, D. Hamada, S. Wakui, and T. Tatsukawa. A Study on Development of Airfoil Shape Toward Low Reynolds-Number Dependence of Aerodynamic Characteristics Under Low-Reynolds-Number-Flow conditions. In *2018 AIAA Aerospace Sciences Meeting*, Kissimmee, FL, January 2018. AIAA-2018-1085.

[13] F. J. Argus, G. A. Ament, and W. J. F. Koning. The Influence of Laminar-Turbulent Transition on Rotor Performance at Low Reynolds Numbers. In *VFS Aeromechanics for Advanced Vertical Flight Technical Meeting*, San Jose, CA, January 2020. https://rotorcraft.arc.nasa.gov/Publications/files/Finbar_Argus_TVF_2020.pdf.

[14] J. Babajee. *Detailed numerical characterization of the separation-induced transition, including bursting, in a low-pressure turbine environment*. PhD thesis, École Centrale de Lyon, 2013.

[15] J. D. Baeder, S. Medida, and T. S. Kalra. OVERTURNS Simulation of S-76 Rotor in Hover. In *52nd Aerospace Sciences Meeting*, page 0045, 2014.

[16] B. Balaram, M. Aung, and M.P. Golombek. The ingenuity helicopter on the perseverance rover. *Space Science Reviews*, 217(4):1–11, 2021.

[17] B. Balaram, T. Canham, C. Duncan, H. F. Grip, W. Johnson, J. Maki, A. Quon, R. Stern, and D. Zhu. Mars helicopter technology demonstrator. In *2018 AIAA Atmospheric Flight Mechanics Conference*, Kissimmee, Florida, 8–12 January 2018. AIAA-2018-0023.

[18] J. Baumgarte. Stabilization of constraints and integrals of motion in dynamical systems. *Computer methods in applied mechanics and engineering*, 1(1):1–16, 1972.

[19] L. Becce, N. Bloise, and G. Guglieri. Optimal Path Planning for Autonomous Spraying UAS framework in Precision Agriculture. In *2021 International Conference on Unmanned Aircraft Systems (ICUAS)*, pages 698–707. IEEE, 2021.

[20] F. Bellelli. Development and validation of a Vortex Particle code to evaluate Rotor and Propeller Performance. Master's thesis, Politecnico di Torino, 2022. https://webthesis.biblio.polito.it/23364/.

[21] O. Bergmann, F. Götten, C. Braun, and F. Janser. Comparison and evaluation of blade element methods against RANS simulations and test data. *CEAS Aeronautical Journal*, 13(2):535–557, 2022.

[22] O. Bergmann, F. Möhren, C. Braun, and F. Janser. Comparison of Various Aeroacoustic Propeller Noise Prediction Methodologies in Static Operations. In *AIAA SciTech 2022 Forum*, January January 2022. AIAA 2022-2529.

[23] H. Bézard, T. Désert, T. Jardin, and J-M. Moschetta. Numerical and Experimental Aerodynamic Investigation of a Micro-UAV for Flying on Mars. In *76th Annual Forum & Technology Display*, Virginia Beach, VA, October 2020.

[24] H. Bézard, T. Désert, J-M. Moschetta, and T. Jardin. Aerodynamic design of a Martian micro air vehicle. In *EUCASS 2019*, MADRID, Spain, July 2019.

[25] M. J. Bhagwat and J. G. Leishman. Generalized viscous vortex model for application to free-vortex wake and aeroacoustic calculations. In *Annual forum proceedings-American helicopter society*, volume 58, pages 2042–2057. American Helicopter Society, Inc, 2002.

[26] A. Biglia, M. Grella, N. Bloise, L. Comba, E. Mozzanini, A. Sopegno, M. Pittarello, E. Dicembrini, L. E. Alcatrão, G. Guglieri, et al. UAV-spray application in vineyards: Flight modes and spray system adjustment effects on canopy deposit, coverage, and off-target losses. *Science of the Total Environment*, 845:157292, 2022.

[27] N. Bloise, M. Carreño Ruiz, D. D'Ambrosio, and G. Guglieri. Preliminary design of a remotely piloted aircraft system for crop-spraying on vineyards. In *2020 IEEE International Workshop on Metrology for Agriculture and Forestry (MetroAgriFor)*, pages 1–6. IEEE, 2020.

[28] N. Bloise, M. Carreño Ruiz, D. D'Ambrosio, and G. Guglieri. Wind tunnel testing of remotely piloted aircraft systems for precision crop-spraying applications. In *2021 IEEE International Workshop on Metrology for Agriculture and Forestry (MetroAgriFor)*, pages 378–383. IEEE, 2021.

[29] N. Bloise, M. Carreño Ruiz, E. Mai, D. D'Ambrosio, and G. Guglieri. Analysis and Design of Unmanned Aerial Systems for Precision Agriculture applications on Vineyards. In *EUCASS 2022*, 2022.

[30] N. Bloise, S. Primatesta, R. Antonini, G. Fici, M. Gaspardone, G. Guglieri, and A. Rizzo. A survey of unmanned aircraft system technologies to enable safe operations in urban areas. In *2019 International Conference on Unmanned Aircraft Systems (ICUAS)*, pages 433–442. IEEE, 2019.

[31] H. Bolandi, M. Rezaei, R. Mohsenipour, H. Nemati, and S. M. Smailzadeh. Attitude control of a quadrotor with optimized PID controller. *Intelligent Control and Automation*, 4(3):335–342, 2013.

[32] J. U. Brackbill, D. B. Kothe, and C. Zemach. A continuum method for modeling surface tension. *Journal of computational physics*, 100(2):335–354, 1992.

[33] J. Brandt, R. Deters, G. Ananda, O. Dantsker, and M. Selig. UIUC propeller database, Vols 1-4, university of illinois at urbana-champaign, department of aerospace engineering, 2001. Accessed: 2023-01-01.

[34] H. Brugger, M. Brodmann, R. Turner, A. Nollo, H. Gatterer, and G. Strapazzon. terraXcube: A new hi-tech training facility for EMS teams. *Resuscitation*, 130, e79, 2018.

[35] S. Burgmann, J. Dannemann, and W. Schröder. Time-resolved and volumetric PIV measurements of a transitional separation bubble on an SD7003 airfoil. *Experiments in fluids*, 44(4):609–622, 2008.

[36] F.X. Caradonna and C. Tung. Experimental and analytical studies of a model helicopter rotor in hover. In *European rotorcraft and powered lift aircraft forum*, number A-8332, 1981.

[37] L. Caros, O. Buxton, T. Shigeta, T. Nagata, T. Nonomura, K. Asai, and P. Vincent. Direct Numerical Simulation of Flow over a Triangular Airfoil Under Martian Conditions. *AIAA Journal*, 60(7):3961–3972, 2022.

[38] M. Carreño Ruiz, F. Bellelli, and D. D'Ambrosio. Numerical Investigation on the Aerodynamic Design of Quadrotor Blades Operating in the Martian Atmosphere. In *EUCASS 2022*, 2022.

[39] M. Carreño Ruiz and D. D'Ambrosio. Validation of the $\gamma - Re_\theta$ Transition Model for Airfoils Operating in the Very Low Reynolds Number Regime. *Flow, Turbulence and Combustion*, pages 1–30, 2022.

[40] M. Carreño Ruiz. CFD simulation of propellers: Best Practices Analysis. Master's thesis, Politecnico di Torino, 2019.

[41] M. Carreño Ruiz, N. Bloise, E. Capello, D. D'Ambrosio, and G. Guglieri. Assessment of Quadrotor PID Control Algorithms using six-Degrees of Freedom CFD simulations. In *2022 61st IEEE Conference on Decision and Control (CDC)*, 2022.

[42] M. Carreño Ruiz, N. Bloise, E. Capello, D. D'Ambrosio, and G. Guglieri. Assessment of Quadrotor Near-Wall behaviour using six-Degrees of Freedom CFD simulations. In *AIAA SciTech 2023 Forum*, National Harbor, MD, January 2023. AIAA-2023-2272.

[43] M Carreño Ruiz, N. Bloise, G. Guglieri, and D. D'Ambrosio. Numerical Analysis and Wind Tunnel Validation of Droplet Distribution in the Wake of an Unmanned Aerial Spraying System in Forward Flight. *Drones*, 6(11), 2022.

[44] M. Carreño Ruiz and D. D'Ambrosio. Validation and application of aerodynamic simulations in the Martian atmosphere. In *26th Conference of the Italian Association of Aeronautics and Astronautics-AIDAA 2021*, 2021.

[45] M. Carreño Ruiz and D. D'Ambrosio. Aerodynamic optimization and analysis of quadrotor blades operating in the Martian atmosphere. *Aerospace Science and Technology*, 132:108047, 2023.

[46] M. Carreño Ruiz and D. D'Ambrosio. Aerodynamic Optimization of Quadrotor Blades Operating in the Martian Atmosphere. In *AIAA SciTech 2022 Forum*, San Diego, CA, January 2022. AIAA-2022-0743.

[47] M. Carreño Ruiz and D. D'Ambrosio. Hybrid Fidelity Optimization of Efficient Airfoils and Rotors in Ultra-Low Reynolds Numbers Conditions. In *AIAA SciTech 2023 Forum*, National Harbor, MD, January 2023. AIAA-2023-0652.

[48] M. Carreño Ruiz, A. Manavella, and D. D'Ambrosio. Numerical and experimental validation and comparison of reduced order models for small scale rotor hovering performance prediction. In *AIAA SciTech 2022 Forum*, January 2022. AIAA 2022-0154.

[49] M. Carreño Ruiz, M. Scanavino, D. D'Ambrosio, G. Guglieri, and A. Vilardi. Experimental and numerical analysis of hovering multicopter performance in low-Reynolds number conditions. *Aerospace Science and Technology*, 128:107777, 2022.

[50] M. Carreño Ruiz, M. Scanavino, D. D'Ambrosio, G. Guglieri, and A. Vilardi. Experimental and numerical analysis of multicopter rotor aerodynamics. In *AIAA Aviation 2021 Forum*, Virtual Event, August 2021. AIAA 2021-2539.

[51] Manuel Carreño Ruiz and Domenic D'Ambrosio. ROT8: A Matlab App for Low Reynolds number Airfoil and Rotor Aerodynamic Design. In *AIAA AVIATION 2023 Forum*, San Diego, CA, June 2023. AIAA-2023-3379.

[52] C. Carton de Wiart and K. Hillewaert. DNS and ILES of Transitional Flows around a SD7003 Using a High Order Discontinuous Galerkin Method. In *Seventh International Conference on Computational Fluid Dynamics (ICCFD7)*, July 2012.

[53] D. Casalino, G. Romani, R. Zhang, and H. Chen. Lattice-Boltzmann calculations of rotor aeroacoustics in transitional boundary layer regime. *Aerospace Science and Technology*, 130:107953, 2022.

[54] P. Catalano and R. Tognaccini. Turbulence modeling for low-Reynolds-number flows. *AIAA journal*, 48(8):1673–1685, 2010.

[55] P. Catalano and R. Tognaccini. Large eddy simulations of the flow around the SD7003 airfoil. In *AIMETA Conference*, pages 1–10, 2011.

[56] P. Catalano and R. Tognaccini. RANS analysis of the low-Reynolds number flow around the SD7003 airfoil. *Aerospace Science and Technology*, 15(8):615–626, December 2011.

[57] M. Ceze, M. Hayashi, and E. Volpe. A study of the CST parameterization characteristics. In *27th AIAA applied aerodynamics conference*, page 3767, 2009.

[58] N.M. Chaderjian and P.G. Buning. High resolution navier-stokes simulation of rotor wakes. In *Proceedings of the American Helicopter Society 67th Annual Forum*, 2011.

[59] P. Chen, J. P. Douzals, Y. Lan, E. Cotteux, X. Delpuech, G. Pouxviel, and Y. Zhan. Characteristics of unmanned aerial spraying systems and related spray drift: A review. *Frontiers in plant science*, page 2726, 2022.

[60] S. Chen, Y. Lan, Z. Zhou, F. Ouyang, G. Wang, X. Huang, X. Deng, and S. Cheng. Effect of droplet size parameters on droplet deposition and drift of aerial spraying by using plant protection UAV. *Agronomy*, 10(2):195, 2020.

[61] A. Choudhry, M. Arjomandi, and Ri. Kelso. A Study of Long Separation Bubble on Thick Airfoils and Its Consequent Effects. *International Journal of Heat and Fluid Flow*, 52:84–96, 2015.

[62] J. G. Coder. OVERFLOW rotor simulations using advanced turbulence and transition modeling. In *55th AIAA Aerospace Sciences Meeting*, page 1432, 2017.

[63] S. A. Conyers. *Empirical evaluation of ground, ceiling, and wall effect for small-scale rotorcraft*. PhD thesis, University of Denver, 2019.

[64] R. Corral and F. Gisbert. Prediction of Separation-Induced Transition Using a Correlation-Based Transition Model. volume Volume 7: Turbomachinery, Parts A, B, and C of *Turbo Expo: Power for Land, Sea, and Air*, pages 897–908, June 2010.

[65] H. Cummings, B. N. Perez, W. J. F. Koning, W. Johnson, L. Young, F. Haddad, E. Romander, J. Balaram, T. Tzanetos, J. Bowman, et al. Overview and Introduction of the Rotor Optimization for the Advancement of Mars eXploration (ROAMX) Project. In *Aeromechanics for Advanced Vertical Flight Technical Meeting, Transformative Vertical Flight 2022*, 2022.

[66] A. Datta, B. Roget, D. Griffiths, and G. Pugliese. Design of a Martian Autonomous Rotary-Wing Vehicle. *Journal of Aircraft Vol. 40, No. 3*, pages 461–472, May-Jun. 2003.

[67] C. De Santis, P. Catalano, and R. Tognaccini. Model for enhancing turbulent production in laminar separation bubbles. *AIAA Journal*, 60(1):473–487, 2022.

[68] K. Deb. Multi-objective optimisation using evolutionary algorithms: an introduction. In *Multi-objective evolutionary optimisation for product design and manufacturing*, pages 3–34. Springer, 2011.

[69] T. Désert, T. Jardin, H. Bézard, and J-M. Moschetta. Numerical predictions of low Reynolds number compressible aerodynamics. *Aerospace Science and Technology*, 92:211–223, 2019.

[70] T. Desert, J-M. Moschetta, and H. Bézard. Numerical and experimental investigation of an airfoil design for a Martian micro rotorcraft. *International Journal of Micro Air Vehicles*, 10(3):262–272, 2018.

[71] R. W. Deters. *Performance and slipstream characteristics of small-scale propellers at low Reynolds numbers*. PhD thesis, University of Illinois at Urbana-Champaign, 2014.

[72] M. Di Martino, D. Ahirwal, and P. L. Maffettone. Three-dimensional computational fluid dynamics simulation of the hollow-cone spray process: The stability of the conical liquid sheet. *Physics of Fluids*, 33(6):063301, 2021.

[73] P. Dini and M. D. Maughmer. A computationally efficient modelling of laminar separation bubbles. NASA-CR-185854, January 1989.

[74] M. Drela. Low-Reynolds-number airfoil design for the M.I.T. Daedalus prototype- A case study. *Journal of Aircraft*, 25(8):724–732, 1988.

[75] M. Drela. XFOIL: An analysis and design system for low Reynolds number airfoils. In *Proceedings of the Conference Notre Dame, Indiana, USA, 5–7 June 1989*, pages 1–12. Springer, 1989.

[76] M. Drela. QPROP Formulation. https://web.mit.edu/drela/Public/web/qprop/qprop_theory.pdf, 2006. Accessed: 2023-01-01.

[77] I. D. Du Mutel de Pierrepont, E. Capello, A. Vilardi, R. Parin, et al. Experimental evaluation of Wall Effect for small UAVs in Climate-Controlled Environments. In *2022 IEEE 9th International Workshop on Metrology for AeroSpace (MetroAeroSpace)*, pages 119–123. IEEE, 2022.

[78] L. Edelman. Xfoil interface updated. https://www.mathworks.com/matlabcentral/fileexchange/49706-xfoil-interface-updated, 2014. Accessed: 18 February 2022.

[79] R. A Eppler and D. M. Somers. A computer program for the design and analysis of low-speed airfoils. NASA-TM-80210, August 1980.

[80] D. Escobar, I. Chopra, and A. Datta. Vacuum Chamber Testing of 1.5 Foot Diameter Mars Rotor. San Francisco, CA, USA, Jan. 16-19 2018. American Helicopter Society.

[81] EURAC Research. Climate in cubes. https://terraxcube.eurac.edu/structure/, 2020. Accessed: 2022-01-30.

[82] B. S. Faiçal, H. Freitas, P. H. Gomes, L. Y Mano, G. Pessin, A. de Carvalho, B. Krishnamachari, and J. Ueyama. An adaptive approach for UAV-based pesticide spraying in dynamic environments. *Computers and Electronics in Agriculture*, 138:210–223, 2017.

[83] M. Galbraith and M. Visbal. Implicit large eddy simulation of low-Reynolds-number transitional flow past the SD7003 airfoil. In *40th fluid dynamics conference and exhibit*, page 4737, 2010.

[84] M. Galbraith and M. Visbal. Implicit large eddy simulation of low-Reynolds-number transitional flow past the SD7003 airfoil. In AIAA, editor, *40th Fluid Dynamics Conference and Exhibit*, Chicago, Illinois, 2010.

[85] A. Garofano-Soldado, P. J. Sanchez-Cuevas, G. Heredia, and A. Ollero. Numerical-experimental evaluation and modelling of aerodynamic ground effect for small-scale tilted propellers at low Reynolds numbers. *Aerospace Science and Technology*, page 107625, 2022.

[86] M. Gaster. The Structure and Behaviour of Laminar Separation Bubbles. Aeronautical Research Council Reports and Memoranda No. 3595, March 1967.

[87] R. Gerboni, G. Ledda, A. Moscatello, A. C. Uggenti, and A. Carpignano. Fluid-Dynamic Calibration of an Atmospheric Wind Tunnel Applied to Test Offshore Infrastructures. In *OMC Med Energy Conference and Exhibition*. OnePetro, 2021.

[88] M. Germano, U. Piomelli, P. Moin, and W.H. Cabot. A dynamic subgrid-scale eddy viscosity model. *Physics of Fluids A: Fluid Dynamics*, 3(7):1760–1765, 1991.

[89] H. Glauert. The effect of compressibility on the lift of an aerofoil. *Proceedings of the Royal Society of London. Series A, Containing Papers of a Mathematical and Physical Character*, 118(779):113–119, 1928.

[90] H. Glauert. Aerodynamic theory. *The Aeronautical Journal*, 34(233):409–414, 1930.

[91] F. Götten, D. F. Finger, M. Havermann, M. Marino, and C. Bil. A highly automated method for simulating airfoil characteristics at low Reynolds number using a RANS-transition approach. In *German Aerospace Congress 2019*, 2019.

[92] S. Grant, J. Perine, F. Abi-Akar, T. Lane, B. Kent, C. Mohler, C. Scott, and A. Ritter. A Wind-Tunnel Assessment of Parameters That May Impact Spray Drift during UAV Pesticide Application. *Drones*, 6(8):204, 2022.

[93] L. Greengard and V. Rokhlin. A fast algorithm for particle simulations. *Journal of computational physics*, 135(2):280–292, 1997.

[94] R. Hain, C. Kähler, and R. Radespiel. Dynamics of Laminar Separation Bubbles at Low-Reynolds-Number Aerofoils. *Journal of Fluid Mechanics*, 630:129–153, 2009.

[95] K. Hansen, R. Kelso, A. Choudhry, and M. Arjomandi. Laminar separation bubble effect on the lift curve slope of an airfoil. In *19th Australasian Fluid Mechanics Conference*, pages 8–11. RMIT University, 2014.

[96] N. S. Hariharan. An overview of wake-breakdown in high-fidelity simulations of rotor in hover. In *AIAA Scitech 2020 Forum*, page 0530, 2020.

[97] N. S. Hariharan, T. A. Egolf, and L. N. Sankar. Simulation of rotor in hover: Current state, challenges and standardized evaluation. In *52nd Aerospace Sciences Meeting*, National Harbor, MD, USA, January 2014. AIAA-2014-0041.

[98] M. Hepperle. JavaProp - Design and Analysis of Propellers. http://www.mh-aerotools.de/airfoils/javaprop.htm, 2001. Accessed: 2023-01-01.

[99] M. Idrissi, M. Salami, and F. Annaz. A Review of Quadrotor Unmanned Aerial Vehicles: Applications, Architectural Design and Control Algorithms. *Journal of Intelligent & Robotic Systems*, 104(2):1–33, 2022.

[100] Y. Jo, T. Jardin, R. Gojon, M.C. Jacob, and J-M. Moschetta. Prediction of noise from low Reynolds number rotors with different number of blades using a non-linear vortex lattice method. In *25th AIAA/CEAS Aeroacoustics Conference*, page 2615, 2019.

[101] W. Johnson, S. Withrow-Maser, L. Young, C. Malpica, W. J. F. Koning, W. Kuang, M. Fehler, A. Tuano, A. Chan, A. Datta, C. Chi, R. Lumba, D. Escobar, J. Balaram, T. Tzanetos, and H. Grip. Mars Science Helicopter Conceptual Design. *NASA TM-2020-220485*, Mar. 2020.

[102] W. Johnson, S. Withrow-Maser, L. Young, C. Malpica, W. J. F. Koning, W. Kuang, M. Fehler, A. Tuano, A. Chan, A. Datta, et al. Mars science helicopter conceptual design. Technical report, 2020.

[103] A. I. Jose. *Investigation into the Aerodynamics of Swashplateless Rotors Using CFD-CSD Analysis*. PhD thesis, University of Maryland, 2012.

[104] M. Kazim, A. T. Azar, A. Koubaa, and A. Zaidi. Disturbance-rejection-based optimized robust adaptive controllers for UAVs. *IEEE Systems Journal*, 15(2):3097–3108, 2021.

[105] W. J. F. Koning, W. Johnson, and B. G. Allan. Generation of Mars Helicopter Rotor Model for Comprehensive Analyses. *AHS Aeromechanics Design for Transformative Vertical Flight*, 2018.

[106] W. J. F. Koning, W. Johnson, and H. F. Grip. Improved Mars helicopter aerodynamic rotor model for comprehensive analyses. *AIAA Journal*, 57(9):3969–3979, 2019.

[107] W. J. F. Koning, E. A. Romander, and W. Johnson. Low reynolds number airfoil evaluation for the mars helicopter rotor. In *Annual Forum and Technology Display*, number ARC-E-DAA-TN53889, 2018.

[108] W. J. F. Koning, E. A. Romander, and W. Johnson. Optimization of Low Reynolds Number Airfoils for Martian Rotor Applications Using an Evolutionary Algorithm. In *AIAA SciTech 2020 Forum*, Orlando, FL, January January 2020. AIAA-2020-0084.

[109] B. M. Kulfan. The CST universal parametric geometry representation method, recent extensions and applications. In *Proc R Aeronaut Soc Conf*, volume 114, pages 157–176, 2007.

[110] A. Kummerländer, S. Avis, H. Kusumaatmaja, F. Bukreev, M. Crocoll, D. Dapelo, N. Hafen, S. Ito, J. Jeßberger, J. E. Marquardt, J. Mödl, T. Pertzel, F. Prinz, F. Raichle, M. Schecher, S Simonis, D. Teutscher, and M. J. Krause. OpenLB Release 1.6: Open Source Lattice Boltzmann Code, April 2023.

[111] P. J. Kunz. *Aerodynamics and design for ultra-low Reynolds number flight*. PhD thesis, Standford University, 2003.

[112] R. Langtry, J. Gola, and F. Menter. Predicting 2D airfoil and 3D wind turbine rotor performance using a transition model for general CFD codes. In *44th AIAA aerospace sciences meeting and exhibit*, page 395, 2006.

[113] R. .B. Langtry, F. Menter, S. R. Likki, Y. Suzen, P. Huang, and S. Völker. A Correlation-Based Transition Model Using Local Variables — Part II: Test Cases and Industrial Applications. *Journal of Turbomachinery*, 128(3):423–434, July 2006.

[114] R. B. Langtry and F. R. Menter. Correlation-Based Transition Modeling for Unstructured Parallelized Computational Fluid Dynamics Codes. *AIAA Journal*, 47(12):2894–2906, 2009.

[115] R.B. Langtry. *A Correlation-Based Transition Model using Local Variables for Unstructured Parallelized CFD Codes*. PhD Thesis, Universität Stuttgart, Fakultät Maschinenbau, 2006.

[116] E. Laurila, J. Roenby, V. Maakala, P. Peltonen, H. Kahila, and V. Vuorinen. Analysis of viscous fluid flow in a pressure-swirl atomizer using large-eddy simulation. *International Journal of Multiphase Flow*, 113:371–388, 2019.

[117] G. Le Bouar, M. Costes, A. Leroy-Chesneau, and P. Devinant. Numerical simulations of unsteady aerodynamics of helicopter rotor in maneuvering flight conditions. *Aerospace Science and Technology*, 8(1):11–25, 2004.

[118] A. H. Lefebvre and V. G. McDonell. *Atomization and sprays*. CRC press, 2017.

[119] Gordon J Leishman. *Principles of helicopter aerodynamics*. Cambridge university press, 2006.

[120] X. Li, D. K. Giles, F. J. Niederholzer, J. T. Andaloro, E. B. Lang, and L. J. Watson. Evaluation of an unmanned aerial vehicle as a new method of pesticide application for almond crop protection. *Pest Management Science*, 77(1):527–537, 2021.

[121] D. K. Lilly. A proposed modification of the germano subgrid-scale closure method. *Physics of Fluids A: Fluid Dynamics*, 4(3):633–635, 1992.

[122] M. Liou. A sequel to ausm: Ausm+. *Journal of computational Physics*, 129(2):364–382, 1996.

[123] Q. Liu, S. Chen, G. Wang, and Y. Lan. Drift Evaluation of a Quadrotor Unmanned Aerial Vehicle (UAV) Sprayer: Effect of Liquid Pressure and Wind Speed on Drift Potential Based on Wind Tunnel Test. *Applied Sciences*, 11(16):7258, 2021.

[124] P. Malan, K. Suluksna, and E. Juntasaro. Calibrating the $\gamma - Re_\theta$ Transition Model for Commercial CFD. In *47th AIAA Aerospace Sciences Meeting*, Reno, NV, USA, January 2009. AIAA-2009-1142.

[125] A. Manavella. Low Reynolds number propeller performance validation by CFD analysis and reduced order models. Master's thesis, Politecnico di Torino, 2021. https://webthesis.biblio.polito.it/18279.

[126] C. Manca. Swashplateless MAV: performance evaluation through CFD analysis and comparison with experimental bench tests. Master's thesis, Politecnico di Torino, 2021. https://webthesis.biblio.polito.it/20010/.

[127] D. Marten, M. Lennie, G. Pechlivanoglou, C. N. Nayeri, and C. O. Paschereit. Implementation, optimization, and validation of a nonlinear lifting line-free vortex wake module within the wind turbine simulation code QBLADE. *Journal of Engineering for Gas Turbines and Power*, 138(7), 2016.

[128] D. Marten, J. Wendler, G. Pechlivanoglou, C. N. Nayeri, and C. O. Paschereit. QBLADE: an open source tool for design and simulation of horizontal and vertical axis wind turbines. *International Journal of Emerging Technology and Advanced Engineering*, 3(3):264–269, 2013.

[129] J. Martinez-Guanter, P. Agüera, J. Agüera, and M. Pérez-Ruiz. Spray and economics assessment of a UAV-based ultra-low-volume application in olive and citrus orchards. *Precision Agriculture*, 21(1):226–243, 2020.

[130] The Mathworks, Inc., Natick, Massachusetts. *MATLAB version 9.10.0.1613233 (R2021a)*, 2021.

[131] A. Matus-Vargas, G. Rodríguez-Gómez, and J. Martínez-Carranza. Aerodynamic disturbance rejection acting on a quadcopter near ground. In *2019 6th International Conference on Control, Decision and Information Technologies (CoDIT)*, pages 1516–1521. IEEE, 2019.

[132] A. Matus-Vargas, G. Rodriguez-Gomez, and J. Martinez-Carranza. Ground effect on rotorcraft unmanned aerial vehicles: A review. *Intelligent Service Robotics*, 14(1):99–118, 2021.

[133] R. J. McGhee, B. S. Walker, and B. F. Millard. Experimental Results for the Eppler 387 Airfoil at Low Reynolds Numbers in the Langley Low-Turbulence Pressure Tunnel. NASA-TM-4062, NASA Langley Research Center, 1988.

[134] Y. Meng, J. Su, J. Song, W.-H. Chen, and Y. Lan. Experimental evaluation of UAV spraying for peach trees of different shapes: Effects of operational parameters on droplet distribution. *Computers and Electronics in Agriculture*, 170:105282, 2020.

[135] F. R. Menter. Two-equation eddy-viscosity turbulence models for engineering applications. *AIAA Journal*, 32(8):1598–1605, 1994.

[136] F. R. Menter and M. Kuntz. Adaptation of eddy-viscosity turbulence models to unsteady separated flow behind vehicles. In *The aerodynamics of heavy vehicles: trucks, buses, and trains*, pages 339–352. Springer, 2004.

[137] F. R. Menter, R. Langtry, and S. Völker. Transition Modelling for General Purpose CFD Codes. *Flow, Turbulence and Combustion*, 77:277–303, 2006.

[138] F. R. Menter, R. B. Langtry, S. R. Likki, Y.B. Suzen, P.G. Huang, and S. Völker. A correlation-based transition model using local variables: Part I—model formulation. In *Turbo Expo: Power for Land, Sea, and Air*, volume 41693, pages 57–67, 2004.

[139] F. R. Menter, P. E. Smirnov, T. Liu, and R. Avancha. A One-Equation Local Correlation-Based Transition Model. *Flow, Turbulence and Combustion*, 95:583–619, 2015.

[140] D. Montagnani, M. Tugnoli, F. Fonte, A. Zanotti, M. Syal, and G. Droandi. Mid-fidelity analysis of unsteady interactional aerodynamics of complex vtol configurations. In *45th European Rotorcraft Forum (ERF 2019)*, pages 100–110, 2019.

[141] J. Morgado, R. Vizinho, M.A.R. Silvestre, and J.C. Páscoa. XFOIL vs CFD performance predictions for high lift low Reynolds number airfoils. *Aerospace Science and Technology*, 52:207–214, 2016.

[142] F. Moukalled, L. Mangani, and M. Darwish. Gradient computation. In *The Finite Volume Method in Computational Fluid Dynamics*, pages 273–302. Springer, 2016.

[143] P. M. Munday, K. Taira, T. Suwa, D. Numata, and K. Asai. Nonlinear lift on a triangular airfoil in low-Reynolds-number compressible flow. *Journal of Aircraft*, 52(3):924–931, 2015.

[144] K. Nguyen and W. Johnson. Evaluation of dynamic stall models with uh-60a airloads flight test data. In *Annual forum proceedings-American helicopter society*, volume 54, pages 576–588. American Helicopter Society, 1998.

[145] F. Nicoud and F. Ducros. Subgrid-scale stress modelling based on the square of the velocity gradient tensor. *Flow, turbulence and Combustion*, 62(3):183–200, 1999.

[146] G. Niedrist, A. Nollo, H. Brugger, A. Vilardi, G. Leitinger, and U. Tappeiner. terraXcube: An emerging ecotrone to converge chamber experiments and environmental studies in alpine ecology. In *Proceedings of the 20th EGU General Assembly, EGU2018*, page 13616, Vienna, Austria, April, 4-13, 2018.

[147] D. Nuyttens, K. Baetens, M. De Schampheleire, and B. Sonck. Effect of nozzle type, size and pressure on spray droplet characteristics. *Biosystems engineering*, 97(3):333–345, 2007.

[148] M. V. Ol, B. McCauliffe, E. Hanff, U. Scholz, and C. Kähler. Comparison of Laminar Separation Bubble Measurements on a Low Reynolds Number Airfoil in Three Facilities. In *35th AIAA Fluid Dynamics Conference and Exhibit*, June 2005. AIAA-2005-5149.

[149] D. Park, H. Shim, and Y. Lee. PIV measurement of separation bubble on an airfoil at low Reynolds numbers. *Journal of Aerospace Engineering*, 33(1):04019105, 2020.

[150] L. L. Pauley, P. Moin, and W. C. Reynolds. The Structure of Two-Dimensional Separation. *Journal of Fluid Mechanics*, 220:397–411, 1990.

[151] J. Paulos, B. Caraher, and M. Yim. Emulating a fully actuated aerial vehicle using two actuators. In *2018 IEEE International Conference on Robotics and Automation (ICRA)*, pages 7011 – 7016. IEEE, 2018.

[152] J. Paulos and M. Yim. An underactuated propeller for attitude control in micro air vehicles. In *2 013 IEEE/RSJ International Conference on Intelligent Robots and Systems*, pages 1374 – 1379. IEEE, 2013.

[153] J. Paulos and M. Yim. Flight performance of a swashplateless micro air vehicle. In *2015 IEEE International Conference on Robotics and Automation (ICRA)*, pages 5284 – 5289. IEEE, 2015.

[154] J. Paulos and M. Yim. Scalability of cyclic control without blade pitch actuators. In *2018 AIAA Atmospheric Flight Mechanics Conference*, page 0532, 2018.

[155] S. Pawar and S. Brizzolara. Relevance of transition turbulent model for hydrodynamic characteristics of low Reynolds number propeller. *Applied Ocean Research*, 87:165–178, 2019.

[156] C. Paz, E. Suárez, C. Gil, and C. Baker. CFD analysis of the aerodynamic effects on the stability of the flight of a quadcopter UAV in the proximity of walls and ground. *Journal of Wind Engineering and Industrial Aerodynamics*, 206:104378, 2020.

[157] G. Pedrizzetti. Insight into singular vortex flows. *Fluid Dynamics Research*, 10(2):101–115, August 1992.

[158] B. N. Perez Perez. Forward Flight Rotor Performance at Martian Atmospheric Densities and Sensitivity to Low Reynolds Numbers. In *VFS Technical Meeting on Aeromechanics for Advanced Vertical Flight*, San Jose, CA, January 21–23, 2020.

[159] M. Peric and S. Ferguson. The advantage of polyhedral meshes. *Dynamics*, 24:45, 2005.

[160] M. A. Potsdam and R. C. Strawn. CFD simulations of tiltrotor configurations in hover. *Journal of the American Helicopter Society*, 50(1):82–94, 2005.

[161] S. Prothin and J. Moschetta. A vectoring thrust coaxial rotor for micro air vehicle: Modeling, design and analysis. In *ERCOFTAC international symposium «Unsteady separation in fluid-structure interaction»*, June 2013.

[162] S. Puneet. *Aeromechanics of Coaxial Rotor Helicopters using the Viscous Vortex Particle Method*. PhD thesis, University of Michigan, 2020. https://deepblue.lib.umich.edu/handle/2027.42/163227.

[163] R. Radespiel and J. Windte. Numerical simulation of laminar separation bubbles with RANS solutions. In *Low Reynolds Number Aerodynamics on Aircraft including applications in emerging UAV technology*. RTO-EN-AVT-104, 2003.

[164] P. Radoglou-Grammatikis, P. Sarigiannidis, T. Lagkas, and I. Moscholios. A compilation of UAV applications for precision agriculture. *Computer Networks*, 172:107148, 2020.

[165] F. Ricci, P. Silva, P. Tsoutsanis, and A. F. Antoniadis. Hovering rotor solutions by high-order methods on unstructured grids. *Aerospace Science and Technology*, 97:105648, 2020.

[166] D. C. Robinson, H. Chung, and K. Ryan. Computational investigation of micro rotorcraft near-wall hovering aerodynamics. In *2014 International Conference on Unmanned Aircraft Systems (ICUAS)*, pages 1055–1063. IEEE, 2014.

[167] G. Romani, E. Grande, F. Avallone, D. Ragni, and D. Casalino. Performance and noise prediction of low-Reynolds number propellers using the lattice-Boltzmann method. *Aerospace Science and Technology*, 125:107086, 2022.

[168] C. L. Rumsey. Langley Research Center. Turbulence Modeling Resource. 2D NACA 0012 airfoil validation case. Effect of farfield boundary. https://turbmodels.larc.nasa.gov/naca0012_val_ffeffect.html, 2014. Accessed: January 24, 2022.

[169] C. L. Rumsey and P. R. Spalart. Turbulence Model Behavior in Low Reynolds Number Regions of Aerodynamic Flowfields. *AIAA Journal*, 47(4):982–993, 2009.

[170] C. R. Russell and M. K. Sekula. Comprehensive Analysis Modeling of Small-Scale UAS Rotors. In *AHS International 73rd Annual Forum & Technology Display*, pages 1–16, Fort Worth, TX, May 9-11, 2017.

[171] M. Sahin, J. Hall, K. Mohseni, and K. Hillewaert. Direct Numerical Simulation of Separated Low-Reynolds Number Flows around an Eppler 387 Airfoil. In *46th AIAA Aerospace Sciences Meeting and Exhibit*, January 2008. AIAA-2008-422.

[172] A. L. Salih, M. Moghavvemi, H.A.F. Mohamed, and Khalaf Sallom Gaeid. Flight PID controller design for a UAV quadrotor. *Scientific research and essays*, 5(23):3660–3667, 2010.

[173] E. Salimipour. A modification of the k-kL-ω turbulence model for simulation of short and long separation bubbles. *Computers & Fluids*, 181:67–76, 2019.

[174] T. Sant. *Improving BEM-based Aerodynamic Models in Wind Turbine Design Codes*. PhD thesis, Delft University of Technology, 2007. http://resolver.tudelft.nl/uuid:4d0e894c-d0ad-4983-9fa3-505a8c6869f1.

[175] D. Sarri, L. Martelloni, M. Rimediotti, R. Lisci, S. Lombardo, and M. Vieri. Testing a multi-rotor unmanned aerial vehicle for spray application in high slope terraced vineyard. *Journal of Agricultural Engineering*, 50(1):38–47, 2019.

[176] L. Scagnellato, M. Lecce, N. Bloise, M. Carreño Ruiz, E. Capello, and G. Guglieri. Adaptive path planning for spraying UAS in vineyard under variable wind condition. In *ICAS 2022*, 2022.

[177] M. Scanavino. *Design and testing methodologies for UAVs under extreme environmental conditions*. PhD thesis, Politecnico di Torino, 2021.

[178] M. Scanavino, A. Avi, A. Vilardi, and G. Guglieri. UAS testing in low pressure and temperature conditions. In *2020 International Conference on Unmanned Aircraft Systems (ICUAS)*, pages 1757–1765, Athens, Greece, September 2020. IEEE.

[179] M. Scanavino, A. Vilardi, and G. Guglieri. An Experimental Analysis on Propeller Performance in a Climate-controlled Facility. *Journal of Intelligent & Robotic Systems*, 100(2):505–517, 2020.

[180] A. R. Schenk. Computational investigation of the effects of rotor-on-rotor interactions on thrust and noise. Master's thesis, Brigham Young University, 2020.

[181] L. Schiller. Über die grundlegenden Berechnungen bei der Schwerkraftaufbereitung. *Z. Vereines Deutscher Inge.*, 77:318–321, 1933.

[182] H. Schlichting and K. Gersten. *Boundary-layer theory*. Springer, 2016.

[183] M. Selig. Low reynolds number airfoil design lecture notes. *VKI Lecture Series*, pages 24–28, November, 2003. https://m-selig.ae.illinois.edu/pubs/Selig-2003-VKI-LRN-Airfoil-Design-Lecture-Series.pdf.

[184] A. A. Shabana. *Computational dynamics*. John Wiley & Sons, 2009.

[185] K. V. Sharma, R. Straka, and F. W. Tavares. Current status of Lattice Boltzmann Methods applied to aerodynamic, aeroacoustic, and thermal flows. *Progress in Aerospace Sciences*, 115:100616, 2020.

[186] Q. Shi, Y. Pan, B. He, H. Zhu, D. Liu, B. Shen, and H. Mao. The airflow field characteristics of UAV flight in a greenhouse. *Agriculture*, 11(7):634, 2021.

[187] R. Shrestha, M. Benedict, V. Hrishikeshavan, and I. Chopra. Hover Performance of a Small-Scale Helicopter Rotor for Flying on Mars. *Journal of Aircraft, Vol. 53, No. 4*, pages 1160–1167, Jul.-Aug. 2016.

[188] PLM Siemens. STAR-CCM+ User Guide Version 14.06. *Siemens PLM software Inc*, 2019.

[189] Siemens Digital Industries Software. Simcenter STAR-CCM+ User Guide v. 2019.3, Siemens 2019.

[190] M. A. Silvestre, J. P. Morgado, and J. Pascoa. JBLADE: a propeller design and analysis code. In *2013 International Powered Lift Conference*, page 4220, 2013.

[191] M. Sommerfeld. Theoretical and experimental modelling of particulate flows. *VKI Lecture Series*, 6:3–7, 2000.

[192] P. R. Spalart and S. Allmaras. A one-equation turbulence model for aerodynamic flows. In *30th Aerospace Sciences Meeting and Exhibit*, January January 1992. AIAA 1992-0439.

[193] P. R. Spalart, S. Deck, M. L. Shur, K. D. Squires, M. K. Strelets, and A. Travin. A new version of detached-eddy simulation, resistant to ambiguous grid densities. *Theoretical and computational fluid dynamics*, 20:181–195, 2006.

[194] P. R. Spalart and C. L. Rumsey. Effective Inflow Conditions for Turbulence Models in Aerodynamic Calculations. *AIAA journal*, 45(10):2544–2553, 2007.

[195] R. Strawn and J. Ahmad. Computational modeling of hovering rotors and wakes. In *38th Aerospace Sciences Meeting and Exhibit*, page 110, 2000.

[196] P. Strobel, P. Tsoutsanis, A. Antoniadis, and K. Jenkins. Unstructured high-order solutions of hovering rotors with and without ground effect. In *8th European Congress on Computational Methods in Applied Sciences and Engineering*, January 2022.

[197] M. Sugiura, Y. Tanabe, H. Sugawara, K. Kimura, A. Oyama, M. Sato, K. Yoshikawa, Y. Buto, M. Kanazaki, and et al. Blade Shape Optimization of Mars Helicopter Exploring Pit Craters. Fort Worth, Texas, USA, May 10-12 2022. Vertical Flight Society.

[198] K. Suluksna, P. Dechaumphai, and E. Juntasaro. Correlations for modeling transitional boundary layers under influences of freestream turbulence and pressure gradient. *International Journal of Heat and Fluid Flow*, 30(1):66–75, 2009.

[199] T. Suwa, K. Nose, D. Numata, H. Nagai, and K. Asai. Compressibility Effects on Airfoil Aerodynamics at Low Reynolds Number. *30th AIAA Applied Aerodynamics Conference*, Jun. 25-28 2012.

[200] G. Szafranski and R. Czyba. Different approaches of PID control UAV type quadrotor. 2011.

[201] L. A. Barba T. Wang, R. Yokota. ExaFMM: a high-performance fast multipole method library with C++ and Python interfaces. *The Journal of Open Source Software*, 2021.

[202] T. Theodorsen. General theory of aerodynamic instability and the mechanism of flutter. NACA TR 496, 1949.

[203] N. Tsuzuki, S. Sato, and T. Abe. Conceptual Design and Feasibility for a Miniature Mars Exploration Rotorcraft. In *Proceedings of the 24th International Congress of the Aeronautical Sciences*, pages 1–10, Yokohama, Japan, Sept. 2004. International Congress of Aeronautical Sciences Paper 2004-1.8.2.

[204] UIUC Applied Aerodynamics Group. Low Reynolds Number Airfoil Data and Documentation. https://m-selig.ae.illinois.edu/uiuc_lsat.html. Accessed: March 13, 2020.

[205] A. Uranga. *Investigation of Transition to Turbulence at Low Reynolds Numbers using Implicit Large Eddy Simulations with a Discontinuous Galerkin Method*. PhD thesis, University of California, Berkeley, 2010.

[206] A. Uranga, P. O. Persson, M. Drela, and J. Peraire. Implicit Large Eddy Simulation of Transitional Flows Over Airfoils and Wings. In *19th AIAA Computational Fluid Dynamics*, June 2009. AIAA 2009-4131.

[207] K. Uwatoko, M. Kanazaki, H. Nagai, K. Fujita, and A. Oyama. Blade Element Theory Coupled with CFD Applied to Optimal Design of Rotor For Mars Exploration Helicopter. AIAA, Jan. 6-10, 2020.

[208] K. P. Valavanis and G. J. Vachtsevanos. *Handbook of Unmanned Aerial Vehicles*. New York, NY, USA: Springer, 2014.

[209] M. Van Dyke. *An album of fluid motion*, volume 176. Parabolic Press Stanford, 1982.

[210] A. Van Garrel. Development of a wind turbine aerodynamics simulation module. ECN-C–03-079, ECN Wind Energy, 2003. https://publications.ecn.nl/WIN/2003/ECN-C–03-079.

[211] V. Venkatakrishnan. On the convergence of limiters and convergence to steady state solutions. In *AIAA, 31st Aerospace Sciences Meeting*, 1994.

[212] P. Ventura Diaz and S. Yoon. High-fidelity computational aerodynamics of multi-rotor unmanned aerial vehicles. In *2018 AIAA Aerospace Sciences Meeting*, page 1266, 2018.

[213] P. Ventura Diaz and S. Yoon. High-Fidelity Simulations of a Quadrotor Vehicle for Urban Air Mobility. In *AIAA SciTech 2022 Forum*, San Diego, CA, January 2022. AIAA-2022-0152.

[214] D. K. Walters and D. Cokljat. A three-equation eddy-viscosity model for Reynolds-Averaged Navier-Stokes simulations of transitional flow. *ASME Journal of Fluids Engineering*, 130(12), October 2008.

[215] C. Wang, A. Herbst, A. Zeng, S. Wongsuk, B. Qiao, P. Qi, J. Bonds, V. Overbeck, Y. Yang, W. Gao, et al. Assessment of spray deposition, drift and mass balance from unmanned aerial vehicle sprayer using an artificial vineyard. *Science of The Total Environment*, 777:146181, 2021.

[216] G. Wang, Y. Han, X. Li, J. Andaloro, P. Chen, W. C. Hoffmann, X. Han, S. Chen, and Y. Lan. Field evaluation of spray drift and environmental impact using an agricultural unmanned aerial vehicle (UAV) sprayer. *Science of the Total Environment*, 737:139793, 2020.

[217] L. Wang, M. Xu, Q. Hou, Z. Wang, Y. Lan, and S. Wang. Numerical verification on influence of multi-feature parameters to the downwash airflow field and operation effect of a six-rotor agricultural UAV in flight. *Computers and Electronics in Agriculture*, 190:106425, 2021.

[218] P. Wang, Z. Man, Z. Cao, J. Zheng, and Y. Zhao. Dynamics modelling and linear control of quadcopter. In *2016 International Conference on Advanced Mechatronic Systems (ICAMechS)*, pages 498–503. IEEE, 2016.

[219] A. N. Watkins, B. D. Leighty, W. E. Lipford, K. Z. Goodman, J. Crafton, and J. W. Gregory. Measuring surface pressures on rotor blades using pressure-sensitive paint. *AIAA Journal*, 54(1):206–215, 2016.

[220] J. Webster. *Design and Analysis of Low Reynolds Number Marine Propellers with Computational Fluid Dynamics (CFD) Transition Modeling*. PhD thesis, Virginia Tech, 2019.

[221] J. Webster, W. Neu, and S. Brizzolara. Reynolds Stress Transition Modeling for Marine Propellers at Low Reynolds Number. In *Sixth International Symposium on Marine Propulsors: Smp19*, Rome, Italy, May 2019.

[222] J. M. Weiss, J. P. Maruszewski, and W. A Smith. Implicit solution of preconditioned navier-stokes equations using algebraic multigrid. *AIAA journal*, 37(1):29–36, 1999.

[223] J. M. Weiss and W. A. Smith. Preconditioning applied to variable and constant density flows. *AIAA journal*, 33(11):2050–2057, 1995.

[224] S. Wen, J. Han, Z. Ning, Y. Lan, X. Yin, J. Zhang, and Y. Ge. Numerical analysis and validation of spray distributions disturbed by quad-rotor drone wake at different flight speeds. *Computers and Electronics in Agriculture*, 166:105036, 2019.

[225] G. S. Winckelmans and A. Leonard. Contributions to vortex particle methods for the computation of three-dimensional incompressible unsteady flows. *Journal of Computational Physics*, 109(2):247–273, 1993.

[226] G. S. Wincklemans. *Topics in vortex methods for the computation of three- and two-dimensional incompressible unsteady flows*. PhD thesis, California Institute of Technology, February 1989.

[227] J. Windte, U. Scholz, and R. Radespiel. Validation of the RANS-simulation of laminar separation bubbles on airfoils. *Aerospace science and technology*, 10(6):484–494, 2006.

[228] F. Yang, X. Xue, C. Cai, Z. Sun, and Q. Zhou. Numerical simulation and analysis on spray drift movement of multirotor plant protection unmanned aerial vehicle. *Energies*, 11(9):2399, 2018.

[229] S. Yoon, N. Chaderjian, T.H. Pulliam, and T. Holst. Effect of turbulence modeling on hovering rotor flows. In *45th AIAA Fluid Dynamics Conference*, page 2766, 2015.

[230] Y. Zhan, P. Chen, W. Xu, S. Chen, Y. Han, Y. Lan, and G. Wang. Influence of the downwash airflow distribution characteristics of a plant protection UAV on spray deposit distribution. *Biosystems Engineering*, 216:32–45, 2022.

[231] H. Zhang, L. Qi, Y. Wu, E. M. Musiu, Z. Cheng, and P. Wang. Numerical simulation of airflow field from a six–rotor plant protection drone using lattice Boltzmann method. *Biosystems Engineering*, 197:336–351, 2020.

[232] Y. Zhang, Z. Chen, X. Zhang, Q. Sun, and M. Sun. A novel control scheme for quadrotor UAV based upon active disturbance rejection control. *Aerospace Science and Technology*, 79:601–609, 2018.

[233] P. Zhao, Q. Quan, S. Chen, D. Tang, and Z. Deng. Experimental investigation on hover performance of a single-rotor system for Mars helicopter. *Aerospace Science and Technology*, 86:582–591, 2019.